

Report Title

Electrochemical Energy Summit--An International Summit in Support of Societal Energy Needs

ABSTRACT

On October 10 to 12, 2011, The Electrochemical Society, Inc., held its first Electrochemical Energy Summit, E2S. The objective of the first E2S was to bring policy makers and researchers together to discuss what the world's energy needs are and what answers electrochemical science and technology can provide. The first E2S consisted of a poster session, which provided an opportunity for scientists to present their solutions, a panel discussion made of representatives from the U.S.A., Japan, and Germany and a plenary lecture.

These proceedings present a selected number of papers presented as posters at the summit.

Conference Name: Electrochemical Energy Summit 2011

Conference Date: October 10, 2011

Electrochemical Energy Summit – An International Summit in Support of Societal Energy Needs

Editors:

C. Bock

National Research Council Canada
Ottawa, Ontario, Canada

J. Leddy

The University of Iowa
Iowa City, Iowa, USA

Sponsoring Divisions:



All Divisions



Published by

The Electrochemical Society

65 South Main Street, Building D
Pennington, NJ 08534-2839, USA

tel 609 737 1902

fax 609 737 2743

www.electrochem.org

ecstransactions™

Vol. 41, No. 31

Copyright 2012 by The Electrochemical Society.
All rights reserved.

This book has been registered with Copyright Clearance Center.
For further information, please contact the Copyright Clearance Center,
Salem, Massachusetts.

Published by:

The Electrochemical Society
65 South Main Street
Pennington, New Jersey 08534-2839, USA

Telephone 609.737.1902
Fax 609.737.2743
e-mail: ecs@electrochem.org
Web: www.electrochem.org

ISSN 1938-6737 (online)
ISSN 1938-5862 (print)
ISSN 2151-2051 (cd-rom)

ISBN 978-1-56677-971-5 (PDF)
ISBN 978-1-60768-330-8 (Softcover)

Printed in the United States of America.

PREFACE

On October 10 to 12, 2011, The Electrochemical Society, Inc., held its first Electrochemical Energy Summit, E2S. The objective of the first E2S was to bring policy makers and researchers together to discuss what the world's energy needs are and what answers electrochemical science and technology can provide. The first E2S consisted of a poster session, which provided an opportunity for scientists to present their solutions, a panel discussion made of representatives from the U.S.A., Japan, and Germany and a plenary lecture.

The plenary lecture was delivered by Mark Verbrugge, Director of the Materials and Processes Laboratory of General Motors and was entitled "Energy and Personal Transportation". The panel discussion was lively and emphasized the need for education and discussions. A H₂ fuel cell car was available for viewing by ProtonOnSite during the course of E2S.

This issue of *ECS Transactions* presents a selected number of papers presented as posters at the summit. The first E2S was well received and ECS hopes to continue this activity and engage policy makers and scientists in fruitful dialogues and to find solutions to address the world's energy needs. The organizers of the summit hope that this activity will continue and become a tradition and a part of regular ECS meetings.

The E2S was organized by the ECS Treasurer, Christina Bock, National Research Council of Canada, and ECS Secretary Johna Leddy, The University of Iowa. The meeting was supported by the Army Research Office and the extraordinary efforts of the staff and Executive Committee of the Electrochemical Society.

Table of Contents

<i>Preface</i>	<i>iii</i>
Study of Alkaline Water Electrolysis <i>A. Manabe, T. Hashimoto, and M. Kashiwase</i>	1
Microbial Tango with <i>Shewanella Oneidensis</i> : Design Elements and Application of a Novel Renewable Energy Source Using Wastewater Containing Organic Compounds <i>H. E. Braustein</i>	9
Rechargeable Batteries for the 300-Mile Electric Vehicle and Beyond <i>K. Abraham</i>	27
Hydrogen and Fuel Cell Technology Demonstrations in Developing Countries: Turkey Example <i>M. Yazici, N. LyMBERopoulos, and M. Hatipoglu</i>	35
Pressurized Solid Oxide Fuel Cells with Reformate as Fuel <i>C. Willich, C. Westner, M. Henke, F. Leucht, J. Kallo, U. Maier, and K. Friedrich</i>	43
Nano Facilitated Charge Transfer for an 11 Electron Redox Couple for Anodic Charge Storage: VB_2 <i>S. Licht, J. Lau, C. Hettige, H. Wu, B. Wang, J. Asercion, U. Cubeta, and J. Stuart</i>	55
$\text{LiNi}_{0.4}\text{Mn}_{1.6}\text{O}_4$ / Electrolyte and Carbon Black / Electrolyte High Voltage Interfaces: To Evidence the Chemical and Electronic Contributions of the Solvent on the Cathode-Electrolyte Interface Formation <i>J. Demeaux, M. Caillon-Caravanier, H. Galiano, D. Lemordant, and B. Claude-Montigny</i>	65
Fuel Cell Performances of Bio-Membranes Made of Chitosan-Polyelectrolyte Thin Films and Nanowires into Anodic Alumina Membranes <i>P. Bocchetta, F. Conciauro, M. Santamaria, and F. Di Quarto</i>	79

Magnesium Recycling of Partially Oxidized, Mixed Magnesium-Aluminum Scrap through Combined Refining and Solid Oxide Membrane Electrolysis Processes <i>X. Guan, P. A. Zink, U. B. Pal, and A. C. Powell</i>	91
Eutectic Mixtures of Ionic Liquids Electrolytes for Electric Double Layer Capacitors <i>S. Higashiya, T. Devarajan, M. V. Rane-Fondacaro, and P. Haldar</i>	103
Evaluation of Anode Electrode Materials for Cu-Cl/HCl Electrolyzers for Hydrogen Production <i>S. Ranganathan, P. S. Edge, and E. Easton</i>	111
Very Low Impedance Battery Architecture for Electrified Vehicles <i>T. D. Kaun and J. Sandahl</i>	121
Influence of Impurities in TiO ₂ Coatings on Electrode Potential of Photocatalytic Anode Assembling to Marine Microbial Fuel Cell <i>S. Motoda, S. Uematsu, and T. Shinohara</i>	129
Author Index	137



Facts about ECS

The Electrochemical Society (ECS) is an international, nonprofit, scientific, educational organization founded for the advancement of the theory and practice of electrochemistry, electrothermics, electronics, and allied subjects. The Society was founded in Philadelphia in 1902 and incorporated in 1930. There are currently over 7,000 scientists and engineers from more than 70 countries who hold individual membership; the Society is also supported by more than 100 corporations through Corporate Memberships.

The technical activities of the Society are carried on by Divisions. Sections of the Society have been organized in a number of cities and regions. Major international meetings of the Society are held in the spring and fall of each year. At these meetings, the Divisions and Groups hold general sessions and sponsor symposia on specialized subjects.

The Society has an active publications program that includes the following.

Journal of The Electrochemical Society — JES is the peer-reviewed leader in the field of electrochemical and solid-state science and technology. Articles are posted online as soon as they become available for publication. This archival journal is also available in a paper edition, published monthly following electronic publication.

Electrochemical and Solid-State Letters — ESL is the first and only rapid-publication electronic journal covering the same technical areas as JES. Articles are posted online as soon as they become available for publication. This peer-reviewed, archival journal is also available in a paper edition, published monthly following electronic publication. It is a joint publication of ECS and the IEEE Electron Devices Society.

Interface — *Interface* is ECS's quarterly news magazine. It provides a forum for the lively exchange of ideas and news among members of ECS and the international scientific community at large. Published online (with free access to all) and in paper, issues highlight special features on the state of electrochemical and solid-state science and technology. The paper edition is automatically sent to all ECS members.

Meeting Abstracts (formerly Extended Abstracts) — Abstracts of the technical papers presented at the spring and fall meetings of the Society are published on CD-ROM.

ECS Transactions — This online database provides access to full-text articles presented at ECS and ECS-sponsored meetings. Content is available through individual articles, or as collections of articles representing entire symposia.

Monograph Volumes — The Society sponsors the publication of hardbound monograph volumes, which provide authoritative accounts of specific topics in electrochemistry, solid-state science, and related disciplines.

For more information on these and other Society activities, visit the ECS website:

www.electrochem.org

Study of Alkaline Water Electrolysis

A. Manabe^a, T. Hashimoto^b, M. Kashiwase^b

^a Chlor-Alkali Div., Chlorine Engineers Corp., Ltd. Tokyo, 104-0044, Japan

^b C/A Div. Tech. Dept., Chlorine Engineers Corp., Ltd. Okayama, 706-0134, Japan

Chlorine Engineers Corp., Ltd. (CEC) is special electrochemical company in Japan and was established in 1973, when mercury process of chlor-alkali industry was abandoned by Japanese government. Since then, CEC has accumulated electrolysis technology and has an interest for future hydrogen society. In the background, zero gap system was applied for cell evaluation of alkali water electrolysis based on CEC's technology. A special electric collector for cathode was used to create zero gap without damaging the separator. Cell voltage was 1.76V at 40A/dm², 80 deg.C. Raney Ni alloy coating had advantage for oxygen over-voltage. (100mV – 200mV saving against Ni metal) Thermal decomposition coating of cathode showed low hydrogen over-voltage (around 100mV). Ion exchange membranes N117 and F8020 showed high cell voltage (over 2.2V) but high purity of H₂ gas (over 99.95%). Porous polyolefin film showed low cell voltage but had less durability.

Introduction

In these days, it is increasingly important to cut greenhouse gas emissions. The fuel cell vehicle is one alternative for reduction of CO₂ emission. SPE type pure water electrolysis shows good performance for hydrogen generation⁽¹⁾. However, if we consider the actual amount of hydrogen used in fuel cells, hydrogen plants of large capacity will be required to satisfy the ultimate demand of hydrogen. SPE type electrolysis would face real difficulty meeting such a large demand. Chlorine Engineers Corp., Ltd. (CEC) is one of the major electrolyzer manufacturers in the chlor-alkali industry and has great experience in cell design and cell technology. Alkaline water electrolysis is very similar to chlor-alkali electrolysis. We (CEC) can apply our chlor-alkali cell technology to alkaline water electrolysis. Table I shows the comparison between PEM type water electrolysis and alkaline type one.

Table I. Comparison between PEM type and Alkaline type

Type	Electrode reaction	Raw material	Advantage	Disadvantage
PEM-WE Polymer Electrolyte Membran Water Electrolysis	*Anode $\text{H}_2\text{O} \rightarrow 1/2\text{O}_2 + 2\text{H}^+ + 2\text{e}^-$ *Cathode $2\text{H}^+ + 2\text{e}^- \rightarrow \text{H}_2$	Pure water	High current density ----> Compact Safe raw material(=water) High purity of product H ₂	Expensive catalysts Short lifetime Hard to scale up capacity
AWE Alkaline Water Electrolysis	*Anode $2\text{OH}^- \rightarrow 1/2\text{O}_2 + \text{H}_2\text{O} + 2\text{e}^-$ *Cathode $2\text{H}_2\text{O} + 2\text{e}^- \rightarrow \text{H}_2 + 2\text{OH}^-$	Pure water in Strong Alkali solution (KOH, NaOH etc.)	Easy to scale up capacity Conventional technology Cheap initial cost Long life Atmospheric operation	High cell voltage ---->Low current density Dangerous chemical Treatment of alkali mist

Figure 1 shows the difference between chlor-alkali electrolysis and alkaline water electrolysis.

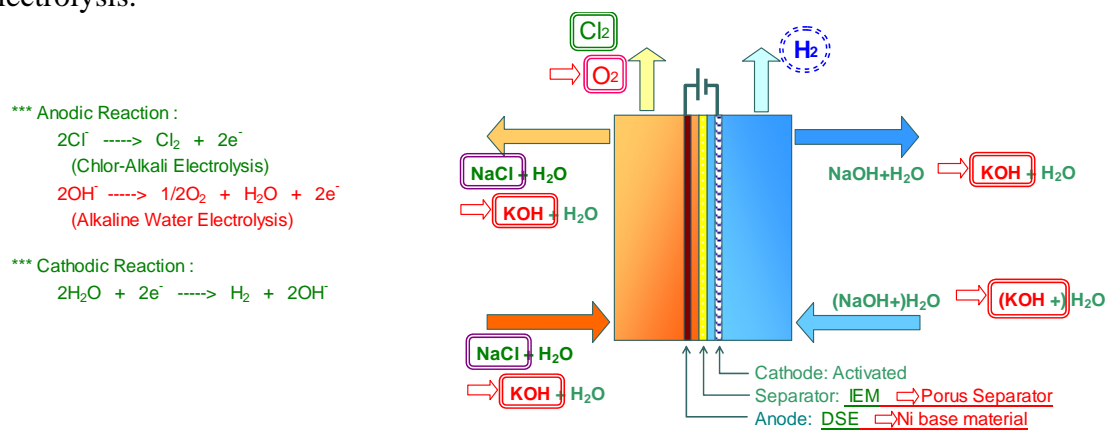


Figure 1. Comparison between Chlor-alkali and Alkaline water electrolysis

In order to utilize CEC's technology for alkaline water electrolysis, CEC applied its advanced cell concept and studied operating conditions and performance of each electrode and separator.

Standard bipolar electrolyzer (BiTAC®) of CEC is shown in Figure 2.

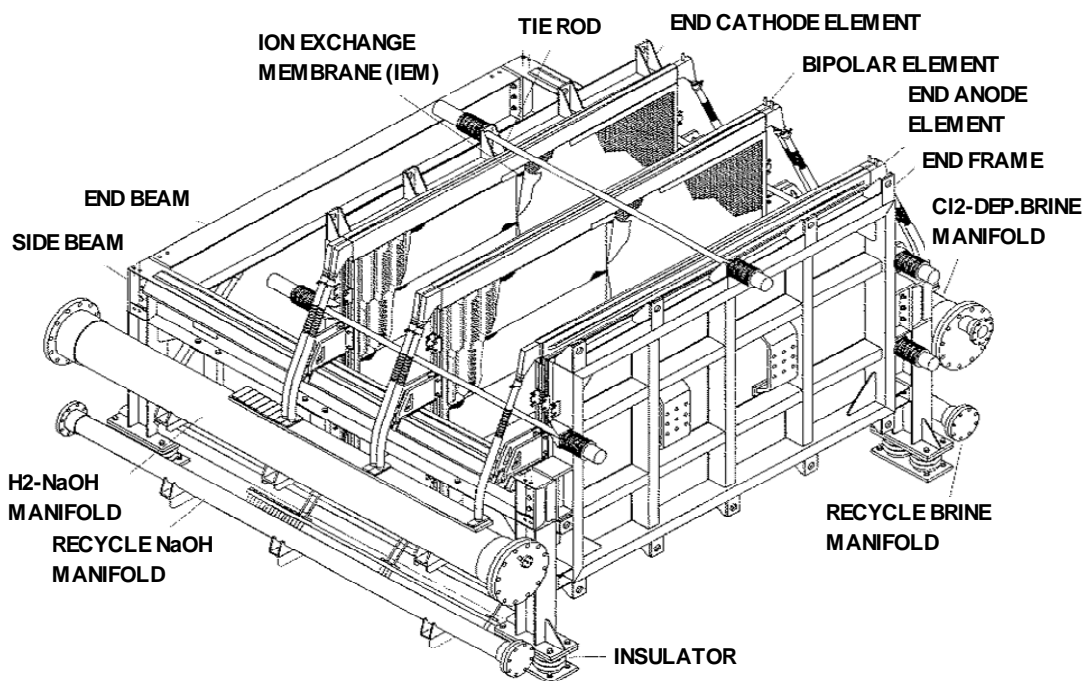


Figure 2. Bipolar electrolyzer (BiTAC) of CEC

Experimental

Evaluation tests were carried out in 0.2dm^2 and 1.0dm^2 cells using 10-25wt% KOH at 40A/dm^2 and $73 - 79^\circ\text{C}$. Pressure of cathode side is $100\text{mmH}_2\text{O}$, and that of anode

side is 50mmH₂O. Anode and cathode cell chambers consist of Ni material and both electrode substrates are selected as Ni mesh.

A zero gap system was applied for cell evaluation; that is each electrode surface directly touches the separator between anode and cathode. A special electric collector for cathode side was used to create zero gap without damaging the separator as shown in Figure 3. This spring collector is made from Ni and there is no need to weld the cathode mesh and collector for connection because many contact points reduce the total contact resistance.

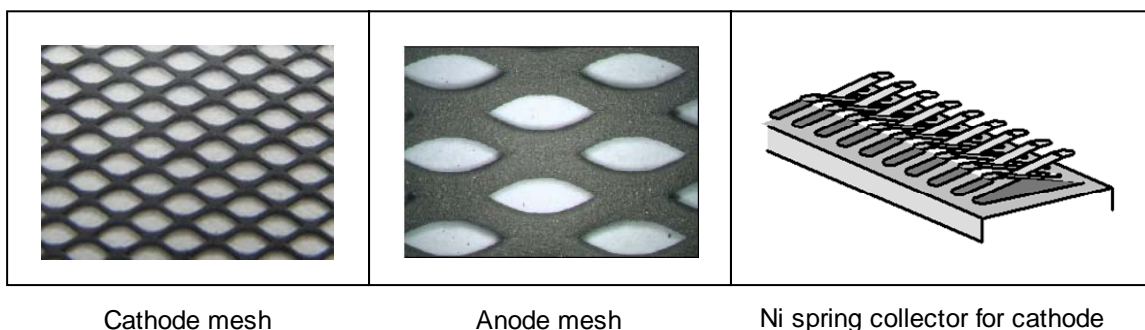


Figure 3. Cathode, Anode and collector for cathode

The study was carried out with a couple of anodes and many separators including ion exchange membrane. The picture of 1dm² cell and a typical test flow are shown in Figure 4 for continuous operation.

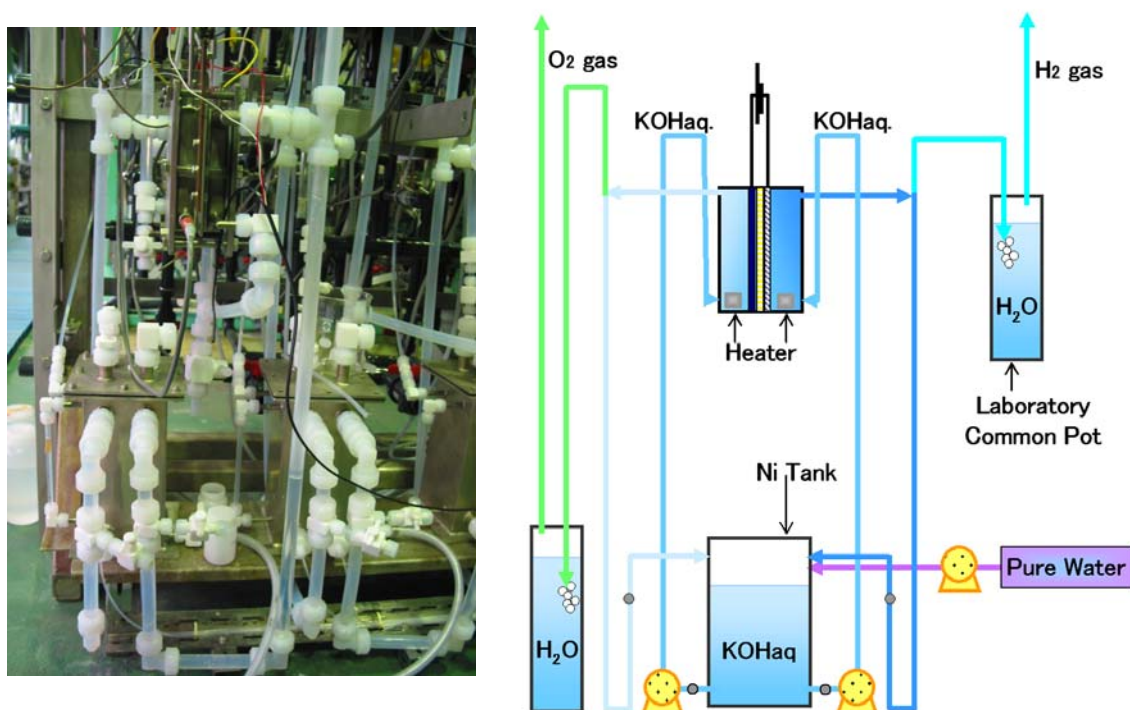


Figure 4. Photo image and flow chart of 1dm² cell

Results and Discussion

Best test result indicates that CEC's zero gap system contributes to achieve a low cell voltage 1.76V at 40A/dm², 80 degC. However, some corrosion of Ni anode and short operation life of the separator were found in the system.

Anode: Raney Ni alloy coating had advantage for oxygen over-potential. It showed 100mV – 200mV saving against Ni base metal.

Cathode: Thermal decomposition coating of mixed noble metal on Ni base metal showed low hydrogen over-voltage of around 100mV.

Separator: Cell voltage trend of each separator is summarized in Figure 5. In alkaline water electrolysis, it is apparently not necessary to have ion exchange function in membrane, but to compare the performance with other separators, ion exchange membranes were tested. Figure 6 shows the result of ion exchange membrane (Flemion® F8020)⁽²⁾. It showed high cell voltage over 2.3V but low O₂ content in H₂ gas. Hydrogen purity was over 99.95%. Figure 6 also indicates that ion exchange membrane has enough durability in alkali water electrolysis. The test results of polyolefin separator are shown in Figure 7. The cell voltages are very low, less than 1.9V at 40A/dm². The voltage is one of the top level performances (1.76V), however, the separator faces to durability issue for long operation.

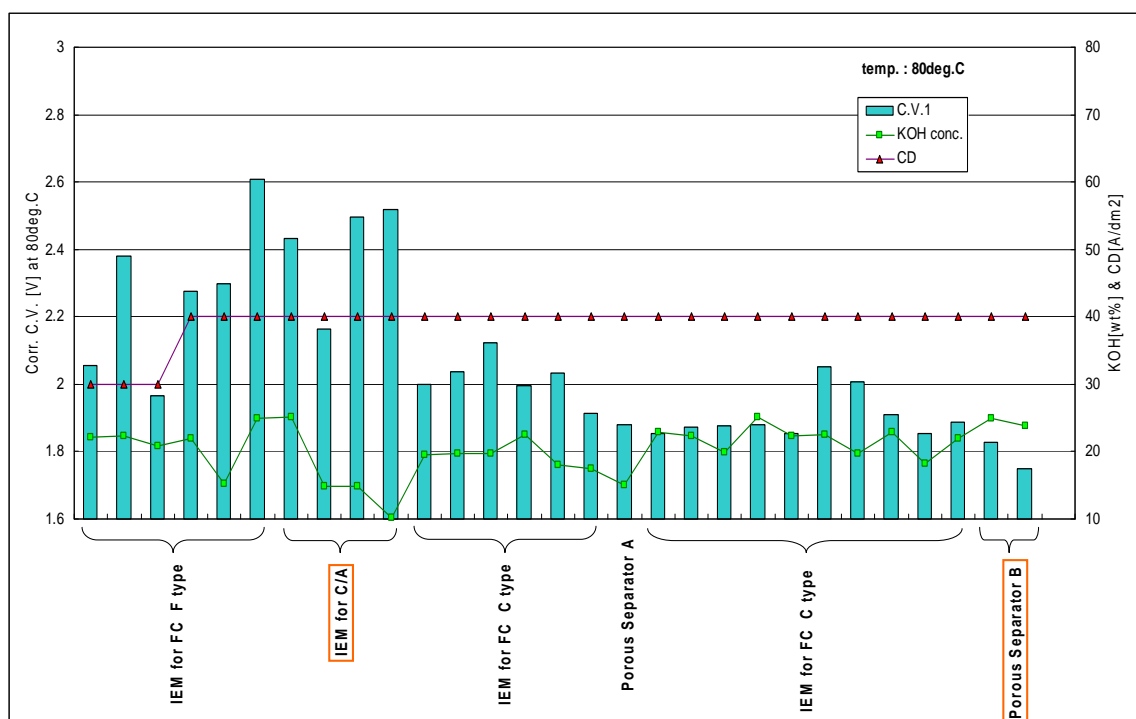


Figure 5. Screening test results of separators by 0.2dm² cell

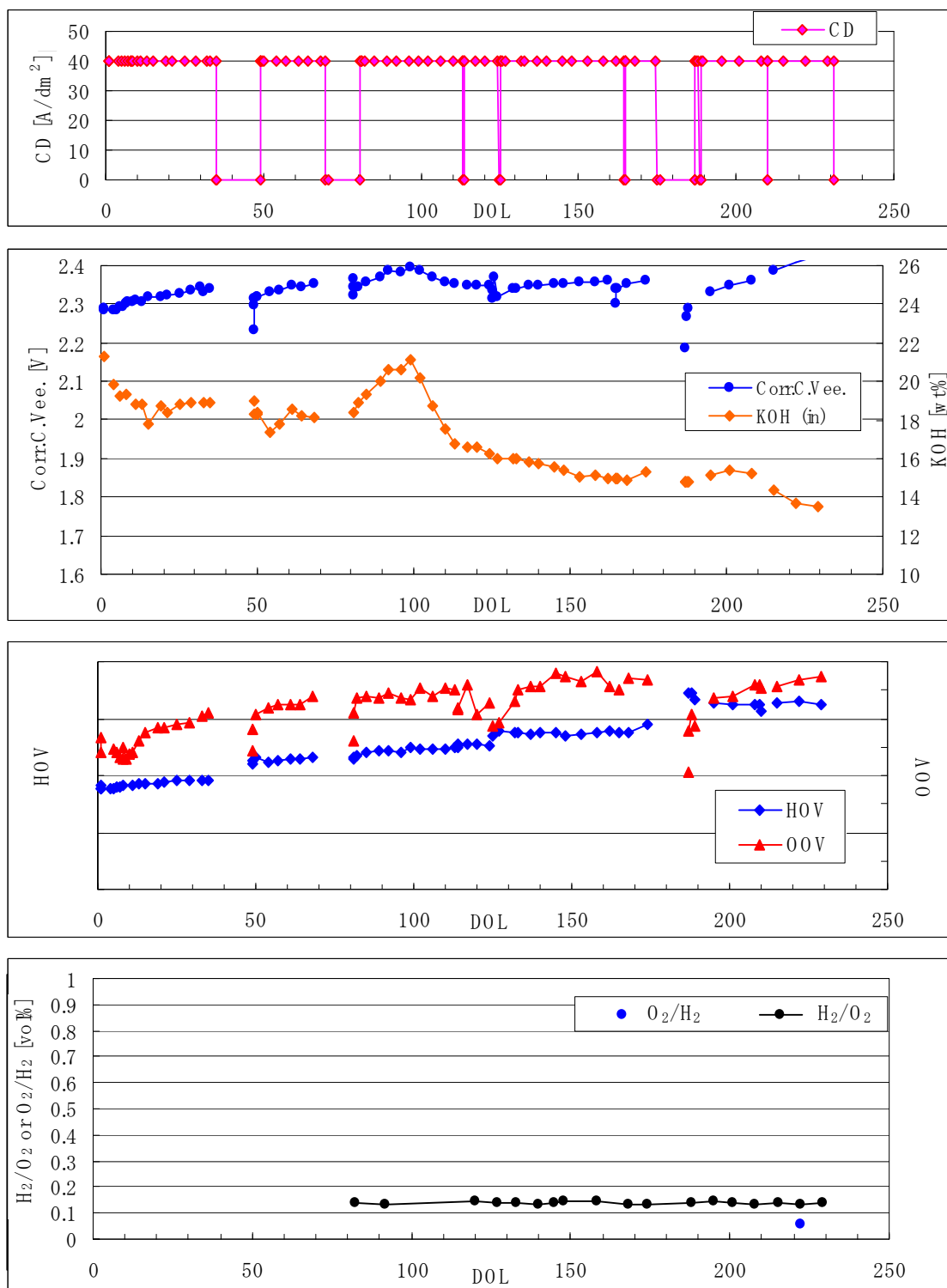


Figure 6. Continuous operation-1 (separator: Ion exchange membrane)

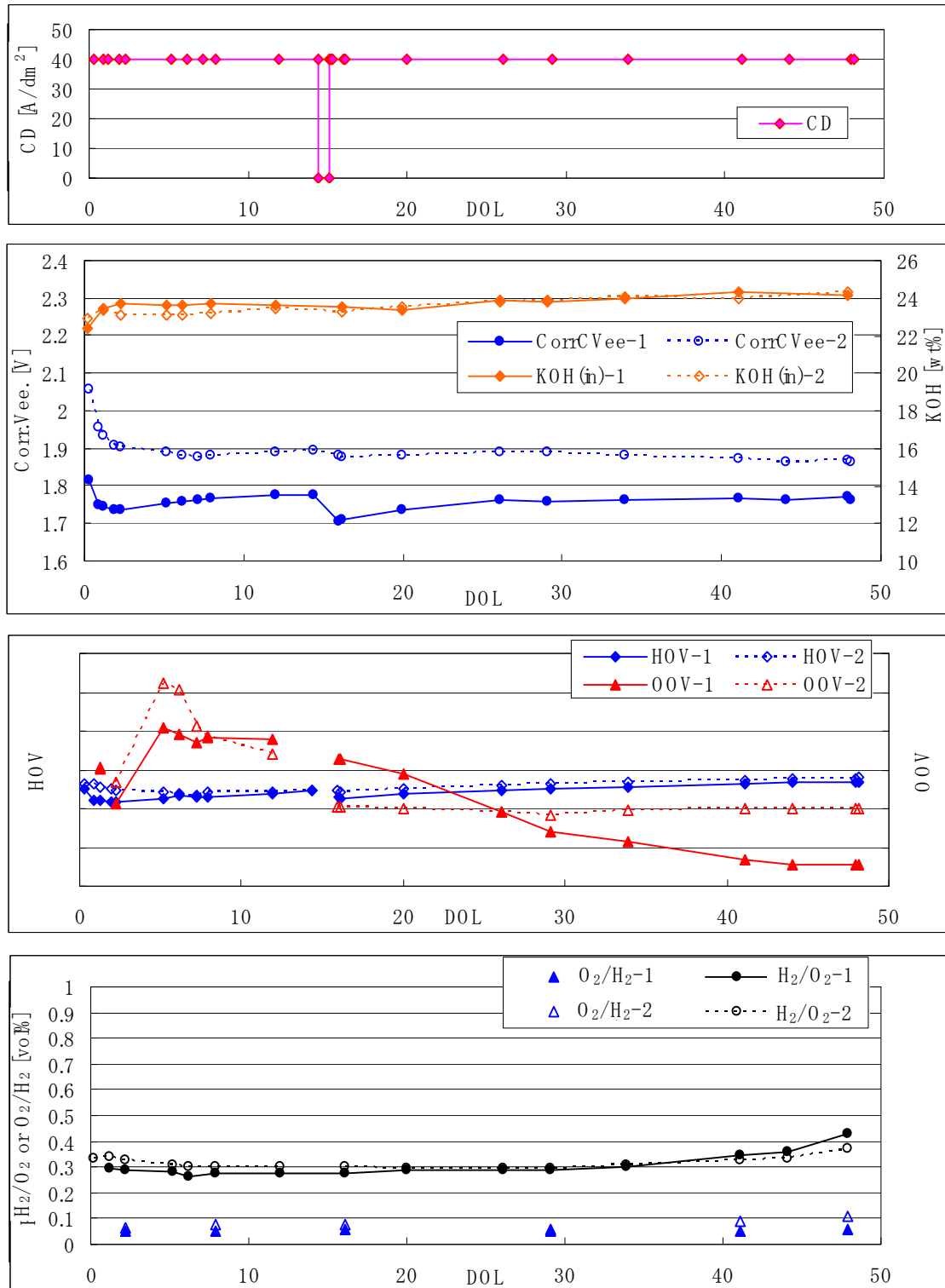


Figure 7. Continuous operation-2 (separator: Polyolefin membrane)

Zero gap operation: Small particles of grey precipitation were detected on the membrane and the edges of the anode surface when the cell was disassembled. It is thought to be some corrosion of Ni anode but is not yet clarified.

In order to achieve good performance and long life of cell or electrolyzer, cell design concept is important, but anode and separator development are also key factors for improvements. Oxygen over-potential of the anode remains 300-400 mV using standard Ni base mesh. There is large scope for development. Long membrane life and low membrane IR drop are achievable using membranes of several types and thickness. The concept of CEC's zero gap cell system does not damage membrane during operation.

References

1. H. Takenaka, "Development Trends of Hydrogen Production Technology by Water Electrolysis", *Journal of the Fuel Society of Japan*, pp.487-496, Vol.70, No.6(1991)
2. K. Umemura, T. Nishio, T. Kimura, "Properties of Flemion F-8020", *Reports Res. Lab. Asahi Glass Co., Ltd.*, pp.79-82, Vol.55(2005).
3. H. Micishita, H. Matsumoto, T. Ishihara, "Effects of Pressure on the Performance of Water Electrolysis of the Cell Using Nafion Membrane Electrode", *Electrochemistry*, pp.288-292, Vol.76, No.4(2008).
4. H. Wendt, "*Electrochemical Hydrogen Technologies*", pp.137-262, Elsevier (1990).
5. M.Pourbaix, "*Atlas of Electrochemical Equilibria in Aqueous Solutions*", p.333, NACE, Houston (1966).
6. Japan Soda Industry Association, "Soda Technology Handbook (2009)", pp. 305-317(2009).
7. K. Ohta, A. Ishihara, *Electrochemistry*, 78(1) 50 (2010)

Microbial Tango with *Shewanella Oneidensis*: Design Elements and Application of a Novel Renewable Energy Source Using Wastewater Containing Organic Compounds

Harold Braustein^a

^a Department of Molecular Microbiology and Biotechnology, Tel Aviv University,
Ramat-Aviv, 69978, Tel Aviv, Israel

Microbial fuel cells (MFC) gather the catabolic energy of microbial colonies and communities. For many years I been tested and improved various designs to create usable technology for real world applications with maximum efficiency and economic viability. A variety of microbes are being tested or peak performance in terms of metabolism, growth, and reductive potential, and mediator-less unction. MFCs are in the early stages of application with numerous goals for future research on the horizon. We produce electricity also, directly from degradation of organic matter – wastewater-containing phenols-in a microbial fuel cell (MFC). Like any fuel cell, a MFC has an anode chamber and a cathode chamber. The anaerobic anode chamber is most commonly connected internally to the cathode chamber by an ion exchange membrane, and an external wire that completes the circuit. Microbial fuel cells use wastewater as a fuel, or more generally a dilute solution of a variety of organic materials in water (like phenols and poly phenols).

Introduction

Whereas wastewater management was formerly focused on nutrient removal, research nowadays focuses on joint solutions for wastewater treatment and energy/resource revival. Microbial fuel cells (MFC) are a innovative generation of wastewater treatment that enable direct translation of the chemical energy of electron donors, such as waste organics, into electrical energy. The main benefit of MFC is the production of electrical energy but devoid of the unwanted formation of excess microbial sludge. It was confirmed that microorganisms successfully convert glucose (and in addition other organics) to electricity at rates and efficiencies, which are of interest to the environmental technologist *Shewanella oneidensis* is one of the best-known organisms that drive biocorrosion through dissimilatory iron reduction (1).

Microorganisms that cause biocorrosion of metals, such as iron and stainless steel, are phylogenetically diverse, but are mainly sulphate-reducing, sulphur-oxidizing, iron-oxidizing/reducing, manganese-oxidizing bacteria and bacteria secreting organic acids and slime (2).

Ennoblement, the occurrence in which the open-circuit potential (E_{corr}) is elevated to noble values (over 200 mV) has been observed in association with biocorrosion (3).

The open-circuit potential or free corrosion potential is the potential of a corroding surface (in the absence of a net electrical current) and is measured in relation to a

reference electrode. Ennoblement is caused by biofilm formation and has mainly been observed for stainless steels in natural seawater (3, 4, 5 and 6). The observation that one type of bacteria can shift E_{corr} of one metal in the positive direction while another type can shift E_{corr} of another metal in the negative direction suggests that it might be possible to construct a bacterial battery that has a larger cell voltage than the same battery that does not contain bacteria. This has lead to the construction of microbial fuel cells (MFCs) (5).

A microbial fuel cell is a device that converts chemical energy into electricity with the aid of electrochemically active microorganisms. Bacteria gain energy by the transfer of electrons from an electron donor (e.g. glucose) to an electron acceptor (e.g. oxygen, nitrate). The larger the difference in potential between the electron donor and the acceptor, the more energy that is generated and generally, the higher bacterial growth yield that is obtained. In a MFC, bacteria transfer their electrons towards an electrode i.e. anode, instead of towards their characteristic electron acceptor (7). On the other hand, microorganisms can also accept electrons from an electrode at low redox potentials (the cathode). For instance, *Geobacter* species accept electrons from the cathode for their anaerobic respiration (8). At present, the most-studied MFCs are those in which bacteria oxidize dissolved organic matter and transfer the obtained electrons towards the anode (9).

1.2.1 Architecture

Biogenic metals have oxidative or catalytic properties and can be used for the elimination of micropollutants from secondary effluent amongst other remediation applications. Hennebel and coauthors discussed the precipitation of biogenic manganese and iron species and the microbial reduction of precious metals, such as palladium, platinum, silver and gold, with specific attention to the application of these biogenic metals in innovative remediation technologies for advanced water treatment. In this fact sheet, the focus is on biogenic manganese oxides (BioMnOx) for the oxidative removal of pharmaceuticals and biocides and on biogenic zero valent palladium (BioPd) as a catalyst for the reductive dehalogenation of iodinated X-ray contrast media (ICM).

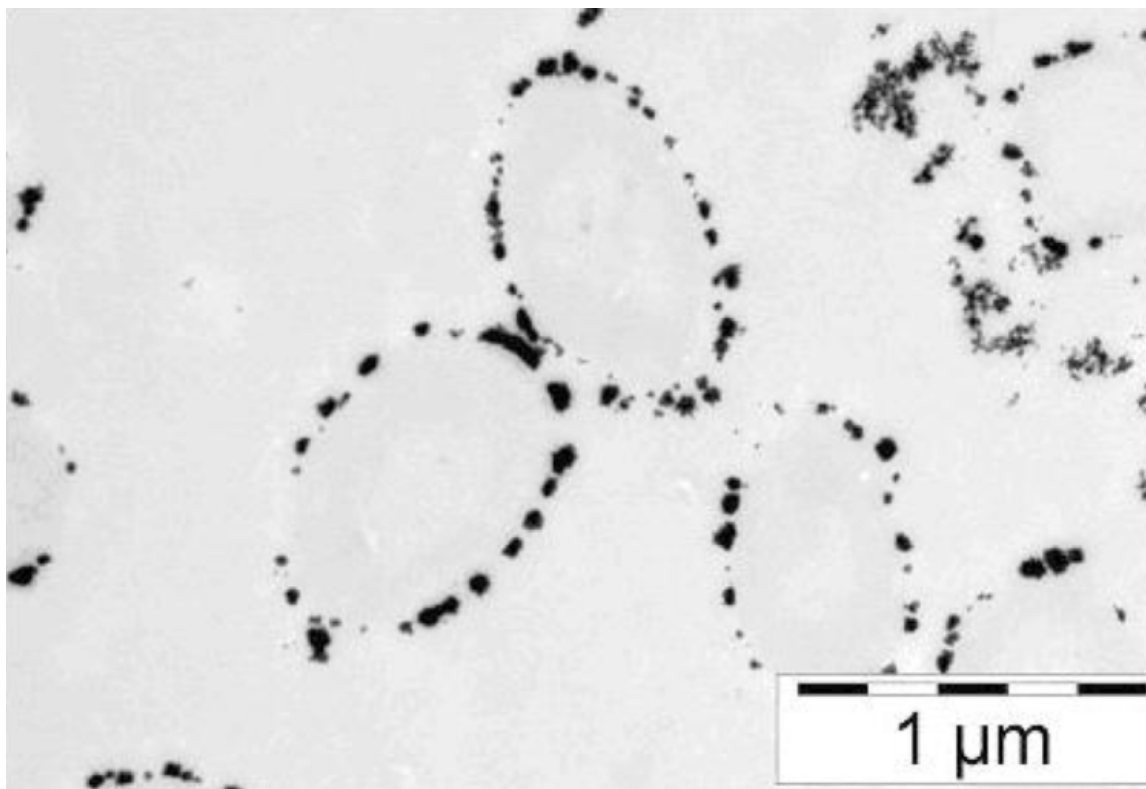


Figure 1. Transmission electron microscopy picture of bacteria with zero valent palladium nanoparticles on their cell walls

A typical MFC consists of an anode receiving electrons generated by the bacterial metabolism and a cathode, accepting the electrons from the anode. Subsequently, the cathode transfers the electrons to an electron acceptor such as oxygen (10) or nitrate (11). Thus, electrons flow from the anode to the cathode through an external electrical connection over a resistor. The anodic compartment is typically maintained under anoxic conditions whereas the cathode is suspended in an aerated solution or exposed to air. The anodic and cathodic compartments are separated by a semipermeable membrane that allows the migration of protons released from the oxidation of the organic matter, from the anodic towards the cathodic compartment (10).

Advantages of electricity production by MFCs

The direct transformation of energy to electricity results in a high conversion efficiency (12). For instance, Rabaey et al.(13) reached up to 80 % glucose-topower transition efficiency with a consortium originating from methanogenic sludge and mainly consisting of facultative anaerobes. Chaudhuri & Lovley (14) recovered 80 % of the electrons, derived from sugar oxidation, as electricity by a pure culture of *Rhodospirillum rubrum*. Moreover, MFCs operate at room temperature which lowers remarkably the heating costs e.g. as required for hydrogen gas oxidation (8, 12)

In addition, the oxidation of organic matter only releases fixed carbon into the atmosphere which avoids the treatment of off-gases (8, 10).

One of the major promising applications of MFCs is the generation of electricity from biowastes (e.g. wastewater) and organic matter (e.g. present in marine sediments) (8, 10), and thus MFCs represent a source of green energy.

Also, MFCs have potential for widespread applications at remote locations or in developing countries (12). Lovley (10) suggested that MFCs, of which the anode is embedded in anaerobic marine sediments while the cathode is put in the overlying aerobic seawater (BUGs; Benthic Unattended Generators) can provide electricity to analytical tools at remote locations such as the ocean floor.

A MFC has no substantial intermediary processes as microorganisms directly transfer electrons from or towards the electrode. This makes MFCs the most efficient biological electricity producing process (8). However, the power output of MFCs is still low (8, 15, 16, 17)

For instance, approximately 26 mW/m² (electrode surface) is obtained with a BUG (18). On average, a MFC fed with wastewater produces 40 W/m³ (reactor volume) (19). Up to now, one of the highest power outputs (228-248 W/m³) was reached by connecting stacked MFCs that were fed with wastewater (15).

In contrast, conventional anaerobic digestion based bioconversion processes, which produce biogas, can yield power outputs twice as high (19).

One of the major challenges for the next years is the processing of waste and wastewater. In order to sustain an ever-growing world population, we will have to use the waste instead of disposing it (20). The ideal scenario is to produce energy from waste, the so-called 'from foul to fuel' principle (21). Wastewaters, e.g. industrial wastewaters from food-processing industries and breweries or agricultural wastewaters from animal confinements, have a high energy value due to the high levels of degradable organic matter and thus constitute an ideal substrate for energy generation (20).

Several biological processes may be applied to recover energy including methanogenic anaerobic digestion and biological hydrogen production. MFCs provide yet another energy harvesting strategy (20). The amount of sludge generated by MFCs is significantly lower than in traditional treatments as the bacterial growth yield is lower (8,22) and aeration can be omitted as the cathode can be passively aerated by placing it in the open air (12).

The elimination of aeration in MFCs is very important as traditional wastewater treatments are expensive due to the large amounts of energy needed for aeration (16).

Liu et al. (16) were the first to generate electrical current from domestic wastewater using a single-chamber MFC while simultaneously executing biological wastewater treatment i.e. the removal of the chemical oxygen demand. The chemical oxygen demand (COD) indirectly measures the organic compounds in water. In fact, it is the amount of oxygen needed to completely oxidize the organic compounds. Electricity generation by a MFC proved to be feasible as up to 80 % of the COD was removed and electricity was produced (16). Since this study, the electrical current production and bacterial populations associated with the electrodes were studied for MFCs fed with different types of waste such as wastewater from a potato-processing factory and a hospital (15), artificial wastewater supplemented (or not) with electron donors (23,24 and 25), sludge from wastewater treatment plants (26, 27, 28 and 29), swine wastewater (30), urban waste (31) and organic waste (32). In all cases, electricity was produced and was maintained for long periods e.g. ranging from two (24) to five years (32).

We realized a MFC based on *Schwannella Oneidensis*, doing several optimization steps to improve the wastewater purification yield and the electricity production.

Experimental Procedures

Biofilm generation

A cathodically polarized electrode was placed in natural aerated seawater as described elsewhere (33,34). Current manufacture on all polarized samples was regularly measured and recorded. The current increased and stabilized at 0.5 A / m² in less than 10 days. Microscopic analysis using an Olympus BX41 epifluorescence microscope coupled with an UV filter block for DAPI showed biofilm formation on the cathode.

Isolation procedures

The biofilm was removed from the stainless steel cathode by sonication (BransonTM 3200) (90 s) in a sterile plastic tube containing 30 ml of 0.85 % NaCl solution. These cell suspensions were used for the construction of a clone library (see below) and for cultivation experiments.

Diluted cell suspensions (10⁻¹ to 10⁻⁶) were inoculated onto 3 different isolation media in order to isolate the heterotrophic cultivable microbial fraction of the marine biofilms: Marine Agar (MA) (DifcoTM 2216), R2A (DifcoTM) and TrypticaseTM Soy Agar (TSA) (BBLTM). The inoculated media were incubated aerobically at 20 °C for several days. Pure cultures were obtained from all 3 different growth media and isolates were stored at – 80 °C using MicroBankTM vials.

FAME analysis

All isolates were grouped and tentatively identified using whole cell fatty acid methyl ester analysis (FAME) as described by Mergaert et al. (33). The isolates were grown routinely on TSA for 24 h at 28 °C or on MA for 48 h at 20 °C if they failed to grow in the former conditions. The obtained FAME profiles were grouped by the unweighted pair-group method using arithmetic averages (UPGMA) and relying on the Bray-Curtis coefficient using the BioNumerics 4.61 (Applied Maths, Belgium) software. The Bray-Curtis coefficient is defined as follows (Bray & Curtis, 1957, Clarke et al., 2006):

$$D_{BC(j,k)} = \frac{\sum_{i=1}^n |x_{ij} - x_{jk}|}{\sum_{i=1}^n |x_{ij} + x_{jk}|} \quad [1]$$

i is the relative proportion of a fatty acid which is compared across samples j and k . Clusters were delineated on the basis of at least 70 % profile similarity. The isolates were cautiously identified by comparing their FAME profiles to a commercial database.

16S rRNA gene sequence analysis

16S rRNA gene sequence analysis was performed on selected representatives of each of the FAME clusters to elucidate their exact taxonomic position. Almost-complete sequences were obtained using the universal primers pA (5' AGA GTT TGA TCC TGG CTC AG 3') and pH (5' AAG GAG GTG ATC CAG CCG CA (Edwards et al., 1989) as described previously (35). For some isolates, only partial 16S rRNA gene sequences were generated using the universal primers pA and pD (5' GTA TTA CCG CGG CTG CTG 3') as described by Coenye et al. (36). The FASTA software was used to find the most similar sequences in public databases. The 16S rRNA gene sequences were aligned using the CLUSTAL_X (37). Finally, neighbour-joining dendrograms (38) were constructed by the BioNumerics 4.61 software.

Construction of a clone library

A clone library of the 16S rRNA genes was constructed in order to investigate the microbial diversity by means of culture independent analyses.

Cell suspensions (see above) were centrifuged at 13 000 rpm for 15 min. The resulting cell pellets were suspended in 750 µl of TNE (100 mM of Tris-HCl pH 8.0; 50 mM of NaCl, 50 mM of EDTA pH 8.0) and 50 µl of 10 mg / ml lysozyme solution was added. After 10 min incubation at room temperature, 0.5 g of glass beads was added and cells

were lysed by bead beating (3 times 30 s at 1.25 rpm) (RetschTM). Subsequently, 100 µl of SDS and 100 µl of sarkosyl were added to the tube. Proteinase K (50 µl of 20 mg / ml solution) was added followed by incubation at 50 °C for 1 hour. Afterwards, 1 volume of phenol:chloroform:isoamylalcohol (25:24:1) was added, mixed thoroughly and centrifuged for 10 min at 13 000 rpm.

Subsequently, the supernatant was transferred to a new eppendorf tube and 1 volume of chloroform:isoamylalcohol was added. The suspension was mixed thoroughly and centrifuged for 10 min at 13 000 rpm. The DNA present in the aqueous phase was precipitated by addition of 0.8 volumes of isopropanol followed by centrifugation at 13 000 rpm. The DNA pellet was resuspended in 50 µl of water and stored at – 80 °C.

Bulk 16S rRNA genes were amplified using the primers F27 (5'-AGAGTTTGATCCTGGCTCAG-3') and S17 (5'-GTTACCTTGTTACGACTT-3'). The PCR mixture (25 µl) consisted of 2.5 µl of 10 X PCR buffer, 0.5 µl of 10 mM dNTPs, 0.4 µl of 10 µM forward primer (F27), 0.4 µl of 10 µM reverse primer (S17), 1 U of DNA polymerase (Sigma) and 2 µl of DNA solution. The thermal cycle used was: 1 cycle at 95 °C for 5 min, 35 cycles at 95 °C for 30 sec, 53 °C for 30 sec and 72 °C for 1.75 min followed by a final extension step of 10 min at 72 °C. The integrity of the PCR products was verified by electrophoresis on a 1 % agarose gel. Bands of 1.5 kb were purified from the gel using the Qioquick gel extraction kit (Qiagen) and finally eluted in 45 µl of TE-buffer (1 M of Tris HCl pH 8, 500 mM of EDTA pH 8).

The 16S rRNA gene fragments were ligated in a pCR®-XL-TOPO® vector using the Topo XL cloning kit (Invitrogen) according to the manufacturer's instructions. The clones were stored at - 80 °C using DMSO as cryoprotectant. Ten percent of the clones were randomly selected for 16S rRNA gene sequencing. In order to check if the clone library was fully identified, the number of operational taxonomic units (OTUs) was plotted against the number of clones. An OTU was defined as a group of clones sharing at least 98.0 % sequence similarity.

All 16S rRNA gene sequences obtained from the isolates and the clones were used to construct a neighbour-joining dendrogram.

Denaturing Gradient Gel Electrophoresis (DGGE) of PCR-amplified bulk 16S rRNA genes DNA was extracted as described above and the V3 region of the bulk 16S rRNA genes was amplified by PCR as described by Muyzer et al. (39). The obtained PCR amplicons were separated by electrophoresis on a polyacrylamide gel with an increasing gradient of denaturants (39). Following staining with SYBR® Gold (Invitrogen) and visualisation with UV illumination, the DGGE fingerprint gel was numerically analysed using the BioNumerics 4.61 software. The DGGE fingerprints were clustered using UPGMA and relying on Pearson product-moment correlation coefficient.

Results and Discussion

Of the three growth media tested, MA yielded the largest number of isolates (3.6×10^5 cfu/ ml) and the highest diversity of morphotypes. Growth was also observed on TSA (2.0×10^3 cfu/ml) and R2A (1.7×10^3 cfu/ml) and was more uniform compared to MA. In total, 356 isolates, representing the morphological diversity of all primary isolation plates, were picked up: 77 % from the MA isolation medium, 14 % from TSA and 9 % from R2A. Whole cell fatty acid analysis was first used to group isolates with similar FAME profiles and as an approximate identification approach (40). Numerical analysis of the obtained FAME profiles grouped the 356 isolates in twenty FAME clusters sharing at least 70 % profile similarity. Fourteen isolates had unique FAME profiles and clustered separately at the 70 % similarity level. The FAME clusters comprised 3 to 91 isolates (Table 2.1). The majority of the isolates were identified as Gram-negative bacteria representing 11 of the 20 FAME clusters (60.8 % of all isolates), while 9 FAME clusters represented Gram-positive bacteria (35.3 % of the isolates). In addition, 5 of the 14 isolates with unique fingerprints were identified as Gram-negative bacteria and 6 isolates as Gram-positive bacteria. Three isolates gave no match to the commercial database but Gram-staining demonstrated that all were Gram-positive bacteria (Fig. 2.1). Comparison of the obtained FAME profiles to a commercial database yielded identification scores that were relatively high for the isolates of two FAME clusters: FAME cluster VII with identification scores of 0.723 ± 0.204 and FAME cluster IX with identification scores of 0.747 ± 0.157 . Isolates of both FAME clusters were identified as

Bacillus strains

In contrast, the FAME identification scores were low (typically less than 0.550) for isolates of all the other FAME clusters (Fig. 2.1).

The isolates belonged to different phylogenetic groups including the Alphaproteobacteria (FAME cluster IV), Gammaproteobacteria (FAME clusters I, II, XIV, XVI – XX), Firmicutes (FAME clusters III, VI – IX), Actinobacteria (FAME clusters V, X, XI) and Flavobacteriaceae (FAME cluster XII). Of the isolates that grouped separately, four were tentatively identified as Gammaproteobacteria, three as Firmicutes, three as Actinobacteria and one as Flavobacteriaceae. Finally, isolates belonging to FAME clusters XIII and XV and four isolates with unique positions remained unidentified (Table 2.1).

In order to obtain a more accurate identification at least one representative isolate per FAME cluster was selected for 16S rRNA gene sequence analysis (Table 2.1, Fig. 2.1). Comparison of the obtained 16S rRNA gene sequences with public databases confirmed that the diversity among the isolates was high and generally also confirmed FAME based identification.

The 16S rRNA gene sequence similarities between representative isolates and the type strains of their closest phylogenetic neighbours ranged between 96.6 % and 100 %, which suggested that several isolates represented novel bacterial species (Stackebrandt & Ebers,

2006). FAME clusters I and IV isolates have been investigated in detailed taxonomic studies and indeed comprised several bacterial taxa (Vandecandelaere et al., in press and unpublished results).

FAME clusters XIII and XV isolates, which could not be identified by FAME analysis, were identified as *Winogradskyella poriferorum* with 99.5 % sequence similarity (Lau et al., 2005) and as *Exiguobacterium* sp. with 98.9 % sequence similarity (Collins et al., 1983), respectively (Fig. 2.1).

Genus level identification was the same in both analyses for strains representing 8 FAME clusters, comprising 96 of the 342 isolates (FAME clusters II, III, VI, VIII, IX, XIV, XIX and XX). For strains of the remaining 12 FAME clusters (I, IV, V, VIII, X, XI, XII, XIII, XV, XVI, XVII and XVIII) representing 245 of the 342 isolates, the identification results only correlated at the higher taxonomic levels. Several reasons may account for this discrepancy. Many of the isolates represented environmental bacteria or novel species for which there are no reference profiles in the commercial databases. In addition, many of the isolates failed to grow in the standard conditions for use of the MIS database. Finally, it is generally known that FAME analysis often yields only approximate identification results (40).

In general, when low (< 0.4) identification scores were obtained the tentative species identification results proved unreliable as revealed by 16S rRNA sequence analysis. In contrast, when high (> 0.4) FAME identification scores were obtained, the results of FAME

Table 1: Summary of the FAME and 16S rRNA gene sequence identification results of the 356 marine isolates.

°: Accession numbers of the isolate and of the type strain are given, respectively

*: Number of isolates of this FAME cluster

§: Average identification score and standard deviation for all isolates within a FAME cluster

¶: The strain number of the isolate for which the 16S rRNA gene sequence was determined, the length of the 16S rRNA gene sequence and the percent of 16S rRNA gene sequence similarity between the isolate and the phylogenetic nearest type strain of an established species

‡: UC: unclustered isolates

FAME Cluster	FAME Identification	16S rRNA gene sequence identification	Accession numbers*
I (n = 68)*	<i>Gammaproteobacteria</i> (0.366 ± 0.190)§	LMG 24078 [†] (1501 bp, 97.9 % <i>Alteromonas macleodi</i> LMG 2843 [‡])¶ LMG 24081 (1426 bp, 99.5 % <i>A. macleodi</i> LMG 2843 [‡]) LMG 24080 (1377 bp, 99.6 % <i>A. macleodi</i> LMG 2843 [‡]) LMG 24083 (1470 bp, 99.5 % <i>A. macleodi</i> LMG 2843 [‡]) LMG 24082 (1425 bp, 99.7 % <i>A. macleodi</i> LMG 2843 [‡]) R – 25514 (1517 bp, 99.4 %, <i>Pseudoalteromonas spongiae</i> JCM 12884 [‡]) R – 25603 (1520 bp, 98.6 %, <i>Pseudoalteromonas rutherfordia</i> LMG 19699 [‡]) R – 26197 (1028 bp, 97.7 %, <i>Pseudoalteromonas allena</i> LMG 22059 [‡]) R – 25580 (1472 bp, 99.7 %, <i>Acinetobacter johnsonii</i> DSM 6963 [‡]) R-25575 (1061 bp, 99 %, <i>Bacillus drentensis</i> LMG 21831 [‡])	AM885866 / X82145 AM885867 / X82145 AM885868 / X82145 AM887685 / X82145 AM885870 / X82145 AM944021 / AY769918 AM944022 / AF316891 AM944023 / AY387858 AM944024 / Z93440 AM944025 / AJ542506
II (n = 5)	<i>Gammaproteobacteria</i> (0.441 ± 0.221)	LMG 24366 [†] (1396 bp, 98.9 % <i>Leisingera methylandivorans</i> LMG 23656 [‡])	AM900415 / AY005463
III (n = 4)	<i>Firmicutes</i> (0.204 ± 0.093)	LMG 24365 [†] (1426 bp, 97.1 % <i>Phaeobacter gallaaciensis</i> LMG 23163 [‡])	AM904562 / Y13244
IV (n = 91)	<i>Alphaproteobacteria</i> (0.316 ± 0.132)	LMG 24367 [†] (1398 bp, 96.6 % <i>Ruegeria atlantica</i> LMG 23161 [‡]) LMG 24372 (1343 bp, 99.9 % <i>Ruegeria mobilis</i> CIP 109181 [‡]) LMG 24369 [†] (1343 bp, 98.1 % <i>Phaeobacter daeponensis</i> LMG 23139 [‡]) R-26162 (234 bp, 99.1 %, <i>Ruegeria pelagia</i> HTCC 2662 [‡]) R-26145 (255 bp, 99.2 %, <i>R. pelagia</i> HTCC 2662 [‡]) R-26160 (410 bp, 97.3 %, <i>P. gallaaciensis</i> LMG 23163 [‡]) R-25598 (331 bp, 99.7 %, <i>Arthrobacter oxydans</i> ATCC 14353 [‡]) R-25657 (1488 bp, 99.0 %, <i>Staphylococcus cohnii</i> CCUG 7322 [‡]) R-25600 (464 bp, 99.6 %, <i>Bacillus finnis</i> LMG 7125 [‡]) R-25542 (1504 bp, 99.0 %, <i>Bacillus pumilus</i> LMG 7132 [‡]) R-28766 (466 bp, 99.8 %, <i>B. pumilus</i> LMG 7132 [‡]) R-25593 (1474 bp, 99.0 %, <i>Frigoribacterium faeni</i> KMM 3907 [‡]) R-26170 (425 bp, 99.5 %, <i>Arthrobacter agilis</i> LMG 17244 [‡]) R-28796 (1360 bp, 99.8 %, <i>Maribacter dokdoensis</i> DSM 17201 [‡]) R-26150 (458 bp, 99.5 %, <i>Winogradskyella poriferorum</i> JCM 12885 [‡]) R-26154 (462 bp, 99.6 %, <i>W. poriferorum</i> JCM 12885 [‡])	AM905330 / AB255399 AM905333 / AB255401 AM943630 / DQ981486 AM944026 / DQ916141 AM944027 / DQ916141 AM944028 / Y132244 AM944029 / X83408 AM944030 / AY688045 AM944031 / D16268 AM944032 / AM237370 AM944033 / AM237370 AM944034 / AM410686 AM944035 / X80748 AM944036 / AY960749 AM944037 / AY848823 AM944038 / AY848823
V (n = 5)	<i>Actinobacteria</i> (0.588 ± 0.207)	R-28056 (437 bp, 100 %, <i>Marinobacter hydrocarbonoclasticus</i> DSM 8798 [‡])	AM944039 / X67022
VI (n = 29)	<i>Firmicutes</i> (0.666 ± 0.148)	R-25570 (477 bp, 98.9 %, <i>Exiguobacterium aurantiacum</i> CCUG 44910 [‡])	AM944040 / X70316
VII (n = 3)	<i>Firmicutes</i> (0.723 ± 0.204)	R-25587 (464 bp, 98.9 %, <i>Exiguobacterium acetylum</i> CCUG 32630 [‡])	AM944041 / X70313
VIII (n = 5)	<i>Firmicutes</i> (0.633 ± 0.154)	R-25588 (455 bp, 98.9 %, <i>E. aurantiacum</i> CCUG 44910 [‡])	AM944042 / X70316
IX (n = 28)	<i>Firmicutes</i> (0.747 ± 0.157)	R-28040 (469 bp, 99.9 %, <i>Idiomarina loihiensis</i> DSM 15497 [‡])	AM944043 / AF288370
X (n = 30)	<i>Actinobacteria</i> (0.508 ± 0.256)	R-28770 (1507 bp, 99.8 %, <i>Marinobacter koreensis</i> DSM 17924 [‡])	AM944523 / DQ325514
XI (n = 15)	<i>Actinobacteria</i> (0.697 ± 0.210)	R-28768 (1506 bp, 99.8 %, <i>M. koreensis</i> DSM 17924 [‡])	AM944524 / DQ325514
XII (n = 4)	<i>Flavobacteriaceae</i> (0.400 ± 0.113)	R-26152 (346 bp, 98.8 %, <i>A. macleodi</i> LMG 2843 [‡])	AM944044 / X82145
XIII (n = 6)	NO MATCH	R-28020 (613 bp, 98.9 %, <i>Pseudoalteromonas</i> sp LMG 2853 [‡])	AM944045 / DQ011614 AM944046 / M93352
XIV (n=23)	<i>Gammaproteobacteria</i> (0.336 ± 0.150)		
XV (n = 7)	NO MATCH		
XVI (n = 6)	<i>Gammaproteobacteria</i> (0.186 ± 0.111)		
XVII (n = 4)	<i>Gammaproteobacteria</i> (0.074 ± 0.055)		
XVIII (n = 3)	<i>Gammaproteobacteria</i> (0.140 ± 0.047)		
XIX (n = 4)	<i>Gammaproteobacteria</i> (0.382 ± 0.105)		
XX (n = 2)	<i>Gammaproteobacteria</i> (0.324 ± 0.042)		
UC‡ (n=14)			

Three hundred and eighty clones of the clone library were picked up and randomly 10 percent (40 clones) were selected for 16S rRNA gene sequence based identification (Table 2.2, Fig. 2.2). Comparison of the obtained 16S rRNA gene sequences with public databases demonstrated that the clones represented Gammaproteobacteria (19 clones), Alphaproteobacteria (14 clones), Flavobacteriaceae (3 clones) and Firmicutes (4 clones). The alphaproteobacterial fraction of the clone sequences represented bacteria belonging to the Roseobacter lineage whereas the majority of the gammaproteobacterial clone sequences were identified as uncultured Gammaproteobacteria or as members of the genus *Alteromonas*.

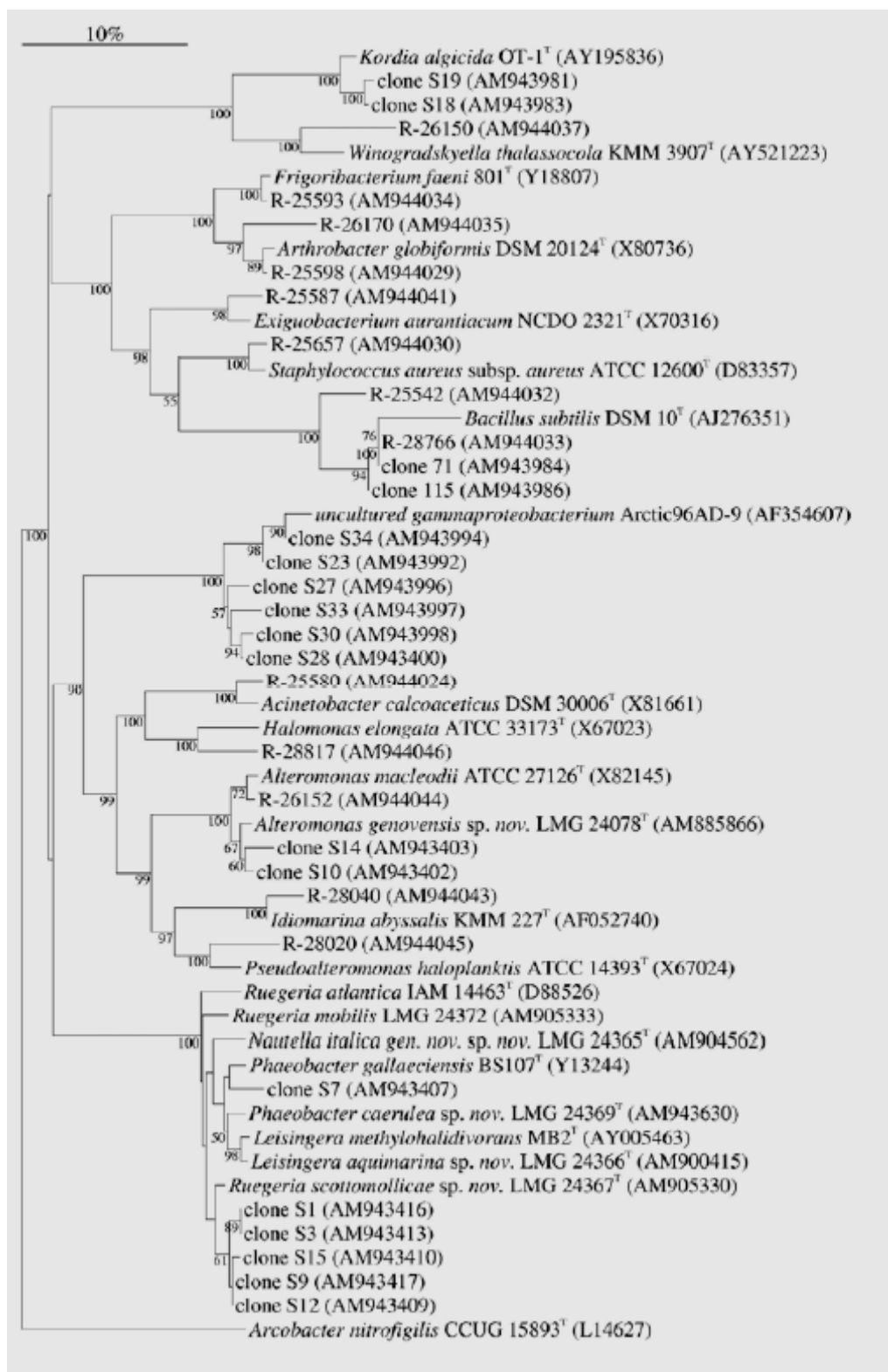


Figure 2.1: Neighbour-joining dendrogram showing the phylogenetic relationships based on 16S rRNA gene sequence similarities, of selected isolates, selected clones and their phylogenetic nearest neighbours. Bootstrap values (1000 replicates) above 50 % are shown. Bar represents 10 % sequence diversity.

Although a relatively small number of clones was sequenced, the number of OTUs stopped increasing with additional clones sequenced and therefore the clone library was considered identified (Fig. 2.2).

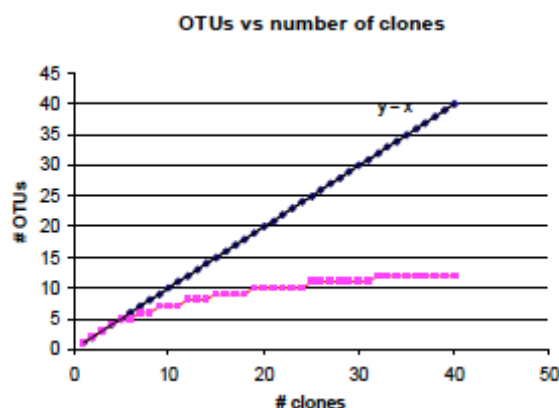


Figure 2.2: Graph showing the number of OTUs versus the number of clones. The pink line represents the number of OTUs versus the number of clones. The blue line is hypothetical and represents a clone library in which every clone belongs to a different OTU.

Largely the same phylogenetic groups of bacteria were detected in both approaches (Table 2.1, Table 2.2 and Fig. 2.1), except for the absence of actinobacterial sequences among the clones. Several reasons may explain this incongruence. Actinobacteria may constitute only a minor fraction of the microbial biofilm population, which was not picked up from the clone library. Alternatively, the techniques used may be less suitable for the construction of a clone library with DNA extracted from Actinobacteria. Finally, cultivation conditions may have favoured the growth of actinobacterial isolates leading to an overestimation of the presence of Actinobacteria in the microbial population.

The predominance of representatives of the Gamma- and Alphaproteobacteria among the isolates and the clones was remarkable. Holmes et al. (41) investigated the microbial diversity of electroactive biofilms formed on cathodes that were suspended in seawater whereas the anodes were placed in the underlying anoxic aquatic sediments.

Gammaproteobacteria were enriched on the cathode of marine sediment fuel cells while Alphaproteobacteria (primarily *Paracoccus* and *Roseobacter* species) predominated on cathodes from salt marsh sediments. Our study confirmed the predominance of Gamma and Alphaproteobacteria in an electrochemically active biofilm formed on the cathode that was placed in aerobic seawater.

The presence of members of the Firmicutes, Actinobacteria and Flavobacteriaceae in the

present electrochemically active biofilm may reflect their common occurrence in marine environments (42, 43, 44,45, 46 and 47). To verify this hypothesis, DGGE analysis was performed in order to compare the dominant microbial populations of the electroactive biofilms and of the surrounding seawater. DGGE indeed revealed that the predominant populations were highly similar, demonstrating that the present electroactive biofilm community consists primarily of common marine organisms (Fig. 2.3).

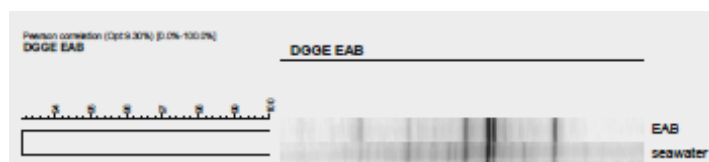


Figure 2.3 : DGGE profiles of the predominant members of the EAB and of the surrounding seawater populations.

It is unclear which of these bacteria contribute to the electrochemical activity. In a first study, FAME cluster IV isolates (identified as members of the Roseobacter lineage of the Alphaproteobacteria) and one FAME cluster XX isolate (*Halomonas aquamarina*), representing six different species, were selected to test their electroactivity by means of cyclic voltammetry (Parot et al., in press). All isolates exhibited high efficiency towards the catalysis of oxygen reduction. These results indicate that these bacteria might be all involved in electroactivity (Parot et al., in press). These data also suggest that multiple species, possibly representing a large fraction of the present biofilm community, are responsible for electrochemical features of the biofilm.

For checking the MFC efficacy we projected and realized a novel optical and chemical wastewater purification system, formed from a quartz reactor standing between two Philips UV lamps, with a mirror jacket. The novel system uses the Fenton reaction for free radicals production with high yields purification from wastewater of different aromatic compounds as: Aniline, N,N Dimethyl-p- Phenillendiamine, p-Nitroso-N,N Dimethyl Aniline, Phenol and Azoic Dye Red Acid 97 (49,53). (Fig.2.4).

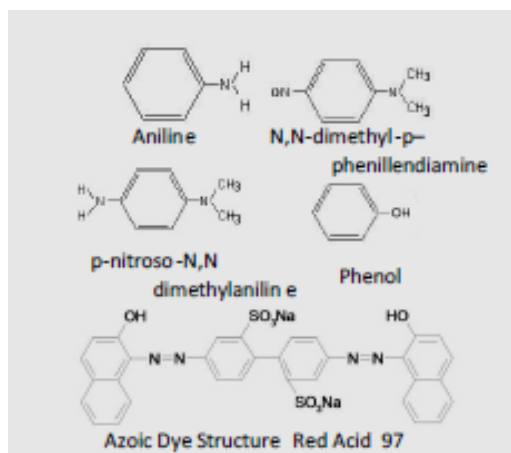


Fig.2.4 The Aromatic Compounds studied for the MFC Proposed

The Photo-reactor proposed is shown in Fig.2.5, working as an ozone producer, and cleaning the Wastewater (48).

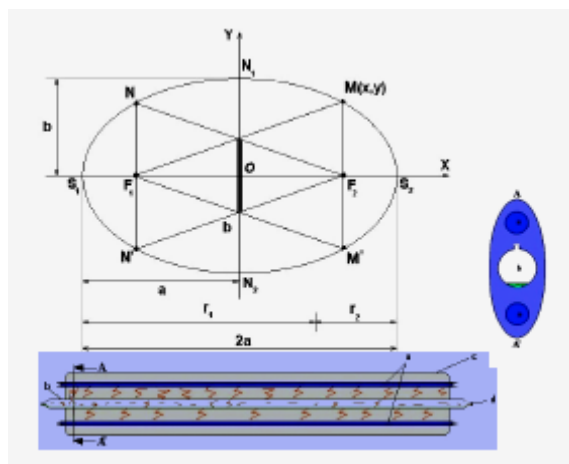


Fig.2.5 The photo-reactor and his section(transversal – right and longitudinal – down)
The photo reactor working principle is showed in the Fig.2.6.

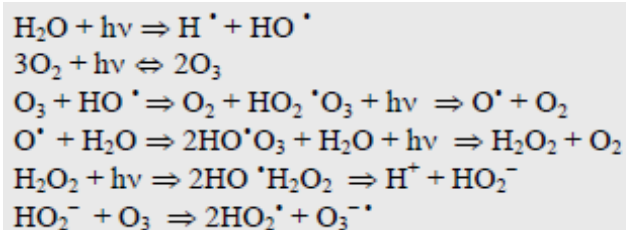


Fig.2.6. Water Photoradiolysis- The working principle of the photoreactor(General reactions of the oxidant species)

Comparing those two methods of wastewater purification by using the MFC based on *Sewanella Oneidensis* and the Photoreactor, are observed different aspects in the aromatic compounds purification and producing electricity.

Conclusions:

Many *Sewanella* strains can be used as biocatalysts in MFC's.

Some *Sewanella* strains have demonstrated approximately 30% coulombic efficiency. Maximum power output is achieved when a developed biofilm has formed on the anode electrode. EIS has been effective in monitoring changes of the MFC electrode surfaces.

The use of different electrochemical systems facilitates the complete characterization of the electrochemical properties of the anode and cathode with different analytes as a function of time.

1) QA tool, 2) Determine the reaction rates, 3) as a tool to monitor the internal resistance for different operating conditions.

By labeling intact cells with biotinylation reagents reacting with free amino groups, the proteins exposed at the surface of the cells can be enriched using avidin affinity chromatography. Of particular importance are the differences seen when cells are grown with insoluble iron oxides.

Anodic biofilms can be created on carriers such as granules, which can consequently be used in other reactors, such as those for anaerobic digestion or nitrification, etc. The bioanode can also be used to "deposit" on the electrode the beneficial microbes that would die or be less competitive if presented as single cells, which can further be used for medical treatment or biocontrol, etc.

References

1. Beech et al., *Proc. Of the Semin. For Arabian Stud* **35**(2005):37-56
2. Beech IB, Gaylarde CC (1999). *Rev Microbiol* **3**
3. BAKER, C., et al (2003) *British Journal of Psychiatry*, **183**, 498 -506.
4. Kolari, et al, (1998).. *Real Estate Economics* **26**, 667-677.
5. Mansfield KJ, et al. 2007. *Neurourol Urodynam* **26**:433-438

6. Lee et al. 2003: *Appl. Opt.*, **42**, 2653-2664
7. Rabaey, K. and Verstraete, W. (2005). *Trends Biotechnol.*, **23**(6), 291 – 298.
8. Gregory, J.M.,etal, (2004), *Geophys. Res. Lett.*, **31**, L15312,
9. Lovley, D. R. (2006). *Nat Rev Microbiol* **4**, 497- 508.
10. Clauwaert P, Rabaey K, et al, (2007a) *Environ Sci Technol* **41**:3354–3360
11. Rabaey and Verstraete, 2005 . *Trends Biotechnol.*, **23** 6 (2005), pp. 291–298
12. Rabaey, K., et al. (2004b). Submitted.
13. Chaudhuri, S.K., Lovely, D.R., 2003. *Nat. Biotechnol.* **21** (10), 1129–1232.
14. Aelterman, P., Rabaey, K., Clauwaert, P. & Verstraete, W. (2006). *Water Sci Technol* **54**, 9-15.,
15. Liu et al., 2004: *J. Quant. Spectrosc. Radiat. Transfer*, **88**, 97-109, doi:10.1016/j.jqsrt.2004.03.031.
16. Logan, B. E., et al. *Water Res* **39**, 4961-4968.
17. Bond, D. R., Holmes, D. E., Tender, L. M. & Lovley, D. R. (2002). *Science* **295**, 483-485.
18. Pham et al., 2006 *AMB Express* 2011, 1:22
19. Angenent, et al, 2004. *Trends Biotechnol.*, **22**: 477-485
20. Ehrenman, G. (2004) *Mech. Eng.* **126**, May, pp. 26–29.
21. Ghangrekar M.M. and V.B. Shinde. 2006 *N Engl J Med*; **352**:686-691,
22. Kim, et al, 2007. *Applied Microbiol. Biot.*, **75**: 989-998.
23. Phung, et al , 2004. *FEMS Microbiol. Lett.* **233**, 77–82.
24. Jung, S., Regan, J.M., 2007. *Appl. Microbiol. Biotechnol.* **77**, 393–402.,
25. Kim et al., *Journal of the European Ceramic Society* **26** (2006) 73–80
26. Kim, et al, (2007). *Int J Syst Evol Microbiol* **57**, 1554–1560.
27. Lee, et al,: *Appl. Opt.*, **42**, 2653-2664, doi:10.1364/AO.42.002653.
28. Logan, B. E., et al, (2005). *Water Res* **39**, 4961-4968.
29. Rodrigo, M.A., Canizares, P., Lobato, J., Paz, R., S ~ aez, C., Linares, J.J., 2007. *J. Power Sources* **169** (1), 198–204
30. Kim, J. R., & Logan, B. E. (2005). *Water Res* **39**, 4961-4968.
31. Bergel, A., Féron, D. & Mollica, A. (2005). *Electrochem commun* **7**, 900-904.,
32. Faimali, M., *Electrochim Acta.*, in press
33. Mergaert, J., Verhelst, A., Cnockaert, M. C., (2001). *Syst Appl Microbiol* **24**, 98-107
34. Coenye, T., & Vandamme, P. (1999). *Int J Syst Bacteriol* **49**, 405-413.
35. Thompson, et al, (1997). *Nucleic Acids Res* **25**, 4876-4882
36. Saitou, N. & Nei, M. (1987). *Mol Biol Evol* **4**, 406-425.
37. Muyzer, G., et al,. (1993). *Appl Environ Microbiol* **59**, 695-700.
38. Vandamme, P., et al, (1996). *Microbiol Rev* **60**, 407-438.
39. Holmes., & Lovley, D. R. (2004). *Microb Ecol* **48**, 178-190.
40. Gontang, E. A., Fenical, W. & Jensen, P. R. (2007). *Appl Environ Microbiol* **73**, 3272-3282
41. Ivanova, et al, (1999). *Int Microbiol* **2**, 267-271.
42. Montalvo, et al, (2005). *Antonie van Leeuwenhoek* **87**, 29-36.
43. Van Trappen, et al, (2004). *Int J Syst Evol Microbiol* **54**, 1157-1163.

44. Yoshpe-Purer, Y. & Golderman, S. (1987). *Appl Environ Microbiol* **53**, 1138-1141.
45. Brauștein, et al, *Journ.of Optoelectronics and Advanced Materials*, vol 9,p.65-71,(2007)
46. Brauștein, et al, *Proceedings of Advanced Oxidation Processes Conference, Greece*, p. 32-38, (2006)
47. Brauștein, et al, *Proceedings of Advanced Oxidation Processes Conference, Greece*, September p. 88-94, (2006)
48. Brauștein, et al, *Environmental Engineering and Management Journal*, Vol. 4, no. 4, p. 519-535,(2005)
49. Brauștein, *Environmental Engineering and Management Journal*, Vol. 4, no. 4, p. 463-472,(2005)
50. Brauștein, et al, *Anal.Știin. Univ.,Al. I. Cuza”*, secția Chimie, tome XII (2), p. 41-50,(2004)
51. Brauștein, et al , *Environmental Engineering and Management Journal*, Vol. 1, no. 4, p. 551-556, (2002)

Rechargeable Batteries For The 300-mile Electric Vehicle and Beyond

K.M. Abraham
E-KEM Sciences,
Needham, MA 02492
kmabraham@comcast.net;
www.e-kemsciences.com

Abstract

The energy density required for rechargeable batteries to power 300-mile range electric vehicles on a single charge is about 600 Wh/kg. Li-ion batteries are unable to meet this need in the foreseeable future. The prospects for advanced rechargeable batteries for the 300-mile EV are presented with brief discussions on the status of Li-air and Li-S batteries

Batteries for the 300-mile EV

Lithium-ion batteries have played a key role in the modern portable electronic technology revolution and they are indispensable for our everyday life. Despite their huge success and ubiquitous presence, there is an ever increasing need for batteries with significantly higher energy and power densities to meet the demands of new consumer devices, electric automobiles, aerospace technologies, power tools, and various other energy hungry applications. Notably, all-electric family automobiles with a driving range of 300 miles or more on a single charge require batteries with more than twice the energy density, a step increase in cycle life and significant reduction in cost compared with today's Li-ions. It can be shown from calculations using a typical family car such as a Toyota Camry that a 300-mile range all-electric vehicle would need Li-ion cells with specific energy >500 Wh/kg as opposed to the 230-240 Wh/kg available today (1). In the Camry weighing about 1500 kg, the engine plus gasoline tank contributes approximately 400 kg. This is the weight available for the battery pack without altering the conveniences in the car. Assuming that a kilowatt-hour of battery will provide 3 miles of driving, a 100 kWh battery is required for driving 300-miles on a single charge. In practice, it is necessary to oversize the battery by about 40 percent for two purposes; i) to have a 20 % reserve capacity in the normal operation of the car, and ii) to compensate for the capacity fade of 20% during the life of the battery. Thus, the 300-mile car would be powered by a 140 kWh battery initially. The weight energy density of such a 400 kg battery pack then is 350 Wh/kg. If the efficiency for the conversion of cells to battery pack is 60 %, the energy density of the cells to build the 300-mile range battery pack is ~580 Wh/kg, more than two and a half times that of today's Li-ion cells. In order to build such batteries using Li-ion technology, positive electrode materials having significantly higher specific capacities than those presently available are needed

Status of Li-ion Batteries

The highest specific capacity Li-ion positive electrode today is $\text{LiNi}_{0.80}\text{Co}_{0.15}\text{Al}_{0.05}\text{O}_2$ (NCA), a variant of the original Li intercalating layered LiCoO_2 (2). NCA has a reversible specific capacity of about 190 milli-ampere hours per gram (mAh/g), which is in the neighborhood of 70% of the theoretical one-electron reaction of this electrode material. Commercial 18650 size Li-ion cells built with NCA and graphite negative electrode is approaching 240 Wh/kg.

The reversible capacity for a transition metal oxide positive electrode material capable of one-electron reaction is ~ 270 mAh/gram. A 3.6 V Li-ion cell built with such an oxide cathode and a graphite negative electrode would exhibit a specific energy of about 300 Wh/kg. Presently, a class of positive electrode materials potentially capable of such high capacity is the lithium rich layered manganese oxides (layered LMO) (3). For example, $\text{Li}[\text{Li}_{0.2}\text{Mn}_{0.54}\text{Ni}_{0.13}\text{Co}_{0.13}]\text{O}_2$ and other oxides related to it have shown practical reversible capacities up to 250 mAh/gram, albeit at low rates. The projected energy density of the corresponding 18650 Li-ion cells is 280 Wh/kg, increasing to approximately 320 Wh/kg if the graphite negative electrode is replaced with silicon. This evolution in the energy density of Li-ion batteries is presented in Figure 1 using the highly engineered 18650 Li-ion cells as examples. Clearly, this is still short of the 580 Wh/kg cells required for the 300-mile vehicles. On a more positive outlook all- electric-vehicles with 150-200 mile range are possible with such batteries, and they will become prevalent if they can be made cost effective. The 200 mile range cars will be powered by 90 kWh battery packs which at the best case scenario price of \$400/kWh will cost \$36000, too high for an average family car.

Li-ion battery cost reduction should thus be a major objective of EV battery development ‘

Long-term Prospects

The specific energy (Wh/kg) of an electrochemical couple is given by Equation 1.

$$\text{Energy density (Wh/kg)} = \frac{\text{Cell Voltage (V)} \times 1000(\text{g}) \times 26.8 \text{ Ah}}{(\text{kg}) \times \text{Eqv.wt(g)}} \quad [1]$$

Where, V is voltage and 26.8 Ah is the theoretical capacity of the electrochemical couple for reactions involving one equivalent weight (eqv. wt) of the reactants. Equation [1] teaches that electrochemical couples exhibiting very low equivalent weights and high voltages are needed for building super high energy density batteries (Figure 2) (4).

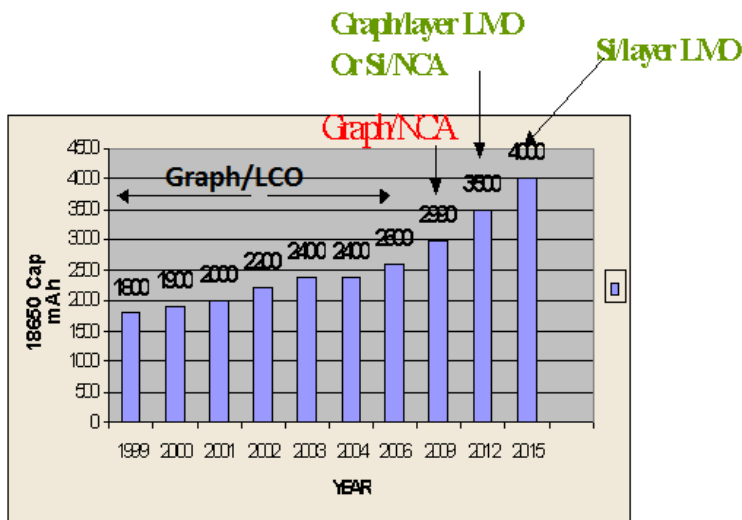


Figure 1: Past and projected capacity evolution of 18650 Li-ion cells. The layer LMO represents the Li-rich layered manganese oxides such as $\text{Li}[\text{Li}_{0.2}\text{Mn}_{0.54}\text{Ni}_{0.13}\text{Co}_{0.13}]\text{O}_2$. This 18650 cell with silicon anode is projected to have 4000 mAh capacity and ~ 320 Wh/kg. Their approximate volumetric energy densities may be obtained by multiplying this value by 2.5.

The equivalent weights of Li-ion batteries range from 130 (for the best case scenario with a silicon anode capable of reversibly alloying with 4 moles Li per mole of Si and a lithiated metal oxide with a specific capacity about 250 mAh/gram as discussed above) to 235 for the graphite/LiCoO₂ cell intercalating 0.6 moles of Li per LiCoO₂ to yield 140 mAh/gram capacity (5). It should be noted that Li-ion cells utilizing silicon anodes and layered LMO are far way from being practical due to many materials and cell design challenges. Clearly, advanced super high energy density battery couples should be sought and developed.

Figure 2 shows that coupling the most electropositive element Li with highly electronegative and light elements from groups VIB and VIIB of the periodic table provide the best opportunities for building super high energy density batteries. Figure 3 displays the theoretical energy densities of several such high energy density Li battery couples along with those of several well-known practical batteries and the hydrogen-oxygen (H₂-O₂) fuel cell. The Lithium-Fluorine (Li-F₂) battery couple is the highest energy density system theoretically possible but it is impractical because of the extreme chemical reactivity of F₂.

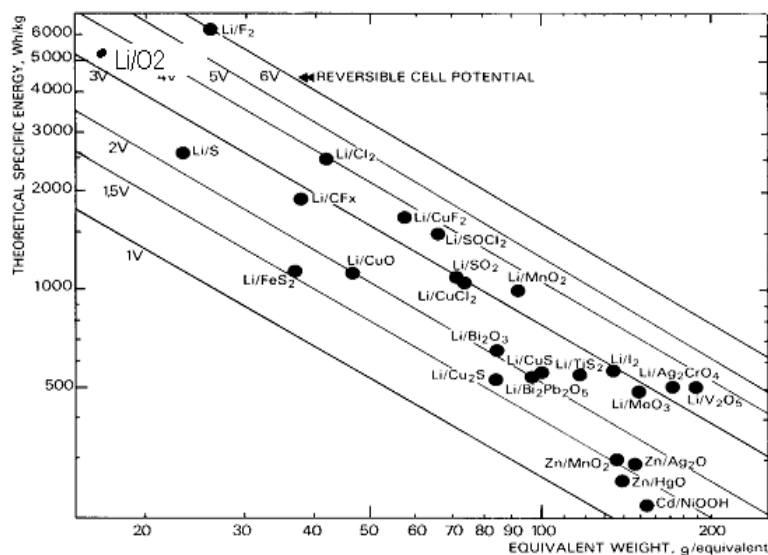


Figure 2: Energy density map depicting theoretical energy densities of battery couples versus equivalent weights for various cell voltages

Similarly, the Li-Cl₂ couple is a difficult system to practically implement. This leads to the lithium-oxygen (Li-O₂) couple as perhaps the most logical candidate for the ultimate high energy density battery. The Lithium-Sulfur (Li-S) system places a distant second.

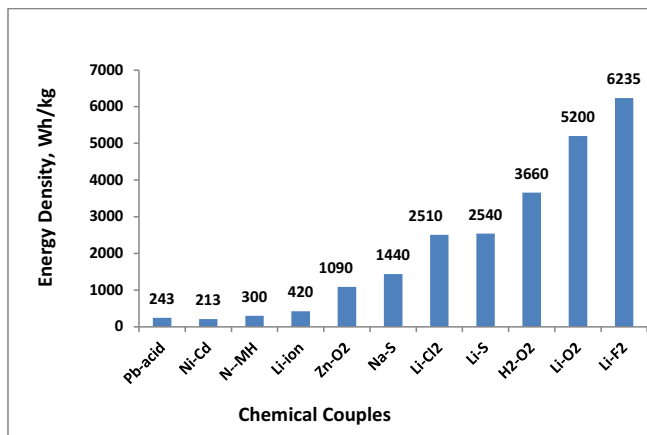


Figure 3: Theoretical Energy densities of battery chemical couples

Li/O₂ Battery

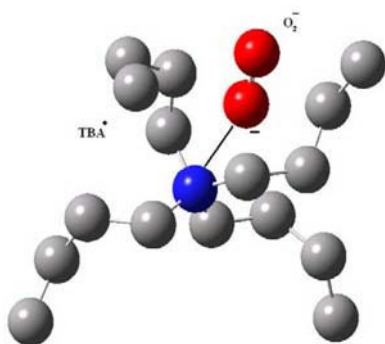
We reported on the first non-aqueous rechargeable Li-air battery in 1996 (6). Recently, we have carried out in-depth studies of the kinetics and mechanisms of O₂ reduction reaction (ORR) in solutions of hexafluorophosphate salts of the general formula X⁺PF₆⁻, where, X = tetra butyl ammonium (TBA), K, Na and Li, in several solvents possessing varying basicity, defined by donor numbers (DN) (7,8). Our results show that cation in the electrolyte strongly influences the reduction mechanism of O₂. Large cations such as TBA⁺ facilitate reversible O₂ reduction to form the one-electron reduction product, O₂⁻, which is stabilized by the large TBA⁺. In contrast, small cations like Li⁺ (and Na⁺) promote irreversible electrochemical oxygen reduction. The initial reaction in lithium battery

electrolytes is one-electron reduction of O_2 to LiO_2 . The LiO_2 formed either decomposes to Li_2O_2 or undergoes further reduction to Li_2O_2 and Li_2O . The lithium oxides formed via electrochemical and chemical reactions passivate the electrode surface inhibiting the kinetics and reversibility of the processes. The Lewis acid characteristics of the cation appear to be crucial in determining the reversibility of the system.

We also found that the organic solvent present in the Li^+ -conducting electrolyte has a major role on the reversibility of each of the O_2 reduction products formed. We studied ORR in either tetrabutylammonium hexafluorophosphate ($TBAPF_6$) or lithium hexafluorophosphate ($LiPF_6$) electrolyte solutions in five different solvents. They included dimethyl sulfoxide (DMSO), acetonitrile (MeCN), dimethoxyethane (DME), a mixture of ethylene carbonate (EC) and ethylmethyl carbonate (EMC), and tetraethylene glycol dimethyl ether (TEGDME), possessing a range of DN. We have found that the solvent and the supporting electrolyte cations in the solution act in concert to influence the nature of reduction products and their rechargeability. In general, O_2 reduction in solutions containing TBA^+ is a highly reversible one-electron process involving the O_2/O_2^- couple with little effect in this case on the nature of the solvent. On the other hand, in Li^+ -containing electrolytes relevant to the Li-air battery, O_2 reduction proceeds in a stepwise fashion to form O_2^- , O_2^{2-} and O^{2-} as products. These reactions in presence of Li^+ are irreversible or quasi-reversible electrochemical processes and the solvents have significant influence on the kinetics, and reversibility or lack thereof, of the different reduction products. The stabilization of the one-electron reduction product, superoxide (O_2^-) in TBA^+ solutions in all of the solvents examined can be explained using Pearson's Hard Soft Acid Base (HSAB) theory involving the formation of the $TBA^+ \cdots O_2^-$ complex. The HSAB theory coupled with the relative stabilities of the $Li^+(\text{solvent})_n$ complexes existing in the different solvents also provide an explanation for the different O_2 reduction products formed in Li^+ -conducting electrolyte solutions.

The ions present in the solutions used in our study were the supporting electrolyte ions TBA^+ , PF_6^- , Li^+ , and the electrochemically generated ions superoxide (O_2^-), peroxide (O_2^{2-}) and monoxide (O^{2-}). The TBA^+ is classified as a soft acid due to its large radius of 0.494 nm (in DMSO) and low charge density. It has been shown that tetraalkylammonium ions, NR_4^+ , are poorly solvated in organic electrolytes due to their large size and the small surface charge (9). A solvent's basicity is usually characterized by its donor number (DN) which for the solvents used here follows the order $MeCN(14.1) < TEGDME(16.6) < DME(20.0) < DMSO(29.8)$. Solvent acidity can be characterized by its acceptor number (AN) which in these solvents follow the order $DME(10.2) < TEGDME(10.5) < MeCN(18.9) < DMSO(19.3)$. In $TBA/DMSO$ electrolytes, although DMSO has a high DN, TBA^+ is weakly solvated. Consequently solvent- TBA^+ interactions are weak in the electrolytes allowing TBA^+ to roam more or less as a naked ion. Among the oxides formed from the reduction of oxygen, O_2^- has a relatively large radius and low charge density, which makes it a moderately soft base. In keeping with the HSAB theory, the naked soft acid TBA^+ stabilizes the soft base O_2^- in the electrolyte with the formation of an ion pair complex of the type, I.

Reversibility of the O_2/O_2^- redox couple in TBA^+ solutions is a result of this stable solution species I. As O_2^- is strongly coordinated to TBA^+ in I, further reduction of superoxide to peroxide (O_2^{2-}) is hindered. DMSO exhibits excellent electrochemical reversibility for the O_2/O_2^- couple.

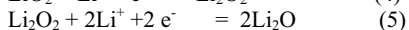
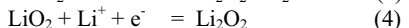
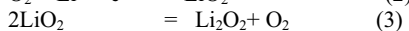


Structure I: Ion pair between TBA^+ and O_2^- . Nitrogen is blue, carbon is gray and O is red. (Alkyl hydrogens are omitted in the structure)

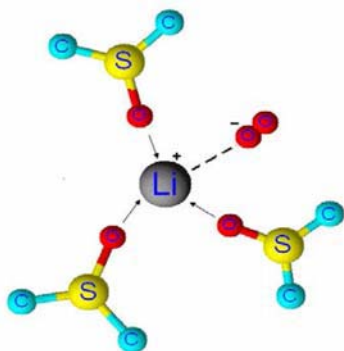
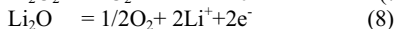
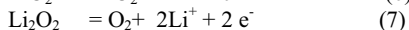
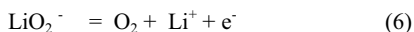
In electrolyte solutions, the hard Lewis acid Li^+ ions are solvated by the solvents; usually by about four solvent molecules per Li^+ to form solvent separated ion pairs, for example $Li^+(DMSO)_4PF_6^-$ in DMSO solutions. The Li^+ -solvent bond strength in the complexes would follow the solvent DN scale as $DMSO > MeCN > DME > TEGDME$. Nuclear magnetic resonance studies have revealed that these solvated ion pairs are fluxional complexes even

down to $-20\text{ }^{\circ}\text{C}$ (9-11). Although Li^+ behave as a hard acid, its acidity is modulated (or more precisely lowered) by the strength of the co-ordination bonds in $\text{Li}^+(\text{Solvent})_n$ formed with the solvent. Since superoxide is a moderately soft base it has low affinity for the hard acid Li^+ present in Li^+ -conducting electrolytes. Consequently, the superoxide formed as the first reduction product of O_2 will want either to decompose or undergo a fast second reduction to form the hard base, peroxide (O_2^{2-}), as shown in equations 2-4. The following equations describe the anodic and cathodic reactions that occur in a Li air battery during discharge and charge.

Cathodic reactions



Anodic reactions



Structure II. Ion pair between solvated Li^+ and O_2^- . (The methyl hydrogen's are omitted in the structure)

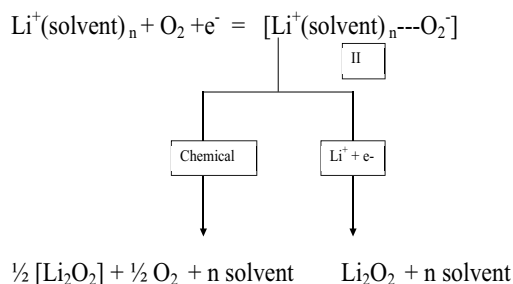
In DMSO solutions of LiPF_6 , the Li^+ Lewis acidity is decreased more than in other solvents due to its higher DN. As a result, the superoxide, O_2^- , formed as the first O_2 reduction product has an increased affinity for these solvated Li^+ , the O_2^- is stabilized longer in solution, in a structure of the type II, reminiscent of the $\text{TBA}^+ \cdots \text{O}_2^-$ complex I.

The multi-step electrochemical reduction of O_2 in Li^+ -containing electrolyte solutions can be schematically represented in the reaction scheme 1 and equations 2-5 and the reverse anodic processes in equations 6-8.

The Li-air battery is rechargeable as we have further demonstrated in the cycling of a Li/O_2 cell with TEGDME-based electrolytes and uncatalyzed carbon electrodes (12). The principal discharge product has been confirmed in this study to be Li_2O_2 . Catalysts facilitate the oxidation of Li_2O_2 as shown by several investigators (13, 14).

The development of the rechargeable Li-air battery is in its infancy. Significant progress in the discovery of improved electrolytes, catalysts to recharge the O_2 cathode and high efficiency Li anode cyclability are essential in order to fully assess the viability of this battery for electric vehicle propulsion.

Scheme 1



Rechargeable Li/S Battery

A recent review by this author has summarized the state of development and the major advantages and disadvantages of this battery (15).

The concept of electrochemical energy conversion and storage utilizing sulfur as the positive electrode in an alkali metal anode battery dates back to at least the 1960s. Early Li-S batteries included both ambient and high temperature versions. They utilized elemental sulfur as the cathode active material contained in a porous electrode matrix, usually carbon. The high temperature batteries operating at $\sim 450^\circ\text{C}$ employ Li-alloy anodes and LiCl-LiBr-KBr molten salt electrolytes, whereas their room temperature counterparts utilize elemental Li anodes in conjunction with organic electrolytes (16). Sodium-sulfur (Na-S) batteries operating at medium ($\sim 130^\circ\text{C}$) to high temperatures ($\sim 400^\circ\text{C}$) have also been developed with an anode consisting of metallic Na contained in a Na^+ -conducting ceramic tube such as $\beta\text{-Al}_2\text{O}_3$ which serves also as the separator in the battery.

In ambient temperature Li-S batteries employing organic electrolytes, poor discharge capacities were a serious problem due to the precipitation of Li_2S_2 and Li_2S in the cathode electrode pores and the consequent increase in the battery's internal resistance and low discharge capacities due to poor S utilization (15). The use of solutions of lithium polysulfides (Li_2S_n where $n = 8-10$) in organic electrolytes was pursued to counter this. Lithium polysulfides are prepared by treating Li_2S with an appropriate amount of elemental sulfur in an organic solvent. For example, to prepare Li_2S_8 , a typical catholyte for ambient temperature Li-S cells, one mole of Li_2S is stirred with seven moles of sulfur in a solvent such as tetrahydrofuran (THF), until all the solid sulfur is converted to a solution of the lithium polysulfide (equation 9 (15))



The solubility of the polysulfides varies with the solvents used. Li_2S_n in which n varying from 5 to 8 has been used to construct cells. Because S is in a slightly reduced state as S_n^{2-} , there is a small sacrifice in the theoretical energy density. For example if $n = 8$, then full reduction to Li_2S yields a capacity of $1.75e^-/\text{S}$ (equation 10) instead of $2e^-/\text{S}$ for the S/S^{2-} couple (15)

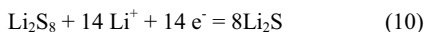


Figure 4 displays the discharge/charge cycling data for a Li- Li_2S_8 cell. The cell discharges at an average 2V and charges at a slightly higher voltage. A unique feature of the charge half-cycle is the absence of an end-point. This cell was completely discharged at the 13th discharge to calculate the average efficiency of cycling, found to be about 90%. This poor cycling efficiency is primarily attributed to self-discharge of the cell during charge, as indicated by the absence of an end-point. During charge of a Li- Li_2S_n cell, the soluble Li_2S_n diffuse to the Li anode through the porous separator and reacts with the Li anode to form insoluble Li_2S_2 and Li_2S which deposit on the Li anode surface. These reduced polysulfides react with the longer chain soluble Li_2S_n , where $n = 8-10$, present in solution to form intermediate chain length soluble Li_2S_n which diffuse back to the positive electrode and are re-oxidized.

This parasitic process takes place repeatedly, creating an internal "shuttle" phenomenon. It decreases the active mass utilization in the discharge process and markedly reduces the coulombic efficiency in the charge process. This is the reason for the absence of an end-point for the charge half-cycle. Interestingly, the shuttle provides intrinsic overcharge tolerance for Li-S batteries, which is essential for all non-aqueous batteries, removing the need for electronic controls to balance individual cells and terminate their charging in a series-connected battery pack.

At the end of each of each discharge, the soluble polysulfides are reduced to Li_2S_2 and Li_2S and precipitates on the cathode. These insoluble agglomerates become electrochemically inaccessible over prolonged cycling; causing active mass loss and the build-up of impedance layers that result in cathode capacity fading. Capacity fading is also caused by the accumulation of a net amount of the insoluble Li_2S and Li_2S_2 on the Li anode which in turn seriously lowers its rechargeability.

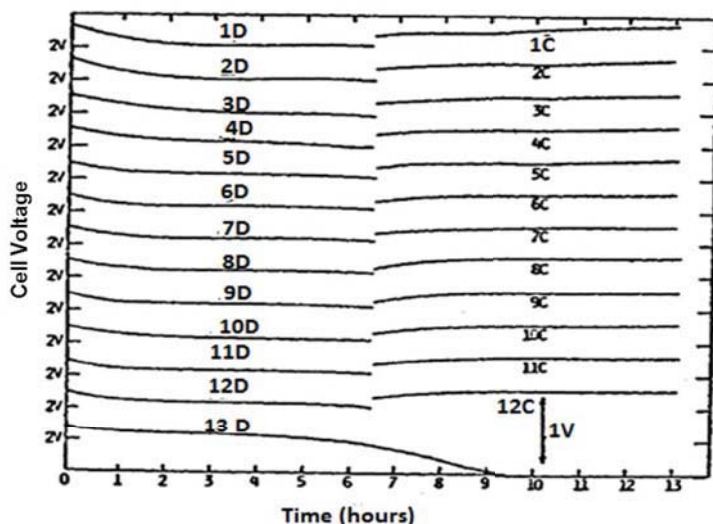


Figure 4: Galvanostatic cycling data for a $\text{Li}/\text{Li}_2\text{S}_n$ cell built with Li_2S_8 in THF as the active material. The discharge and charge half cycles are identified on the curves. The total S concentration is about 5 M. Current density is $1 \text{ mA}/\text{cm}^2$.

Among the solutions sought to improve the rechargeability of the sulfur electrode includes decreasing the solubility of Li polysulfides through the use of improved electrolytes (17), confining sulfur in mesoporous carbon matrix electrode (18) and the use of Li^+ conductive solid electrolytes to isolate the anode from the cathode to prevent self-discharge has been studied (19). One example is sulfide glasses such as $\text{Li}_2\text{S}-\text{SiS}_2$, and $\text{Li}_2\text{S}-\text{P}_2\text{S}_5$ (20).

Na/Metal Sulfide Batteries

A major factor limiting the cycle life of rechargeable the Li/S battery is the solubility of the lithium polysulfides in organic electrolytes, and the related sulfur shuttle reactions. An avenue to overcome this problem would be to decrease the solubility of sulfur with the use of metal sulfides as cathodes (21). Some past work I have done on such batteries is worth revisiting. Specific examples are Na/NiS , Na/CuS , Na/FeS_2 and Na/NiS_2 (10) rechargeable batteries, (Figure 5), and possibly their Li counterparts for the future. Interestingly, renewed interest in these batteries is beginning to emerge (22) which should be highly encouraged. Ultimately, energy from electrochemical reactions is limited due to constraints imposed by the Periodic Table of elements. Moore's law cannot predict the evolution of high energy density batteries (4).

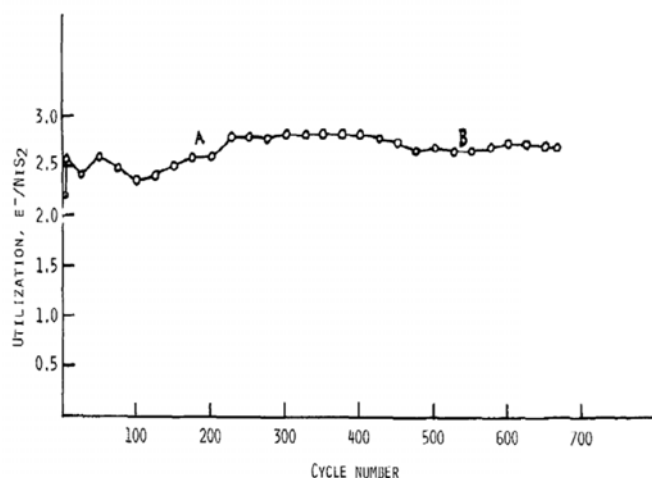


Figure 5: Cycle life data for a Na/NiS₂ cell (10)

References:

1. K.M. Abraham, "Rechargeable Lithium Batteries For The 300-mile Electric Vehicles And Beyond", lecture at the 15th International Meeting on Lithium Batteries, Montreal, Canada, June 2010.
2. Panasonic battery company catalog: http://industrial.panasonic.com/www-ctlg/ctlg/qACA4000_WW.html
3. Y. Wu and A. Manthiram, *Electrochem. Solid-State Lett.*, 9(5), A221 (2006)
4. K.M. Abraham, "Prospecting for a Counterpart of Moore's Law for Rechargeable Batteries", MRS Fall meeting, Boston, MA, November 2006 .
5. K.M. Abraham, . "Evolution of Lithium Batteries-where do we go from here ?", Workshop on Long Life Lithium-ion Batteries, Jet Propulsion Lab and Caltech, Pasadena, CA, February 2008.
6. K.M. Abraham, Z. Jiang, *J. Electrochem. Soc.* 143, 1 (1996) .
7. C.O. Laoire, S. Mukerjee, K.M. Abraham, E.J. Plichta, M.A. Hendrickson, *J. Phys. Chem. C* 114, 9178 (2010).
8. C.Ó. Laoire, S. Mukerjee, E.J. Plichta, M.A. Hendrickson, and K.M. Abraham, *J. Electrochem. Soc.*, 158, A302 (2011).
9. Gnanaraj, J. S.; Thompson, R. W.; DiCarlo, J. F.; Abraham, K. M. *Journal of The Electrochemical Society* 2007, 154, A185-A191.
10. Tsierkezos, N. G.; Philippopoulos, A. I. *Fluid Phase Equilibria* 2009, 277, 20-28.
11. Abraham, K. M.; Pasquariello, D. M.; Martin, F. J. *Journal of The Electrochemical Society* 1986, 133, 661-666(1979).
12. Cormac O Laoire , Sanjeev Mukerjee , Edward J. Plichta, Mary A. Hendrickson and K. M. Abraham , *Journal of The Electrochemical Society*, 158, A302-A308 (2011).
13. Débart, A.; Paterson, Allan J.; Bao, J.; Bruce, Peter G. *Angewandte Chemie International Edition* 47, 4521-4524 (2008).
14. Lu, Y.-C.; Xu, Z.; Gasteiger, H. A.; Chen, S.; Hamad-Schifferli, K.; Shao-Horn, Y. *Journal of the American Chemical Society*, 132, 12170.
15. Peter G. Bruce, Laurence J. Hardwick, and K.M. Abraham, *MRS Bulletin*, 36 506 (2011)
16. R.D. Rauh, K.M. Abraham, G.F. Pearson, J.K. Surprenant and S.B. Brummer ,*J. Electrochem. Soc.*, 126, 523 (1979)
17. J.H. Shin, E.J. Cairns, *J. Power Sources* 177, 537 (2008).
18. B.L. Ellis, K.T. Lee and L.F. Nazar, *Chem. Mater.* **22**, 691 (2010)
19. S.J. Visco and M.Y. Chu, *U.S. Pat.*, 6 210 832 (2001)
20. A. Hayashi, R. Ohtsubo, T. Ohtomo, F. Mizuno and M. Tatsumisago, *J. Power Sources* **183**, 422 (2008)
21. K.M. Abraham and J.E. Elliot, *J. Electrochem.Soc.*, 131, 2211 (1984)
22. D.C. Bogdan and M.Vallance Extended Abstract No.216, Fall ECS Meeting Las Vegas, October 2010

Hydrogen and Fuel Cell Technology Demonstrations in Developing Countries: Turkey Example

M. S. Yazici, N. Lymberopoulos, M. Hatipoglu

International Center for Hydrogen Energy Technologies, Istanbul, 34015, Turkey

The International Center for Hydrogen Energy Technologies (ICHET) has been implementing measures to demonstrate potential benefits of “hydrogen and fuel cell systems” in developing countries. To achieve its mission, ICHET implements pilot demonstration projects, provides applied research and development funding, and organizes workshops, education and training activities together with industry for early adaptation. Project results from various demonstrations including fuel cell forklift, fuel cell based Uninterrupted Power Supply (UPS), an island project, and renewable energy systems integrated mobile house will be covered below.

Introduction

There has been growing worldwide interest in renewable hydrogen economy and fuel cell technology, as reflected in the dramatic increase in public and private sector funding. Hydrogen together with renewable energy sources has been promoted as a potential solution to the climate change issue. High efficiency fuel cells, with their numerous possible applications, may actually be the main driver for the hydrogen economy (1). China, India, South Africa are setting serious demonstration projects to introduce hydrogen and fuel cell technologies due to new economic opportunities for reducing poverty and the availability of dramatically cleaner renewable energy sources (2). Energy independence can truly be possible when each individual can produce their own energy.

Turkey was late in its involvement with hydrogen and fuel cell technology development. The Turkish Ministry of Energy has been supporting the International Centre for Hydrogen Energy Technologies (ICHET) through a trust fund administered by UNIDO to implement hydrogen and fuel cell demonstrations in Turkey and other developing countries. ICHET has acted as a catalyst to involve Turkey in international hydrogen and fuel cell platforms.

Hydrogen and Fuel Cells in Turkey

The Turkish Scientific and Technical Research Council (TUBITAK) has been the main driver for hydrogen and fuel cell research at academic and industrial level in Turkey. More than \$15 million has been spent on hydrogen and fuel cell research last 10 years. Research arm of TUBITAK, Marmara Research Centre has been working on new technology development with emphasis on fuel cell stack and system prototypes, transportation applications and gasification/reforming research. Several Turkish universities have engineering faculties with research programs on hydrogen and fuel cell subjects. However, corporate activities are very limited to a few companies working on contract research.

UNIDO-ICHET Effort on Hydrogen and Fuel Cell in Turkey

ICHET implements various mechanisms to promote hydrogen and fuel cell research, demonstrations and education in Turkey. These mechanisms are explained in greater detail below.

Feasibility Studies. ICHET is aiming to become a catalyst to implement hydrogen and fuel cell demonstrations in Turkey and other developing countries. Limited resources prevent developing countries from giving priorities to hydrogen and fuel cell research and development. ICHET takes a proactive role by supporting pre-feasibility studies in several countries on various technologies before turning feasible proposals into full scale projects. In addition to 20 feasibility studies in more than 15 countries, there are five feasibility studies in Turkey: “Bozcaada Hydrogen Island Proposal”, “Hydrogen Bus Pilot Project for Istanbul”; “Market Potential for Hydrogen Production from Hydrogen Sulfide in Black Sea and Industrial Waters”; “Hydrogen Generation Using City Wastes”; and “Process for One Stage Production of NaBH_4 from Borax”. Hydrogen Island project has been implemented as full scale project to demonstrate potential benefit of fuel cells to produce electricity.

Demonstrations. ICHET has several national projects for various hydrogen and fuel cell technology demonstrations (3). Universities, small and big companies, public entities have all been involved in these projects for widespread acceptance of hydrogen technologies. One of the flagship demonstration projects is implemented in an island called Bozcaada where wind-solar-hydrogen combination showcased. Wind turbine with 30 kW capacity is combined with 20 kW PV panels to provide power for 50 kW alkaline electrolyzer where hydrogen is produced for 35 kW gen-set and 20 kW fuel cells (Fig. 1). System is operated at grid-connected mode to sell excess energy. This demonstration will help penetration of renewable energy sources in the energy systems of islands and demonstrate storage of excess electricity in the form of hydrogen.

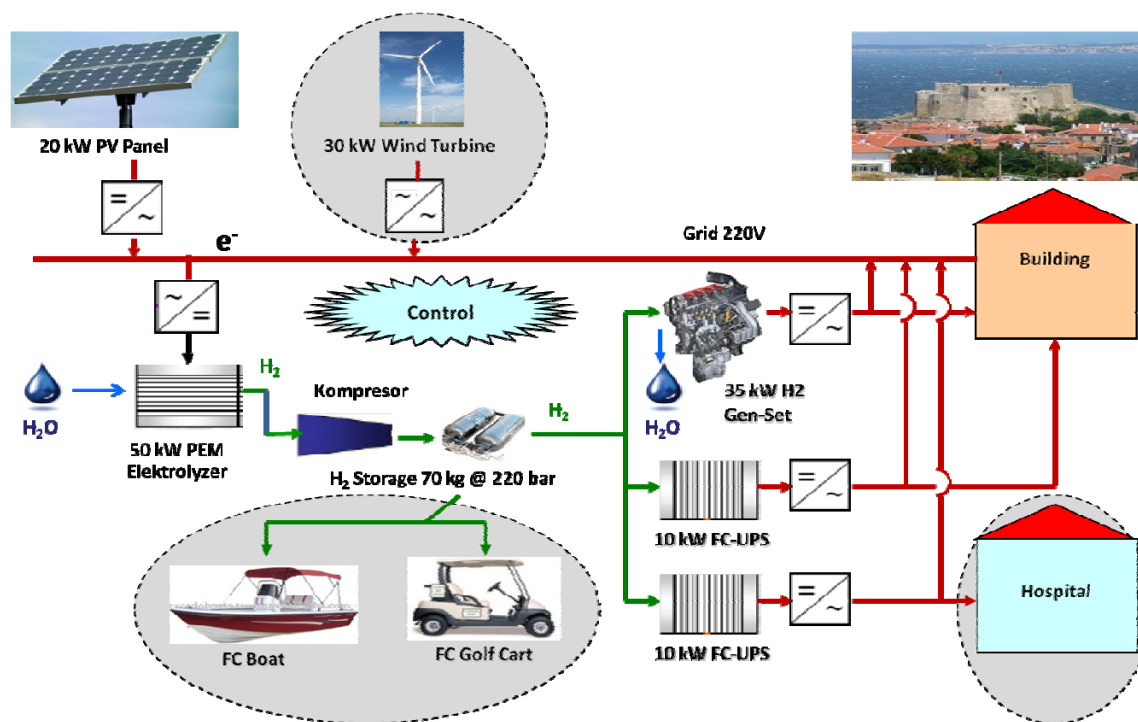


Fig. 1. Renewable-hydrogen installation in Bozcaada, Turkey

ICHET is promoting the use of zero-emission transportation technologies to protect water resources. Battery-fuel cell hybrid drive systems will be advantageous especially for use on lakes and rivers whose pristine environments need to be preserved from green house gas emissions and petroleum contamination. ICHET is supporting six universities to construct boats measuring up to 7 m long and 3 m wide. Each boat will have a single 8 kW fuel cell receiving power from high pressure hydrogen stored on board. The theoretical knowledge of engineers from various fields will be brought together for design, control, power management and system integration.

A conventional forklift is converted to a zero-emission fuel cell forklift, named Ecolift, and operated at ICHET. The H₂ Ecolift is based on a vehicle with 1.5 tone lifting capacity and accommodates a power pack comprising an 8 kW PEM fuel cell, and a hydrogen tank with 1.6 kg hydrogen storage capacity (Fig. 2a). It is refilled from high pressure cylinders with commercial refueling nozzles (Fig. 2b). Replacing existing battery technology in forklifts is expected to increase productivity by reducing refueling times and reduce cost by eliminating additional batteries and forklifts. Preliminary tests have demonstrated that both improved overall performance and an extended run time between fills, which together significantly increase the forklift's productivity, thus proving functionality in a more efficient way through the use of innovative technology. A new project with large number of deployment sites is in progress based on ICHET's previous experience. The European Commission is financing production of 10 fuel cell forklifts (FC FLT) with required hydrogen refueling infrastructure at sites in Turkey, the United Kingdom and Spain. Each deployment site is representative of one of the market segments deemed likely for early commercialization including: airports; light logistics; and industry. Real time data will be gathered with the intention of demonstrating the advantages inherent with the use of fuel cells fuelled by hydrogen generated via zero-carbon technologies in comparison to those such as diesel, LPG, and batteries etc currently in widespread use.



Fig. 2 (a) Fuel cell forklift and (b) filling process with portable nozzle

Fuel cell performance and energy consumption under idle, idle lifting, lifting and driving with and without load on a predefined time period was recorded over the Controller Area Network (CAN Bus) data collection device. Figure 3 shows power requirements under different operating mode.

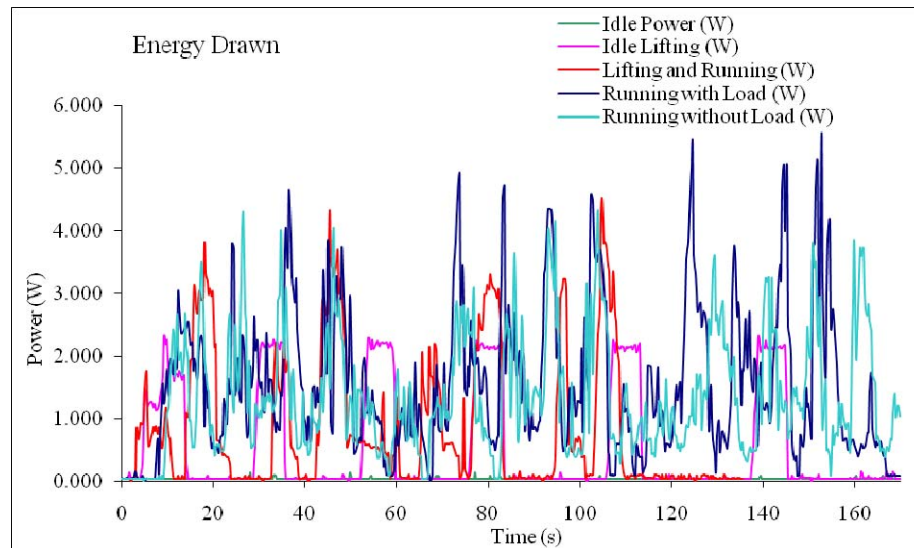


Figure 3: Power requirement under different operational mode (Idle, Idle- lifting with load, driving with and without load at average speed of 20 km/h, driving and lifting with load).

The Hydrogen filling station project aims to establish a hydrogen production, storage and refueling facility adjacent to the Golden Horn in Istanbul. This will be Turkey's first commercial hydrogen filling station and will put ICHET firmly on the map for European network of filling stations. System, as shown in figure 4, will provide hydrogen fuel both at 350 bar (for bus) and 200 bar (ship). This will be the first facility of its kind supplying both sea and land transport vehicles from the same refueling facility. In parallel with this project, ICHET is providing technical support and facilities for project design and implementation of a fuel cell ship in a demonstration project managed by the BELBIM Corporation of Istanbul Municipality. The Istanbul City Ferry Lines plans to operate a ferry capable of carrying some 52 passengers around the waters of the Golden Horn in Istanbul. The ship will be constructed and integrated with a hybrid electric drive system powered by four fuel cells and balance of plant (BoP) components. In conjunction with filling station, a hybrid bus powered by a hydrogen fuelled internal combustion engine (HICE) is in the manufacturing stage. The HICE will act as an electrical generator that charges on board Li-ion batteries for powering an electrical drive system. Both the boat and bus will be able to fuel from the same filling station at the same time at different operating pressures.

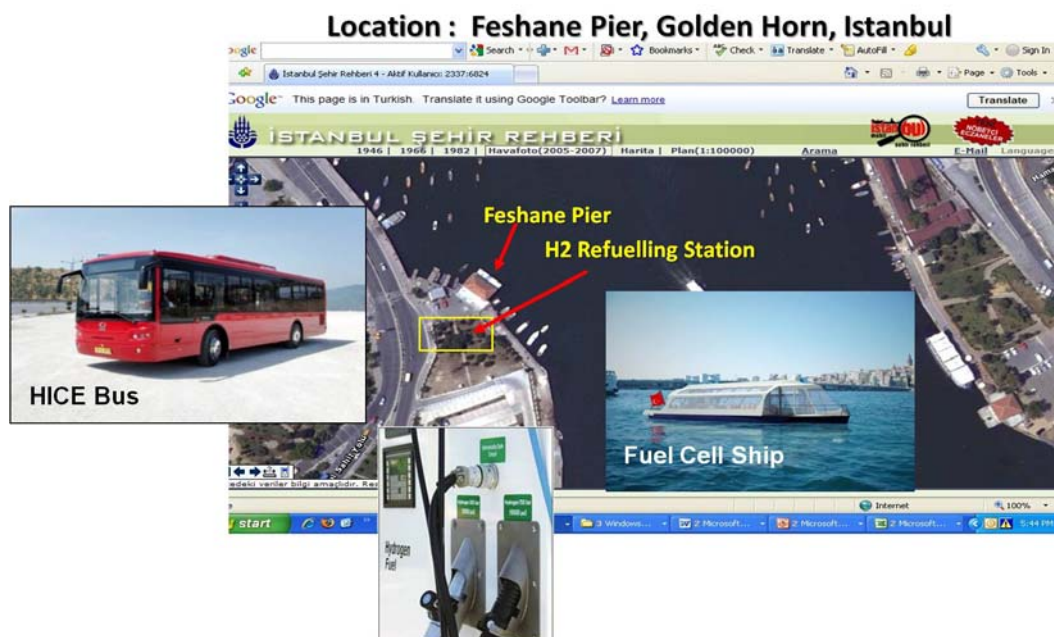


Fig. 4. Map showing location of the future filling station

Availability of hydrogen has become an issue in Turkey as more and more prototypes are developed by ICHET and others. A small hydrogen re-fuelling point is being set-up for the purpose of providing fuel at 200 bars pressure to the various demonstration vehicles and for refilling low pressure metal hydride cylinders. ICHET is working with a Turkish company to produce a PEM electrolyzer with 5 liters/min production capacity in the 15-20 bars pressure range. The purpose of the project is to encourage local involvement in hydrogen production technologies whilst at the same time creating opportunities for market environment with a low cost electrolyzer. Similar approaches have been implemented with university-industry consortia for other projects.

Fuel cell based un-interruptible power supply (UPS) systems are considered as an early commercial opportunity for market penetration of fuel cells (4). ICHET is in the process of installing several FC-UPS systems at various locations in Istanbul. Two such systems with maximum 5 kW power capacities have been installed in locations of commercial activity (Istanbul Ferry Headquarters and OSTIM Industrial Area) (Fig. 5). In continuation of this project with representatives from fuel cell manufacturers, suppliers, end users and R&D centers, the European Commission is financing four additional units in Turkey, two being considered for telecommunication application. This demonstration project will involve benchmarking of units from fuel cell suppliers following test protocols applicable for telecommunications environments. In accordance with these protocols, extensive field trials at sites selected by end users in Italy, Switzerland and Turkey will be conducted allowing lifecycle cost analyses to be undertaken for the determination of the real economic value in comparison with existing battery and diesel generator based technologies.

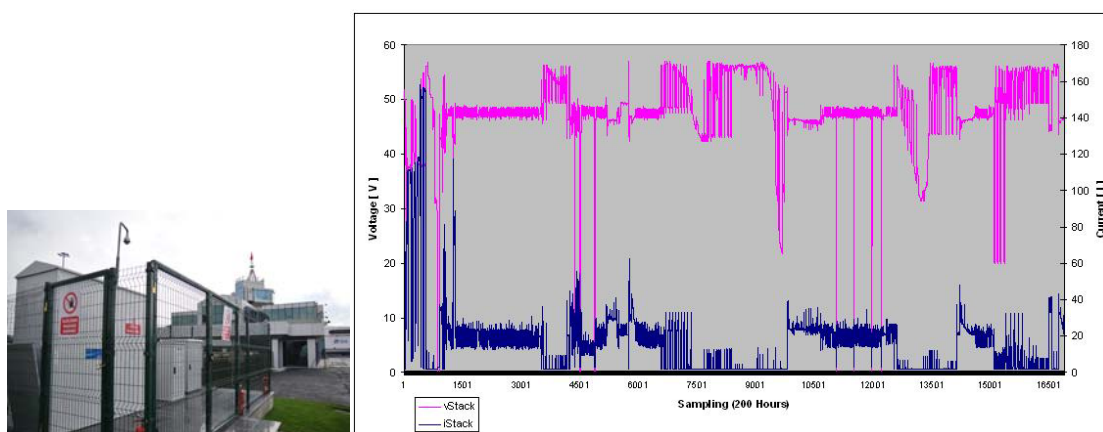


Fig. 5. Fuel cell back-up power system in commercial operation in Istanbul and voltage-current response during power shortages

Hydrogen should be considered an essential component of the majority of renewable energy systems. In order to promote this aspect of hydrogen, PV panels, wind turbine, electrolyser, fuel cell and batteries have been integrated into a mobile vehicle (Fig. 6). In this vehicle, batteries are being used to store some of the excess energy produced by the solar panels (1.7 kW) and wind turbine (1 kW) which in normal use feed DC power directly to the inverter. Any excess power is used to electrolyze water for hydrogen production which in turn be used to power a fuel cell or burnt as fuel in the stove. The system has many potential uses including off-grid power needs, emergency power and energy training.

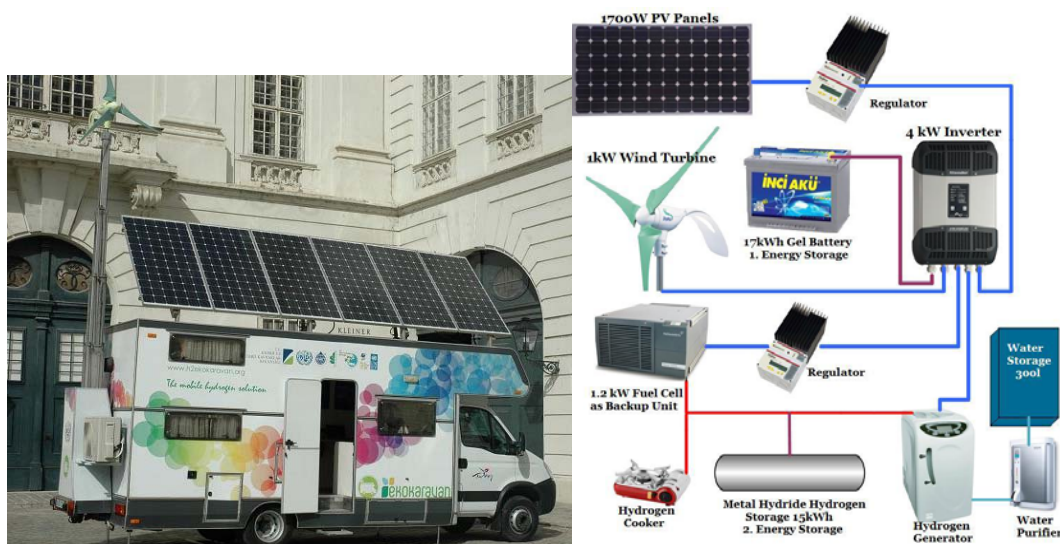


Figure 6. Eco-caravan and system components

R&D Support. ICHET provides comprehensive support for R&D activities involving both industry and academia. Project calls with multi-partner involvement under university coordination are routinely published and circulated. The purpose of this approach is to turn academic R&D programs and expertise into product development and industrial commercialization. One example is a call to produce 3 kW fuel cell systems in Turkey. Within this project, a consortium will develop a 3 kW fuel cell and deliver the

final prototype to ICHET for evaluation. The consortium consists of partners from academia, industry and R&D organizations, each having individual expertise in the areas of catalysts, membranes, system assembly, electronics and control systems. In the final part of the project, the consortium is expected to provide plans for developing the prototype to a pre-production level. Another such project is production of a fuel cell Combined Heat and power (CHP) system in which a 3 kW CHP system is developed and brought to a pre-production stage by a consortium using expertise in the country's industrial and academic research centers. In comparison with conventional systems, fuel cell based CHP systems provide far higher levels of efficiency (better than 80%) and thus are essential elements in any power efficient economy. Finally, a similar university-industry based consortium has been working on developing an internal combustion engine that can burn both hydrogen and a mixture of hydrogen/methane to improve emission characteristics of internal combustion engines. Pure methane has a relatively narrow flammability range that limits achievable fuel efficiencies and results in poor NO_x emission characteristics at lean air/fuel ratios. This project will result in internal combustion engines using hydrogen/methane mix that produce low (or zero) emissions.

Education & Training. Turkey has not been at the forefront of fuel cell development. In order to close the gap, ICHET is offering short courses, training courses, sponsorships, internships and collaborations on hydrogen and fuel cell technologies (5). ICHET's permanent research capabilities including fuel cell testing; hydrogen production and storage facilities; and equipment for analytical characterization and testing, offer a wide range of hydrogen energy related facilities to Turkish universities and industry. ICHET has state of the art fuel cell test stations ranging from 120 watt, 1 kW, 2 kW and 12 kW testing capabilities supported with on-site hydrogen production (electrolysis) capabilities (Fig. 7).

Universities are given the opportunity to send engineering students and staff to ICHET where they can work on various topics for thesis or post doctoral studies. Every summer ICHET accepts about 7-10 interns to work on various subjects for durations between 20-30 days. Master and doctoral students are supported on a part-time basis to work at ICHET and help staff while working towards their degrees in hydrogen fuel cell related activities. Since 2005, more than 50 students have been supported under this program and this approach has opened up new avenues for engineers to pursue careers in fuel cell system and application development (6). This capacity building is leading towards establishing a fuel cell system integration base in Turkey.



Fig. 7. Fuel cell assembly and test stations at ICHET laboratory

Conclusions

ICHET is promoting hydrogen and fuel cell energy technologies for social and economic benefits. However, the most significant impact will come from educating the public about hydrogen energy and its future role. This eventually will create sufficient momentum to influence policies, accelerate public interest in hydrogen technologies, lead to the creation of a technology network for competitive advantage, and unlock the energy potential of Turkey. Government involvement is necessary to bridge the time and cost gap for encouraging public for use of hydrogen and fuel cells. Government subsidies and tax incentives should be used to encourage foreign investors for mass production, with government-industry partnerships enabling mass production of affordable fuel cells and the provision of the suitable hydrogen infrastructure needed to support them. To achieve significant progress with hydrogen technologies, Turkey must develop and implement favorable policies that treat renewable and hydrogen energies as priority issues.

Acknowledgments

ICHET projects were supported financially by the Turkish Ministry of Energy and Natural Resources. Projects were implemented by teams of scientists and engineers from ICHET, Turkey and abroad. All contributions are gratefully acknowledged.

References

1. F. Barbir, PEM Fuel Cells: Theory and Practice, Academic Press, 2005.
2. <http://www.fuelcelltoday.com/online/survey-landing-page/Geographic>
3. M.S. Yazici, Int. J. of Hydrogen Energy, V. 35, p. 2754 (2010)
4. F. Barbir, M.S. Yazici, Int. J. of Energy Research, V. 32, p. 369-378 (2007)
5. M. S. Yazici, Hydrogen and Fuel Cell Education-Outreach Activities at ICHET, Proc. of 17th World Hydrogen Energy Conference, Brisbane, Australia (2008)
6. M. S. Yazici, Role of Hydrogen on Engineering Education: ICHET Example, Proceedings of 18th World Hydrogen Energy Conference, Essen, Germany (2010)

Pressurized Solid Oxide Fuel Cells with Reformate as Fuel

C. Willich^a, C. Westner^a, M. Henke^a, F. Leucht^a, J. Kallo^a, U. Maier^b, K.A. Friedrich^a

^a German Aerospace Centre (DLR), Pfaffenwaldring 38-40, 70569 Stuttgart, Germany

^b ElringKlinger AG, Max-Eyth-Straße 2, 72581 Dettingen/Erms

In this contribution the influence of pressure on an SOFC is studied with steam-reformed methane as a fuel. Experiments were performed with a reformate containing 58.4% H₂, 20% H₂O, 12.2% CO, 5.5% CO₂ and 3.9% CH₄ and another mixture containing 18% H₂, 34% H₂O, 2% CO, 27% CO₂ and 19% CH₄ as well as a hydrogen/nitrogen mixture. The influence of pressure on OCV, power density at constant voltage and constant current as well as on gas composition was examined for the different fuels. Power density increases of up to 70% were found.

Introduction

The demand for electrical energy increases and will continue to increase. Therefore new power plants with high efficiencies and low emissions have to be developed. A hybrid power plant consisting of a pressurized solid oxide fuel cell (SOFC) system coupled with a gas turbine is seen to fulfill both requirements because such a power plant may reach electrical efficiencies above 60% with low emissions (1). This kind of hybrid power plant also has the advantage of being suitable for a wide range of applications ranging from several 10 kW to the MW class. The German Aerospace Center (DLR) aims at setting up a hybrid power plant in the 50 kW class starting in 2013. For developing this power plant the Institute of Technical Thermodynamics (TT) and the Institute of Combustion Technology (VT) at DLR combine their expertise in fuel cells and gas turbine technology. The SOFC system is developed at the Institute of Technical Thermodynamics while the Institute of Combustion Technology focuses on the gas turbine. A schematic of the hybrid power plant is shown in Figure 1. Highest efficiencies and power are to be expected when the SOFC is operated at elevated pressures (2). In the context of the hybrid power plant the fuel cell will be operated at elevated pressures up to 8 bar. During operation of the hybrid power plant air is compressed in the compressor of the gas turbine. It is then preheated and fed to the SOFC system. The off-gases of the SOFC system are used in the combustion chamber of the gas turbine where additional fuel may be added for example for starting the system. After expansion of the gas in the gas turbine the off-gas is used to preheat the air for the fuel cell system.

For the realization of the power plant it is necessary to understand the behavior of each subsystem as well as their interactions. The pressurized solid oxide fuel cell is an essential part of the system but there is still little data available from literature concerning the behavior of SOFC at elevated pressures. Since it cannot quantitatively be derived from measurements at ambient pressure because of complex and interdependent

mechanisms taking place at the cell, a test rig for the characterization of SOFC stacks exposed to pressures up to 8 bar has been built at DLR (3).

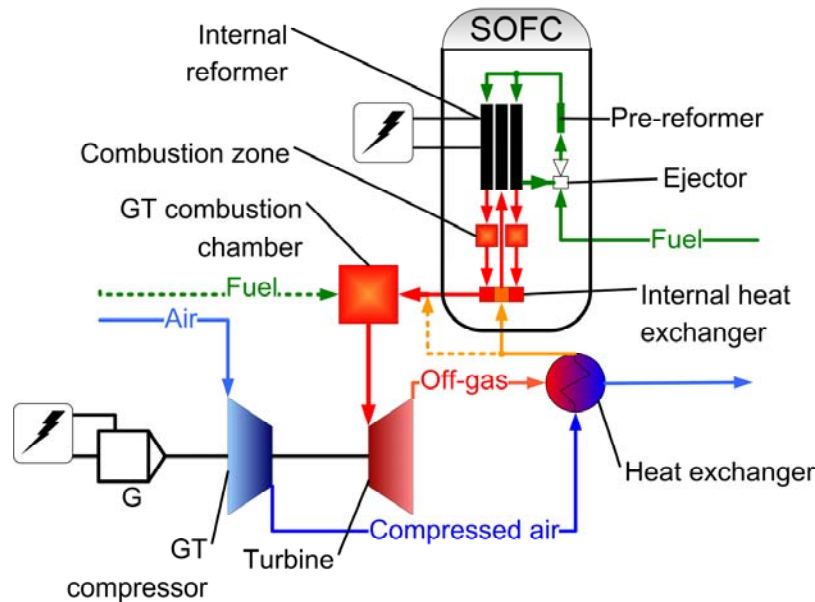


Figure 1: Schema of a hybrid power plant consisting of an SOFC system and a gas turbine.

The hybrid power plant will eventually run on natural gas, therefore the SOFC stack will be operated with prereformed reformat gases. The effect of elevated pressure on reformat gas composition, reforming reactions, electrochemical processes and the general behavior of the cells are of great interest. The knowledge of steady state as well as transient operational behavior and of course of operational limits is essential for the integration of the SOFC into the hybrid power plant system.

Experimental setup

In the pressurized SOFC test rig SOFC short stacks can be characterized at pressures of 1 to 8 bar. Pressure difference between anode and cathode gas compartments and the furnace can be controlled by a pressure control system up to 500 mbar. This pressure control is important to keep pressure differences low since a large pressure difference may lead to the destruction of the cells or stack. To control the pressure difference between anode, cathode and the furnace two equalizing tanks of 400 l each are used balancing the small volumes of the anode and cathode gas compartment against the far greater volume of the furnace.

The maximum temperature for testing is 950°C and the stack in the test rig can be supplied with mixtures of hydrogen, nitrogen, methane, carbon monoxide, carbon dioxide and steam on the anode side that can be mixed to represent reformat gases. At the cathode air, oxygen, nitrogen and helium are available. The test rig offers the possibility

to measure current-voltage characteristics of the stack and its individual cells as well as performing impedance spectroscopy on the cells. The gas composition at the in- and outlet of the anode and cathode can be measured by means of a gas chromatograph (3).

For the results presented here anode-supported 5-cell short stacks provided by ElringKlinger AG with an active area of 84 cm² per cell were used. They consist of sintered cells which are integrated into stamped metal sheet bipolar plates as shown in Figure 2. These are referred to as cassettes. The cells consist of an anode substrate (Ni/YSZ) and functional layer. The YSZ electrolyte is 10 μm thick and the cathode consists of two layers, a functional layer made of LSM/YSZ and a current collector made of LSM.

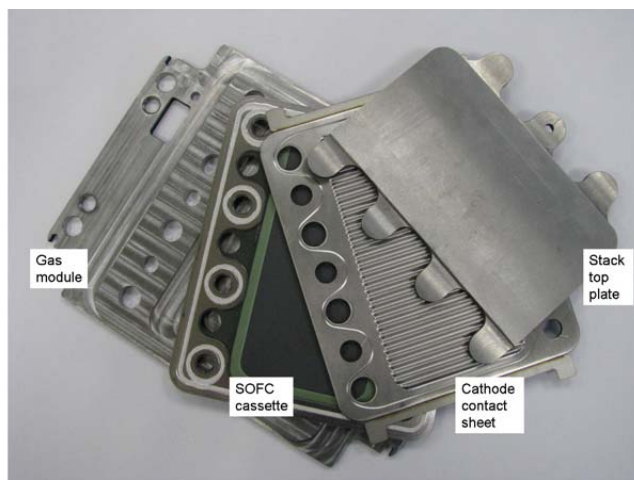


Figure 2: Cell integrated into metal bipolar plates.

Measurement were done with a 1/1 hydrogen/nitrogen mixture with a water content of 3%, a partially reformed reformat containing 18% H₂, 34% H₂O, 2% CO, 27% CO₂ and 19% CH₄ (reformat 1) as well as a steam-reformed reformat containing 58.4% H₂, 20% H₂O, 12.2% CO, 5.5% CO₂ and 3.9% CH₄ (reformat 2). The temperature was varied between 700°C and 800°C and pressure variations were done ranging from 1.35 bar up to 8 bar. The flow rate for the hydrogen/nitrogen mixture was 5 l/min of hydrogen. The flow rate for the reformates was chosen to obtain the same theoretical current as for H₂/N₂ resulting in a total flow rate of 5.63 l/min for the first reformat and 5.06 l/min for the second. The results shown in this contribution are for one of the cells from the middle of the stack since outer cells often show a deviation in performance due to temperature effects (4).

Results

In Figure 3 to Figure 4 current voltage characteristics for one cell from the middle of the stack at different pressures can be seen for the three gas compositions at 700°C and 800°C. Each diagram shows the current-voltage curves for one gas composition and one temperature at different pressures. It can be seen in these diagrams that elevated pressure leads not only to a higher OCV but also affects the gradient of the curve under load. This

can be seen for all gas compositions and temperatures. The higher the current density the greater is the difference between the i-V curves for the different pressures. In the following chapters the behaviour shown in the characteristic curves is examined more closely.

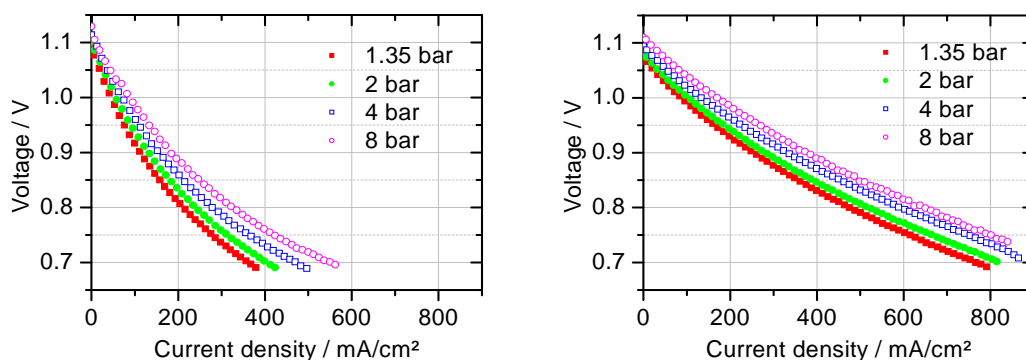


Figure 3: Pressure dependent current voltage curves for H_2/N_2 at 700°C (left) and 800°C (right).

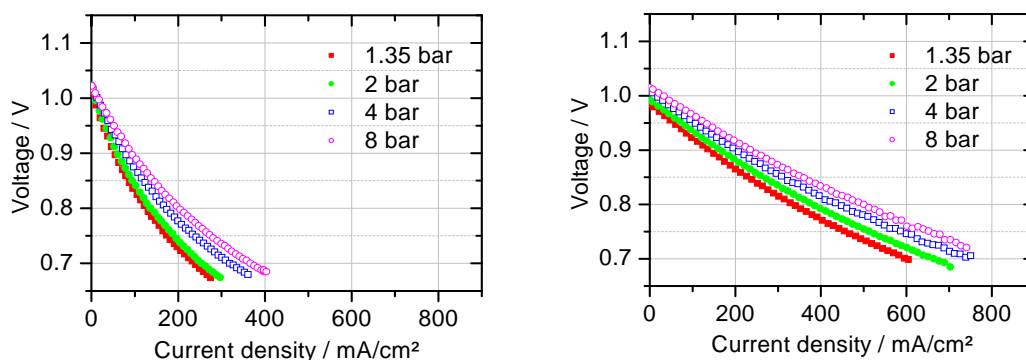


Figure 4: Pressure dependent current voltage curves for reformat 1 at 700°C (left) and 800°C (right).

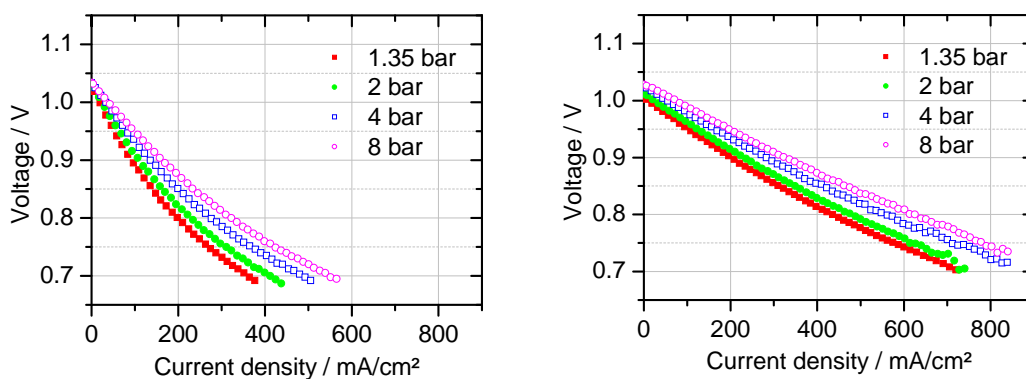


Figure 5: Pressure dependent current voltage curves for reformat 2 at 700°C (left) and 800°C (right).

Pressure influence on gas composition and open circuit voltage

Figure 6 shows the development of OCV of one cell from the middle of the stack with increasing pressure for the three different gas compositions that were examined. The squares show the experimentally obtained values. The lines show the theoretical OCV that was calculated using equation [1] and assuming equilibrium composition of the fuel at the cell. For determining equilibrium composition and OCV the open-source software CANTERA (5) was used.

$$\text{OCV} = -\frac{RT}{2F} \ln \frac{\sqrt{p_{\text{O}_2, \text{cathode}}}}{\sqrt{p_{\text{O}_2, \text{anode}}}} \quad [1]$$

Filled symbols are experimental values at 800°C while open symbols represent measurements at 700°C. The continuous lines are calculated for 800°C and the dotted lines for 700°C. Colour and symbol shape stand for the three different gas compositions measured. Calculated and experimental values show similar tendencies. For all gas compositions OCV increases with pressure but not to the same extent. Temperature has an influence on the OCV and its increase through pressure. The hydrogen/nitrogen mixture shows a greater increase in OCV than the reformat gases. For the following comparisons theoretical OCV values are taken. For a pressure increase from 1.35 bar to 8 bar the OCV of the hydrogen/nitrogen mixture rises by 40 mV (3.7 %) at 800°C while for reformat 1 it rises only 30 mV (3.1%) and for reformat 2 by 23 mV (2.3%). The increase in OCV through pressure at different temperatures varies only slightly for the H₂/N₂ mixture. At 700°C the increase is 36 mV (3.3%) compared to the 40 mV (3.7 %) at 800°C mentioned above. For the reformat gases temperature has a stronger influence on OCV increase through pressure. For both reformates the increase in OCV remains below 10 mV for a temperature of 700°C (9 mV or 0.9% for reformat 1 and 4 mV or 0.4% for reformat 2). In the case of the reformates the lower temperature leads to a higher OCV at low pressures, but at high pressures the difference in OCV because of temperature gets smaller. For reformat 2 the OCV at 8 bar is almost the same for both temperatures.

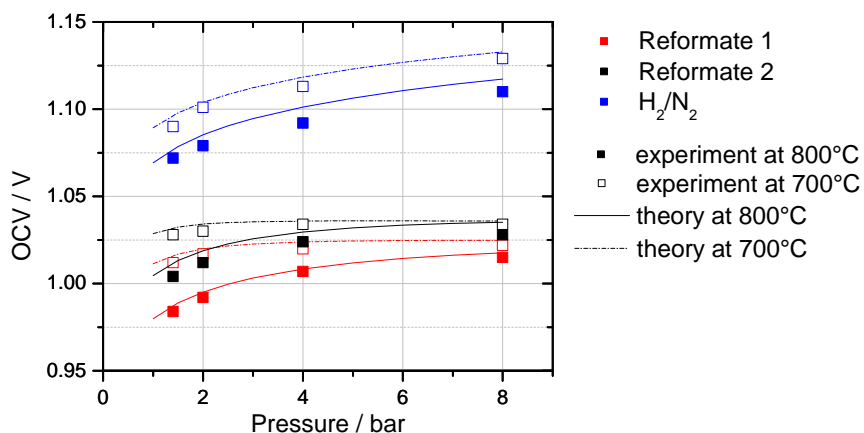


Figure 6: Pressure and temperature dependence of OCV for three different gas compositions

This can be explained by looking at the pressure dependency of the equilibrium compositions of the reformat gases at different temperatures. The lines in Figure 7 show the calculated equilibrium compositions for reformat 1 that were determined using CANtera for pressures ranging from 1 to 8 bar for 700°C and for 800°C. The symbols are the gas compositions that were measured at OCV after the stack for the different conditions using a gas chromatograph. The measured values match well with the theoretical equilibrium composition, although there is a discrepancy especially for the water content.

At 700°C the gas composition varies far more with pressure than at 800°C. The higher the pressure the smaller is the hydrogen and CO content of the equilibrium fuel gas. While at 800°C the hydrogen content decreases from 46% to 41% for the theoretical equilibrium and stays constant in the measurements, it decreases at 700°C from 46% to 32% for the theoretical equilibrium and from 48% to 36% for the measured values. The pressure increase leads to an increase in OCV of the cell but it also leads to a less favourable gas composition with smaller fuel content which is decreasing this OCV gain through pressurization.

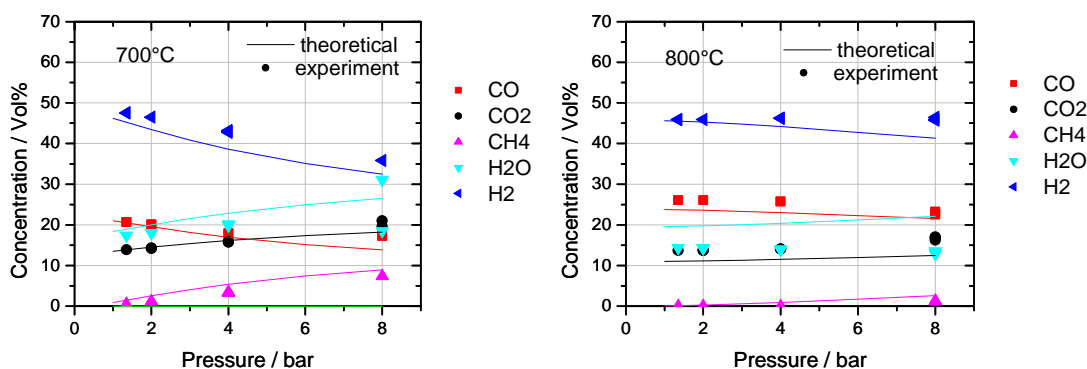


Figure 7: Calculated equilibrium gas composition and measured values over pressure for reformat 1 at 700°C and 800°C.

A similar tendency is seen for reformat 2 in Figure 8. The H₂ content is higher than for reformat 1 but the decrease in hydrogen content for the theoretical equilibrium is similar to that of reformat 1.

The calculated H₂ content of the H₂/N₂ mixture hardly varies with pressure for either temperature as can be seen in Figure 9 which is why OCV rises more strongly with pressure for this fuel.

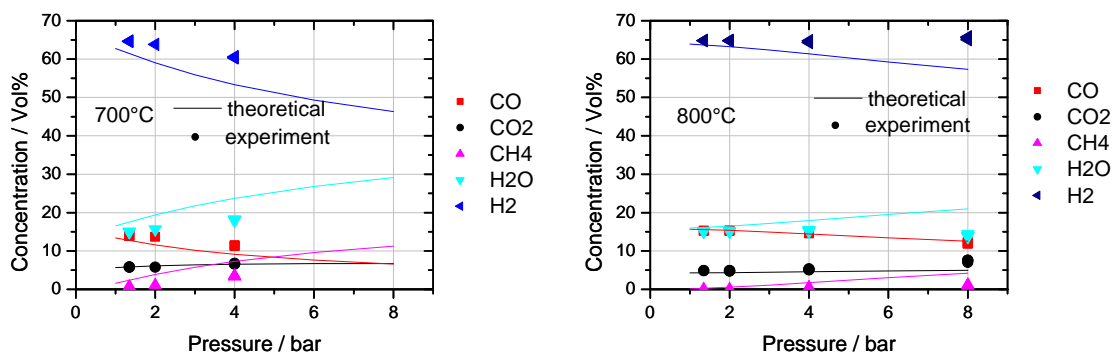


Figure 8: Calculated equilibrium gas composition and measured values over pressure for reformat 2 at 700°C and 800°C.

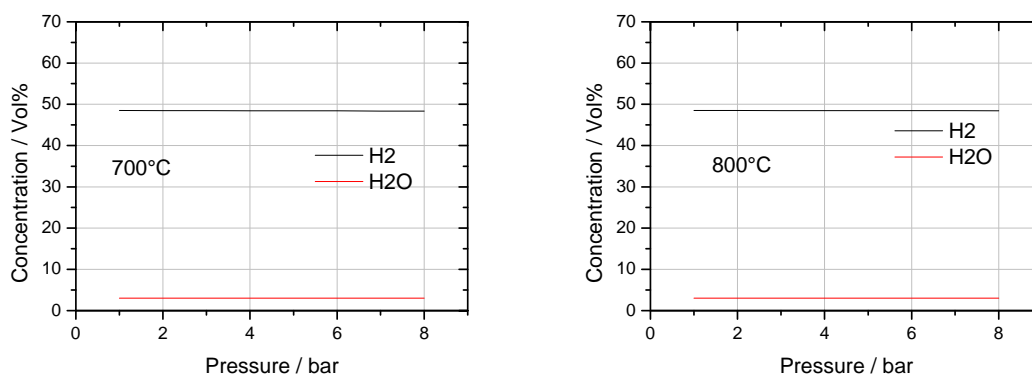


Figure 9: Calculated equilibrium gas composition over pressure for H_2/N_2 mixture at 700°C and 800°C.

Performance gain under pressure at constant voltage

In Figure 10 the influence of pressure on performance at a constant voltage of 750 mV can be seen for the different fuels. The filled symbols are the measured values at 800°C, the open symbols at 700°C. The pressure dependency shows a logarithmic behavior for all fuels increasing more strongly at low pressures and leveling out at elevated pressures. At 800°C power density is highest for H_2/N_2 but the relative as well as the absolute power density gain through pressurization is slightly greater for the reformates. At a pressure rise from 1.35 bar to 8 bar power density at 750 mV rises by 138 mW/cm² or 30% for the H_2/N_2 mixture, while it rises by 146 mW/cm² (42%) for reformat 1 and by 154 mW/cm² (35%) for reformat 2. Here the reformat gas with the greater methane content (reformat 1) shows a smaller absolute increase but a higher relative increase than the almost entirely reformed reformat 2. It can be seen from Figure 10 that at a constant cell voltage of 0.75 V the curves for 700°C have a smaller gradient than those for 800°C. A lower temperature leads to a smaller increase in power density while a higher temperature leads to a stronger increase in performance with rising pressure for all fuels measured. At 700°C the increase with pressure for reformat 1 is

smaller than for both the other fuels. The increase is only 78 mW/cm² if pressure is increased from 1.35 bar to 8 bar while for H₂/N₂ the increase is 106 mW/cm². Nevertheless the relative gain is highest (60%) for reformat 1 in comparison to 51% for H₂/N₂. At 700°C reformat 2 and the H₂/N₂ mixture hardly differ from each other although the absolute power density increase through pressurization at 700°C as well as at 800°C was highest for reformat 2 (115 mW/cm² or 57 % at 700°C). For clarity the power density gains in comparison to 1.35 bar are shown also in table I.

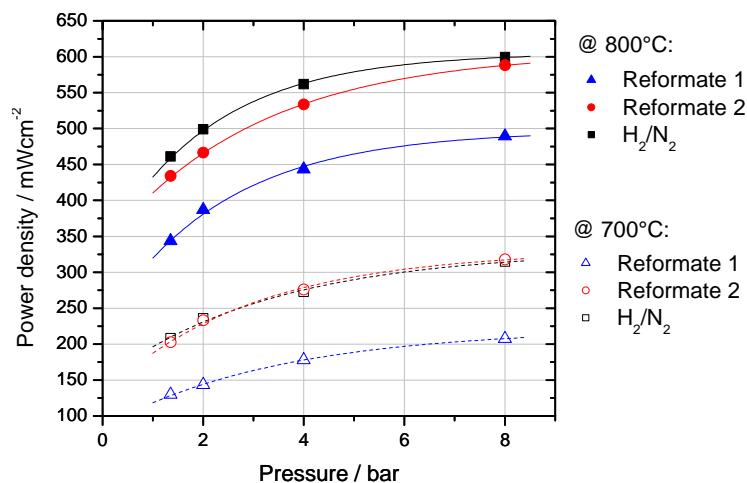


Figure 10: Power density at 750mV cell voltage at different pressures

TABLE I: Power density gain through pressurization at 750 mV compared to 1.35 bar.						
700°C	→ 2 bar		→ 4 bar		→ 8 bar	
	mW/cm²	%	mW/cm²	%	mW/cm²	%
H ₂ /N ₂	28	13	65	31	106	51
Reformat 1	14	11	48	37	78	60
Reformat 2	30	15	73	36	115	57

800°C	→ 2 bar		→ 4 bar		→ 8 bar	
	mW/cm²	%	mW/cm²	%	mW/cm²	%
H ₂ /N ₂	38	8	101	22	138	30
Reformat 1	43	13	99	29	146	42
Reformat 2	33	8	100	23	154	35

At a higher cell voltage tendencies are similar with only minor differences. In Figure 11 power densities for different pressures at a cell voltage of 850 mV are shown. At 850 mV the absolute power density level is lower for all fuels compared to 750 mV. The absolute power density gain through pressurization is also lower although the relative increase in performance is greater. At this voltage the absolute power density gain for reformat 1 which contains a greater part of methane shows a smaller gradient than the

other fuels for both temperatures (51 mW/cm² at 700°C and 108 mW/cm² at 800°C) while relative power density gain is highest (70% and 55%). Although the hydrogen/nitrogen mixture shows the highest performance for both temperatures, reformat 2 shows the greatest increase in absolute power density gain of the examined fuels (80 mW/cm² at 700°C and 134 mW/cm² at 800°C) while the hydrogen/nitrogen mixture gains 77 mW/cm² at 700°C and 118 mW/cm² at 800°C. For clarity the values are shown again in table II.

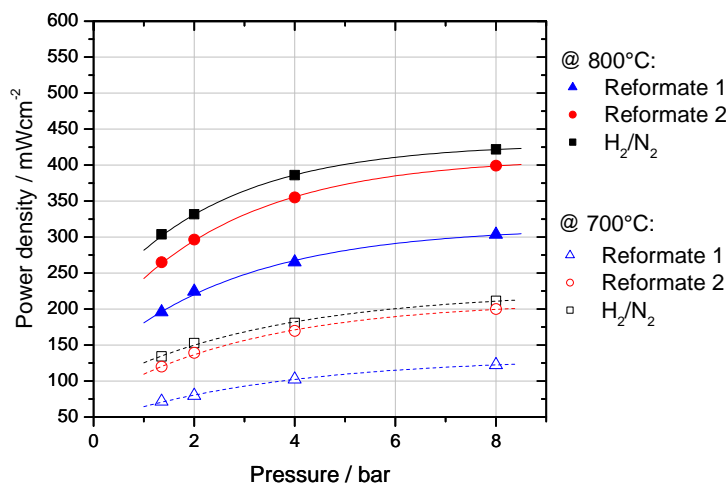


Figure 11: Power density at 850mV cell voltage at different pressures.

TABLE II: Power density gain through pressurization at 850 mV compared to 1.35 bar.						
700°C	→ 2 bar		→ 4 bar		→ 8 bar	
	mW/cm²	%	mW/cm²	%	mW/cm²	%
H ₂ /N ₂	18	14	46	35	77	57
Reformat 1	8	4	31	43	51	70
Reformat 2	19	16	50	41	80	67

800°C	→ 2 bar		→ 4 bar		→ 8 bar	
	mW/cm²	%	mW/cm²	%	mW/cm²	%
H ₂ /N ₂	28	9	82	27	118	39
Reformat 1	29	15	69	35	108	55
Reformat 2	31	12	90	34	134	51

Performance gain under pressure at constant current density

If power density is regarded at constant current density instead of constant voltage the power density increase through pressurization is smaller. Figure 12 shows the development of power density under pressure at a constant current density of 0.4 A/cm². As in Figure 10 the full symbols are the measured values at 800°C, the open symbols at

700°C. At 700°C the curve for reformat 1 fuel is missing since for that condition 0.4 A/cm² were only reached at 8 bar.

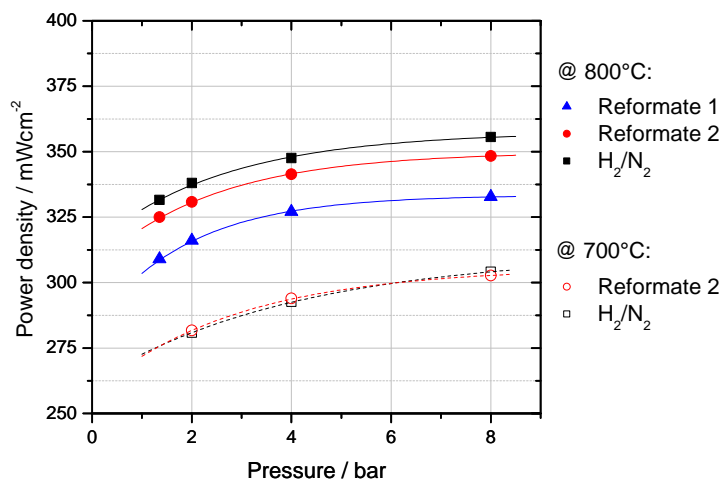


Figure 12: Power density at constant current density of 0.4 A/cm².

Power density increase through pressurization is similar for all fuels as can be seen also from table III. A pressure increase from 1.35 to 8 bar at 800°C leads to an increase of 24 mW/cm² for the H₂/N₂ mixture and reformat 1. For reformat 2 the increase is 23 mW/cm². The relative increase in power density is 7% for H₂/N₂ and reformat 2 and 8 % for reformat 1. At 700°C there is hardly any difference in performance for the H₂/N₂ mixture and reformat 2.

TABLE III: Power density gain through pressurisation at 0.4 A/cm ² compared to 1.35 bar.						
800°C	→ 2 bar		→ 4 bar		→ 8 bar	
	mW/cm ²	%	mW/cm ²	%	mW/cm ²	%
H ₂ /N ₂	6	2	16	5	24	7
Reformat 1	7	2	18	6	24	8
Reformat 2	6	2	16	5	23	7

At 700°C the increase in power density is slightly higher than at 800°C. For the hydrogen/nitrogen mixture and reformat 2 power density increases by 23 mW/cm² and 21 mW/cm² respectively when increasing pressure from 2 bar to 8 bar at 700°C while at 800°C the increase is 18 mW/cm².

Summary

The behavior of pressurized solid oxide fuel cells was examined using reformates as fuel. Two different reformat gases were used as well as a hydrogen/nitrogen mixture with 3% of water. Reformat 1 contained 18% H₂, 34% H₂O, 2% CO, 27% CO₂ and

19% CH₄ while reformat 2 contained 58.4% H₂, 20% H₂O, 12.2% CO, 5.5% CO₂ and 3.9% CH₄. Measurements were done at 700°C and 800°C at pressures ranging from 1.35 bar to 8 bar.

Pressure dependency of OCV was found to be highest for the hydrogen/nitrogen mixture. The pressure increase of OCV through pressurization for reformates showed a strong dependency on temperature. At lower temperatures the increase in OCV with pressure was found to be considerably smaller than for higher temperatures. This was explained by considering the gas compositions in equilibrium for the different temperatures as well as measurements of the gas composition after the stack. Measurements and calculated equilibrium compositions showed a good agreement. At lower temperatures gas composition varied strongly with pressure resulting in smaller hydrogen content at high pressures, which explains the smaller gain in OCV.

Under load pressurization showed a positive effect on performance for all fuels. At constant voltage a higher temperature led to a higher increase in power density for all fuels. The absolute increase in power density was found to be greatest for reformat 2 where up to 154 mW/cm² were gained at a voltage of 750 mV while the relative increase was greatest for reformat 1 which contained the greater part of methane and for which up to 70% of power increase was measured. The lower the voltage the greater was the absolute increase in power density through pressure while the relative increase got smaller. At constant current density the increase in power density because of pressure was similar for all fuels. At a current density of 0.4 A/cm² an increase of 24 mW/cm² or 8% was obtained.

References

1. S. Singhal, K. Kendall, *High Temperature Solide Oxide Fuel Cells Fundamentals, Design and Application*, Elsevier, Oxford, pp. 374 (2003).
2. T. Panne, A.Widenhorn, J. Boyde, D. Matha, V. Abel, M. Aigner, *Thermodynamic Process Analyses of SOFC/GT Hybrid Cycles*, 5th International Energy Conversion Engineering Conference and Exhibit, St. Luis, Missouri (2007).
3. S. Seidler, M. Henke, J. Kallo, W.G. Bessler, U. Maier and K.A. Friedrich, *Pressurized solid oxide fuel cells: Experimental studies and modeling*. Journal of Power Sources, 196, p. 7195-7202 (2011).
4. M. Lang, C. Westner, R.Geieregger, B. Bentlohner, R.Schwub, *SOFC Stacks for Mobile Applications*, European Solid Oxide Fuel Cell Forum, Lucerne, Switzerland (2010).
5. D.G. Goodwin, *An Open-Source, Extensible Software Suite for CVD Process Simulation*. in Proceedings of Chemical Vapor Deposition XVI and EUROCVI 14, Electrochemical Society (2003).

Nano Facilitated Charge Transfer for an 11 Electron Redox Couple for Anodic Charge Storage: VB₂

S. Licht^a, J. Lau^a, C. Hettige^a, H. Wu^{a,b}, B. Wang^{a,b},
J. Asercion^a, U. Cubeta^a, and J. Stuart^a

^a Department of Chemistry, George Washington University,
Washington, DC 20052, USA

^b Present address: College of Chemistry & Chemical Engineering,
Northeast Petroleum University, Daqing, China.

The storage of multiple electrons per molecule provides opportunities to greatly enhance electrochemical energy capacity. VB₂ releases, via electrochemical oxidation, 11 electrons per molecule at a favorable, electrochemical potential. Nanochemical improvements of VB₂ are probed to facilitate charge transfer and discharge voltage. Mechanochemical synthesized VB₂ exhibit higher voltage, sustain higher rate, and depth of discharge than macroscopic VB₂. Recently, we introduced a synthetic pathway to nanorod VB₂. In addition, here a straightforward synthetic route to nano-VB₂ particles, via planetary ball milling of elemental vanadium and boride in a 1:2 equivalent ratio is presented. Variation of the mechanochemical synthesis milling speed and milling time is used to optimize this nano-VB₂ for use as a high capacity anode material with enhanced charge transfer and increase voltage. Coupled with an air cathode, this 4060 mAh/g intrinsic capacity anode has an energy capacity greater than that of gasoline.

Introduction

In today's society, there is a strong demand for a high capacity battery for use in a variety of applications including consumer electronics, industry, medical, military applications, and recently in hybrid and electric vehicles. Zirconia stabilized vanadium diboride has recently been introduced as a potential high capacity anode, with a VB₂-air battery being shown to have at least one order of magnitude higher energy capacity than lithium-ion batteries (1).

VB₂ undergoes an extraordinary 11 electron per molecule oxidation, and provides an intrinsic 11 Faraday, per 72.6 g mol⁻¹ molecular weight, which is an anode capacity of 4060 mAh/g. With a density, $d = 5.10$ kg/L, it has a capacity of 20,700 Ah/L. This is respectively 10-fold, or 3.5-fold, higher than the volumetric capacity of lithium or zinc. Discharge of all 11e⁻ per molecule occurs at a singular, favorable anodic potential, which includes oxidation of the tetravalent transition metal ion, V(+4 → +5), and each of the two boron's 2xB(-2 → +3). This charge capacity combined with the thermodynamic potential, eq. 1, yields a theoretical energy capacity of 27,000 Wh/L, which exceeds that of gasoline (9,000 Wh/L).

Recently we calculated the theoretical discharge potential of the VB₂/air discharge based on the from available enthalpy and entropy of the reaction components (2,3):



The equation 1 products are generalized as B₂O₃ and V₂O₅, but will vary with the hydroxide concentration, hydration, and depth of discharge. In addition to the speciation of borate and the anhydride salt of boric acid previously described (H₃BO₃, H₂BO₃⁻, HBO₃²⁻, BO₃³⁻, B₂O₃⁻, K_xH_zBO₃^{3-x-z}, K_yB₄O₇^{2-y}) B₂O₃, a distribution of vanadate species will occur. Vanadate is the deprotonated form of a triprotic acid, vanadic acid (H₃VO₄ with pK_{1,2,3} = 3.8, 7.8 and 13.0). Equilibrium driven speciation of VO₄³⁻, HVO₄²⁻, H₂VO₄⁻, as well as the anhydride product, V₂O₅, and potassium cation species will occur.

It was recently shown that the charge transfer and voltage of efficiency of the VB₂/air batterieis is enhanced by through synthesis and cathode use of mechanochemically synthesized of VB₂ nanorods (4). Interestingly, as seen in the bottom right SEM 100 to 500 nanometer wide nanorods are formed when macroscopic VB₂ is mixed with fatty acid (10% lauric, “dodecanoic,” acid, CH₃(CH₂)₁₀COOH) and followed by 1 hour of planetary ball milling of the mix in a tungsten carbide vessel. Figure 1 presents SEM, with higher and lower magnification, of the 100 to 500 nanometer wide nanorods formed following 1 hour of planetary ball milling of conventional VB₂, mixed with fatty acid (10% lauric “dodecanoic” acid), in a tungsten carbide vessel.

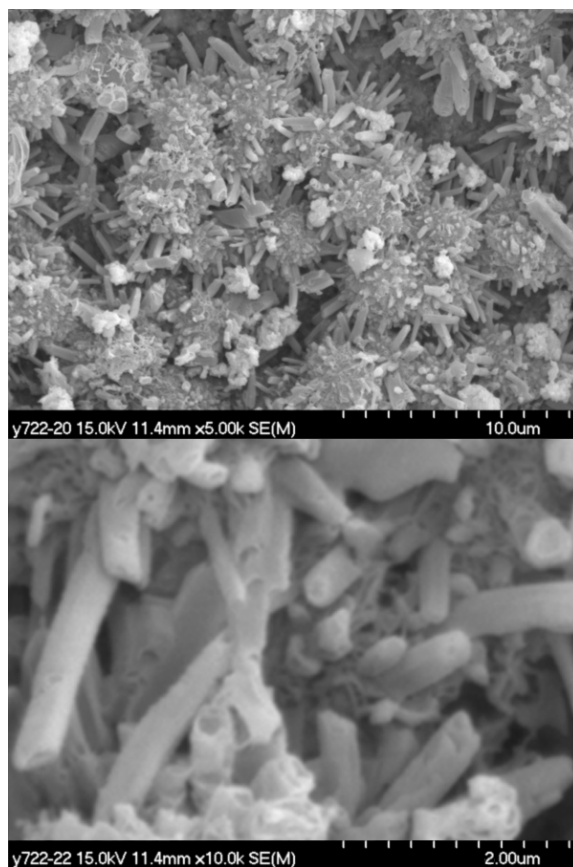


Figure 1. High resolution scanning microscopy of nano-rods formed from VB₂ formed when mixed with 10% lauric acid (8).

There have been a variety of synthetic methods presented for the preparation of vanadium diboride, including a self-propagating high temperature synthesis from the elemental forms of vanadium and boron, a nanocrystalline synthesis of VB_2 from VCl_4 , NaBH_4 and Mg, as well as a mechanochemical procedure that utilized VCl_3 , LiH and LiBH_4 (5, 6, 7). A nanometer dimensioned VB_2 , significantly increases the surface to volume ratio compared to micrometer dimensioned VB_2 . In principal, this will enhance charge transfer and sustain higher rates of anode discharge. However, we found that such syntheses led to VB_2 , which was passive to anodic charge transfer (8), and instead have explored alternative synthetic pathways which will be discussed in this report.

Experimental

Elemental vanadium (99.5%, -325 Mesh, Alfa Aesar) and boron (98%, -325 Mesh, Alfa Aesar) were used to prepare VB_2 . A set amount of 0.5g of vanadium was used for all synthesis, with the amount of boron varying depending on the molar ratio of the synthesis desired. Self-ignition of boron in air was prevented by confining the boron, or mixture, to an argon atmosphere, and the mixture placed into a 50 mL tungsten carbide ball milling jar (Retsch part number 01.462.0156) along with ten tungsten carbide bearings that had a diameter of 10mm. As previously discussed, the material is milled in a tungsten carbide vessel, as the hardness of VB_2 is greater than that of a conventional steel vessel.³ The jar containing the bearings and vanadium and boron mixture was sealed in an argon atmosphere and transferred to a Retsch PM 100 ball milling machine. Initial results were obtained by milling the material at 600 RPM for 4 hours continuously. One set of experiments focused on varying the milling time at a fixed rotation speed (600 RPM) and another focused on varying rotation speed at a fixed milling time (4 hours). Upon completion of the ball milling program, the temperature of the jar was allowed to return to room temperature and the powdered material was collected in an argon atmosphere.

The nano- VB_2 formed in ball milling was evaluated as an anode material in VB_2 air batteries as well as with x-ray powder diffraction analysis (XRD) and Transmission electron microscopy (TEM).

Panasonic 675 Zinc Air batteries (Panasonic Corporation, Japan) with 1 cm^2 anode surface area were used to fabricate the cells. The anode from the Panasonic battery was replaced with a mixture of the synthesized VB_2 and 2 micron graphite powder in a ratio such that 20% of the total weight of the mixture was graphite. A solution mixture of 5M each KOH and NaOH was used as the electrolyte and the loading of the anode material for each cell was 10 mAh. VB_2 cells were discharged across a resistor loading of 3000 Ω and the battery discharge data was recorded using a DAQ module (National Instruments NI-USB-6211) and LabVIEW software. For the purpose of comparison of results, we have fabricated equivalent cells using macroscopic VB_2 purchased from American Elements, U.S.A with a purity of 99.999%.

Results and Discussion

We have developed a straightforward, alternative nano-VB₂ particle synthesis, which, as with our previous nanorod VB₂ can lead to effective anode discharge. We synthesized vanadium diboride in a mechanochemical process from elemental vanadium and boron, and it will be shown that the resultant nano-VB₂ exhibits higher anodic discharge potential and capacity compared to the monoboride. We have utilized a mixture of 1:2 equivalent ratio of the elements V:B for the synthesis of VB₂, while ratios of 1:1 and 1:0.5 have been studied for the purpose of comparison with previous work (9). In the high temperature synthesis, it was previously shown that the combination of the elemental vanadium and boron in the ratio of 1:2 primarily formed VB₂ (9), which suggests that the mechanochemical reaction of the elements in a 1:2 ratio would primarily form VB₂.

VB₂ mechanochemically synthesized here from the elements, exhibits a higher discharge capacity than macroscopic commercial vanadium diboride as shown in Figure 2, and discharges to a majority of the intrinsic 4060 mAh/g capacity. The discharges of the synthesized material also exhibit a higher discharge voltage that is characteristic of nano-sized VB₂,² and is ~0.2 V (25%) higher than reported for vanadium monoboride mechanochemically synthesized from the elements (9). Note that the cells under 3000 ohm discharge load require ~a day to discharge. At 1000 ohm discharge load (not shown) the coulombic efficiency is only modestly impacted, but the average discharge potential decreases by ~0.05 V. As expected, an increase in the carbon fraction in the anode improves both efficiency and discharge potential. Under the same discharge conditions, pure boron provides no observable discharge, while pure vanadium discharges at a lower potential than the VB₂ product. Pure vanadium discharges at a level potential (starting at ~0.6V and terminating at 0.4 V) to an experimental capacity of 2.1 kAh/kg, approaching the 2.6 kAh/kg theoretical intrinsic capacity for the 5 electron oxidation (of V(0 → +5) of vanadium (element weight =50.94 g/mol).

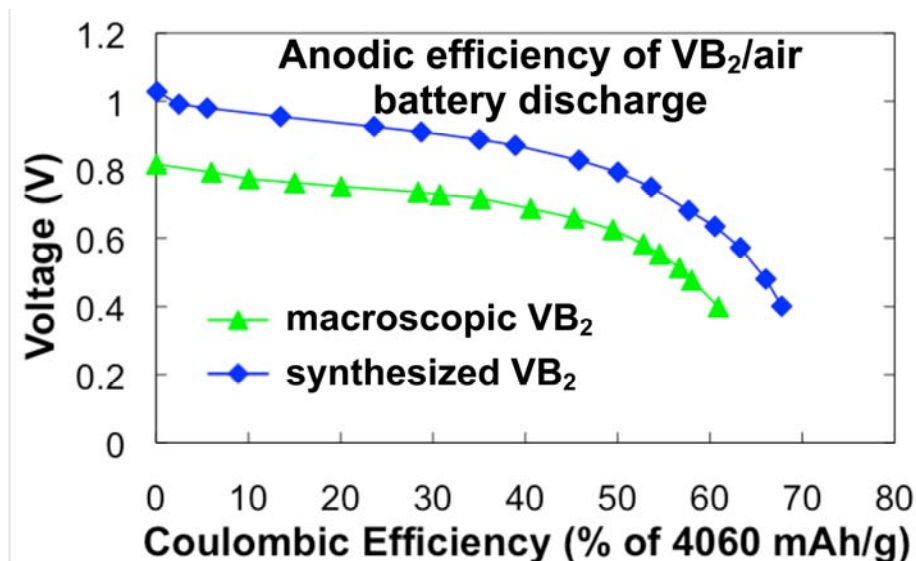


Figure 2. Discharge curves from VB₂-air cells. 10 mAh cells were discharged over 3000 Ω loads. Synthesized material was prepared by ball milling a mixture of V:B=1:2 ratio in a Retsch PM 100 ball mill in Argon atmosphere for 4 hours at 600 RPM.

Figure 3 presents TEM images of the milled mix of 1:2 elemental vanadium and boron measured with a JOEL JEM-1200 EX Transmission Electron Microscope. Prior to milling, the vanadium and boron particles consist of 325 mesh (up to 44 micron particles). After only 20 minutes of 600 RPM ball milling the vanadium boron mix consist of a heterogeneous distribution of submicron particles in the 100 to 400 nm range (Figure 3a), although agglomerates of larger particles are also evident. Extended milling, such as after a 4 hour mill under the same conditions (Figure 23), does not significantly alter the particle size or distribution, but as will be indicated from both XRD and electrochemical evidence, provides time required for a more complete reaction to VB_2 . The lack of crystalline character or shape evident in Figure 2B is also typical of this high capacity anode material, and subsequent XRD suggests that the majority phase present is VB_2 . FTIR analysis, as conducted in accord with our prior experiments (1,4,10),⁵ provides further evidence that the product of this mechanochemical stoichiometric reaction of elemental V and B is VB_2 and includes a prominent absorption at 1630 cm^{-1} . Further details of this analysis will be provided in an expanded study.

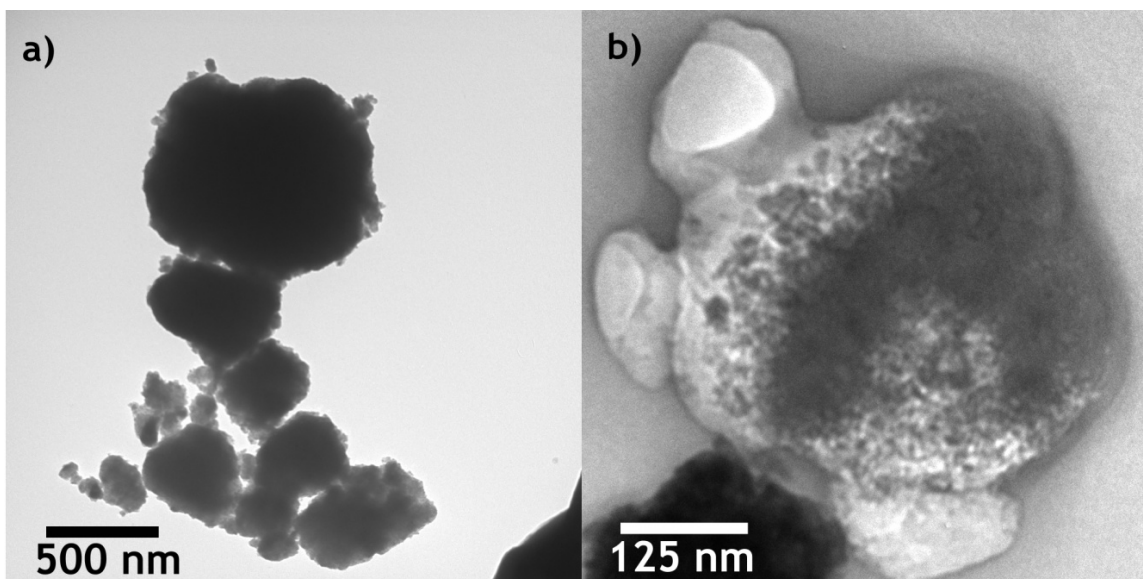


Figure 3. a) TEM image of Vanadium diboride prepared by milling elemental boron and vanadium in a 1:2 ratio for 20 minutes at 600RPM. b) A TEM image of a sample of Vanadium Diboride prepared by milling elemental boron and vanadium in a 1:2 ratio for 4 hours at 600RPM

When the V: B ratio was changed to 1:1, it was previously suggested that VB is formed, and when the V: B ratio was changed to 1:0.5, excess, unreacted vanadium was observed (9). With its lower discharge capacity the presence of VB (2.6 kAh/kg for a 6 electron oxidation), should cause a decrease in the anodic coulombic efficiency (coulombic efficiency is the measured percentage of the theoretical charge), and would remain low in presence of unreacted vanadium. This expected result is confirmed in the top portion of Figure 4 comparing discharge of cells containing a 1:0.5, 1:1 or 1:2 ratio of mixed, milled V: B. The new 1:2 (VB_2) material exhibits both higher potential and considerably higher discharge capacity than the 1:0.5 or 1:1 materials. The discharge potential of the 1:0.5 and 1:1 material is comparable to that previously observed, and while the absolute coulombic efficiencies of these two materials are lower than previously observed, their relative capacities are comparable (9). Note that the decreased anodic

efficiency of the 1:1 or lower ratio materials, compared to the 1:2 material, does not rule out the possibility that for those lower ratio materials the majority product may have been vanadium diboride plus excess vanadium, rather than vanadium monoboride. The expected discharge plateau which would occur, for unreacted vanadium of ~ 0.5 V was not observed in the top portion of Figure 3, but is observed at lower milling speed or at shorter milling time conditions in the middle and lower portions of the figure, and will be seen to correlate with the observation of unreacted vanadium via XRD in Figure 5.

In prior results of macroscopic VB_2 anodes, used in conjunction with a Fe(VI) , rather than air, cathode, we have shown that systematic variation of preparation parameters can substantially improve VB_2 anode characteristics.¹⁵ In order to optimize the mechanochemical process the synthesis mill time was varied between 10 minutes and 5 hours. The anodic discharge efficiency of these materials is compared in the middle portion of Figure 4, and improved for times longer than 20 minutes, with a peak efficiency was observed at ~ 4 hours of mill time. Over milling (5 hours) led to decreased anodic efficiency. Studies of mill velocity variation provide evidence that better coulombic efficiencies were also linked to higher mill speeds. As shown in the lower portion of Figure 3, discharge efficiencies continually increased with increasing RPM. At 200 RPM the discharge efficiencies observed were lower than 40% and the highest efficiencies were noticed for 600 RPM. Limitations of the Retsch PM 100 did not allow us to study mixtures synthesized above 600 RPM.

The ball milling process requires sufficient thermal energy and impact conditions to impart the energy to VB_2 from the elemental metals. This idea is supported by the observation that using low energy conditions such as low RPM, formation of VB_2 led to lower coulombic efficiencies in the cells. XRD data, shown in Figure 5, corroborate this fact as at increasing milling times the peak that is the predominant peak for VB_2 , which is located at $2\theta = 45.8^\circ$, increases in size. Neither elemental vanadium nor boron exhibit a significant XRD intensity at this value of 2θ . This increase in peak size follows the similar pattern of discharge efficiencies as a function of milling time. The observed XRD peaks of ball milled material are generally broad, which we attribute to an increase in reflections of smaller grains of varied shape and size dominated by short range order that occurs during the ball milling synthesis process. As seen in the figure, the XRD data from macroscopic and mechanochemical synthesized nano VB_2 match the peaks corresponding to the VB_2 standard library spectra, while incomplete reaction due to slow milling speed and short milling times leads to an XRD dominated by the elemental vanadium peak; the small, but evident, shoulder in the 600 RPM XRD at $2\theta = 42^\circ$ indicates that a potential vanadium impurity is present in the final mix.

The mechanochemical synthetic process of ball milling of elemental vanadium and boron is a straightforward method for synthesis of VB_2 and has been shown to produce a material that has a very high discharge efficiency. This efficiency is a result of the fact that this method does not involve other chemicals beyond the elemental metals of vanadium and boron so that VB_2 of high purity can be obtained via optimization of reaction conditions at high yields. The macroscopic VB_2 consists of 1 to 5 micron particles³. VB_2 synthesized by the alternative elemental route are tenfold smaller. With a particle as sphere simple assumption, a tenfold radius decrease, increases the relative surface area and decreases the overpotential, by decreasing the surface current density and decreasing the rate of surface passivation.

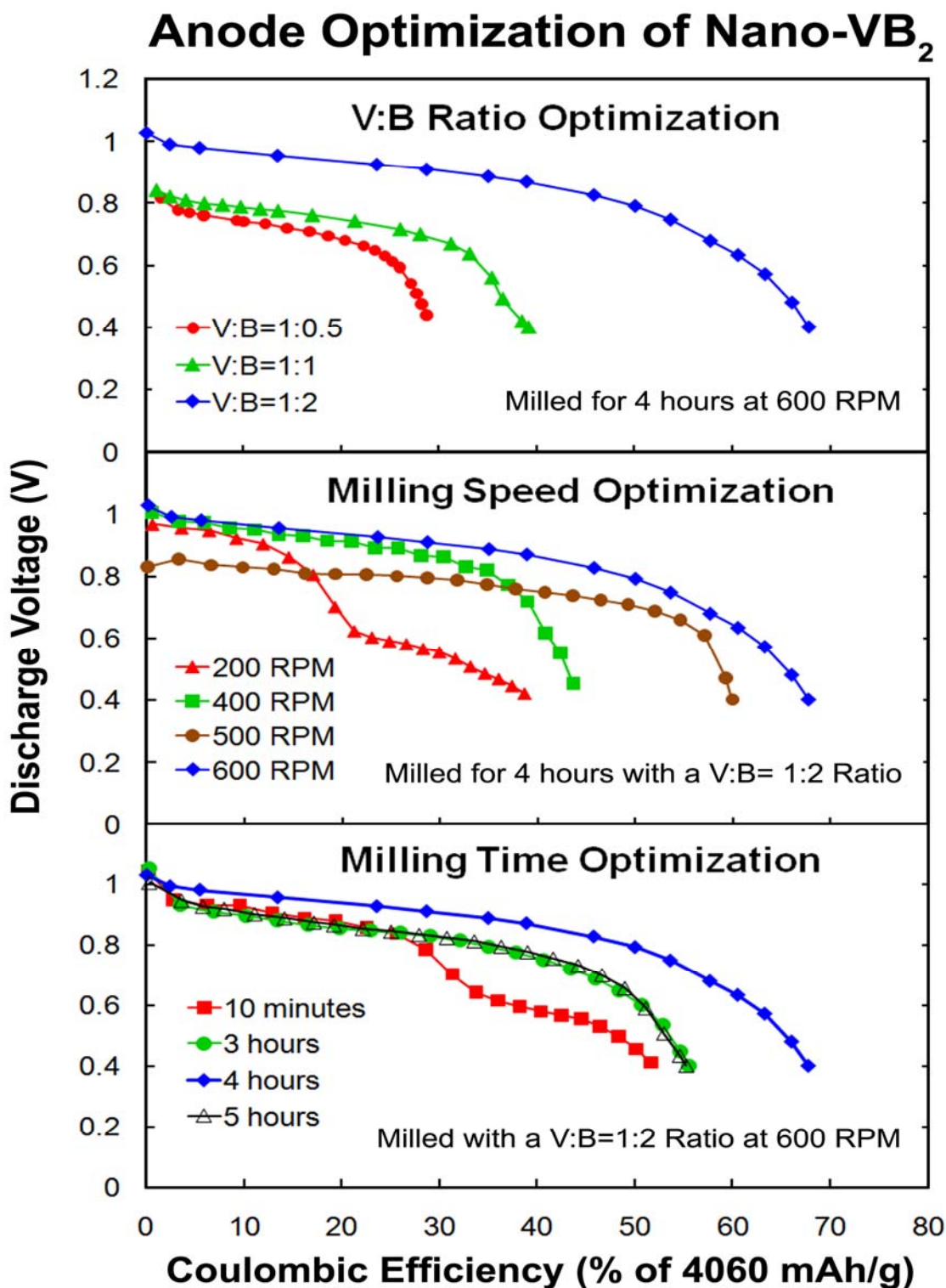


Figure 4. Discharge curves of cells made with Retsch PM 100 ball milled mixtures of elemental vanadium and boron in an equivalent ratio of V:B=x:y. Cells of 10 mAh capacity were discharged over 3000 Ω loads. Top: Variation of V:B ratio. V:B =1:2, V:B =1:1 or V:B = 1:0.5. Mixtures were milled at 600 RPM for 5 hours in an argon atmosphere with a mill. Middle: Variation of mill time with V:B=1:2 mixtures at fixed 600RPM. Bottom: Variation of mill velocity with V:B=1:2 mixtures for a fixed 4 hours milling time.

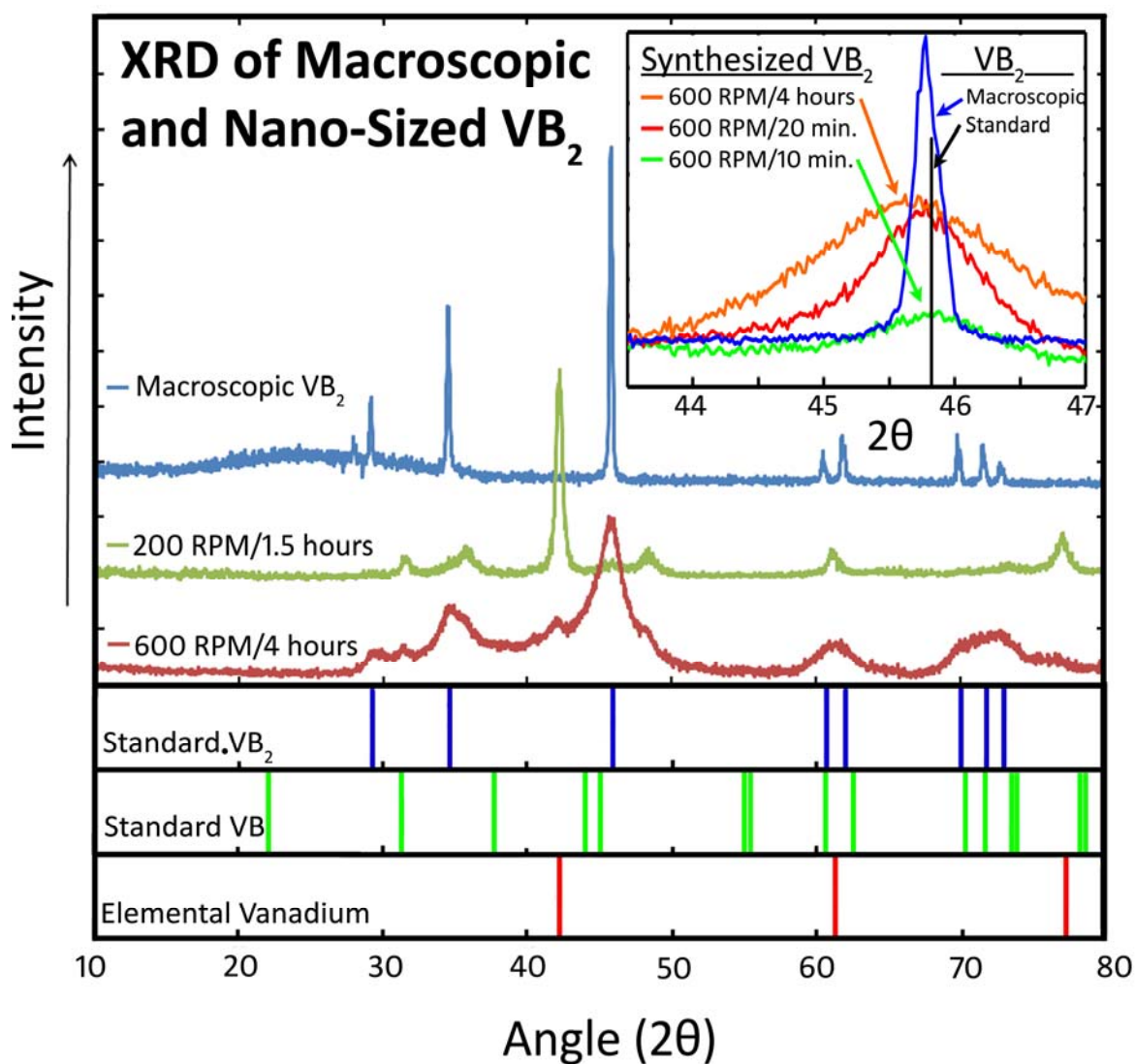


Figure 5. XRD data of various ball mill synthesized and macroscopic vanadium diboride. All synthesized materials started with a mixture of 1:2 V: B elemental ratio and are milled at 600 RPM. Commercial (macroscopic) vanadium diboride was purchased from American Elements. The vertical lines in the lower portion of the figure, as well as the line at 45.8° in the inset, corresponds to the Inorganic Crystal Structure Database standard for VB_2 .

Acknowledgments

This work was funded by in part NSF DMR award 1006568.

Acknowledgments

This work was funded by in part NSF DMR award 1006568, and we are grateful for ongoing collaborative input from Chris Rhodes at Lynntech, Inc., College Station Texas.

References

1. S. Licht, H.Wu, X. Yu, and Y. Wang, *Chem. Commun. (Cambridge)*, **2008**, 3527 (2008).
2. B. R. Emerich, Literature Survey on Synthesis, Properties and Applications of Selected Boride Compounds, *Air Force Systems Command*, **37**, 441-444 (1962).
3. NIST-Chemweb Thermochemical Data, data interactively available at:
<http://webbook.nist.gov/chemistry/form-ser.html>
4. S. Licht, X. Yu, and D. Qu, *Chem. Commun. (Cambridge)*, **2007**, 4341 (2007).
5. C.L. Yeh and H.J. Wang, *J. Alloy. Compd.*, **509**, 3527, (2011).
6. L. Shi, Y. Gu, L. Chen, Z. Yang, J. Ma, and Y. Qian, *Mater. Lett.*, **58**, 2890 (2004).
7. J.W. Kim, J.-H. Shim, J.-P. Ahn, Y. W. Cho, J.-H. Kim, and K. H. Oh, *Mater. Lett.*, **62**, 2461 (2008).
8. S. Licht, S. Ghosh, B. Wang, D. Jiang, J. Asercion, H. Bergmann, *Electrochemical and Solid State Letters*, **14**, A83-A85 (2011).
9. Y. Wang, X. Y. Guang, Y. L. Cao, X. P. Ai and H. X. Yang, *J. Alloy. Compd.*, **501**, L12 (2010).
10. S. Licht, X. Yu, Y. Wang and H. Wu, *J. Electrochem. Soc.*, **155**, A297 (2008).

**LiNi_{0.4}Mn_{1.6}O₄ / Electrolyte and Carbon Black / Electrolyte High Voltage Interfaces:
To Evidence the Chemical and Electronic Contributions of the Solvent on the
Cathode- Electrolyte Interface Formation**

Julien Demeaux^a, Magaly Caillon-Caravanier^b, Hervé Galiano^a, Daniel Lemordant^b,
Bénédicte Claude-Montigny^b

^a CEA/DAM Le Ripault, F-37260, Monts, France

^b Université François Rabelais, Laboratoire de Physico- Chimie des Matériaux et
Biomolécules (EA 4244), équipe CIME, Parc de Grandmont, F-37200, France

Solvent and lithium salt decomposition products on LiNi_xMn_yO₄-type electrodes are known to be ROM, ROCO₂M (M= Li, Ni, Mn), LiF, Li_xPF_yO_z, polycarbonates and polyethers. These compounds are chemically formed due to the high nucleophilic character of spinel oxide and LiPF₆ decomposition. The high potentials (> 4.7 V vs. Li/Li⁺) may cause EC and PC polymerization, while DMC forms oligomers. The use of carbon black-based electrodes highlights electronic and, surprisingly, chemical contributions to the cathode-electrolyte interface. A comparison between EC/DMC (1:1 in weight) 1 M LiPF₆ and PC/DMC (1:1 in weight) 1 M LiPF₆ electrolytes for Li/carbon black-PVdF cells demonstrated a superior ability of the EC/DMC solution to form a well-covering passivation film via faradaic reactions thanks to a higher stability toward oxidation. Electrochemical cycling in Li/LiNi_{0.4}Mn_{1.6}O₄ cells confirms this EC/DMC superiority when it comes to forming passivation films, in turn leading to reduced capacity losses and a higher Coulombic efficiency.

Introduction

The lithium-ion battery is a crucial power source for the electronic equipment required by today's high-tech society. This technology is believed to be the most competitive energy storage device for the electric vehicles (EVs), hybrid electric vehicles (HEVs), or photovoltaic solar cells that will be needed in the future. A Li-ion battery system comprises at least two electrodes, both based on intercalation compounds, and an electrolyte, which enables the ion transfer between the anode and the cathode. A recent development at CEA-LITEN concerning cathode materials has given rise to a spinel oxide with the following composition: LiNi_{0.4}Mn_{1.6}O₄. It presents an elevated voltage and a high rate ability (1). Moreover, LiNi_{0.4}Mn_{1.6}O₄ is an attractive positive electrode material either for '5 V' high-energy cells or for '3 V' secure and high-power units. However, the development of cells using high voltage intercalation compounds is still challenging due to the inherent instability of the organic solvents and of the lithium salt. In order to improve the stability of the electrolytic solution, it is necessary to identify the possible decomposition mechanisms of these components via both chemical and the electrochemical routes.

Based on the '4-V' Li-ion technology, the most suitable compositions for Li-ion battery solvents may be mixtures of cyclic alkylcarbonates, such as propylene carbonate (PC), and ethylene carbonate (EC), as well as linear alkylcarbonates, such as dimethyl carbonate (DMC) and ethyl methyl carbonate (EMC) (2). In this work, we focus on binary mixtures of EC/DMC (1:1 in weight) and PC/DMC (1:1 in weight) using LiPF_6 (1M) as the lithium salt. The solvent and the lithium salt decomposition products on $\text{LiNi}_x\text{Mn}_y\text{O}_4$ (usually $x=0.5$ and $y=1.5$) are well known to be ROM, ROCO_2M ($\text{M}=\text{Li}, \text{Mn}, \text{Ni}$), LiF , $\text{LiP}_x\text{F}_y\text{O}_z$, polycarbonates, and polyethers (3-8). These compounds are chemically formed due to the high nucleophilic character of $\text{LiNi}_x\text{Mn}_y\text{O}_4$ and the decomposition of LiPF_6 . The high potentials ($> 4.7 \text{ V vs. Li/Li}^+$) during the anodic polarization may cause EC and PC polymerization, while DMC forms oligomers. Electrochemical measurements are performed in lithium cells comprising either $\text{Li/LiNi}_{0.4}\text{Mn}_{1.6}\text{O}_4$ or Li/carbon black , and ex-situ surface analysis is carried out by FT-IR spectroscopy and SEM on stored and 'cycled' carbon black-PVdF and $\text{LiNi}_{0.4}\text{Mn}_{1.6}\text{O}_4$ electrodes. The present study highlights both the electronic and the chemical contributions to the formation of the cathode/electrolyte interface (CEI).

Experimental section

Electrochemical tests are realized in a 2032-type coin cell, using a $\text{LiNi}_{0.4}\text{Mn}_{1.6}\text{O}_4$ composite, provided by CEA-LITEN (Grenoble, France), as the positive electrode. Carbon black composite electrodes is prepared by mixing 50 wt.% or 63 wt.% Super P carbon black (Timcal) with 50 wt.% or 37 wt.% polyvinylidene difluoride (PVdF) binder. Electrodes (1.54 cm^2 discs) were dried for 24 h at 60°C , pressed (6.5 t.cm^{-2}), and then dried again for 48 h at 80°C under vacuum. Coin cells are assembled in an argon-filled dry box ($< 1 \text{ ppm O}_2/\text{H}_2\text{O}$) with polyethylene and polypropylene separators (Celgard[®] 2400 and Viledon Separator[®]). The liquid electrolyte consists of mixtures of ethylene carbonate and dimethyl carbonate (1:1 in weight), propylene carbonate and dimethyl carbonate (1:1 in weight), containing LiPF_6 (1M) as the salt (Merck). A $135\text{-}\mu\text{m}$ thick lithium foil (Aldrich) is used as the counter electrode. Electrochemical measurements are performed on a Versatile Multichannel Potentiostat (Bio-logic SA, Claix, France) piloted by an EC-Lab V10.12 interface. AC impedance spectroscopy is carried on the two-electrode coin cells in the frequency range 1 MHz-10 mHz with an amplitude of 10 mV. Ex-situ characterizations are done by scanning electronic microscopy with a Leica 440 microscope using a tungsten filament, and FT-IR in attenuated total reflectance (ATR) mode is conducted with a Bruker IFS 55 Equinox using a diamond plate. The coin cells are taken apart in a glove box, the electrode is pressed against the ATR crystal and the FTIR spectrum is obtained immediately after.

Results and Discussion

Breakdown voltage of electrolyte solutions

In order to test the oxidation potential of EC-, PC-, and DMC-based electrolytes, cells consisting of $\text{Li/electrolyte/materials}$ is investigated by fixing the potential from OCV to 8.0 V at a rate of 5.0 mV.s^{-1} for the carbon black-PVdF and aluminum positive electrode, and from OCV to 6.5 V at a rate of 0.1 mV.s^{-1} for the $\text{LiNi}_{0.4}\text{Mn}_{1.6}\text{O}_4$ composite electrode. However, the electrolyte oxidation voltage could not be precisely

determined since it depends on the charging rate of the cell, the electrode materials, as well as the methods used to establish it. It is thus decided that V_{ox} be determined by means of tangent (V_{ox}^{tg}) and fixed current density (V_{ox}^j , $j=0.025 \text{ mA.cm}^{-2}$) methods. The experimental results summarized in Table I are of differing accuracy, i.e., 0.1 V for the tangent method and 0.01 V for the current density technique.

TABLE I. Oxidation potential of electrolytic solutions (V_{ox} / V vs. Li/Li^+) with LiPF_6 (1M).

Working Electrode	Method	DMC	PC	EC	PC/DMC	EC/DMC
Al	V_{ox}^{tg}	6.5	-	6.4	6.8	6.8
	V_{ox}^j	7.64	-	7.61	6.94	6.97
Carbon black-PVdF (50-50 in weight)	V_{ox}^{tg}	5.0	4.4	4.8	4.8	5.0
	V_{ox}^j	4.94	5.16	5.37	4.86	4.93
Carbon black-PVdF (63-37 in weight)	V_{ox}^{tg}	Gas	5.0	-	4.8	5.0
	V_{ox}^j	Gas	5.47	5.54	4.86	4.90
$\text{LiNi}_{0.4}\text{Mn}_{1.6}\text{O}_4$ (Active material, CB, PVdF, Al)	V_{ox}^{tg}	5.5	4.7	4.5	4.7	5.0
	V_{ox}^j	5.43	5.07	4.44	4.73	4.96

Positive aluminum electrode. The resistance of the electrolyte solutions toward oxidation decreases according to the following sequence: $\text{DMC} > \text{EC} > \text{PC} > \text{EC/DMC} > \text{PC/DMC}$. These electrolyte compositions are ‘stable’ up to 7.0 V on an aluminum electrode but V_{ox} is leveled up by the reduced j values involving passivation processes with the LiPF_6 salt.

Carbon black-PVdF-based electrodes. The resistance of the electrolyte solutions toward oxidation decreases as: $\text{EC} > \text{PC} > \text{DMC} > \text{EC/DMC} > \text{PC/DMC}$. EC and PC were more stable toward oxidation than DMC. In the EC/DMC and PC/DMC mixtures, DMC was assumed to decompose first on the carbon black-PVdF electrode at high potentials ($> 4.7 \text{ V}$ vs. Li/Li^+).

$\text{LiNi}_{0.4}\text{Mn}_{1.6}\text{O}_4$ composite electrode. DMC ($\mu=0.76$) is more stable than EC and PC toward oxidation according to the sequence $\text{DMC} > \text{PC} > \text{EC} > \text{EC/DMC} > \text{PC/DMC}$. The most polar compounds, i.e., PC ($\mu=4.81 \text{ D}$) and EC ($\mu=4.61 \text{ D}$), could preferentially decompose on the $\text{LiNi}_{0.4}\text{Mn}_{1.6}\text{O}_4$ composite electrode. On the carbon black-PVdF and $\text{LiNi}_{0.4}\text{Mn}_{1.6}\text{O}_4$ electrodes, simple (EC, PC, DMC) and binary (PC/DMC, EC/DMC) solvent mixtures decompose within a potential range of 4.7-5.4 V. Many authors have advanced that $\text{Ni}^{2+}/\text{Ni}^{3+}$ and $\text{Ni}^{3+}/\text{Ni}^{4+}$ redox couples are able to catalyze electrolyte decomposition on $\text{LiNi}_x\text{Mn}_y\text{O}_4$ -type electrodes (9).

Conclusion. By using a pure electronic carbon black-PVdF conductor as well as a $\text{LiNi}_{0.4}\text{Mn}_{1.6}\text{O}_4$ composite electrode, it is demonstrated that redox couples do not catalyze oxidative decomposition. Oxidation potentials are not systematically lower on the carbon black-PVdF electrode as opposed to its $\text{LiNi}_{0.4}\text{Mn}_{1.6}\text{O}_4$ counterpart. The decomposition mechanisms thus strongly depend on the electrode material and could be essentially linked to a high value of the potential. EC/DMC was consistently more resistant than PC/DMC toward oxidation on the Al, carbon black-PVdF, and $\text{LiNi}_{0.4}\text{Mn}_{1.6}\text{O}_4$ electrodes. In the case of $\text{LiNi}_{0.4}\text{Mn}_{1.6}\text{O}_4$, this behavior is linked to the superior solvating effect of EC ($\epsilon=89.78$) as opposed to PC ($\epsilon=64.92$), leading to a greater amount of DMC at the electrode/electrolyte interface. Single solutions of EC, PC, and DMC are more stable than binary mixtures toward oxidation on all electrode materials tested here. However, among

DMC, EC and PC, it is difficult to state which solvent that is the most suitable to use since their oxidation behaviors are strongly dependent on the employed electrode material. Finally, it is difficult to determine how the solvent would react under high potential conditions and which one is preferentially decomposed on a high voltage composite electrode like $\text{LiNi}_{0.4}\text{Mn}_{1.6}\text{O}_4$.

The electrolyte must present good transport properties in a temperature range from at least -20°C to 60°C . Furthermore, for a '5 V' Li-ion device, this electrolyte has to provide suitable passivating properties on both cathodic and anodic materials. For these reasons, single electrolytes cannot be used and the studies describes below are focused on binary mixtures.

Impedance study

This section is an attempt to exhibit the dynamic behavior of the CEI by means of electrochemical impedance spectroscopy (EIS) (10,11). The use of both carbon black-PVdF and $\text{LiNi}_{0.4}\text{Mn}_{1.6}\text{O}_4$ composite electrodes in cells with Li as the reference in a two-electrode electrochemical device aims to display the electronic contribution to the dynamic behavior of the cathode-electrolyte interface. Figure 1 shows the equivalent circuit for the modeling of interfacial electrochemical reactions. In this model, R_1 is assumed to be the electrolyte resistance, C_{dl} the double layer capacitance and R_2 the interface resistance, while the material impedance consists of an active charge transfer resistance R_3 associated with a specific electrochemical element of diffusion W (also called the Warburg element). The material capacitance is a constant phase element denoted Q . Figure 2 shows an example of EIS spectra. In this study, the equivalent circuit of Figure 1 models Nyquist diagrams of Figure 2. Since the major modifications in the EIS spectra occur at low frequency, greater attention is paid to the R_3 and Q parameters. The resistance and capacitance values of carbon black-PVdF or $\text{LiNi}_{0.4}\text{Mn}_{1.6}\text{O}_4$ electrodes (noted R_3 and Q) are determined from the second loop (Figure 2).

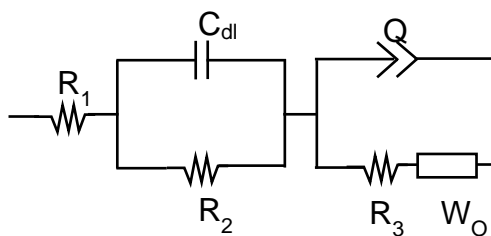


Figure 1. Equivalent circuit used to model EIS spectra.

Potentiostatic cycling. The cells are brought from OCV to 5.4 V and then cycled between 3.0 V and 5.4 V at a rate of 5.0 mV.s^{-1} for Li/carbon black-PVdF and at a rate of 0.1 mV.s^{-1} for Li/ $\text{LiNi}_{0.4}\text{Mn}_{1.6}\text{O}_4$. Cycling up to 5.4 V aims to strongly oxidize the EC/DMC 1-M LiPF_6 or PC/DMC 1M LiPF_6 solutions to induce major modifications in the electrode/electrolyte interface and/or into the porous material. This is then detected by impedance spectroscopy. Despite two-electrode measurements, resistance and capacitance evolutions could be attributed to the carbon black-PVdF/electrolyte (or $\text{LiNi}_{0.4}\text{Mn}_{1.6}\text{O}_4$ /electrolyte) interface and to the porous material for the potentials used.

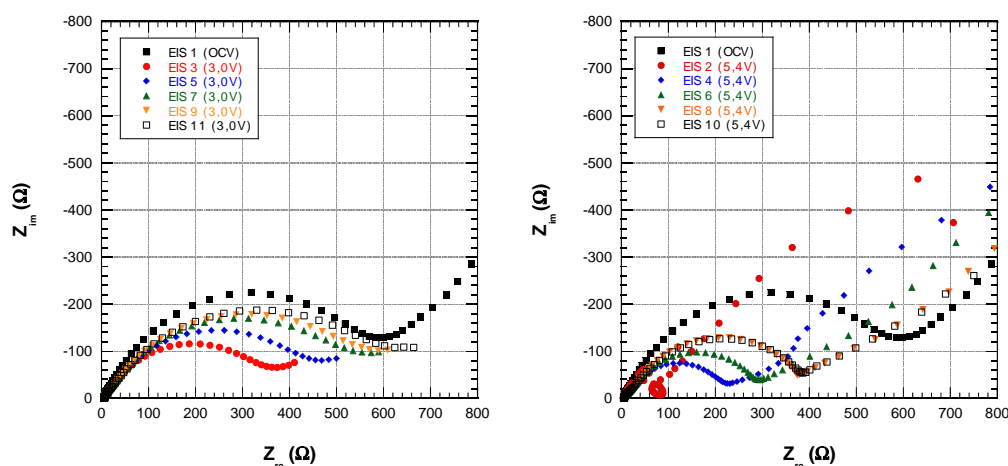


Figure 2. Example of EIS measurements realized at 3.0 V and 5.4 V on a Li/carbon black-PVdF (50-50) cell with EC/DMC + 1M LiPF₆

For the EC/DMC 1M LiPF₆ electrolyte (Figure 3), a low resistance and high capacitance, and a high resistance and low capacitance are observed at respectively 5.4 V and 3.0 V. However, no major evolution in capacitance values is noticed after three cycles (EIS #7). It is believed that the surface film that formed could change the interface permittivity versus potential. According to Figure 4, the use of PC/DMC 1 M LiPF₆ led to an identical behavior of resistance and capacitance.

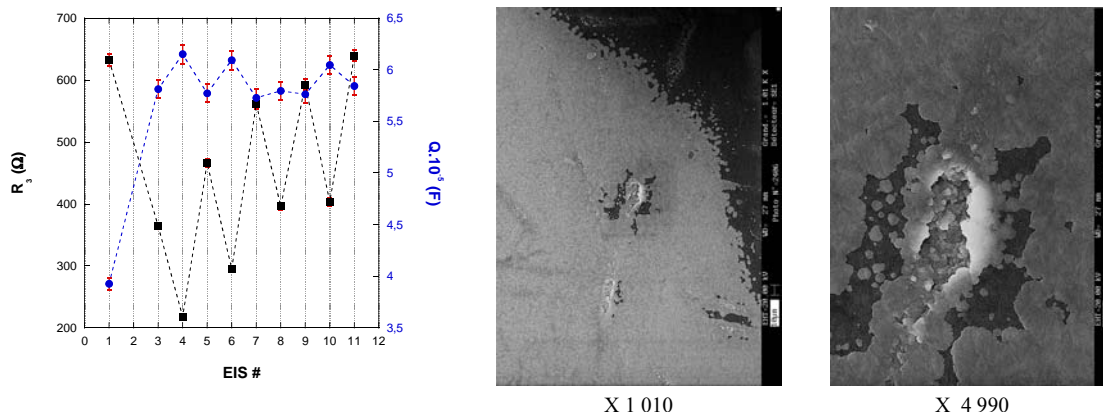


Figure 3. Resistance (■) and capacitance (●) values of the Li/carbon black-PVdF (50-50) cell at 3.0 V and 5.4 V, and SEM micrographs of the carbon-PVdF electrode after potentiostatic cycling in EC/DMC + 1M LiPF₆ electrolyte.

Thus, the formation of a surface film during ‘cycling’ is presumed to be uniform on the carbon black-PVdF positive electrode in contact with EC/DMC 1 M LiPF₆. This was confirmed by SEM observations (Figure 3). When PC/DMC is used as a binary solvent, EIS measurements indicate a non-uniform film formation on the carbon black-PVdF electrode, as also confirmed by SEM (Figure 4). Intense oxidation at 5.4 V generating gases and cracks into the electrode do not lead to the formation of a uniform film surface. Consequently, EC/DMC 1 M LiPF₆ seems to have a better ability to form a well covering surface film on a carbon black-PVdF electrode via electron exchange processes since it has a higher value of V_{ox} . An identical behavior is obtained when EC and PC are used as simple solvents with LiPF₆ (not shown here). A lower V_{ox} could also explain the behavior on the carbon black-PVdF electrode (Table I).

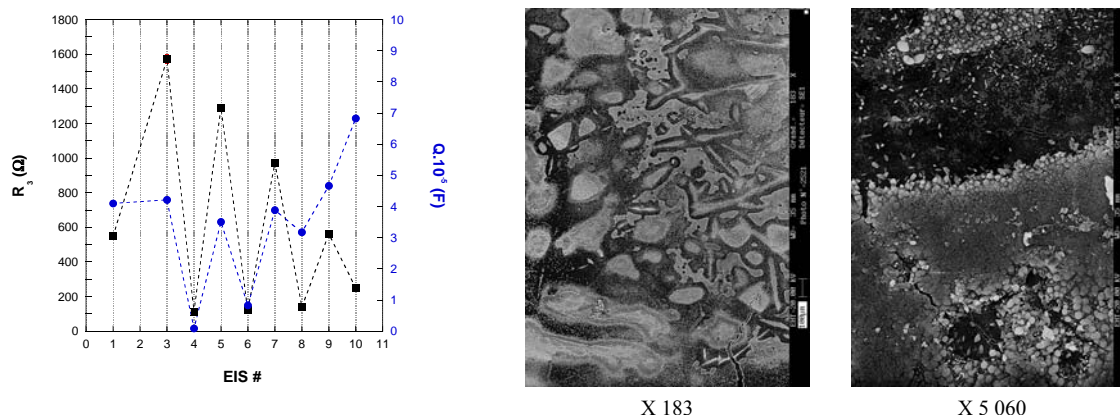


Figure 4. Resistance (■) and capacitance (●) values of the Li/carbon black-PVdF (50-50) cell at 3.0 V and 5.4 V, and SEM micrographs of the carbon black-PVdF electrode after potentiostatic cycling in PC/DMC + 1 M LiPF₆ electrolyte.

On LiNi_{0.4}Mn_{1.6}O₄ (Figure 5), both EC/DMC and PC/DMC electrolytes seem to be able to form surface films. The mechanisms of film formation differ from those on the carbon black-PVdF electrode because of a chemical contribution of the LiNi_{0.4}Mn_{1.6}O₄ nucleophilic material, which could be evidenced by FT-IR measurements and SEM observations. However, the reversible phenomenon observed on the Li/carbon black-PVdF and Li/LiNi_{0.4}Mn_{1.6}O₄ cells may be engendered by other mechanisms.

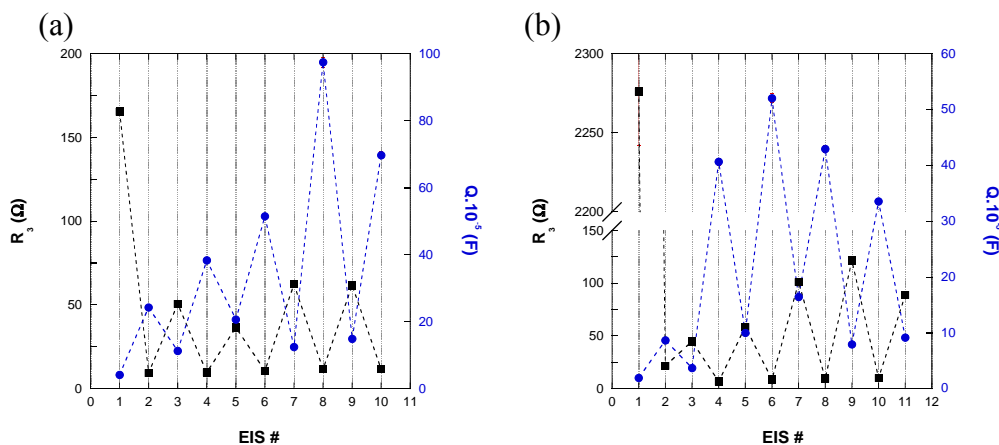


Figure 5. Resistance (■) and capacitance (●) values of the Li/LiNi_{0.4}Mn_{1.6}O₄ cells at 3.0 V and 5.4 V obtained with potentiostatic cycling: (a) EC/DMC + 1 M LiPF₆ and (b) PC/DMC + 1 M LiPF₆ electrolytes.

Storage. Li/LiNi_{0.4}Mn_{1.6}O₄ and Li/carbon black-PVdF cells are assembled and stored at 0% SOC at 40°C. Impedance measurements are carried out once a week during 4 weeks. The corresponding results are respectively reported on Figures 4 and 5. Open circuit potentials, permanently measured, are above 3.2 V for each cell. Because of the two-electrode configuration, the measured impedance is the sum of the Li/electrolyte and carbon black-PVdF/electrolyte (or LiNi_{0.4}Mn_{1.6}O₄/electrolyte) interfaces. Contrary to previous dynamic potentiostatic impedance measurements, storage conditions do not enable the determination of the effect of both interfaces on the impedance. However, PC/DMC appears more reactive than EC/DMC when stored in those cells (Figures 6a and 6b)

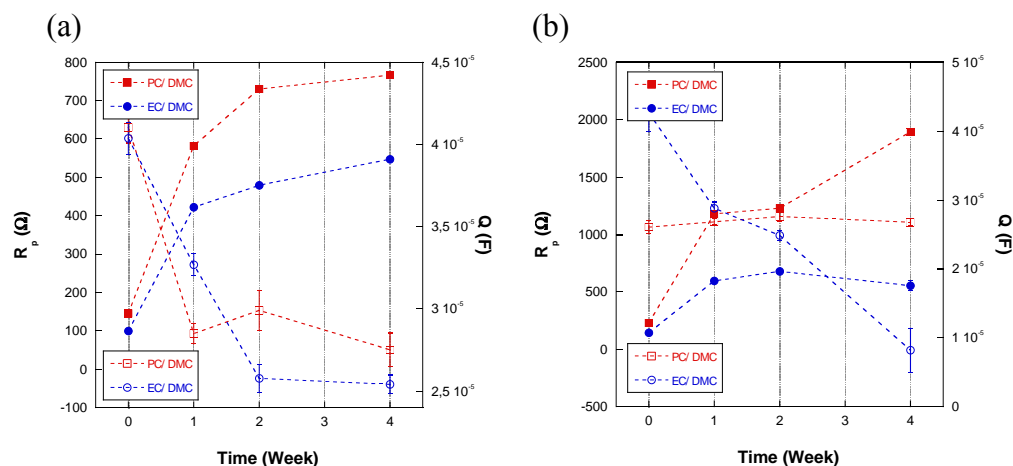


Figure 6. Values of resistance (filled symbol) and capacitance (opened symbol) as measured by EIS in (■ in red) PC/DMC 1 M LiPF_6 , and (● in blue) EC/DMC 1 M LiPF_6 electrolytes on (a) $\text{Li}/\text{LiNi}_{0.4}\text{Mn}_{1.6}\text{O}_4$ and (b) $\text{Li}/\text{carbon black}$ cells stored for 4 weeks at 40.0°C

SEM observations (Figures 4 and 7) confirm that the increase in resistance and the decrease in capacitance reveal a surface film formation on the $\text{LiNi}_{0.4}\text{Mn}_{1.6}\text{O}_4$ active material and surprisingly also on the carbon black-PVdF electrodes.

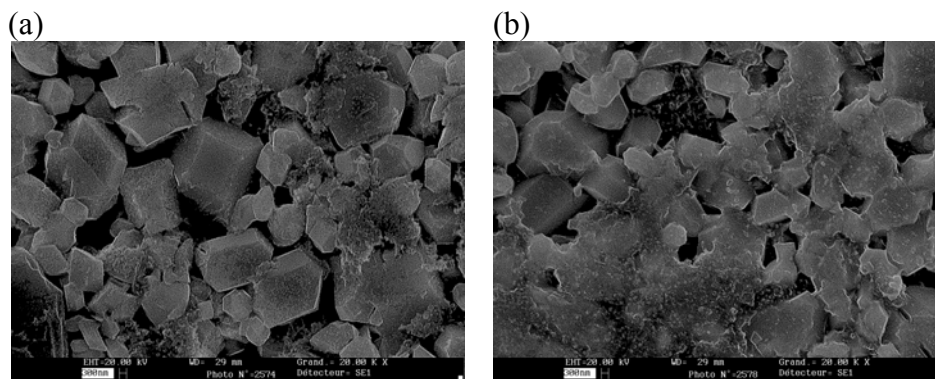


Figure 7. SEM micrographs (X 20 000) of $\text{LiNi}_{0.4}\text{Mn}_{1.6}\text{O}_4$ electrodes stored in $\text{Li}/\text{LiNi}_{0.4}\text{Mn}_{1.6}\text{O}_4$ cells for 4 weeks at 40.0°C using (a) PC/DMC 1 M LiPF_6 and (b) EC/DMC 1 M LiPF_6 electrolytes.

Impedance after cycling. Impedance measurements, reported on Figure 8, are carried out on $\text{Li}/\text{LiNi}_{0.4}\text{Mn}_{1.6}\text{O}_4$ cells after cycling. The cells are cycled 50 times at a rate of C/5 D/5 at 20.0°C (29.3 mA.g^{-1}) and impedance spectroscopy is realized at the end of the 50th cycle at the open circuit potential. It is found that the PC/DMC 1 M LiPF_6 electrolyte gives rise to a higher resistance of $\text{Li}/\text{LiNi}_{0.4}\text{Mn}_{1.6}\text{O}_4$ cells after cycling than its EC/DMC counterpart (Figure 8).

Conclusion. We succeeded in exhibiting the dynamic behavior of the CEI as recently shown in some papers. It is believed that the dynamic behavior of the CEI is mainly caused by electrolyte oxidation generating radicals and ions, which when combine with solvent molecules create polymers on the positive electrode material (3). This behavior is the same on the $\text{LiNi}_{0.4}\text{Mn}_{1.6}\text{O}_4$ intercalation material but is slowed down by

Li^+ insertion/extraction. It is also demonstrated that PC/DMC is more reactive than EC/DMC when anodically polarized or stored. Moreover, it forms the poorest quality film as determined by SEM observations (Figures 9a and 9b). Cycling experiments should demonstrate a high resistive passivating film. Nevertheless, the surface film on the CEI grows with time of storage, temperature, and the number of cycles according to the SPI (*Solid Permeable Interface*) model (4).

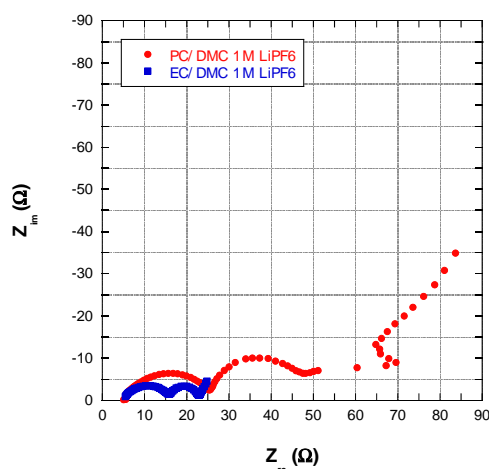


Figure 8. Impedance measurements on $\text{Li}/\text{LiNi}_{0.4}\text{Mn}_{1.6}\text{O}_4$ cells cycled 50 times between 3.5 V and 5.0 V (C/5 D/5 rate) in (■ in blue) EC/DMC 1 M LiPF_6 and (● in red) PC/DMC 1 M LiPF_6 .

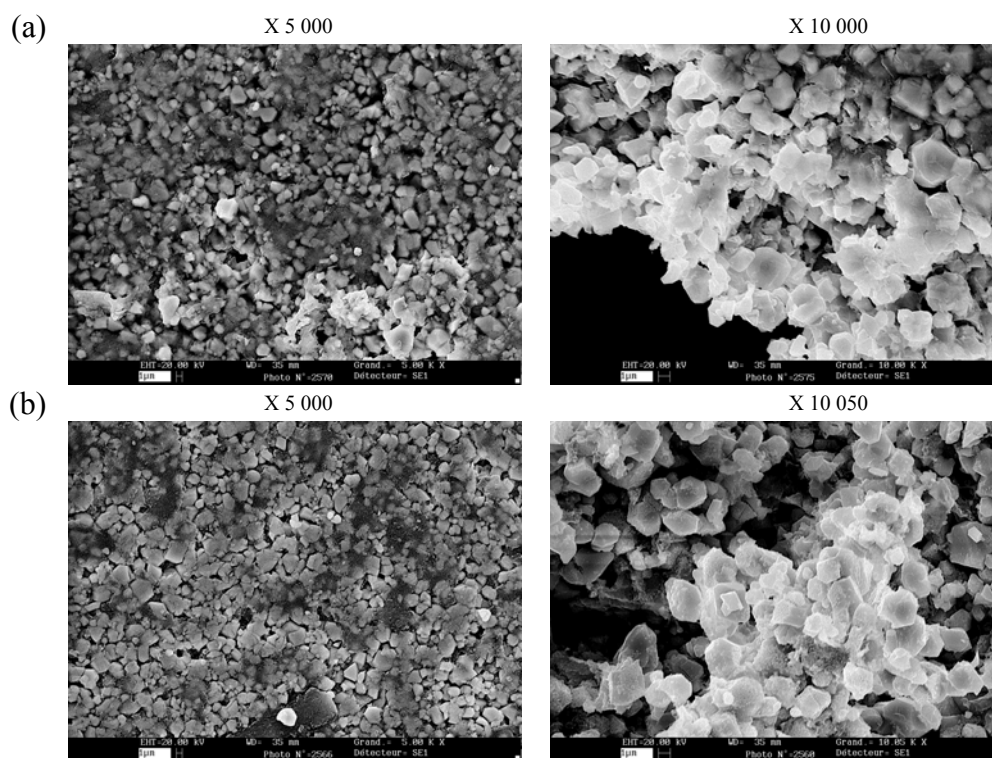


Figure 9. SEM micrographs of the $\text{LiNi}_{0.4}\text{Mn}_{1.6}\text{O}_4$ electrode cycled 50 times between 3.5 V and 5.0 V (C/5 D/5 rate) in (a) PC/DMC 1 M LiPF_6 and (b) EC/DMC 1 M LiPF_6 electrolytes

FT-IR spectroscopy

In order to check the film components, ATR measurements are performed. The ATR spectra of the neat EC, the neat PC, the neat DMC, and the neat LiPF_6 are shown in Figure 10. The main vibration bands are due to the carbonyl group between 1800 and 1700 cm^{-1} (carbonyl stretching), the C-H between 1600 and 1350 cm^{-1} , the C-O between 1300 and 1000 cm^{-1} , and LiPF_6 at 845 cm^{-1} .

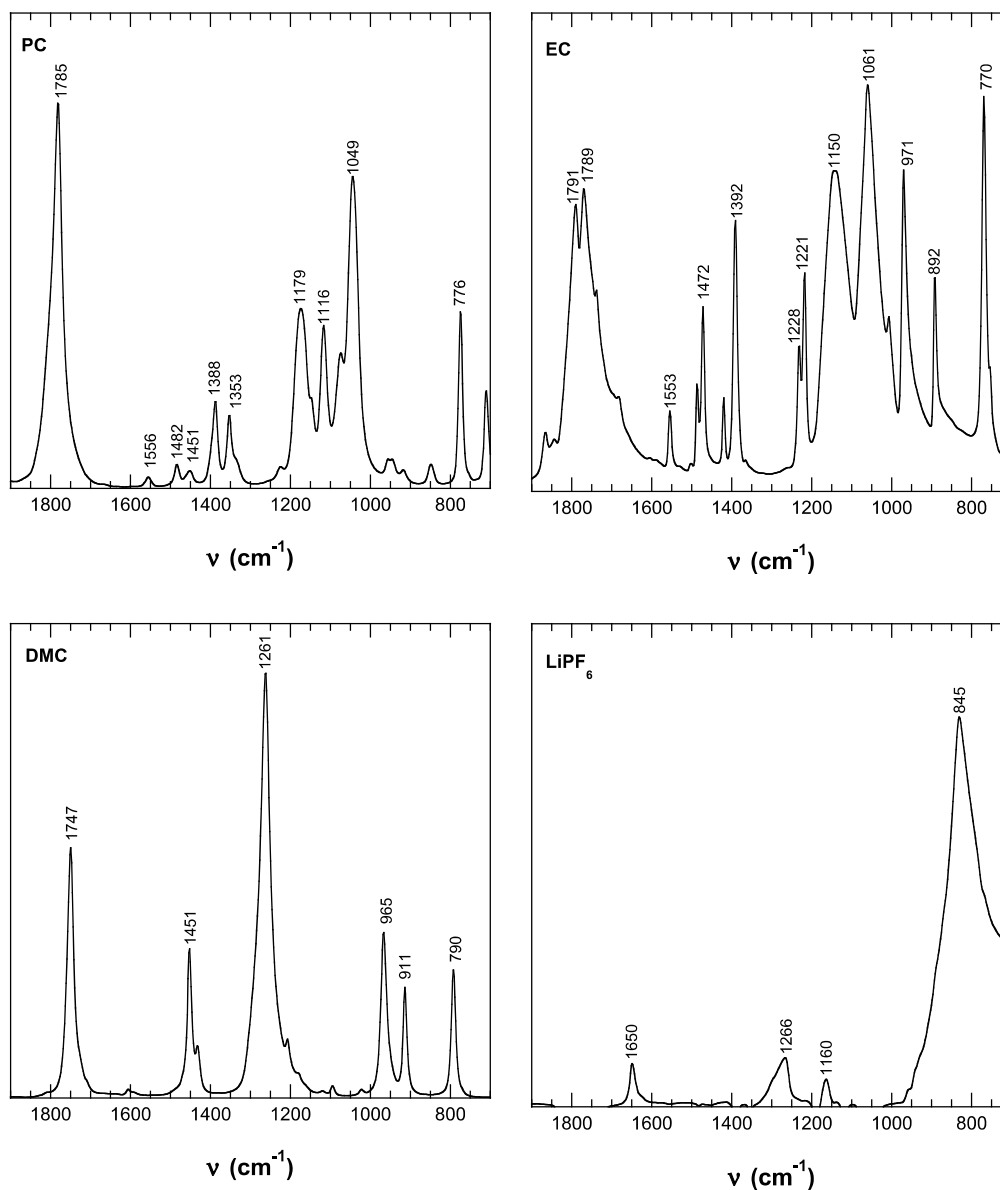


Figure 10. FT-IR spectra of neat PC, neat EC, neat DMC and neat LiPF_6 .

FT-IR studies of the surface films formed on the $\text{LiNi}_{0.4}\text{Mn}_{1.6}\text{O}_4$ and carbon black-PVdF positive electrode materials have focused primarily on $\text{Li}(\text{Ni}, \text{Co})\text{O}_2$, LiMn_2O_4 (5,8), and recently $\text{LiNi}_{0.5}\text{Mn}_{1.5}\text{O}_4$ (6,7). Despite investigations on $\text{LiNi}_x\text{Mn}_y\text{O}_4$ -class electrodes, the carbon black effect has never been explored in cycled or stored cells of Li/carbon black. An increasing resistance over storage as well as a drop in capacity of Li/ $\text{LiNi}_{0.4}\text{Mn}_{1.6}\text{O}_4$ cells is observed beyond 50 cycles involving surface film formation on $\text{LiNi}_{0.4}\text{Mn}_{1.6}\text{O}_4$. Here, the study is performed on $\text{LiNi}_{0.4}\text{Mn}_{1.6}\text{O}_4$ electrodes cycled and stored at 40.0°C for

4 weeks in Li/LiNi_{0.4}Mn_{1.6}O₄ cells (Figure 11). Moreover, carbon black-PVdF electrodes are analyzed after 4 weeks of storage (Figure 12) at 40.0°C in Li/carbon black-PVdF cells. Employed electrolytes include EC/DMC and PC/DMC with LiPF₆ as a lithium salt. The idea is to exhibit the effect of the solvent on the chemical and electrochemical contributions of the surface film formation. LiNi_{0.4}Mn_{1.6}O₄ and carbon black-PVdF electrodes are voluntarily not washed with DMC, as this might dissolve surface species not bound to the surface (polymeric films) whereas mineral species (Li_xPF_x and Li_xPF_yO_z) would remain present on the electrode surfaces (6). In the present study, the electrodes are dried in vacuum for 12 hours at 50°C.

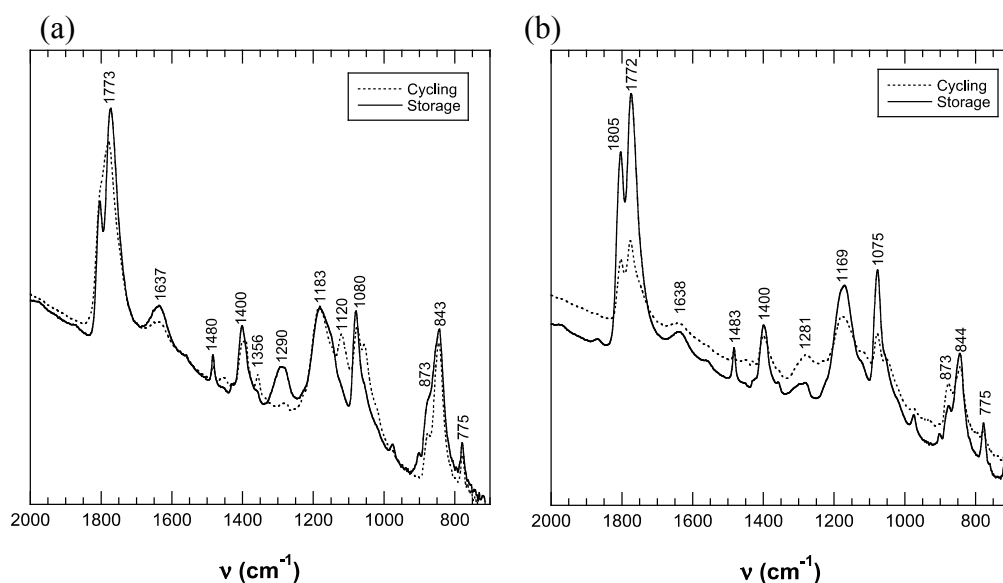


Figure 11. FT-IR spectra in (a) PC/DMC 1M LiPF₆ and (b) EC/DMC 1M LiPF₆ for LiNi_{0.4}Mn_{1.6}O₄ (...) after cycling (50 cycles, C/5 D/5) and (—) after storage of 4 weeks at 40.0°C.

The spectra exhibit the peak corresponding to the P-F vibration (845 cm⁻¹) in LiPF₆ but did not show any peak related to EC, PC, and DMC, which suggests a complete vaporizing of these compounds. The peaks revealed by the FT-IR measurement are consistent with the polymeric films observed by SEM (Figures 7, 9a and 9b). The peak at 1180-1160 cm⁻¹ (C-O-C stretching) is attributed to polycarbonates and/or polyethers (8). The peaks at 1290-1280 cm⁻¹ (C-H stretching), assigned to polyethers, and a shoulder at 1200 cm⁻¹, ascribed to metal alkoxide species (ROM), are observed for LiNi_{0.4}Mn_{1.6}O₄ in the presence of PC/DMC and EC/DMC solutions (Figure 11) (6). Eriksson (8) also suggests that the band at 1290-1280 cm⁻¹ (not present for neat PC or neat EC) can be attributed to Li_xPF_yO_z or P_xO_y. Furthermore, the peak at 1400 cm⁻¹ corresponding to the C-H vibration was broadened compared to the pure PC and the pure EC spectra, possibly as a result of the presence of polyether species (6,7). Bands at 1400 cm⁻¹ and 1290-1280 cm⁻¹ are also present on the stored carbon black-PVdF electrode, and new vibrational bands (carbonyl and CO₂ stretching) appear in the 1800-1630 cm⁻¹ region due to the formation polycarbonates and/or alkyl carbonates (ROCO₂M). Since the C-H, C-O and C=O peaks seem to emerge for cycled and stored electrodes, polyether and polycarbonate species are assumed to be chemically formed (Figure 11). It is believed that, when using the carbon black electrodes, polyethers and polycarbonates are formed by redox reactions since the cells always has an OCV over 3.2 V. The spectra of the

stored carbon black-PVdF and $\text{LiNi}_{0.4}\text{Mn}_{1.6}\text{O}_4$ electrodes are globally the same in the region described above, thus indicating that the carbon black contribution to the film surface surprisingly occurs during cycling and storage (Figure 12).

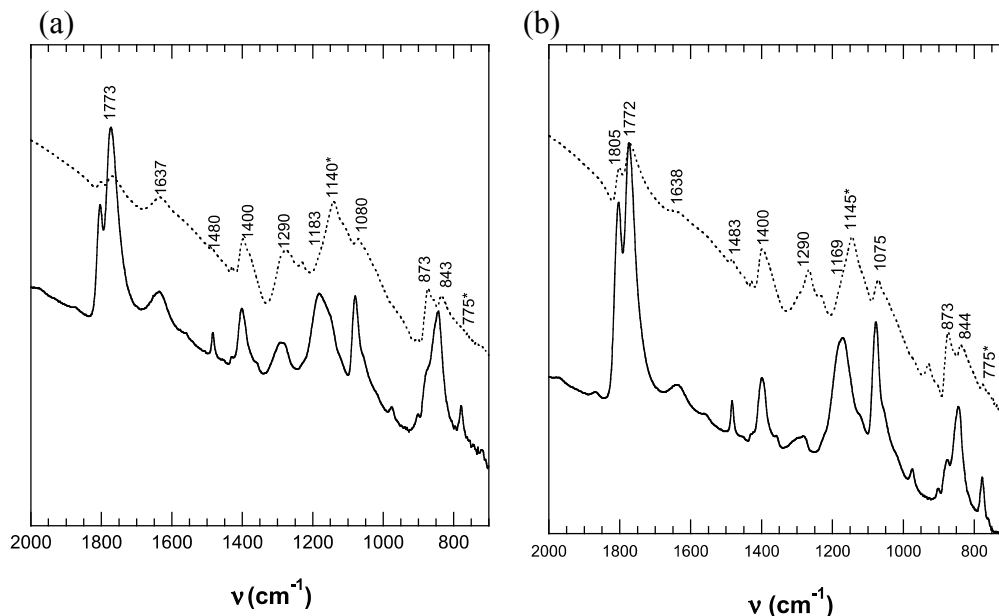


Figure 12. FT-IR spectra for (...) carbon black-PVdF and (—) $\text{LiNi}_{0.4}\text{Mn}_{1.6}\text{O}_4$ after storage for 4 weeks at 40.0°C in (a) PC/DMC 1 M LiPF_6 and (b) EC/DMC 1 M LiPF_6 .

Conclusion. The overall conclusion from the FT-IR studies is that polymeric films (polycarbonates and polyethers) are formed on the $\text{LiNi}_{0.4}\text{Mn}_{1.6}\text{O}_4$ and carbon black-PVdF electrodes not only during cycling but also during storage (Figure 13). Almost identical spectra are detected for both electrodes, which was quite unexpected.

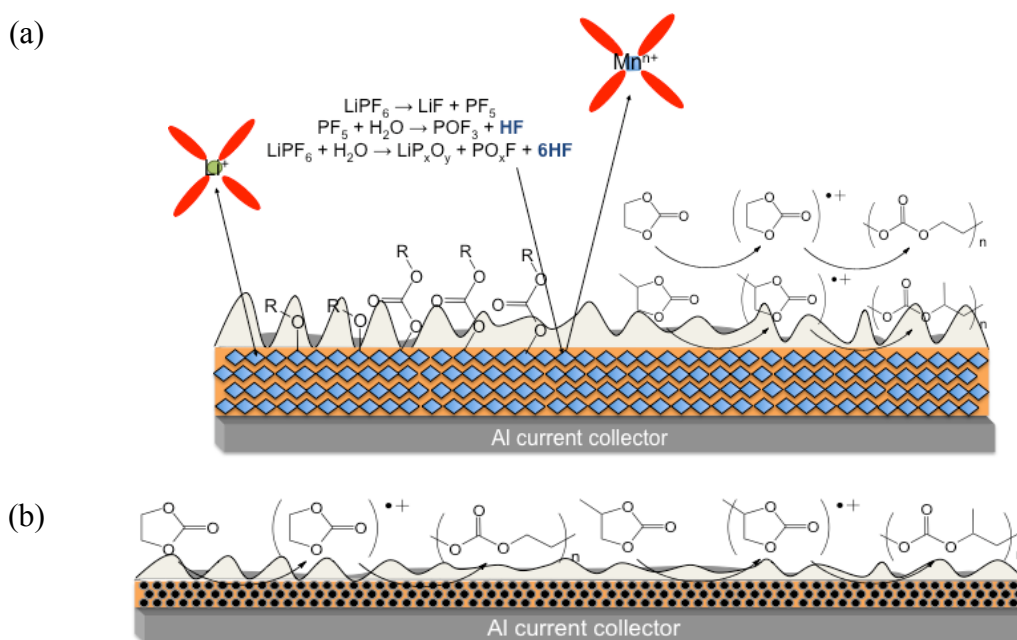


Figure 13. Surface layers formed on (a) $\text{LiNi}_{0.4}\text{Mn}_{1.6}\text{O}_4$ and (b) carbon black-PVdF electrodes.

It is thus believed that carbon black, which covers the active material in the $\text{LiNi}_{0.4}\text{Mn}_{1.6}\text{O}_4$ composite electrodes, catalyzes the solvent decomposition reactions, thereby giving rise to polymeric film formation during cycling and storage. The higher reactivity and lower oxidation potential of PC/DMC 1 M LiPF_6 as opposed to EC/DMC 1 M LiPF_6 in Li/carbon black-PVdF and Li/ $\text{LiNi}_{0.4}\text{Mn}_{1.6}\text{O}_4$ cells suggests the ability of PC/DMC solutions to form polymeric films during storage whereas EC/DMC solutions have a suitable ability to cover the active materials during electrochemical cycling.

Electrochemical cycling

The Li/ $\text{LiNi}_{0.4}\text{Mn}_{1.6}\text{O}_4$ cells are assembled and cycled 50 times at a rate of C/5 D/5 (29.3 mA.g^{-1}) and 100 times at C/2 D/2 (73.6 mA.g^{-1}) at 20.0°C . Normalized charge and discharge capacities of the cells are shown in Figure 14. At the rate of C/5, the maximum capacity is 141 mAh/g at the first charge for both electrolytes EC/DMC 1 M LiPF_6 and PC/DMC 1 M LiPF_6 . At the 50th cycle, the obtained charge capacity is 135 mAh/g and 132 mAh/g for EC/DMC 1 M LiPF_6 and PC/DMC 1 M LiPF_6 , resulting in 4.3% and 6.4% charge capacity losses for EC/DMC 1 M LiPF_6 and PC/DMC 1 M LiPF_6 , respectively.

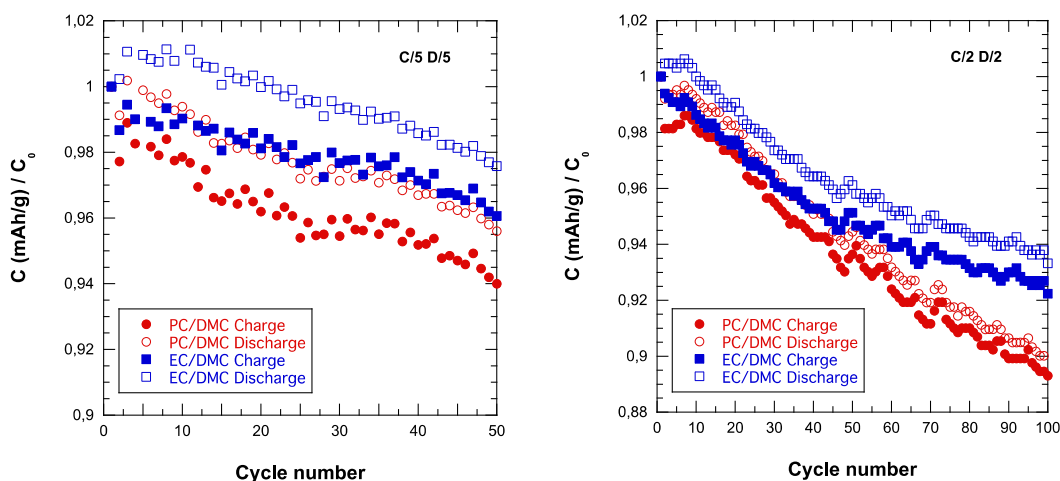


Figure 14. A comparison of charge (filled symbol) and discharge (opened symbol) capacity retention of Li/ $\text{LiNi}_{0.4}\text{Mn}_{1.6}\text{O}_4$ cells at 20.0°C . The electrolyte is PC/DMC + 1 M LiPF_6 (in red) and EC/DMC + 1 M LiPF_6 (in blue).

At the rate of D/5, the maximum discharge capacity is 139 mAh/g obtained at the 8th cycle for EC/DMC 1 M LiPF_6 and 137 mAh/g obtained at the 3rd cycle for PC/DMC 1 M LiPF_6 . At the 50th cycle, the obtained charge capacity is 133 mAh/g and 131 mAh/g for EC/DMC 1 M LiPF_6 and PC/DMC 1 M LiPF_6 , respectively. The discharge capacity loss is 4.4% for both electrolytes. When it comes to C/5 D/5 measurements, the average Coulombic efficiency is 98.88% for EC/DMC 1 M LiPF_6 and 98.84% for PC/DMC 1 M LiPF_6 . At the rate of C/2, the maximum charge capacities are 134 mAh/g and 131 mAh/g at the first charge for the EC/DMC 1 M LiPF_6 and PC/DMC 1 M LiPF_6 electrolytes, respectively. At the end of the 100th cycle, the charge capacities are 123 mAh/g and 117 mAh/g , resulting in 8.3% and 10.7% of charge capacity losses for EC/DMC 1 M LiPF_6 and PC/DMC 1 M LiPF_6 . At the rate of D/2, the

maximum discharge capacities are 132 mAh/g and 128 mAh/g at the first charge for the EC/DMC 1 M LiPF₆ and PC/DMC 1 M LiPF₆ electrolytes, respectively. At the end of the 100th cycle, the respective charge capacities are 122 mAh/g and 116 mAh/g, resulting in 7.6% and 9.4% of discharge capacity losses for EC/DMC 1 M LiPF₆ and PC/DMC 1 M LiPF₆. Concerning the C/2 D/2 measurements, the average Columbic efficiency is 99.22% for EC/DMC 1 M LiPF₆ and 98.65% for PC/DMC 1 M LiPF₆.

Thus, charge and discharge capacity losses are independent of the cycling time (500 hours at C/5 D/5 and 400 hours at C/2 D/2). This may indicate that the solvent oxidation is not the major phenomenon responsible for the capacity losses. Consequently, the great capacity losses and poor Columbic efficiencies are also caused by electrode dissolution in the electrolyte solutions. As the PC/DMC solution forms the poorest quality passivation films on the LiNi_{0.4}Mn_{1.6}O₄ electrode due to lower V_{ox} , PC/DMC do not cover the electrode material enough to stop its dissolution. EC/DMC, on the other hand, has a better ability to form a well-covering surface film that prevents further material dissolution and thus results in a lower capacity loss.

Conclusions

The use of a pure electronic conductor carbon black-PVdF and the LiNi_{0.4}Mn_{1.6}O₄ composite electrode demonstrates that nickel and manganese redox couples do not catalyze the solvent oxidative decomposition. The decomposition mechanisms thus depend significantly on the electrode material and are believed to be essentially linked to a high value of the potential. The EC/DMC 1 M LiPF₆ electrolyte exhibits a higher resistance toward oxidation as opposed to PC/DMC 1 M LiPF₆, regardless of the positive electrode material tested in this study (i.e., Al, carbon black-PVdF and LiNi_{0.4}Mn_{1.6}O₄).

The dynamic behavior of the CEI grows with the time of storage, the temperature and the number of cycles, according to the SPI (*Solid Permeable interface*) model (4). The electronic contribution to the dynamics is also shown by the use of the carbon black electrode. Consequently, the dynamic behavior of the CEI is mainly caused by electrolyte oxidation generating radicals and ions, which combine with solvent molecules to form polymers on LiNi_{0.4}Mn_{1.6}O₄. It is also demonstrated that PC/DMC 1 M LiPF₆ forms the poorest quality film passivation thereby causing an insufficient cover on LiNi_{0.4}Mn_{1.6}O₄ as opposed to EC/DMC 1 M LiPF₆.

FT-IR studies unexpectedly point at a polymeric surface film formation on LiNi_{0.4}Mn_{1.6}O₄ and carbon black-PVdF not only after cycling but also after storage for 4 weeks at 40°C. Carbon black, which covers the active material of the LiNi_{0.4}Mn_{1.6}O₄ composite electrode, could catalyze the solvent decomposition reactions thus leading to polymeric film formation during cycling and storage.

Capacity losses and poor Columbic efficiencies are also caused by the electrode dissolution in the electrolyte solutions. In the case of the PC/DMC solution, the film do not cover the electrode material sufficiently to stop its dissolution whereas EC/DMC presented a better ability to form a covering surface film via faradaic reactions, thereby preventing further material dissolution and leading to lower capacity losses.

Acknowledgments

CEA-LITEN is gratefully acknowledged for financial support and for providing the electrode materials. The authors thank Didier Demattei, Evelyne Estrade, Frédéric Montigny and Matthieu Le Digabel for their technical assistance.

References

1. S. Patoux, L. Daniel, C. Bourbon, H. Lignier, C. Pagano, F. Le Cras, S. Jouanneau, S. Martinet, *Journal of Power Sources*, **189**, 344 (2009).
2. K. Xu, *Chem. Rev.*, **104**, 4303 (2004).
3. M. Moshkovich, M. Cojocaru, H. E. Gottlieb, D. Aurbach, *Journal of Electroanalytical Chemistry*, **497**, 84 (2001).
4. K. Edström, T. Gustafsson, J. O. Thomas, *Electrochimica Acta*, **50**, 397 (2004).
5. D. Aurbach, M. D. Levi, E. Levi, H. Teller, B. Markovsky, G. Salitra, U. Heider, L. Heider, *Journal of The Electrochemical Society*, **145**, 3024 (1998).
6. H. Duncan, Y. Abu-Lebdeh, I. J. Davidson, *Journal of The Electrochemical Society*, 157 (4) A528 (2010).
7. H. Duncan, D. Duguay, Y. Abu-Lebdeh, I. J. Davidson, *Journal of The Electrochemical Society*, **158** (5) A537 (2011).
8. T. Eriksson, *Ph.D. Thesis*, Uppsala University (2001).
9. M. Matsui, K. Dokko, K. Kanamura, *Journal of The Electrochemical Society*, **157** (2), A121 (2010).
10. F. Orsini, M. Dollé, J.-M. Tarascon, *Solid State Ionics*, **135**, 213 (2000).
11. M. Dollé, F. Orsini, A. S. Gozdz, J.-M. Tarascon, *Journal of The Electrochemical Society*, **148** (8) A851 (2001).

Fuel Cell Performances of Bio-Membranes Made of Chitosan-Polyelectrolyte Thin Films and Nanowires into Anodic Alumina Membranes

P. Bocchetta, F. Conciauro, M. Santamaria, F. Di Quarto

^a Electrochemical Material Science Laboratory, Facoltà di Ingegneria, Università di Palermo, Viale delle Scienze, Ed.6, 90128 Palermo, Italy

Chitosan (CS) / Phosphotungstic acid (PTA) polyelectrolytes in the shape of thin films and nanowires supported by Anodic Alumina Membranes (AAM) have been fabricated through solution cast and filtration techniques, respectively. Their ability to function in a H₂/O₂ fuel cell under mild conditions (room temperature, low humidity and low Pt loading) is proved for the first time. The fabricated membrane electrode assemblies produce power peaks of ~20 mW cm⁻² for both films and nanowires. The CS/PTA films (20-40 μm thick) are able to produce a quite constant power density of ~10 mW cm⁻² recorded for at least 7 h. The gradual decrease of the power output with time observed for CS/PTA nanowires in AAM supports (50 μm thick) is accompanied by a durability of about 6 h, which represents an improvement with respect to previous results obtained in AAM-based fuel cell.

Introduction

Chitosan (CS) is a cationic linear polysaccharide usually obtained by alkaline deacetylation of crustacean chitin from crab and shrimp shell wastes and represents the second most abundant natural polymer [1]. Chitosan is composed by both free hydroxyl groups and amine groups that after modification to prepare chitosan derivatives gives some sophisticated functional polymers with properties quite different from those of synthetic polymers [2]. Due to its excellent properties, such as biocompatibility, biodegradability, non-toxicity, adsorption properties and positively charged character, chitosan has found applications in medicine, pharmacy, as food additives, antimicrobial agent, in paper and textile industry and other industrial areas [3-4].

As a cationic polyelectrolyte, CS is extremely attractive to prepare polyelectrolyte complexes (PECs) through electrostatic interactions with various natural and synthetic polyanions [5]. In addition, it can be easily converted into thin films [6], and this feature further increases its usefulness and applicability as electrolyte in electrochemical devices [7]. It must be considered that the acids and salts of heteropolyanions constitute a large category of compounds, thus a variety of polyelectrolyte complexes would be formed between heteropolyanions and chitosan. The literature dedicated to chitosan-based polyelectrolytes (PECs) as candidates for proton-conducting membranes to be used in fuel cell is quite recent. To the best of our knowledge, the first paper was published in 2004 [8] and deals with the preparation of PECs by complexing chitosan with poly(acrylic acid) anionic polyelectrolyte without any fuel cell test. Similar papers appeared in the succeeding years report about different anionic polyelectrolytes used to complex chitosan, such as Chitosan–sodium alginate polyion complexes [9], chitosan and methanediphosphonic acid [10] and Nafion® ionomer, chitosan and polyvinyl alcohol

[11]. Very recently, chitosan-based polyelectrolytes have been tested in fuel cells: chitin phosphate membranes have been evaluated in high temperature (120-160 °C) H₂/O₂ fuel cell [12], chitosan–H₃PO₄ electrolytes containing Al₂SiO₅, NH₄NO₃ and Al₂SiO₅, were studied in H₂/air fuel cell [13] and, afterward, cross-linked quaternized-chitosan membranes were investigated in alkaline fuel cell [14].

Phosphotungstic acid (PTA) is a strong Bronsted acid and represents a good inorganic proton conductors at room temperature, but its water solubility causes detrimental consequences on fuel cell durability. Therefore, the chemical stabilization of PTA is necessary in order to fabricate fuel cell with stable power output with time. A way to solve the problem of HPA dissolution during fuel cell operation could be the chemical immobilization of PTA (heteropolyanion) through electrostatic interactions with chitosan (polycation) to form insoluble polyelectrolyte complexes. Recently, novel proton-conducting membranes of PECs of chitosan and phosphotungstic acid (PTA) in the form of thin films have been prepared and measured for their protonic conductivity and methanol permeation [15, 16]. The homogeneous PECs membranes showed good thermal stability up to 210 °C, and exhibited a high proton conductivity ($2.4 \times 10^{-2} \text{ S cm}^{-1}$ at 80 °C) and a low methanol permeability ($3.3 \times 10^{-7} \text{ cm}^2 \text{ s}^{-1}$). Due to the methanol permeation values, authors suggest potential use of such membranes in direct methanol fuel cell, but at present no fuel cell test has been yet reported.

In the last years our research group has explored a novel fuel cell technology based on the use of Anodic Alumina Membrane (AAM) as support of protonic conductors that cannot be used alone due to scarce mechanical properties. The possible functioning of thin film AAM-based fuel cell has been proved in previous works [17, 18] by using CsHSO₄, PTA and Nafion as pore-fillers working at intermediate and low temperatures (25-160 °C). Although the use of CsH₂PO₄ and Cs_{0.86}(NH₄)_{1.14} SO₄ Te(OH)₆ [19, 20] filler of AAM allowed the improvement of AAM-based thin film fuel cell in terms performance and stability at room temperature, the fuel cell durability is still scarce to guarantee long term practical applications. The possible causes of such limitations can be attributed to membrane dissolution in the water produced at cathodic side. Thus, the possibility to use insoluble proton conductors as fillers of AAM appears really appealing.

In this work, we have investigated the possibility to prepare insoluble complex of chitosan (CS) and phosphotungstic acid as proton conductor electrolytes for H₂/O₂ fuel cell. Two different electrolyte configurations were prepared: thin films and anodic alumina membrane supported nanowires. Their morphological features were characterized by scanning electron microscopy, while their performance and stability as proton conductor were tested in a low temperature (25°C) H₂/O₂ fuel cell.

Experimental

Chitosan and hydrate Phosphotungstic acid (H₃PW₁₂O₄₀ x H₂O) was purchased from Sigma–Aldrich. The chitosan membranes were prepared by dissolving 1 g of chitosan flakes in 100 ml of 1 wt.% acetic acid solution. The solution was filtered and after that a volume of 10 ml was cast on a glass plate and left to dry via evaporation for 24 h. The membrane was then transferred into an oven and dried at 60 °C for 6 h. The dried membrane was neutralized in 1 M NaOH and thoroughly washed. The membrane was later immersed in saturated PTA solution for at least 24 h in order to form the insoluble complex of CTS/PTA.

Whatman 0.2 - 47 mm Anodisc (pore diameter 200 nm, thickness 50 µm, porosity 43 %) has been filled with chitosan through a filtration equipment using the same solution used

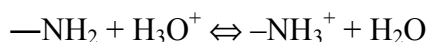
for the preparation of the chitosan film. After drying in air, the AAM/chitosan membranes were immersed in PWA saturated solution for at least 24 h.

Scanning Electron Microscopy analysis were performed by using a Philips XL30 ESEM coupled with EDX equipment. The composite membranes were sandwiched between two carbon paper electrodes (Toray 40% wet Proofed-E-Tek), covered with a mixture Pt black/C black (30 % Pt on Vulcan XC-72, E-Tek)/ Nafion® wt 15 %, stirred in n-butyl acetate for at least 3 hours. The catalyst loading was 1 mg cm⁻² of black platinum. The active area was delimited by insulating silicon rubber having an area of 10 cm². The Membrane Electrode Assembly (MEA) was then assembled in a single fuel cell apparatus (FuelCellTechnologies, Inc.) and fed with oxygen (99.5 % purity, 1 bar), and hydrogen (99.5 % purity, 1 bar) humidified at room temperature. Polarization curves were obtained by using a h-tec Fuel Cell Monitor (item 1950). The current density reported in the following are referred to the apparent AAM area (10 cm²).

Results and discussion

CTS/PTA thin films

Chitosan/PTA film have been prepared by infiltration of PTA into pure CS film by dipping the pre-formed chitosan film in PTA saturated aqueous solution according to the procedure described in [15]. Due to presence of free amine groups, chitosan macromolecule can dissolve in dilute aqueous acidic solvents, such as acetic acid, according to:



The emergence of positive charges along the chitosan chain explains the polyelectrolyte character of chitosan and influences its properties. It is known that complexation reactions can occur at the oxygen and nitrogen atoms in the carbonyl and the amine groups of chitosan [21]. It has been recently proposed [15, 16] that PTA proton conductor can be immobilized into chitosan film through strong electrostatic interactions between PTA anions (Keggin unit) and CS polymer containing cationic $-\text{NH}_3^+$ groups. Since PTA is an optimum proton conductor at room temperature, the formation of insoluble CS/PTA complex which maintains the presence of the Keggin unit of PTA [16], should prevent PTA dissolution in the fuel cell environment.

In Fig. 1 we report the SEM analysis of the cross-section of the pure CS (a) and CS/PTA (b) film soon after preparation. From Fig. 1b it appears that the CS/PTA morphology is uniform, indicating that PTA does not form crystals with phase separation, but it reacts with chitosan to form CS/PTA complex through electrostatic interactions.

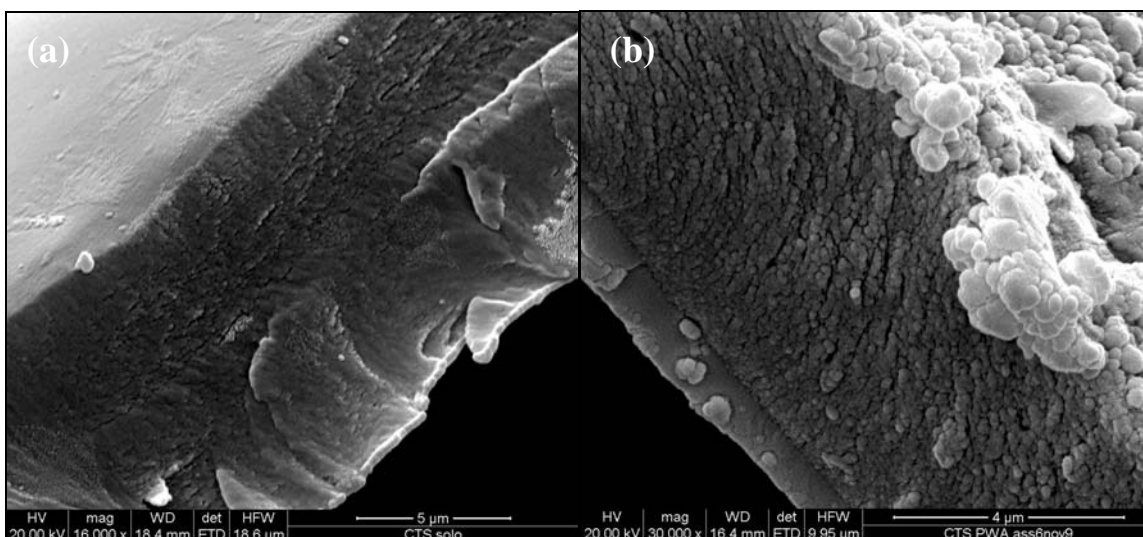


Figure 1 - SEM images showing the side-view of (a) CS and (b) CS/PTA films.

The EDX analysis performed in the cross-section reveal the presence of W, P and O elements, as shown in Figure 2. These results confirm that the polyelectrolyte CS/PTA has been formed also inside the CS membrane, and not only on the surfaces. A homogeneous formation of PTA inside the CS membrane is clearly a necessary requirement to guarantee a good proton transport and membrane stability during fuel cell operation.

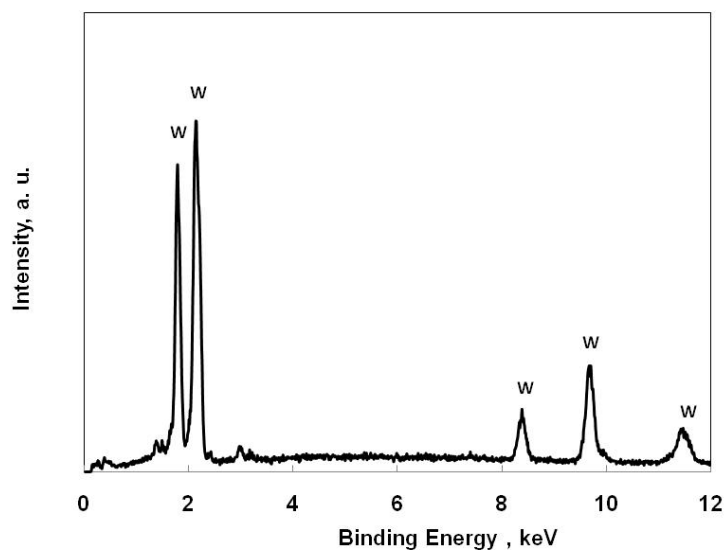


Figure 2 - EDX spectrum relative to the an area 2x2 μm on the film of Fig. 1b.

A detailed SEM analysis of the cross-sections of the CS/PTA membranes shows that their thickness is not uniform along the entire surface of the membrane. As reported in Figures 3 a-d values from 8 to 95 μm have been measured in different region of the same sample. This result indicates that the solution cast technique used in this work doesn't allow a precise control of the thickness.

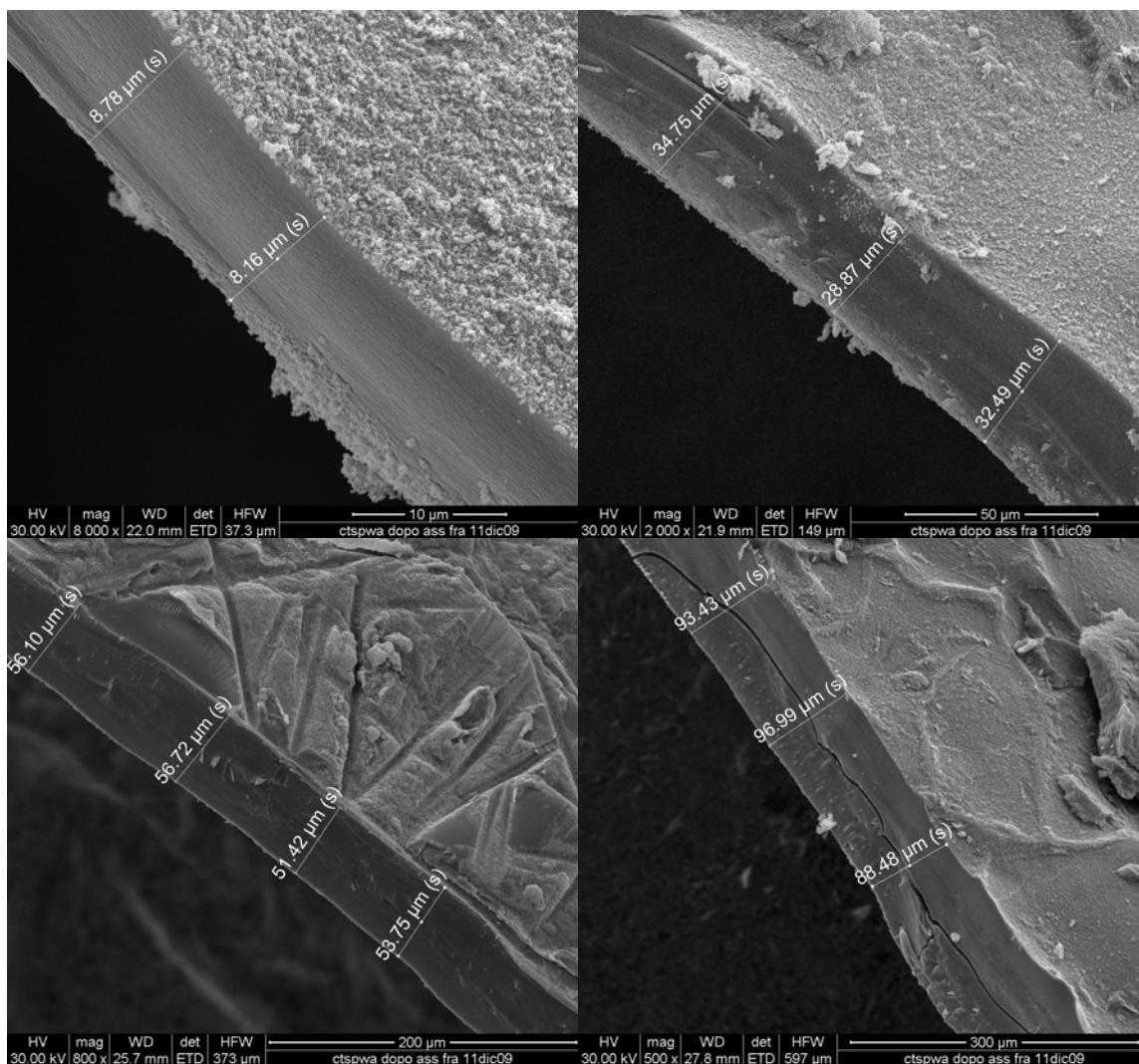


Figure 3 - SEM images showing the thickness of CS/PTA in different areas of the same sample.

Before recording the polarization curves of the fuel cell, the open circuit cell potential (OCP) was monitored until a quasi-steady state condition was reached (~ 15 min). The OCP values range between 0.8 and 1 V, which are lower than the theoretical value expected at 25°C and gas partial pressure of 1 atm (1.22 V). To this large difference both the crossover of the gases through the membrane as well as possible gas leaks through the experimental set-up can contribute.

In Figure 4, we report the best performance obtained with CS/PTA film assembled in a H_2/O_2 fuel cell under mild conditions (room temperature, low humidity and 1 mg cm^{-2} Pt loading). A peak power density of 20 mW cm^{-2} at a load current density of 50 mA cm^{-2} is achieved.

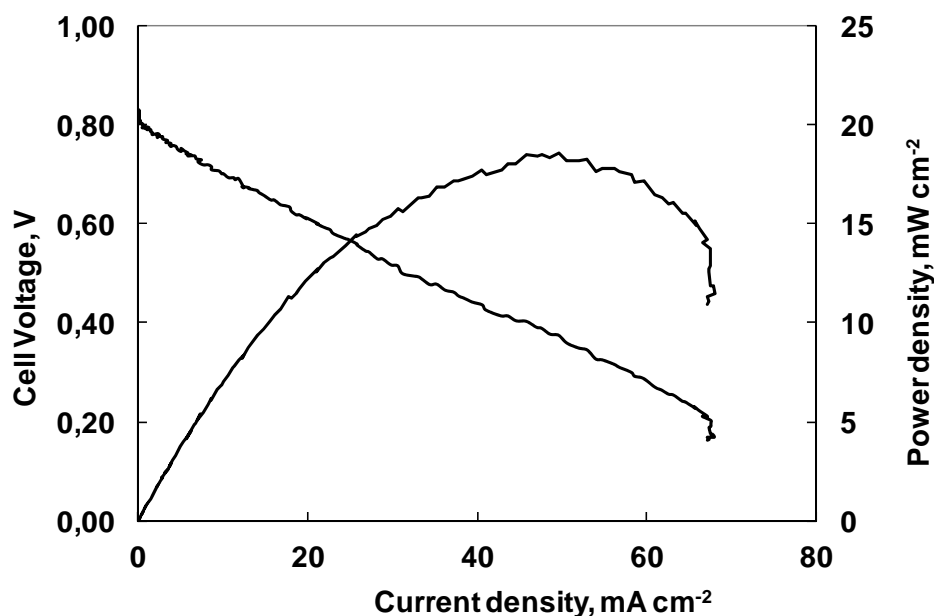


Figure 4. Best polarization curve and power output of a 10 cm² single module H₂/O₂ fuel cell working with CS/PTA film electrolyte ($T_{\text{cell}} = 25^{\circ}\text{C}$, $T_{\text{gas}} = 25^{\circ}\text{C}$, 1 mg cm⁻² Pt loading).

Several CS/PTA membranes were tested in the same single module fuel cell under the same experimental conditions. In table 1 we summarize the measured peak power values obtained from the polarization curves recorded during 20 different assemblies. We believe that the considerable variability can be ascribed to the uncontrolled thickness of CS/PTA films, since the polarization curve are characterized by a ohmic behavior (see for instance Fig. 4).

TABLE I. Average power output of a 10 cm² single module H₂/O₂ fuel cell working with CS/PTA film electrolyte ($T_{\text{cell}} = 25^{\circ}\text{C}$, $T_{\text{gas}} = 25^{\circ}\text{C}$, 1 mg cm⁻² Pt loading) vs. % on the total assemblies (N. 20).

Assemblies, %	Average power peak output, mW cm ⁻²
42	17 ± 3
33	$8,6 \pm 0,3$
25	$3 \pm 0,2$

A rough estimate of the CS/PTA proton conductivity at room temperature has been performed by considering that the polarization curve is totally controlled by the ohmic resistance and the voltage losses relating to charge transfer overpotentials are negligible. Assuming that the predominant contribution to the ohmic resistance is given by the electrolyte, the proton conductivity of CS/PTA at room temperature can be calculated from the slope of the polarization curve. By using the electrode area of 10 cm² and a film thickness of 52 μm (averaged from 8 to 95 μm), a conductivity value of 0.6 mS/cm can be obtained for the assembly of Figure 4, which represents the best measurement. This is more than one order of magnitude lower with respect to the value of 12.2 mS/cm reported in Ref. 16 for similar CS/PTA film. According to the literature, the conductivity of chitosan-based compounds is sensitively influenced by the method employed for the measurements, thus a difference is in some way expected [22, 23]. However, we have

also to take into account that the conductivity value suggested on the base of Fig. 4 suffers an imprecision in the measured thickness, as well to different experimental conditions inside the fuel cell with respect to those of Ref. 16. Anyway, this discrepancy suggests that major improvements in the power output of our fuel cell are still possible. We are actually working on a different procedure able to prepare chitosan film with high controllable thickness and improved proton conductivity and will be presented in a future paper.

At present, the stability of chitosan-based fuel cell has not yet been studied. Here, the power output vs. time of the CS/PTA fuel cell was investigated under a cell voltage of 0.5 V as reported in Figure 5 for the CTS/PTA fuel cell with the highest electrochemical performance.

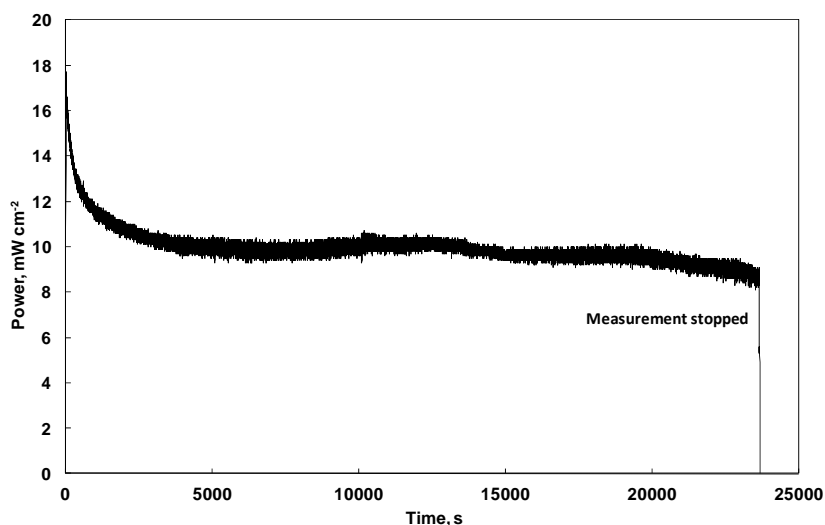


Figure 5 – Power output for a 10 cm² single module H₂/O₂ fuel cell ($T_{\text{cell}} = 25^{\circ}\text{C}$, $T_{\text{gas}} = 25^{\circ}\text{C}$, 1 mg cm⁻² Pt loading) working with Cs/PTA film electrolyte at an applied cell potential of 0.5 V.

The measurement was stopped after 7 hours. The recorded stable power output suggests that there are optimal bonding between electrode and electrolyte interfaces and good electrochemical activities of cell components.

CT/PTA nanowires

In Fig. 6 we report the SEM morphologies of the AAM after filling with CS and subsequent infiltration of the PTA before assembly. From the images of the surfaces (Fig. 6 a, b) the nanowire-type morphology is evidenced. Nanowires of polyelectrolyte CT/PTA into the pores of the alumina membrane are also evidenced from the side-view of Fig. 6c,d. In Fig. 6 some circular little empty areas can be observed and related to the presence of residual air bubbles during the filtration of chitosan solution across alumina membrane. In Fig. 6d it can be clearly evidenced some filled pores, where the alumina pore wall and the CS/PTA nanowire can be easily distinguished. The nanowires are well compact and adherent to the alumina pore wall.

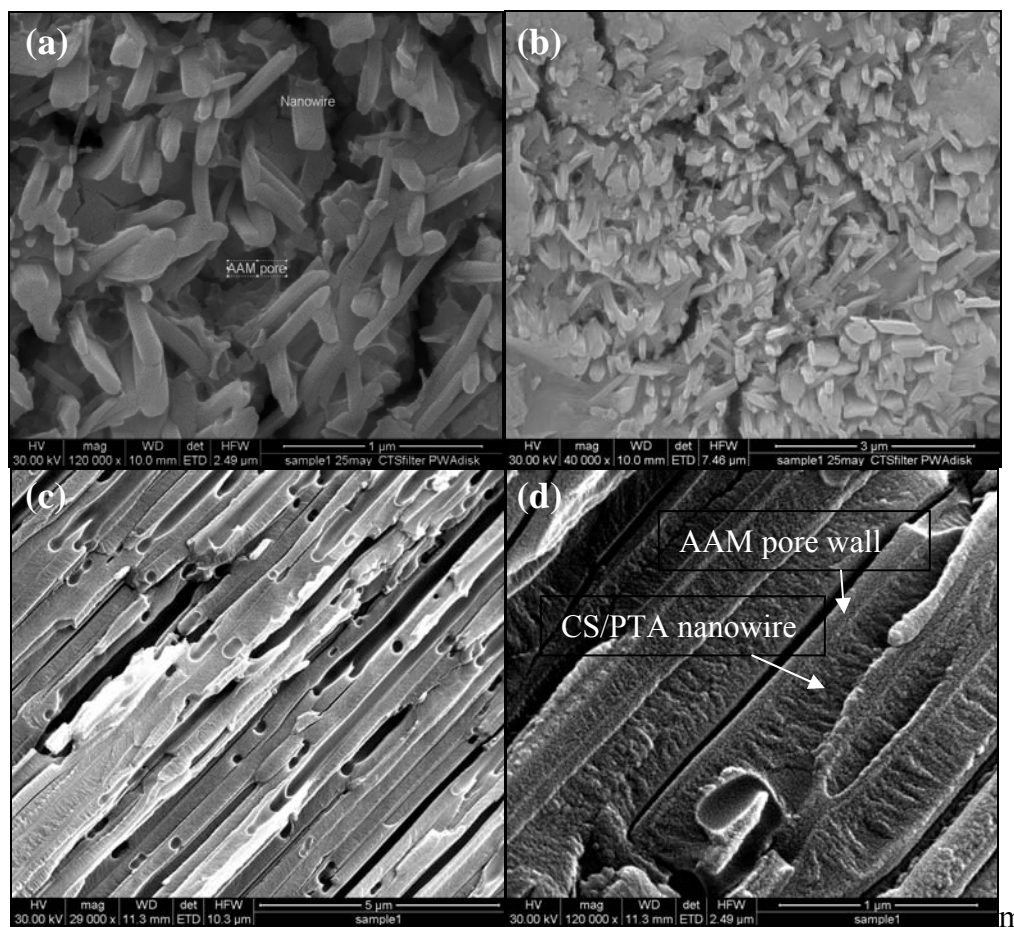


Figure 6 - SEM images showing the (a, b) front-view and side-view (c, d) of composite AAM/CS/PTA membrane at different magnification.

The EDX analysis performed in the AAM/CS/PTA cross-section confirms the presence of W, P and O elements, as shown in Fig. 7.

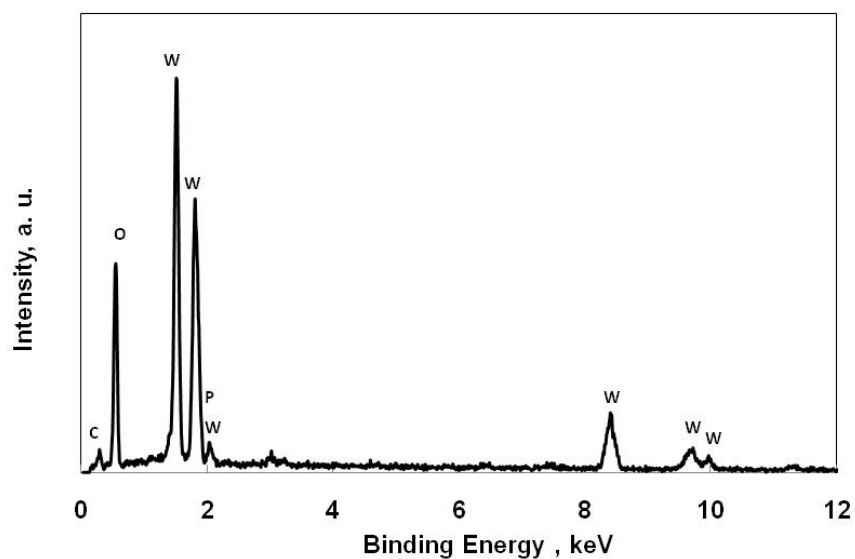


Figure 7 - EDX spectrum relative to the an area 100x100 nm inside the nanowire of Fig. 6d.

The AAM/CS/PTA membranes were assembled in a H_2/O_2 fuel cell under the same conditions used for CS/PTA film (room temperature, low humidity and 1 mg cm^{-2} Pt loading). The best performance is reported in Fig. 8 displaying a power peak density of 20 mW/cm^2 at a load current density of 60 mA/cm^2 .

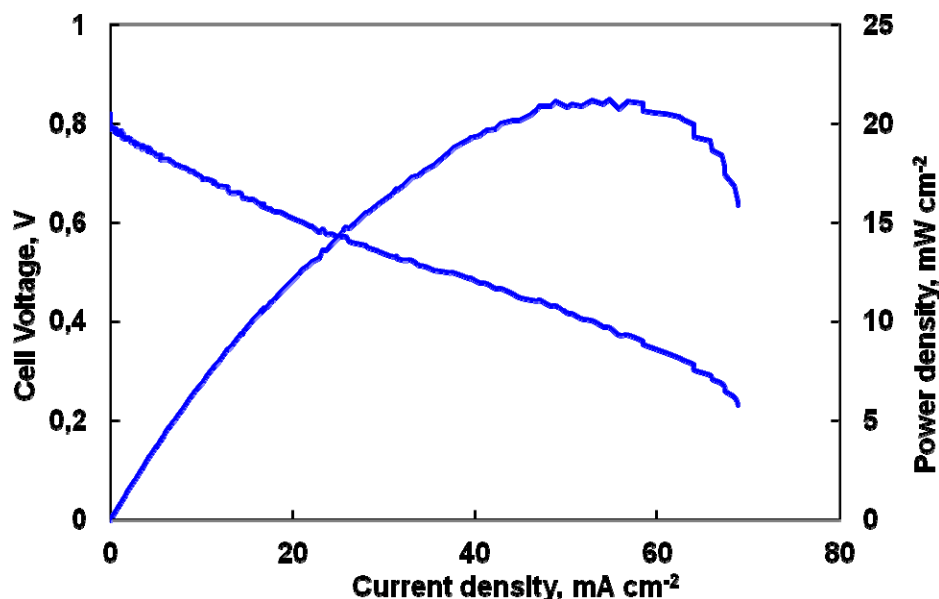


Figure 8. Best polarization curve and power output of a 10 cm^2 single module H_2/O_2 fuel cell working with AAM/CS/PTA electrolyte ($T_{\text{cell}} = 25^\circ\text{C}$, $T_{\text{gas}} = 25^\circ\text{C}$, 1 mg cm^{-2} Pt loading).

In previous works we shown that the use of CsH_2PO_4 and $\text{CsNH}_4\text{SO}_4\text{TeOH}_6$ [19, 20] fillers of AAM allowed the improvement of AAM-based thin film fuel cell in terms of performance and durability at room temperature. In such works a fuel cell durability of about 3-4 hours was obtained, even if the membrane suffers dissolution in the water produced at the cathodic side. As reported in Fig. 9, by using insoluble CS/PTA fillers some problems of power stability are still present in the AAM-based fuel cell. The power output decreases with time very quickly in the first 15 min of functioning and after that it begins to decline gradually. In the mean time, we can also observe that the lifetime of the cell is increased from 3-4 to 5-6 hours of functioning with respect to our previous results. In addition, we have observed an improved reproducibility of the stability curve, as shown in Fig. 9 for three different assemblies. We believe that the degradation of the fuel cell power output can be mainly attributed to the presence of irregularity in the pore filling of alumina discussed above (see Fig 6c). A homogeneous filling of AAM pores is clearly a necessary requirement to guarantee a good proton transport and membrane stability during fuel cell operation. Another problem to solve is related to chitosan swelling, which has a profound effect on both membrane stability and proton conductivity. In the case of composite alumina/CS/PTA the degradation of the membrane is probably enhanced by the presence of ceramic alumina which supports the tensional strengths of swelled chitosan. The presence of water inside the alumina channels, due to hydrophilic character of alumina can also justify the increase in the CS/PTA proton conductivity (1.7 mS/cm) measured by fitting the ohmic part of the curve of Fig. 8 using the real membrane area (AAM porosity = 43%) and $50 \text{ }\mu\text{m}$ of electrolyte thickness. Future work will be focused on the use of chitosan-based fillers by using the chitosan

capability to transport protons through anhydrous mechanism. Such instability has not been observed in the CS/PTA film probably due higher mechanical resistance with respect to filled alumina where tensional strengths are present inside the ceramic pores.

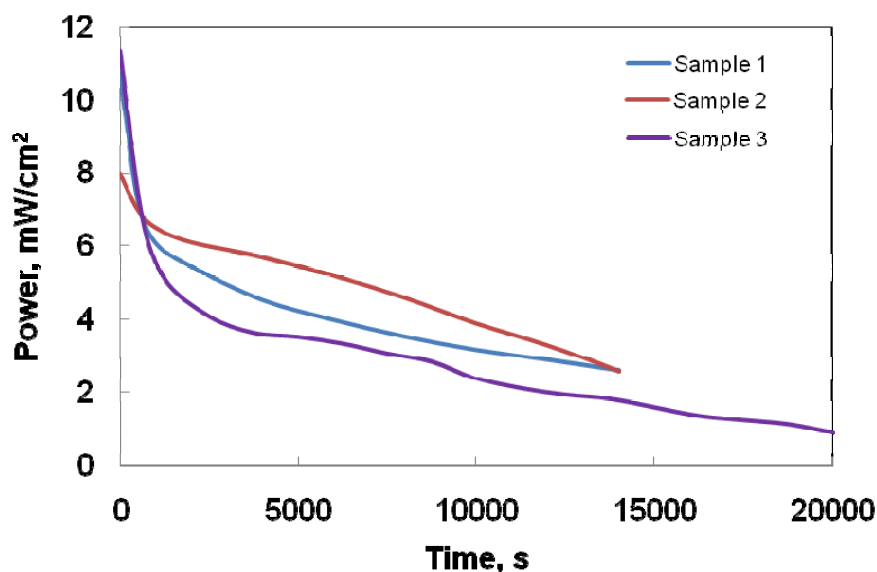


Figure 9– Power output for a 10 cm² single module H₂/O₂ fuel cell ($T_{\text{cell}} = 25^{\circ}\text{C}$, $T_{\text{gas}} = 25^{\circ}\text{C}$, 1 mg cm⁻² Pt loading) working with AAM/Cs/PTA membranes at an applied cell potential of 0.5 V.

Conclusions

The fuel cell behavior of insoluble complex of chitosan and phosphotungstic acid as novel fuel cell proton conducting film and supported nanowires at low temperatures (25°C), low humidity ($T_{\text{gas}} = 25^{\circ}\text{C}$) and low Pt loading (1 mg cm⁻²) has been investigated for the first time. Solution-cast technique allows to prepare thin film CTS membranes and the formation of the insoluble polyelectrolyte CTS/PTA occurs also inside the CTS film, according to EDX results. A limited control of the thickness uniformity along the film has been observed (8-95 μm) which influences the electrochemical performance reproducibility of the fuel cell. Power peaks of 20 mW/cm² has been measured for the best assembly at 25 °C and the cell is able to produce a constant power output of 10 mW/cm² under a cell potential of 0.5 V for at least 7 h. SEM and EDX results indicate that AAM support (50 μm) can be filled with CTS/PTA nanowires and the fuel cell provides peak power of 20 mW cm⁻² at 25°C. This result is encouraging because, if we attribute the main potential loss to the ohmic drop in the electrolyte, thinner AAMs are expected to lead higher power output. Even if the stability of the cell needs further improvements, encouraging results have been obtained in terms of lifetime and reproducibility of the power vs. time curves with respect to soluble fillers. Other experiments are in progress in order to optimize the filling procedure of the AAM. Considering the proven versatility, biocompatibility and low-cost of chitosan, its use to prepare membranes for fuel cells seems really promising in view of a possible Nafion[®] substitution.

Acknowledgments

This work is sponsored by US Army-ONRG (USAITC-A under contract N. W911NF-07-1-0564).

References

1. M. G. Peter, in *Biopolymers: Biology, Chemistry, Biotechnology, Applications. Vol. 6. Polysaccharides II: Polysaccharides from Eukaryotes*, E. J. Vandamme, S. De Baets, A. Steinb-chel, Editors, V. 6, p. 485, Wiley-VCH (2002).
2. K. Kurita, *Prog. Polym. Sci.*, **26**, 1921 (2001).
3. I. Aranaz, R. Harris, A. Heras, *Current Organic Chemistry*, **14**, 308 (2010).
4. S. G. Kim, K.S. Lee, K. H. Lee, *Journal of Applied Polymer Science*, **103**, 2634 (2007).
5. B. Phillip, H. K. Dautzenberg, J. Linow, J. Kotz, *Prog. Polym. Sci.*, **14**, 91 (1989).
6. P.V. Morales, L. N. J. Francois, A. Gandini, *Electrochim. Acta*, **43**(10–11), 1275 (1998).
7. T. Winie, S. R. Majid, A. S. A. Khiair and A. K. Arof, *Polym. Adv. Technol.*, **17**, 523 (2006).
8. B. Smitha, S. Sridhar, A. A. Khan, *Macromolecules*, **37**, 2233 (2004).
9. B. Smitha, S. Sridhar, A. A. Khan, *European Polymer Journal*, **41**, 1859 (2005).
10. M. Yamada, I. Honma, *Electrochimica Acta*, **50**, 2837 (2005).
11. Y. Zhanga, Z. Cuia, C. Liua, W. Xinga, J. Zhangb, *Journal of Power Sources*, **194**, 730 (2009).
12. M. Yamada, I. Honma, *Fuel Cell Bulletin*, (2006).
13. S. R. Majida, A. K. Arofa, *Polym. Adv. Technol.*, **20**, 524 (2009).
14. Y. Wana, B. Peppleyb, K. A.M. Crebera, V. Tam Buia, E. Halliopb, *Journal of Power Sources*, **185**, 183 (2008).
15. Z. Cui, C. Liu, T. Lu, W. Xing, *Journal of Power Sources*, **167**, 94 (2007).
16. Z. Cui, W. Xing, C. Liu, J. Liao, H. Zhang, *Journal of Power Sources*, **188**, 24 (2009).
17. P. Bocchetta, G. P. Chiavarotti, R. Masi, C. Sunseri, F. Di Quarto, *Electrochem. Comm.*, **6**, 923 (2004).
18. P. Bocchetta, F. Conciauro, F. Di Quarto, *J. of Solid State Electrochem.*, **11**, 1253 (2007).
19. P. Bocchetta, R. Ferraro, F. Di Quarto, *J. Power Source*, **187**, 49 (2009).
20. P. Bocchetta, F. Conciauro, M. Santamaria, F. Di Quarto, *Electrochim. Acta*, **56**, 3845 (2011).
21. S. R. Majid, A. K. Arof, *Mol. Cryst. Liq. Cryst.*, **484**(2), 117 (2008).
22. J. Ramírez-Salgado, *Electrochim. Acta*, **52**, 3766 (2007).
23. Z. Jiang, X. Zheng, H. Wu, J. Wang, Y. Wang, *J. Power Sources*, **180**, 143 (2008).

Magnesium Recycling of Partially Oxidized, Mixed Magnesium-Aluminum Scrap Through Combined Refining and Solid Oxide Membrane Electrolysis Processes

X. Guan^a, P. A. Zink^{a,b}, U. B. Pal^{a,b}, and A. C. Powell^c

^a Division of Materials Science and Engineering, Boston University, Brookline, MA 02446, USA

^b Department of Mechanical Engineering, Boston University, Boston, MA 02215, USA

^c Metal Oxygen Separation Technologies, Inc, Natick, MA 01760, USA

Pure magnesium (Mg) is recycled from 19g of partially oxidized 50.5wt.% Mg-Aluminum (Al) alloy. During the refining process, potentiodynamic scans (PDS) were performed to determine the electrorefining potential for magnesium. The PDS show that the electrorefining potential increases over time as the magnesium content inside the Mg-Al scrap decreases. Up to 100% percent of magnesium is refined from the Mg-Al scrap by a novel refining process of dissolving magnesium and its oxide into a flux followed by vapor phase removal of dissolved magnesium and subsequently condensing the magnesium vapor. The solid oxide membrane (SOM) electrolysis process is employed in the refining system to enable additional recycling of magnesium from magnesium oxide (MgO) in the partially oxidized Mg-Al scrap. The combination of the refining and SOM processes yields 7.4g of pure magnesium.

Introduction

Magnesium is the least dense engineering metal, with an excellent stiffness-to-weight ratio. For this reason, U.S. auto makers would like to replace 283.5kg of steel and aluminum parts per vehicle with 153kg of magnesium alloy by the year 2020 [1]. This would reduce vehicle weight by 130.5kg and improve average fuel efficiency by 1.5-2 miles per gallon, reducing petroleum imports by up to 1 million barrels per day. Additionally, the fact that magnesium has good electromagnetic shielding makes it very attractive to the audio and electronic industry [2]. As magnesium consumption increases in the automotive, aerospace and electronic industries, magnesium recycling will become ever more important for both economic and environmental reasons.

Several magnesium recycling processes are currently in use. Some are based on the use of refining fluxes, and others are flux-free methods. Hydro Magnesium [3, 4] has a system for continuous melting under flux. Magnesium alloy is melted in one end of a large multi-chamber furnace and pumped out or cast from the other end. This refining process uses sufficient flux to absorb all the oxides present in the molten metal, but it cannot separate pure magnesium from aluminum and trace impurities such as zinc, iron and nickel; impurities like nickel and iron decrease the corrosion resistance of magnesium [5]. Zhu et al [6] demonstrated vacuum distillation for magnesium recycling, however, the vacuum distillation leaves 20-25% of the original scrap as residue with a magnesium weight content as high as 60%. It is understood that further magnesium

distillation is hindered by magnesium oxide and aluminum oxide (Al_2O_3) scale on the surface of the residue.

In this paper, an innovative process for recycling pure magnesium metal from impure magnesium scrap alloy at high efficiency and low cost is proposed. The typical magnesium alloys in automotive components are AZ91, AM50, and AM60 [7], all of which are predominantly Mg-Al alloys with small amount of impurities (Zn, Mn, Fe and Ni). This paper reports proof of concept experiments of a process with partially oxidized 50.5wt%Mg-Al alloy. The refining efficiency is almost 100% by dissolving magnesium and its oxide from the scrap into a flux followed by vapor phase removal of dissolved magnesium and subsequently condensing the magnesium vapors in a separate condensing chamber. After refining, the SOM electrolysis process is employed in the system to enable additional recycling of magnesium from magnesium oxide in the scrap. The combination of the refining and SOM electrolysis processes proves to be a feasible method for recycling magnesium from partially-oxidized impure magnesium scrap alloy. Future work will involve recovery of magnesium from partially oxidized magnesium scrap containing more impurities which otherwise make it unsuitable for reuse.

Experimental

Figure 1 shows the design of the setup used in this experiment. The setup consists of an upper reaction chamber, heated to 1175°C and a lower condensing chamber with a temperature gradient of $1100\text{--}200^\circ\text{C}$. The setup was fabricated using grade 304 stainless steel (SS-304) and heated as mentioned above in an argon (Ar) atmosphere.

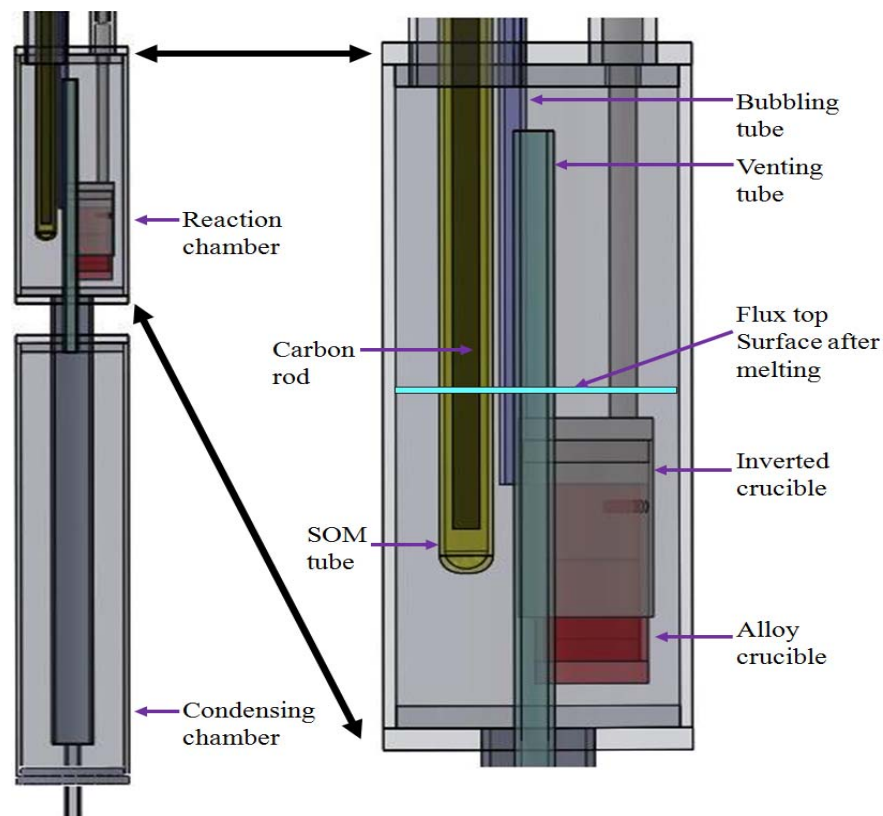


Figure 1. Design of experimental setup for refining and SOM electrolysis processes.

The Mg-Al alloy was prepared by melting a 9.6g piece of magnesium (Mg>99.8%) and another 9.4g piece of aluminum (Al>97.9%) together inside a small SS-304 crucible. The mixture of magnesium and aluminum was stirred with a SS-304 rod for 15 minutes at 800°C in an argon atmosphere, then held at the same temperature without stirring for 15 minutes and subsequently quenched. The alloy was homogeneous and the composition was 50.5wt%Mg-Al.

Since there is a finite solubility of iron in Mg-Al alloy, 2g of iron powder was added on the top of the Mg-Al alloy to decrease dissolution of iron from the crucible during the experiment. The iron powder addition also increases the density of the alloy (which sinks to the flux bottom in the alloy crucible) and lowers the vapor pressure of magnesium. A powdered flux ($\text{MgF}_2\text{-CaF}_2\text{-10wt.\%MgO-2wt.\%YF}_3$) containing a eutectic mixture of 45wt.% $\text{MgF}_2\text{-55wt.\%CaF}_2$ with a melting point of 974°C [8] was used as the electrolyte and was packed both inside and outside the inverted crucible shown in Figure 1. In order to prevent the distillation of magnesium from the Mg-Al alloy during heating to 974°C, a layer of flux is melted on the surface of the alloy crucible to hermetically seal the opening of the alloy crucible before heating. Thus, the alloy is trapped inside the alloy crucible, and direct distillation of magnesium is avoided. A result of pre-melting the flux at the top of the alloy crucible is that some of magnesium in the alloy becomes oxidized. This magnesium oxide is later reduced with the SOM electrolysis process.

During the refining process, the alloy crucible and inverted crucible served as the anode, and the reaction chamber wall and bubbling tube served as the cathode. The SOM tube was held above the flux. An alumina spacer was used to insulate the rod connecting the inverted crucible from the reaction chamber. Potentiodynamic scans were performed to determine the electrorefining potential for magnesium as the refining of magnesium proceeded.

During the SOM electrolysis process, an yttria stabilized zirconia (YSZ) tube was used for reducing magnesium from magnesium oxide. The stainless steel wall of the reaction chamber still served as the cathode, but silver inside the YSZ tube served as the anode, and a carbon rod immersed in the silver acted as the anodic current collector. When the applied electric potential between the cathode and anode exceeds the dissociation potential of magnesium oxide, magnesium vapor is produced at the cathode, and carbon reacts with oxygen to generate carbon monoxide [9, 10]. The overall cell reaction is given as:



It should be noted that during both the refining and electrolysis processes, the reaction chamber is continually purged with 95%Ar-H₂ at 15cc/min through the bubbling tube, and at 30cc/min through the two annuli at the top of the reaction chamber. This is done to lower the partial pressure of magnesium vapor over the flux and to carry the magnesium vapor to the condensing chamber. The inlet of the venting tube is well above the flux surface, to prevent any molten flux from entering the condenser.

A Solartron SI 1280B potentiostat was used for potentiodynamic scans and impedance spectroscopy during the refining process; an Agilent Technologies N5743A power supply was used for potentiodynamic scans and electrolysis during the SOM process.

Results and Discussion

1. Refining process

Once the reaction chamber was at the desired temperature, potentiodynamic scans were performed as shown in Figure 2. The initial melted flux is entirely ionic and acts as an electronic insulator between the anode and the cathode. The current increases linearly as the applied potential increases, except at the two current jumps corresponding to magnesium dissolution and magnesium vapor formation, as can be seen in each potentiodynamic scan. The current-voltage curve is shifting in a positive direction over time from PDS1 to PDS5 due to decreasing magnesium concentration in the alloy as explained later in the paper. The ohmic resistance of the system was measured to be as low as $0.066\ \Omega$ using impedance spectroscopy shown in Figure 3. One potential reason for the low resistance, or high electronic conductivity, is the dissolution of metallic magnesium in the flux. It has been shown that magnesium metal has some solubility in chloride based ionic salts [11]. The magnesium solubility inside the flux after the experiment was found to be 0.03wt% as measured with a hydrogen evolution experiment. In that experiment, dilute acid was added to powdered flux in a closed container and the volume of gas produced, due to hydrogen evolution, was measured. The flux was powdered in a glove box to avoid the oxidation of magnesium in the flux. The magnesium solubility inside a flux of similar composition (50.5%MgF₂-39.5%CaF₂-10%MgO) was reported to be 0.02-0.05wt.% [12], consistent with the experimental results.

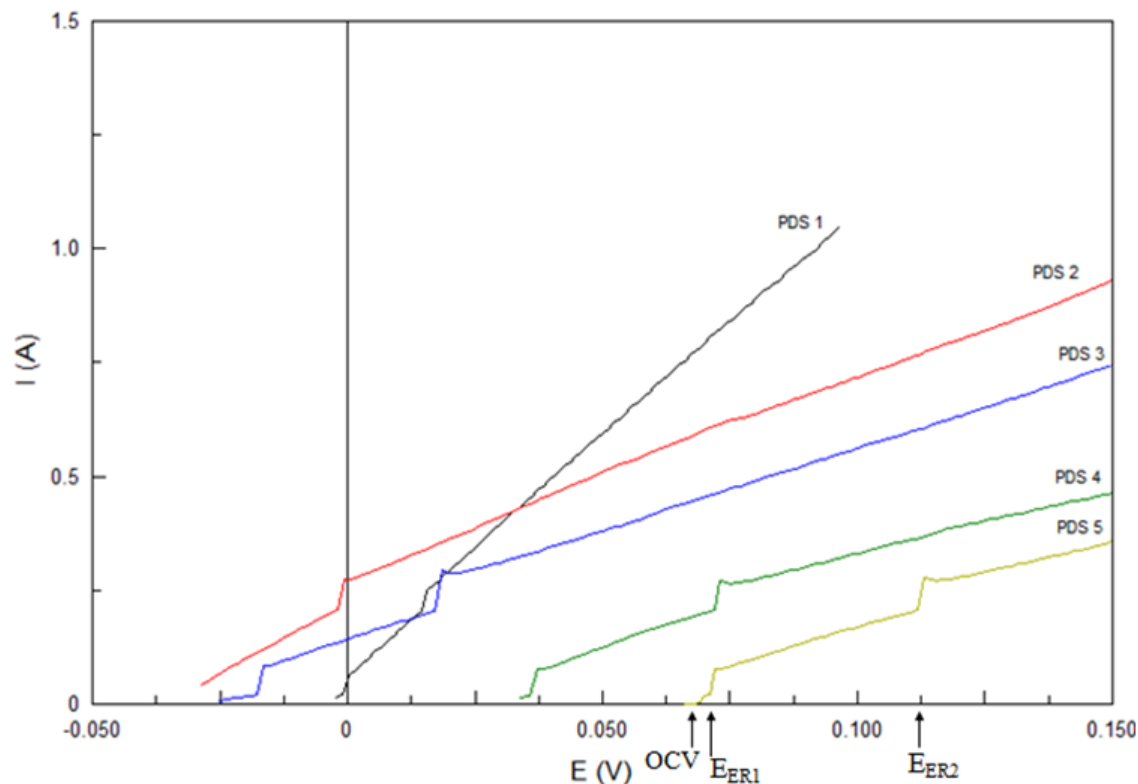


Figure 2. Potentiodynamic scans from the refining process. The open circuit voltage, and the two electrorefining potentials (OCV, E_{ER1} , E_{ER2}) for the last potentiodynamic scan are indicated by arrows.

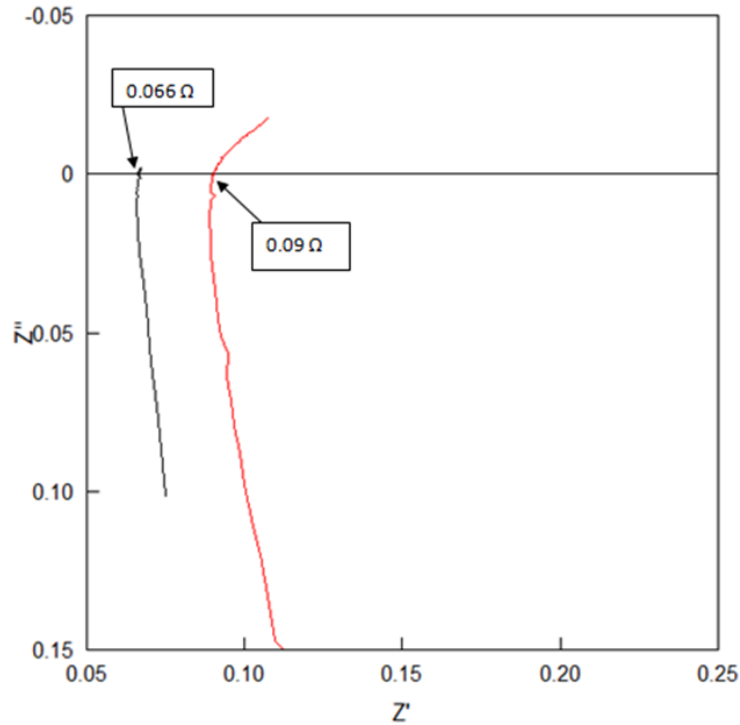
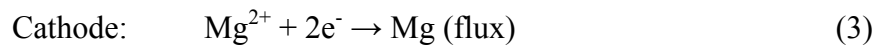
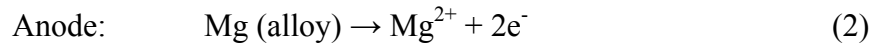


Figure 3. Impedance spectroscopy results during refining.

For each potentiodynamic scan, there are two current jumps which correspond to two different electrochemical reactions (Figure 2). The current jump at the first potential, close to the open circuit voltage is due to the following electrochemical reactions:



And the overall reaction is



This reaction is different from direct dissolution of magnesium from Mg-Al alloy into flux. Theoretically, the first electrorefining potential corresponding to the first current jump should be equal to the open circuit voltage, and its expression is given by

$$E_{\text{ER1}} = E_{\text{OCV}} = E_{\text{anode}} - E_{\text{cathode}} = \frac{RT}{2F} \ln \frac{a_{\text{Mg}(\text{flux})}}{a_{\text{Mg}(\text{alloy})}} = \frac{RT}{2F} \ln \frac{P_{\text{Mg}(\text{flux})} / P_{\text{Mg}}^0}{\gamma x_{\text{Mg}(\text{alloy})}} \quad (5)$$

where

γ is the activity coefficient of magnesium in Mg-Al alloy;

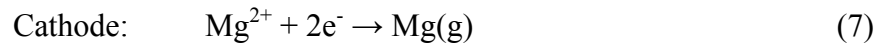
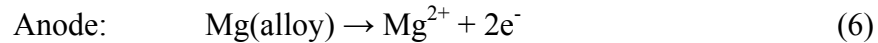
$x_{\text{Mg}(\text{alloy})}$ is the magnesium molar content in Mg-Al alloy;

$P_{\text{Mg}}^0 = 1.9 \text{ atm}$ is the magnesium vapor pressure at $T=1175^\circ\text{C}$;

$P_{\text{Mg}(\text{flux})}$ is the partial pressure of magnesium vapor in equilibrium with liquid magnesium dissolved in flux at the cathode, and $P_{\text{Mg}(\text{flux})} < 1 \text{ atm}$.

According to Equation (5), the first electrorefining potential and the open circuit voltage depends on the ratio of the activity of magnesium dissolved in the flux and the activity of magnesium in the alloy. There is a minor difference between the open circuit voltage and the first electrorefining potential in the experimental measurement caused by the fluctuating value of $P_{Mg(flux)}$.

The second current jump at the higher potential is due to the following reaction:



And the overall reaction is:



The theoretical expression of electrorefining potential for Reaction (8) is given by Equation (9), and is plotted in Figure 4. The electrorefining potential depends on the ratio of magnesium vapor activity at the cathode and magnesium activity in the alloy.

$$E_{ER2} = E_{\text{anode}} - E_{\text{cathode}} = \frac{RT}{2F} \ln \frac{a_{Mg(g)}}{a_{Mg(\text{alloy})}} = \frac{RT}{2F} \ln \frac{P_{Mg(g)} / P_{Mg}^0}{\gamma x_{Mg(\text{alloy})}} \quad (9)$$

where

γ is the activity coefficient of magnesium in Mg-Al alloy;

$x_{Mg(\text{alloy})}$ is the magnesium molar content in Mg-Al alloy;

$P_{Mg}^0 = 1.9 \text{ atm}$ is the magnesium saturated vapor pressure at $T = 1175^\circ\text{C}$; and

$P_{Mg(g)} = 1 \text{ atm}$ is the magnesium vapor partial pressure at the cathode.

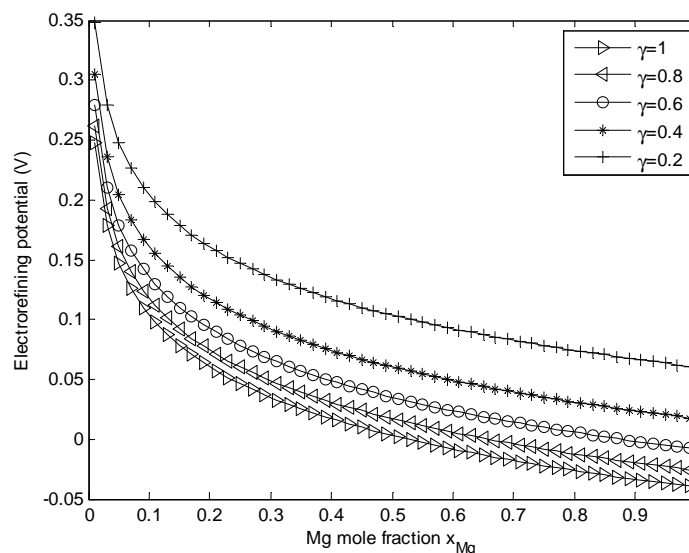


Figure 4. Theoretical values of the second electrorefining potential (based on Equation 9) of magnesium from Mg-Al scrap for different magnesium activity coefficients.

From Figure 4, as the magnesium content in the scrap goes down, the second electrorefining potential increases. The experimental result of the dependence of the second electrorefining potential and the open circuit voltage is shown in Figure 5. The second electrorefining potential and open circuit voltage increase with time, which indicates that the magnesium content in the scrap is decreasing as refining proceeds. The magnesium content in the scrap decreases due to the solubility of magnesium in the flux. Magnesium dissolution in the flux is followed by vapor phase removal of the dissolved magnesium from the flux. The refining process can be expressed as: $\text{Mg (alloy)} \rightarrow \text{Mg (flux)} \rightarrow \text{Mg (g)}$. Overall, pure magnesium is refined from magnesium scrap.

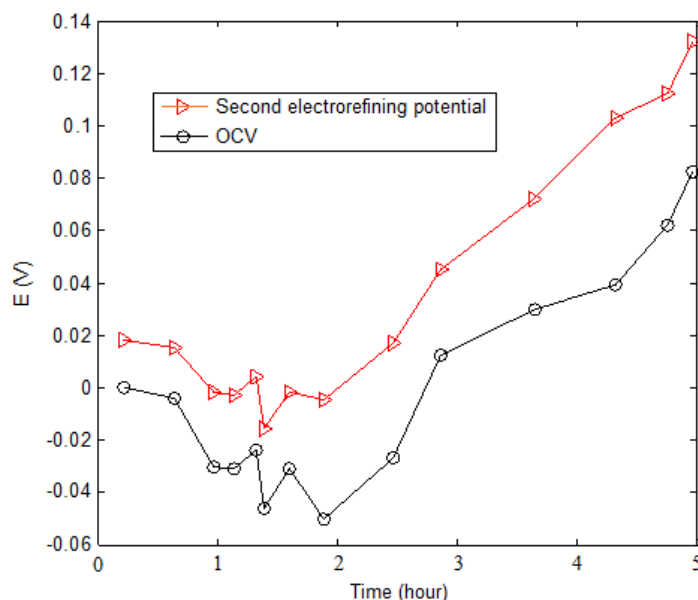


Figure 5. Second electrorefining potential (triangle) and OCV (circle) during refining.

2. SOM electrolysis process

Once the second electrorefining potential reached 0.13V, the anode was switched from the scrap anode to the liquid silver and carbon rod inside the YSZ tube, which was lowered into the flux, and a new potential was applied. When the potential reaches equals dissociation potential of magnesium oxide, oxygen ions are pumped out of the flux through the YSZ membrane and are oxidized at the liquid silver anode by the carbon rod; meanwhile, magnesium ions at the cathode are reduced to magnesium metal vapor, which is collected in the condenser.

Electrolysis was performed for a total of two hours at a potential of 3V. The curve labeled “PDS1” in Figure 6 shows the initial potentiodynamic scan before any SOM electrolysis was performed, and shows an electronic current of 0.35A due to the dissolution of magnesium from the scrap into the flux. The curve labeled “SOM electrolysis 1” in Figure 7 shows the current-time relationship during the first hour of electrolysis. Current efficiency is defined as the ratio of Faradic current to total applied current, and was calculated to be approximately 41% for the first hour of electrolysis. Faradaic current is calculated by measuring the flow rate of carbon monoxide produced from the reaction of the carbon rod and oxygen on the anode side of the YSZ membrane.

Based on the volume of carbon monoxide generated, magnesium reduced at the cathode was calculated to be 0.18g during the first hour of SOM electrolysis.

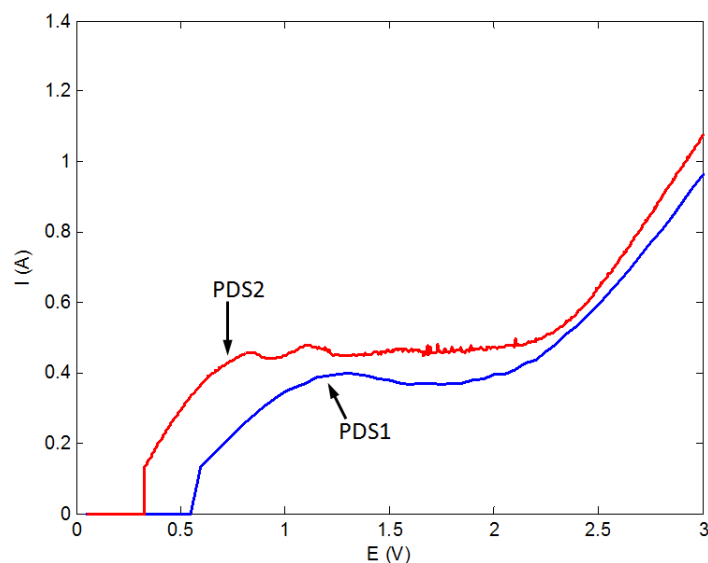


Figure 6. Potentiodynamic scans before the first hour of SOM electrolysis (PDS1) and before the second hour of SOM electrolysis (PDS2).

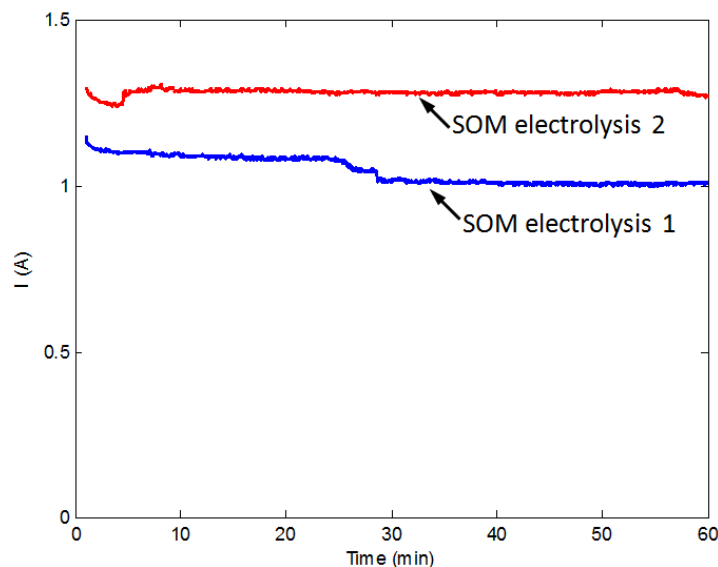


Figure 7. Current-time relationships for the first hour of electrolysis (SOM electrolysis 1) and the second hour of electrolysis (SOM electrolysis 2). Both electrolyses were performed at 3V.

The curve labeled “PDS2” in Figure 6 shows the potentiodynamic scan before the second hour of SOM electrolysis, and shows an increase in leakage current due to a higher concentration of magnesium dissolved in the flux. The curve labeled “SOM electrolysis 2” in Figure 7 shows the current-time relationship during the second hour of SOM electrolysis. For the second hour of electrolysis, the current efficiency was 39%, and the amount of magnesium reduced was 0.22g, very similar to the first hour. The total amount of magnesium reduced in the entire two hours of SOM electrolysis process was 0.4g.

The combination of refining and SOM electrolysis processes are shown in the schematic in Figure 8.

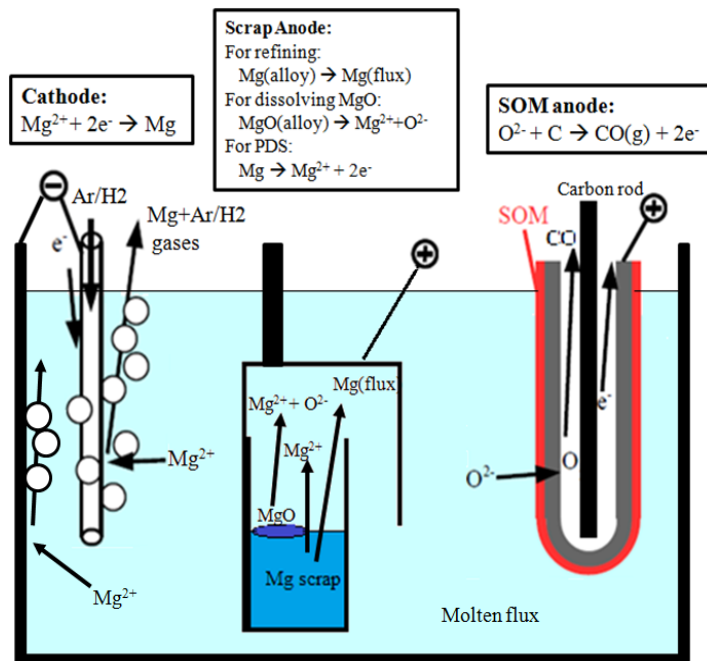


Figure 8. Schematic for refining and SOM electrolysis processes.

The total magnesium collected in the condenser from both the refining and SOM processes was weighed and found to be 7.4g. Energy-dispersive X-ray spectroscopy (EDS) results for the collected magnesium are shown in Figure 9. From these results, the purity of the collected magnesium was determined to be 99.6wt%.

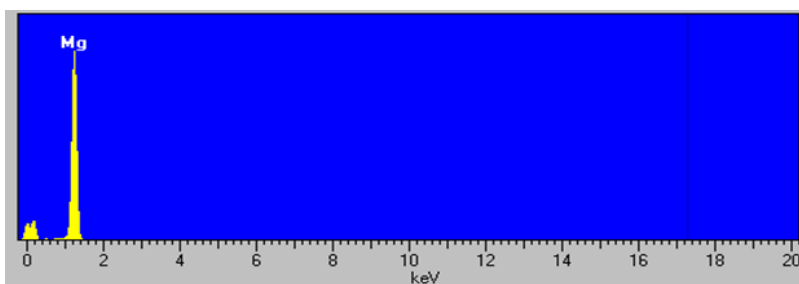


Figure 9. EDS results for the collected magnesium.

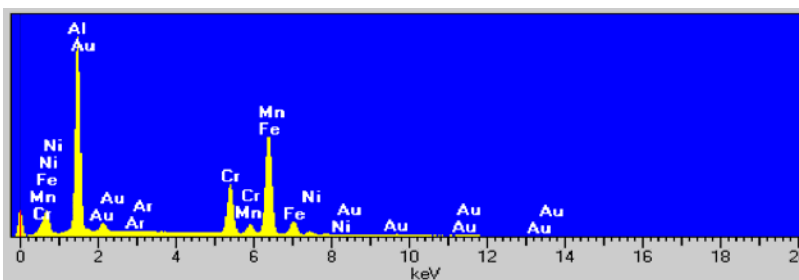


Figure 10. EDS results for the scrap residue inside the alloy crucible.

The scrap residue remained at the bottom of the alloy crucible. The iron powder as well as iron and chromium from the SS 304 crucibles alloyed with the scrap, which has a density higher than the flux. EDS was performed on the magnesium residue, and the

results are shown in Figure 10. Only trace magnesium remained in the alloy, thus approximately 100% of the magnesium was refined. Future experiments are also planned wherein the stainless steel parts will be replaced by low carbon steel to minimize additional dissolution of elements (Cr, Ni and Mn).

Conclusions

The combination of the novel refining process and the SOM electrolysis process for recycling magnesium from magnesium scrap was carried out, and yielded 7.4g of pure magnesium metal. A small amount of magnesium condensed on the walls of the condenser and dissolved in the 680g of flux and thus could not be quantified. No measurable amount of magnesium remained in the magnesium scrap, which implies that the refining efficiency is almost 100% using this novel refining process of dissolving magnesium and its oxide from the scrap into the flux, followed by vapor phase removal of dissolved magnesium. After the refining process, the SOM electrolysis process was employed in the refining system to enable the recycling of an additional 0.4g of magnesium from magnesium oxide in both the scrap and the flux. This paper presented the technical feasibility of recycling magnesium from partially oxidized Mg-Al alloy by the combination of refining and SOM electrolysis processes. In the future, this approach will be tested using larger amounts of oxidized scrap with additional impurities and a lower initial oxide content in the flux.

Acknowledgements

This material is based upon work supported by the Department of Energy under Award No. DE-EE0003454.

References

1. United States Automotive Materials Partnership, *Magnesium Vision 2020: A North American Automotive Strategic Vision for Magnesium*, USCAR, (2006).
2. J. F. Kurgan, *US patent 5053924*, (1991).
3. W. O, R. JB, *US Patent 5167700*, (1992).
4. H. E. Friedrich, B. L. Mordike, *Magnesium Technology: metallurgy, design data, applications*, p. 638, Springer, (2006).
5. S. D. Cramer and B. S. Covino, *ASM Handbook, Volume 13A: Corrosion: Fundamentals, Testing, and Protection*, p. 693, ASM international, (2003).
6. T. Zhu et al., *Magnesium Technology 2001*, p. 55-60, TMS, (2001).
7. G. Hanko, H. Antrekowitsch and P. Ebner, *Journal of the Minerals, Metals and Materials society*, **54** (2) (2002).
8. P. Chartrand and A. D. Pelton, *Metallurgical and Materials Transactions A*, **32** (6) (2001).
9. A. Krishnan, U. B. Pal and X. G. Lu, *Metallurgical and Materials Transaction B*, **36** (4) (2005).
10. U. B. Pal, A. C. Powell, *Journal of the Minerals, Metals and Materials Society*, **59** (5) (2007).

11. J. Wypartowicz, T. Ostvold and H. Oye, *Electrochimica ACTA*, **25** (1980).
12. E. Gratz et al., *Magnesium Technology 2011*, p. 39-42, Wiley-TMS, (2011).

Eutectic mixtures of ionic liquids electrolytes for electric double layer capacitors

Seiichiro Higashiya, Thamarai selvi Devarajan, Manisha V. Rane-Fondacaro, Pradeep Haldar

Energy and Environmental Technology Applications Center (E2TAC), College of Nanoscale Science and Engineering, University at Albany, 257 Fuller Road, Albany, New York 12203

Eutectic mixtures of oxygen-containing spirobipyrrolidinium-based ionic liquids were investigated as prospective room temperature ionic liquid electrolytes (RTILs) for supercapacitor application. These in-house developed novel ionic liquids (IL) possess wide voltage window (6-7 V) and solubility (3-5.5 M) in conventional solvents, such as acetonitrile and propylene carbonate. The potential window of *mixed* RTIL was about 5.5 V (at 50 $\mu\text{A}/\text{cm}^2$ threshold). The RTIL mixtures exhibit higher breakdown potential (> 4.6 V) as compared to conventional molecular solvent (acetonitrile)-based cells (~ 4.0 V) in supercapacitor tests. However, these RTIL mixtures (neat, i.e. w/o any solvent addition) lead to high equivalent series resistance (ESR) initiating around 3.9 V and lower capacitance. Cycling of the negative electrode at 4.6 V led to degradation of the active carbon material, while the positive electrode maintained its integrity.

Introduction

Room temperature ionic liquids (RTIL) possess wide potential window and negligible vapor pressure in comparison with conventional molecular solvent-based electrolytes, making them suitable and safe for energy storage (EES) applications such as electric double layer capacitors (EDLC), or supercapacitors, in addition to batteries (1-4).

Energy storage technologies are increasingly gaining importance, especially since the clean energy revolution, i.e. advent of renewables such as wind and solar. The energy storage devices are expected to fill in the gap when the sun does not shine, nor the wind blows, while our energy requirement remains constant. Ideally, energy storage is expected to provide at least 20-30% of standby capacity, thereby enabling sustenance of continuous electricity during the down time for wind and solar.

We have recently developed oxygen-containing spirobipyrrolidinium salts system capable of high voltage window (up to 7 V) and high solubility (5.5 M in some salts) in conventional solvents typically used for energy storage applications. These electrolytes, together with high performance electrodes are capable of enhanced energy and power density. Many of these ionic liquids possess melting point in the range from 15°C up to 243°C. We are interested in developing room temperature ionic liquid electrolytes, mainly in order to reduce the viscosity, thereby enhancing conductivity without any solvent addition.

Several studies have been reported utilizing eutectic mixtures of RTIL as electrolytes for EDLC (5, 6) and we are interested in the combinations of aliphatic cations and BF_4^- anions since they are expected to give wide potential window and high conductivity eutectic mixtures.

In this publication, we report development of eutectic mixtures of two oxygen-containing spirobipyrrrolidinium-based RTILs (7, 8), namely, 2MOP BF_4 (**1**) and 5MOP BF_4 (**2**), demonstrating lowering of melting point, in addition to wider voltage window in comparison with conventionally available salts for supercapacitor application.

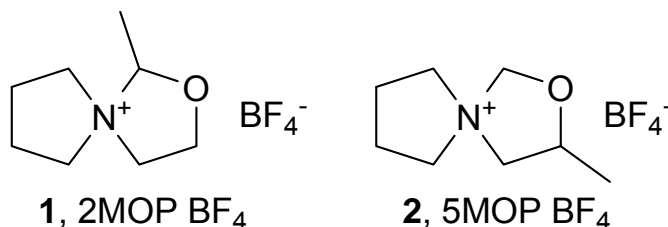


Figure 1: Oxygen-containing spirobipyrrrolidinium IL used in this study.

Experimental section

Materials and methods

RTILs **1** (2MOP BF_4) and **2** (5MOP BF_4) were synthesized and purified by repetitive recrystallization from methanol at $-78\text{ }^\circ\text{C}$ (9). The salts were mixed at specific ratios and dried in vacuo overnight at $90\text{ }^\circ\text{C}$. Moving forward, salts 2MOP BF_4 and 5MOP BF_4 salts will be referred to as **1** and **2**.

GORe™ Electrode Assembly 130 micron (activated carbon layer (100 μm) attached to an aluminum (Al) current collector (30 μm)) and GORe™ Separator 23 micron (PTFE, 23 μm thick, from W. L. Gore) were used for our experiments.

Measurements

Conductivity and viscosity were measured using Radiometer Analytical CDM230 Conductivity Meter and Brookfield DV-II+Pro, respectively, at $25\text{ }^\circ\text{C}$. The melting points were determined using DSC from TA Instruments DSC 2920 differential scanning calorimeter at 1 atm under dynamic N_2 flow, using hermetically sealed aluminum pans, with a ramp rate of $10\text{ }^\circ\text{C}/\text{min}$. Linear sweep voltammetry (LSV) for potential window measurement and bag cell tests were conducted using Princeton Applied Research PARSTAT 2273A potentiostat. LSV was measured using a three-electrode cell with a glassy carbon-working electrode (AFE1E050GC, Pine Research Instrumentation, Grove City, PA, USA), platinum wire counter electrode, and silver wire as a quasi-reference electrode, a scan rate of 5 mV/s from 0 V vs. Ag wire to both positive and negative directions; and the positive and negative limit potentials were determined when the currents exceeded $\pm 50\text{ }\mu\text{A}/\text{cm}^2$ (based on the nominal area of the working electrode, 5 mm^2). Multiple measurements were taken while maintaining the temperature constant at

25°C for each parameter- conductivity, viscosity and potential window. The standard deviation was observed to be within $\pm 1\%$ in each case.

Fabrication and measurement of bag cells

Activated carbon electrodes (2 cm x 2 cm) with extruded Al leads (0.75 cm wide, 3 cm) and PTFE separators (2.5 cm x 2.5 cm) were dried in a vacuum oven at 120 °C for 14 h and transferred to a glove box. Two electrodes and a piece of separator were assembled in a pouch of a metalized blue polymer bag and filled with a mixture of RTIL (~0.5 mL, 0.5 to 0.6 g, warmed in cases of solids) (see figure 2) and then sealed using an impulse heat sealer. The bag cell was subsequently warmed at 70 °C for 24 h for electrolyte impregnation. Prior to testing, the bag cells were clamped under low pressure (<5 lbs) using a C-clamp to reduce the equivalent series resistance (ESR). 8 cycles each of the CV scans were performed between 0 and 1.0, 1.5, 2, 2.5, 3.0, and then 0.1 V step increment up to 4.6 V at a scan rate of 5 mV/s at 30 °C. EIS measurement was performed before and after each voltage increment. The breakdown potential ($Q_{\text{charge}}/Q_{\text{discharge}} - 1$ (Faradaic ratio) > 0.1) was determined following the previous reports (8, 10).

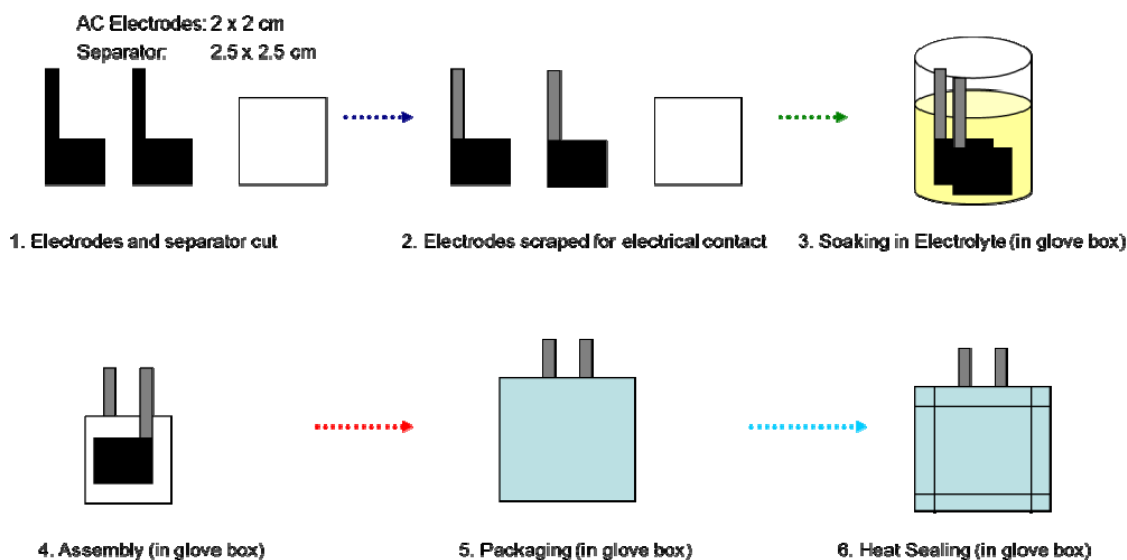


Figure 2: Fabrication of low volume test cell

Results and discussion

The ionic liquids were purified multiple times from MeOH at -80°C (9), prior to measurement. The BF₄ based ILs are difficult to purify and dry owing to their propensity for hydrolysis, which leads to generation of hydrogen fluoride. The acidity of IL mixture was evaluated by mixing the electrolyte with an indicator solution (11), and observing the color. Charge neutrality is indicated by a blue color. Figure 3 shows the effect of purification on the LSV on 2MOP BF₄: 5MOP BF₄ =1:1 mixtures. Purification led to lowering of baseline current thereby widening the potential window by 8-10%.

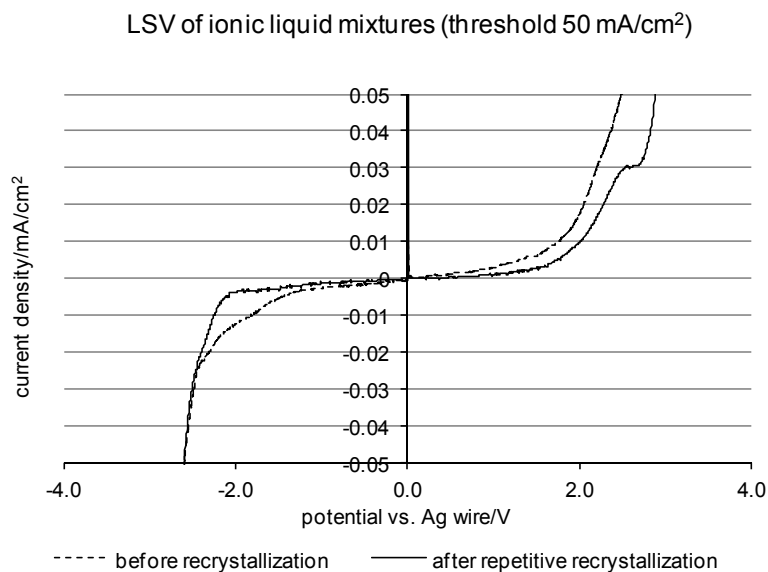


Figure 3: LSV of crude and purified 2MOP BF₄: 5MOP BF₄ in 1:1 ratio

We tested three compositions of eutectic mixtures (at 25°C) in addition to neat ILs, as shown in table 1. Some important properties such as conductivity, viscosity and potential window are also recorded in this table. Lowering of melting point (12 - 25 °C) and viscosity (350 - 395 cP) of eutectic mixtures was observed as compared with the original composition, however, the conductivity (2.0 - 2.2 mS cm⁻¹) was comparable to 2MOPBF₄ at 25°C. The potential windows of mixed IL are about 5.5 V (50 μA/cm² threshold, glassy carbon working electrode, 5 mVs⁻¹ of sweep speed), which is ca. 20% larger than typical commercial workhorse 2M TEABF₄/AN (potential window ca. 4.6 V). There exists an inverse relation between conductivity and viscosity. The eutectic mixtures developed in-house are especially suitable for medium-high temperature (50-100°C) applications such as hybrid electric vehicles, where the supercapacitors are typically used in conjunction with battery or fuel cell, and the temperature often exceeding 60°C (12) Normal supercapacitors operation using conventional electrolytes would compromise their performance due to gas generation at high temperature.

Table 1: Select properties of mixed IL.

2MOP BF ₄ : 5MOP BF ₄ ratio	Melting point/°C	σ /S cm ⁻¹ ^b	η /cP ^c	Negative limit/V ^d	Positive limit/V ^d	Potential window/V
1:0	28	2.031	395.2	<i>a</i>	<i>a</i>	<i>a</i>
3:1	12	2.047	385.5	-2.61	2.88	5.49
1:1	12.	2.201	348.7	-2.60	2.88	5.48
1:3	25	<i>a</i>	<i>a</i>	<i>a</i>	<i>a</i>	<i>a</i>
0:1	56	<i>a</i>	<i>a</i>	<i>a</i>	<i>a</i>	<i>a</i>

^a Solid at the measurement conditions. ^b Conductivity at 25 °C. ^c Viscosity at 25 °C. ^d Threshold at 50 μA/cm².

Next, the eutectic mixtures were evaluated as electrolytes in a bag cell (tested at 30°C) of symmetrical carbon-based EDLC as shown in Figure 3A. Capacitance-voltage

(Figure 3A) cycling was performed until the electrolyte breakdown occurred (> 4.6 V). Eight cycles were performed at each voltage, followed by electrochemical impedance spectroscopy (Figure 3B). The specific cell capacitance was recorded at 3.3 V; maximum specific capacitance, the maximum capacitance, and breakdown potentials, and ESR at 3.0 V and 3.3 V are summarized in Table 2.

Table 2: Test cell results of EDLC using mixed IL at 30 °C.

2MOPBF ₄ : 5MOPBF ₄ ratio	Specific cell capacitance/Fg ⁻¹		Maximum capacitance potential/V	Breakdown potential/V	ESR/ Ωcm^2	
	3.3 V	maximum			3.0 V	3.3 V
1:0	15.85 ± 0.64	16.10 ± 0.99	3.50 ± 0.28	4.36 ± 0.24	7.15 ± 1.82	7.36 ± 1.92
3:1	16.15 ± 1.34	16.20 ± 1.27	3.35 ± 0.07	4.46 ± 0.04	4.68 ± 0.09	4.91 ± 0.23
1:1	14.43 ± 0.12	14.57 ± 0.31	3.13 ± 0.15	4.31 ± 0.26	6.02 ± 0.81	6.37 ± 1.06
1:3	14.25 ± 0.21	14.30 ± 0.28	3.40 ± 0.14	4.28 ± 0.05	20.24 ± 12.73	21.45 ± 14.49

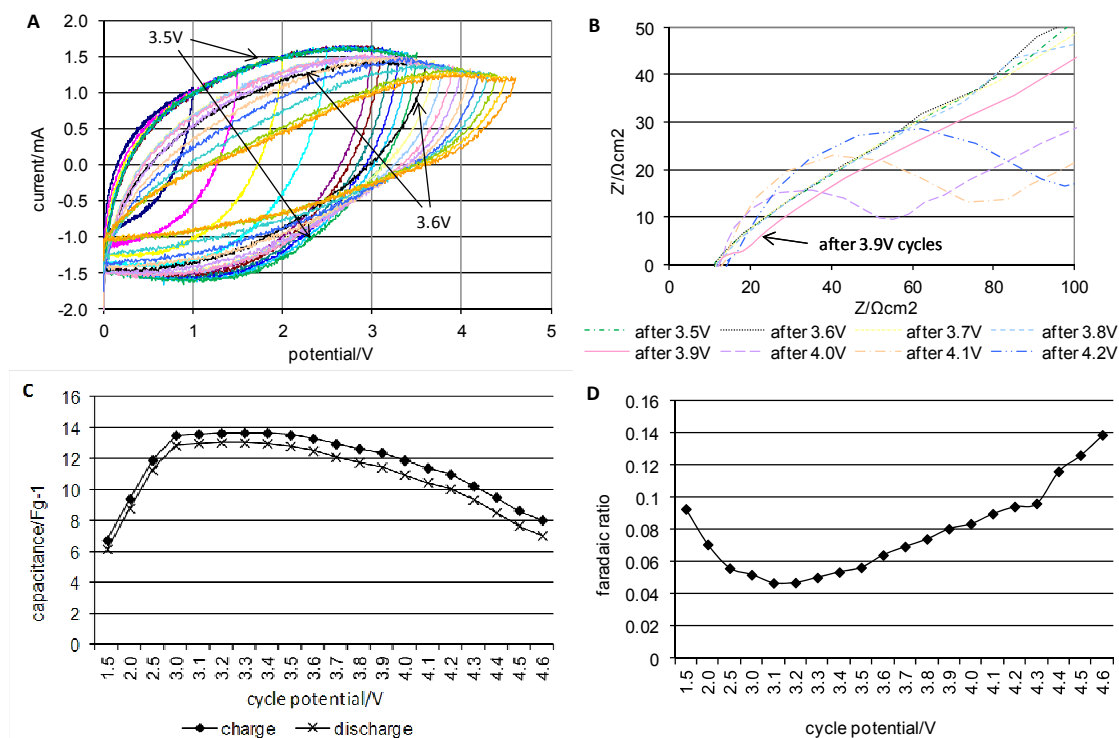


Figure 3: (A) series of representative cyclic voltammograms of each of 8th cycle in each voltage step (A) and selected Nyquist plots after each of the voltage cycle (B) of a test cell using 2MOP BF₄:5MOP BF₄ in 1:3 ratios (C) charge and discharge capacitance vs. cell potential at 30°C for 2MOPBF₄:5MOPBF₄ in 1:3 ratio (D) Faradaic Ratio vs. cycle potential indicating stability up to 4.3 V.

Higher breakdown potential (4.3-4.5 V) was observed in case of eutectic mixtures as compared to conventional molecular solvent (acetonitrile)-based cells (~ 4.0 V) (8). However, these eutectic mixtures had higher equivalent series resistance (ESR) and lower capacitance, probably due to much larger viscosity. Further increase in ESR became prominent around 3.9 V with hemispherical feature in the Nyquist plot (Figure 3B, solid line). The deformation and flattening of CV spectrum occurred after the 3.5 V cycles

(Figure 3A) and further flattened after 4.0 V cycles that corresponds to the hemispherical feature in the Nyquist plot. The increase in ESR most probably arises from poor contact between the active electrode materials and the current collectors, in addition to near solid-liquid temperature limit at operating temperature of 30°C.

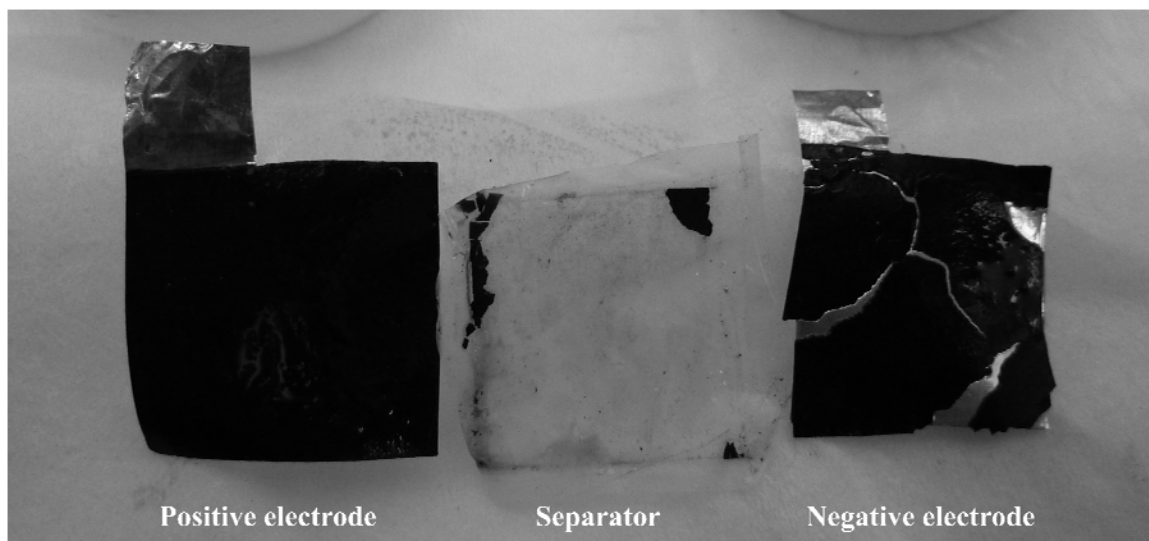


Figure 4: Capacitor assembly after CV cycle test.

Figure 4 shows the electrodes post CV cycling. The active material was seen to easily delaminate from the current collector after measurements. This could either be due to much larger cation size in comparison with anion, embrittlement leading to loss of flexibility, and near solid state of electrolyte near operating temperature.

Conclusions

Purification of RTIL by repetitive recrystallization is important to achieve wider potential window. EDLC test cells with RTIL mixtures exhibit 20% higher breakdown potential (> 4.6 V) as compared to conventional molecular solvent (acetonitrile)-based cells (~ 4.0 V), though with much larger ESR and low capacitance owing to low conductivity, and borderline solid-liquid state.

Further increase in ESR was found to initiate at around 3.9 V, upon embrittlement of the negative electrode leading to delamination of carbon material from the aluminum current collector.

The results show feasibility of using eutectic mixtures of IL for high energy density EDLC applications. Significant improvement in conductivity of eutectic mixtures can be achieved with higher operating temperature, ensuring liquid state of electrolyte, and with better quality of electrode material, particularly negative electrode and electrode-current collector interface.

Recently, carefully textured high-purity electrode materials allow improved rate properties even with RTIL (4, 6, 13) and attempts of current collector-less electrodes for high performance EDLC (14, 15). Therefore, combinations of such advanced electrodes and eutectic mixtures of RTIL will open up new field for high performance EDLC.

Acknowledgements

We are grateful to Professor John T. Welch of University at Albany for his generous support to our project. We are appreciative of W. L. Gore & Associates, Inc. for supplying high performance electrodes.

References

1. D. O. E. Office of Basic Energy Sciences, the United State of America, *Basic Research Needs for Electrical Energy Storage* (2007).
2. A. Lewandowski and M. Galinski, *J. Power Sources*, **173** 822 (2007).
3. P. Simon and Y. Gogotsi, *Nat. Mater.*, **7**, 845 (2008).
4. Y. Zhu, S. Murali, M. D. Stoller, K. J. Ganesh, W. Cai, P. J. Ferreira, A. Pirkle, R. M. Wallace, K. A. Cychosz, M. Thommes, D. Su, E. A. Stach and R. S. Ruoff, *Science*, **332**, 1537 (2011).
5. T. D. J. Dunstan and J. Caja, *ECS Trans.*, **3**, 21 (2007).
6. R. Lin, P.-L. Taberna, S. Fantini, V. Presser, C. R. Pérez, F. Malbosc, N. L. Rupesinghe, K. B. K. Teo, Y. Gogotsi and P. Simon, *J. Phys. Chem. Lett.*, **2**, 2396 (2011).
7. S. Higashiya, A. S. Filatov, C. C. Wells, M. V. Rane-Fondacaro and P. Haldar, *J. Mol. Struct.*, **984**, 300 (2010).
8. T. Devarajan, S. Higashiya, C. Dangler, M. V. Rane-Fondacaro, J. Snyder and P. Haldar, *Electrochem. Commun.*, **11**, 680 (2009).
9. S. Higashiya, T. S. Devarajan, M. V. Rane-Fondacaro, C. Dangler, J. Snyder and P. Haldar, *Helv. Chim. Acta*, **92**, 1600 (2009).
10. K. Xu, S. P. Ding and T. R. Jow, *J. Electrochem. Soc.*, **146**, 4172 (1999).
11. G. A. Baker and S. N. Baker, *Aust. J. Chem.*, **58**, 174 (2005).
12. A. Balducci, R. Dugas, P.L. Taberna, P. Simon, D. Pl'ee, M. Mastragostino, S. Passerini, *J. Power Sources* **165** 922 (2007).
13. W. Lu, L. Qu, K. Henry and L. Dai, *J. Power Sources*, **189**, 1270 (2009).
14. S. Biswas and L. T. Drzal, *ACS Appl. Mater. Interfaces*, **2**, 2293 (2010).
15. A. Izadi-Najafabadi, S. Yasuda, K. Kobashi, T. Yamada, D. N. Futaba, H. Hatori, M. Yumura, S. Iijima and K. Hata, *Adv. Mater.*, **22**, E235 (2010).

Evaluation of Anode Electrode Materials for Cu-Cl/HCl Electrolyzers for Hydrogen Production

Santhanam Ranganathan, Patrick S. R. Edge, E. Bradley Easton*

Faculty of Science (Chemistry), University of Ontario Institute of Technology, Oshawa,
ON Canada L1H 7K4

Ceramic carbon electrodes (CCE) containing poly aminopropyl siloxane (PAPS) were fabricated by the sol-gel method. These CCEs have previously been shown to exhibit high performance towards the anode reaction of the electrolytic process used in the Cu-Cl thermochemical cycle for hydrogen production, with optimal performance being achieved at 36 wt% PAPS. Using cyclic voltammetry, electrochemical impedance spectroscopy, and scanning electron microscopy, the peak performance at 36 wt% PAPS was explained in terms of the optimization of carbon surface area, anionic transport and electronic conductivity. In addition, we also demonstrated the electrolysis performance in the full cell.

Introduction

Hydrogen-based technologies have been touted as a potential solution to the problem of climate change. One of the key challenges associated with the use of hydrogen as a clean energy carrier is the lack of sustainable, low-cost method of producing it in large capacities. Hydrogen is mainly manufactured by reforming fossil fuels. Hence there is a need to develop alternative methods for large scale hydrogen production that does not contribute to greenhouse gas emissions.

The most suitable “carbon free” source of hydrogen would be water, which can be split into hydrogen (and oxygen) in various ways. One such method is the electrolysis of water. While low temperature electrolysis does produce high purity hydrogen, it is energy intensive. Thus, low temperature electrolysis has been limited to smaller distributed applications.

Another promising method to produce hydrogen from water is to employ a thermochemical cycle. A thermochemical cycle consists of a closed loop of chemical reactions that lead to the decomposition of water into hydrogen and oxygen where all of the reagents used in the cycles are regenerated (1). Some thermochemical cycles may employ an electrochemical reaction, in which case these cycles are referred to as hybrid cycles. Numerous thermochemical cycles have been proposed and analyzed for their suitability based on reaction kinetics, thermodynamics, material stability and cost. Prominent cycles include the sulfur-iodine (S-I) (1), hybrid-sulfur (HyS) (2,3) and copper-chloride (Cu-Cl) (4) cycles. Cycles are most appealing if their temperature requirements are a close match to a source of waste heat, such as a nuclear reactor. However, all cycles have design challenges and are still at laboratory scale.

The Cu-Cl thermochemical cycle is a promising cycle that is of great interest to Canadian researchers due the proximity of its temperature requirement (ca. 550 °C) with

* Corresponding author, Email: brad.easton@uoit.ca

the operating temperature of Canada's Generation IV Super Critical Water-cooled Reactor (SCWR) (5,6). The reactions in the Cu-Cl cycle are shown in the Figure 1. The Cu-Cl cycle is a hybrid cycle, employing an electrochemical reaction. A schematic diagram of the electrolysis cell is shown in Figure 2. A proton exchange membrane (PEM) is employed as the electrolyte, which also separates the anode and cathode compartments. The anolyte is composed of CuCl dissolved in HCl, which is oxidized to CuCl₂. Protons travel through the PEM where they are electrochemically converted to H₂ via the hydrogen evolution reaction (HER). The catholyte normally contains HCl (aq). A minimum of 0.4V is required to drive this reaction, which is substantially lower than that required for the electrolysis of water. The US Department of Energy target for this cell is to operate at or below 0.7V at a current density of 500 mA/cm² (7).

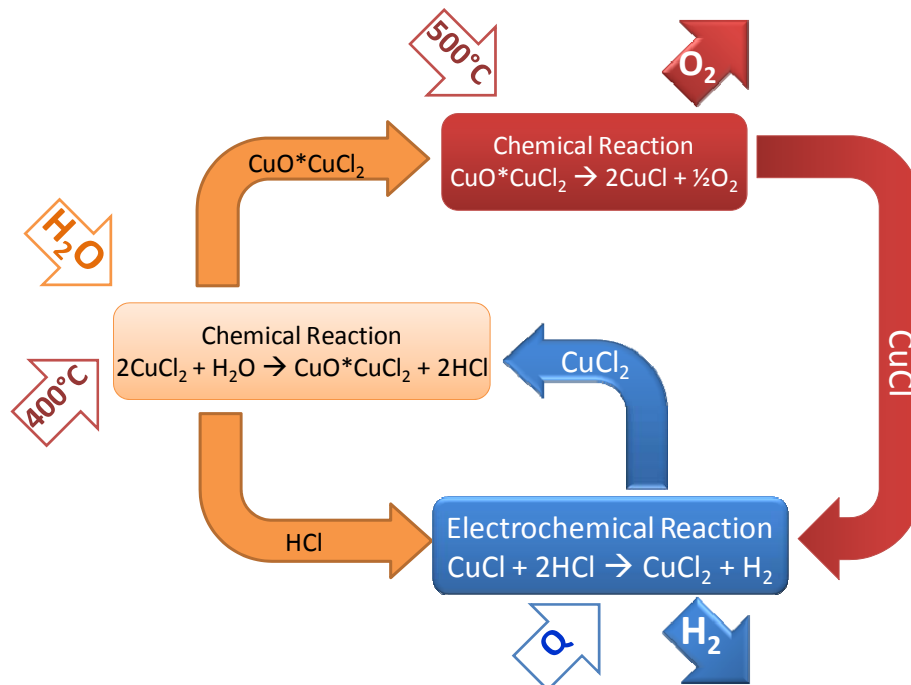


Figure 1: The reactions in the Cu-Cl thermochemical cycle

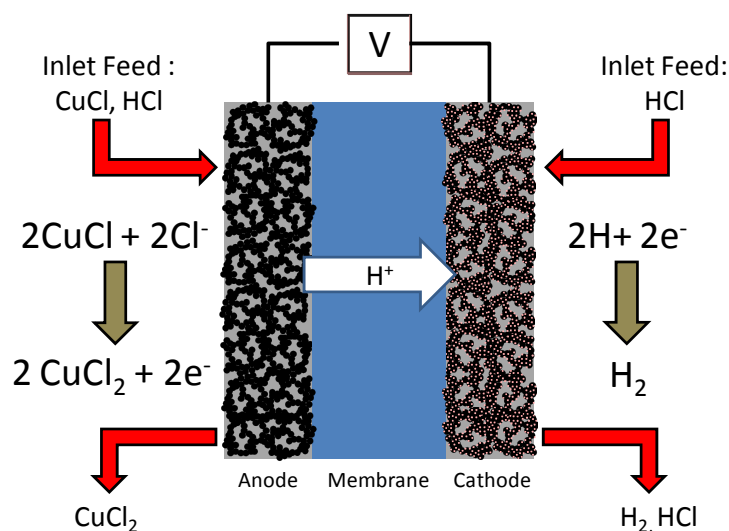


Figure 2: Schematic diagram of the electrolysis cell used in the Cu-Cl thermochemical cycle.

One way to move towards this target is to increase the performance of the anode. Under normal operating conditions, the anode reaction kinetics are partially under mass transfer control (8,9), which will limit the performance of the cell. Our previous work has shown that area-specific activity of Pt towards the anode reaction is approximately three-fold larger than that of carbon (5). However, we would not expect this translate into higher performance due to the fact that most carbon black materials have much higher specific surface areas than Pt. Electrolysis cell performance data reported by Atomic Energy of Canada Limited confirms that there is no performance gain when Pt is added to the anode (5).

Thus, there is a need to develop porous carbon electrodes structures with high surface areas so that higher current densities can be achieved. In addition, such a structure should also be able to promote the transport of Cu(I) species to the carbon surface. Ion transport properties of electrode structures can often be enhanced with the addition of an ionomer binder. For example, proton transport in fuel cell catalyst layers can be enhanced with the addition of Nafion (10,11). In chloride containing solutions, soluble Cu(I) species mainly exist as anionic species such CuCl_2^- , CuCl_3^{2-} . Furthermore, the prevalence of anionic Cu(I) species increases at high concentrations of chloride (12). Thus, the ionomer required for the Cu-Cl anode must aid in the transport of anionic species.

One emerging class of porous electrode structures is ceramic carbon electrodes (CCE). CCEs consist of electronically conductive carbon particles that are bound together by a ceramic binder formed through the sol-gel process (13). CCEs are promising candidates for numerous applications, including fuel cells (14-16), sensors, lithium ion batteries, and super capacitors (17,18). Synthesis parameters (pH, solvent, concentration) can be varied in order to manipulate a variety of electrode properties. We have developed a CCE fabrication procedure where the organosilane precursors are mixed with the (catalyzed or un-catalyzed) carbon in monomer form (prior to any gelation), and subsequently polymerized (16). This coupled with the organosilane's ability to chemically bond to the carbon surface, leads to a highly uniform distribution of ionomer throughout the porous catalyst layer.

The electrolysis cell is quite similar to a PEM water electrolyzer/fuel cell and often these cell components are adapted for this process (6,19). However, since these cells were never designed for this application, the materials are not necessarily ideally suited to this electrolyzer. One major issue is the phenomenon of copper-cross-over, where cationic or neutral Cu species from the anolyte can permeate through the membrane and enter the cathode compartment, where they are reduced to metallic copper. Metallic copper at the cathode acts as a poison, greatly reducing the activity of the Pt catalyst towards the hydrogen evolution reaction.

Work in our lab has focused on the development of better performing MEA materials, with a primary concentration on anode electrode materials. As listed above, the electrode materials must have a high specific surface area and an ability to transport the reagents to the surface of the electrode. In this case, the reagents are actually anionic Cu(I) species. Thus, any ionomer added to the anode catalyst layer must aid in the transport of anionic species.

We have recently reported a new ceramic carbon electrodes (CCE) structure based on poly aminopropyl siloxane (PAPS) that vastly outperformed a traditional carbon fiber paper (CFP) electrode (20). The superior electrode performance was attributed to the CCE's higher carbon surface area and greatly enhanced transport of anionic Cu(I) species. Subsequent studies have shown that the CCE performance advantage is retained

at higher concentrations of CuCl and HCl that closely mimic the targeted cell operating conditions (21).

Here we present a study on the impact of PAPS loading on electrode morphology and its relation to electrochemical behavior in the absence of CuCl. The absence of a Faradaic process allows for diagnostic electrochemical measurements that enable the relationship between PAPS loading and the electrochemical surface area and ionic resistance to be more clearly evaluated. In addition, we also demonstrate the strong performance of the PAPS-based anodes in a full electrolysis cell.

Experimental

Ceramic Carbon Electrode Preparation

A detailed procedure for the synthesis of PAPS-based CCE catalyst layers is reported elsewhere (20). Briefly, a CCE gel was prepared Vulcan XC72 carbon black (Cabot) and 3-aminopropyl trimethoxy silane (Sigma-Aldrich). The reaction was base catalyzed in a mixture of water and methanol. Electrodes were prepared by coating the wet gel onto a 1 cm² region of a strip of carbon fibre paper (CFP, TPGH-090, BASF). The total loading of CCE materials deposited was 3 mg/cm² in all cases.

Electrochemical Measurements

Half-cell electrochemical experiments were performed in a three-electrode cell using a platinum wire counter electrode and a saturated calomel electrode (SCE) served as the reference electrode. The potential of the SCE was calibrated vs. the reversible hydrogen electrode (RHE). All data presented in this work were corrected to the RHE potential. Measurements were made at room temperature in nitrogen purged 1.5 M HCl.

Electrochemical measurements were acquired using a Solartron 1470E Multichannel potentiostat and a 1260 frequency response analyzer, controlled using Multistat software (Scribner Associates). All cyclic voltammograms were recorded at a sweep rate of 50 mV/s. Impedance spectra were collected over a frequency range of 100 kHz to 0.1Hz at a DC bias potential of 0.0 V vs. the open circuit potential.

Membrane and electrode assemblies (MEA) were prepared full electrolysis cell testing by measurements were made by hot-pressing (150 kg cm⁻² for 90s at 130 °C) a 5-cm² test electrode (anode) and a similar sized commercial cathode (ELAT A6STDIV2.1 Pt loading = 0.50 mg cm⁻², proprietary ionomer loading) across a Nafion 115 membrane. MEAs were tested in a 5-cm² fuel cell test fixture (ElectroChem Inc.) at room temperature. The anolyte used consisted of 0.2 M CuCl in 2 M while the catholyte was pure water. The cell was fed using with a dual-channel peristaltic pump (Masterflex L/S Digital Drive Pump: RK-07523-80 and Easyload 3 Pump Heads: RK-77800-52) that supplied the anolyte and catholyte at a flow rate of 60 mL/min. Prior to measurement, HCl (2M, N₂-purged) was circulated through both sides of the cell to ensure there was no air remaining in the cell.

Materials Characterization

Thermogravimetric analysis (TGA) was performed using a TA Instruments Q600 SDT thermal analyzer. Samples (ca. 10 mg) were heated from room temperature to 1000°C at a rate of 20°C/min under flowing air (50 mL/min).

High-resolution images of the catalyst layers were taken using a Zeiss NVision dual beam Focused Ion Beam/Field Emission Gun scanning electron microscope (SEM).

Results and Discussion

Physical Characterization of CCE Layers

Three CCE catalysts layers were prepared with PAPS loadings of 22, 36 and 56 wt%, as determined by TGA. Figure 3 shows the SEM images obtained for each of the CCE catalysts layers. All CCE layers displayed a homogeneous distribution of carbon and PAPS, with little evidence of agglomeration of PAPS. This is one of the advantages of our CCE fabrication method that combines the carbon black with the organosilane monomer before it is polymerized. However, it can clearly be seen that the porosity of the CCE layer containing 22 wt% PAPS is significantly smaller than the others, and also contained larger particles. Thus we would expect this CCE to have a larger surface area of carbon that could participate in the electrochemical reaction.

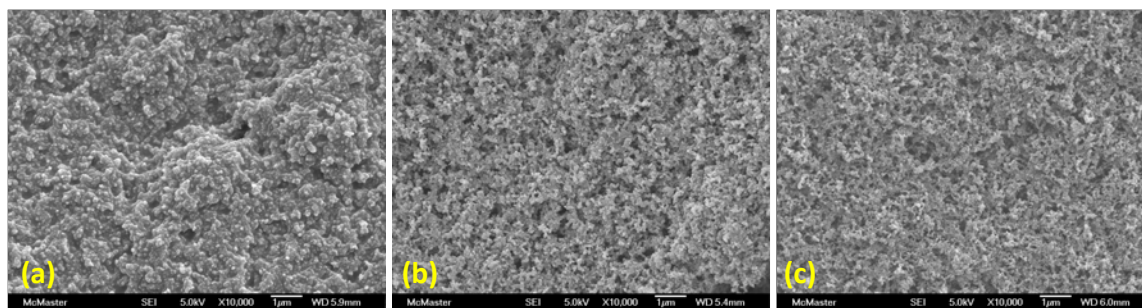


Figure 3: SEM images for CCE catalyst layers containing (a) 22 wt% (b) 36 wt% and (c) 56 wt% PAPS.

Electrochemical Characterization

Figure 4 compares the CVs obtained for each CCE layer. No redox waves were expected nor observed. In all cases, the classical capacitive curves of carbon were obtained. However, the magnitude of the capacitance varied with PAPS loading, which are listed in Table 1. Maximum capacitance was achieved at 36 wt% PAPS. Since double-layer capacitance is generally proportional to surface area (22), we can reasonably conclude that this also corresponds to maximum electrochemical surface area of carbon.

While CV experiments can provide information about the electrochemical surface area, they provide little information about conductivity within the CCE catalysts layers. Thus, EIS experiments were performed. Nyquist plots obtained for these CCE catalyst layers are shown in Figure 5(a). From these plots, it is clear that the CCE that contained 56 wt% PAPS is the most resistive. There are two main sources of resistance in the CCE layer: ionic and electronic. Since PAPS is an ion conductor and its loading is high, it is fair to ascribe this to increased electronic resistance. Increased electronic resistance at high loadings of silicate material in CCEs have been previously observed for SiO_2 -based CCEs (16). The resistances obtained for 22% and 36% PAPS appear to be similar, with the former appearing to have a slightly lower resistance.

Variation in conductivity and active area can be better visualized using capacitance plots (23), which are shown in Figure 5(b). Capacitance plots are advantageous since they allow conductivity within the catalyst layer and active area to be simultaneously visualized (24,25). The steepness of the slope in the high frequency region of the capacitance plot is indicative of the conductivity within catalyst layer (steep slope indicates higher conductivity) and the limiting capacitance is proportional to active

area (26). Thus, a higher limiting capacitance means that a larger fraction of the catalyst layer is being utilized. These plots clearly show that maximum active area is achieved when the PAPS loading is 36%, which agrees with our CV results.

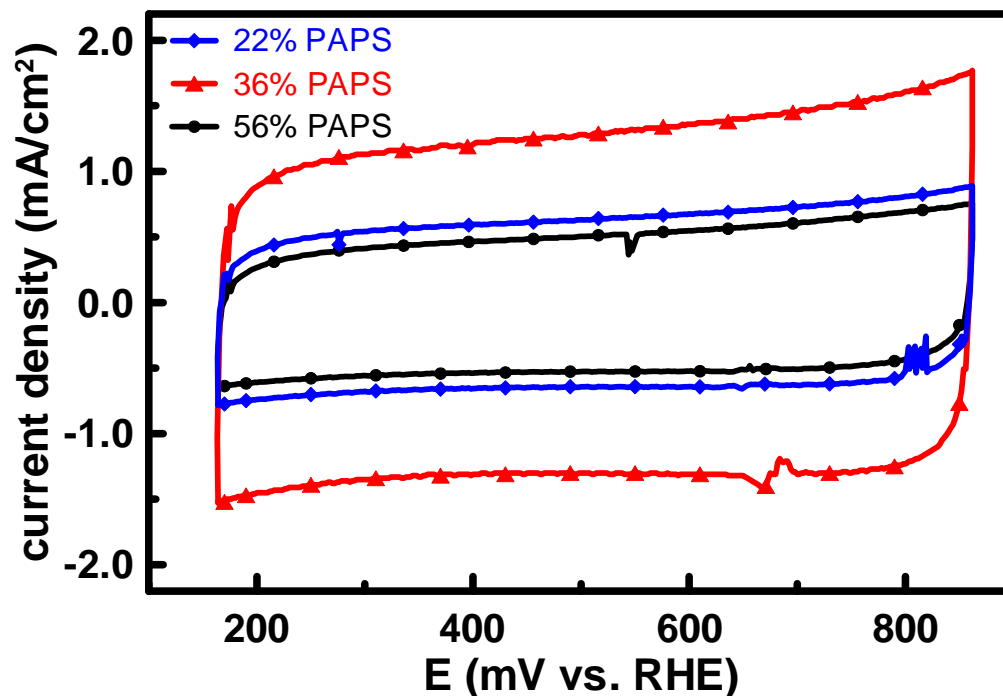


Figure 4: CV's obtained for CCEs with different PAPS loadings. Measurements were made at a sweep rate of 50 mV/s in N_2 -purged 1.5 M HCl at 25°C.

While the total loading of CCE material was kept constant throughout our experiments (at 3 mg/cm²), increasing the PAPS loading does lead to a decrease in amount of carbon in each catalyst layer. In order to account for this difference, mass-specific capacitance plots were constructed and are shown in Figure 5(c). When the mass of carbon in each CCE layer is accounted for, it becomes even more evident that 36 wt% is optimal. The limiting capacitance values obtained for 36% PAPS was approximately 44% larger than that obtained for 22 wt% PAPS (31.3 vs. 21.8 mF/cm²). When we calculate these values on a mass-specific basis, limiting capacitance values obtained for 36% PAPS was approximately 79% larger than that obtained for 22 wt% PAPS. Based on the SEM analysis, we can infer that when the PAPS loading is increased from 22% to 36%, catalyst layer porosity increases, leading to an increase in the electrochemically active carbon surface area. In addition, the increased PAPS loading also promoted better anion transport within the catalyst layer. However, close examination of the EIS data reveals that this increase in PAPS loading does lead to a slight increase in resistance, which must be due to increased electronic resistance. Further increasing the PAPS loading to 56% resulted in a substantial decrease in the active surface area of carbon, despite the high porosity of the electrode structure (as shown in Figure 3). This is likely due to PAPS covering/blocking the surface of carbon as well as drastically increasing the electronic resistance within the catalyst layer.

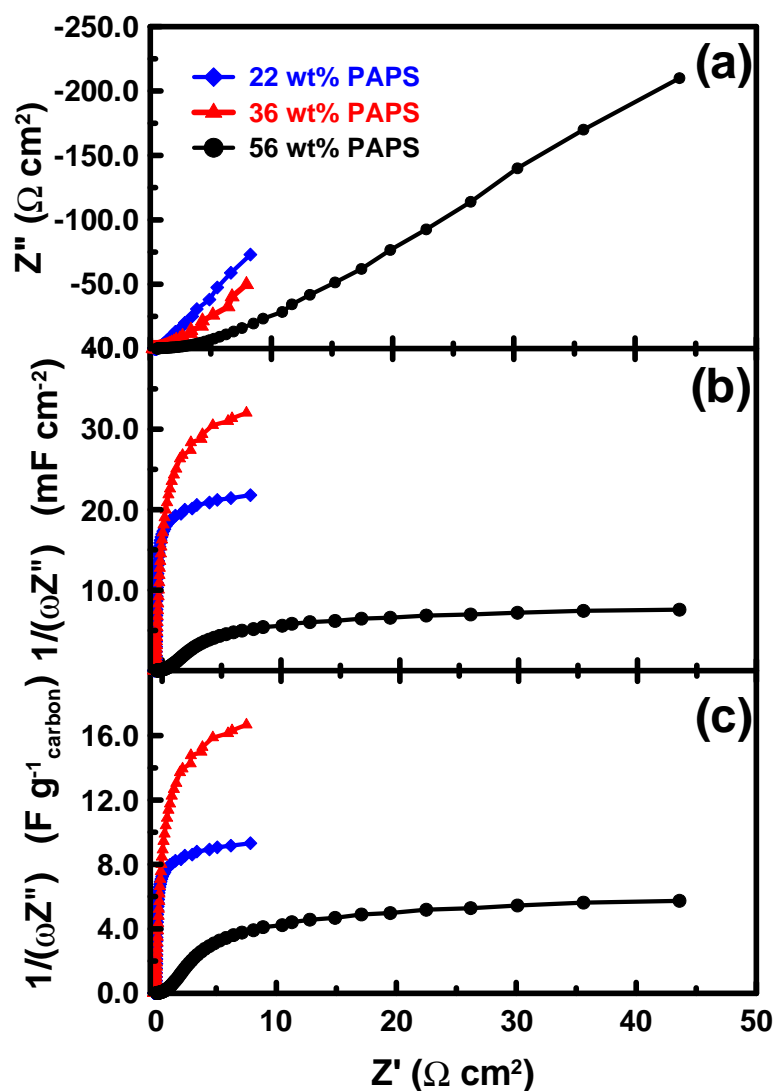


Figure 5: Comparison of the EIS responses obtained for CCEs with different PAPS loadings plotted as (a) Nyquist plots (b) Capacitance plots and (c) mass-normalized capacitance plots. Measurements were made in N_2 -purged 1.5 M HCl at 25°C .

wt% PAPS	Capacitance ^a (mF/cm^2)	Capacitance ^a (F/g of C)	Capacitance ^b (mF/cm^2)	Capacitance ^b (F/g of C)
22	12.66	5.41	21.8	9.32
36	25.71	13.39	31.34	16.68
56	10.15	7.69	7.579	5.74

^a determined by CV

^b determined by EIS

Table 1: Electrode capacitance values for CCEs with different PAPS loading.

Full Cell Tests

With the ideal loading of PAPS determined from half-cell experiments, an MEA at the optimal for electrolysis cell testing was constructed in order to demonstrate its full cell performance, which is shown in Figure 4. Overall the electrolysis cell demonstrated good performance that is on par with the data reported by Lvov's group for HYDRion115 MEAs (19). The variation in full cell performance with PAPS composition and further optimization of full cell conditions will be reported in the near future.

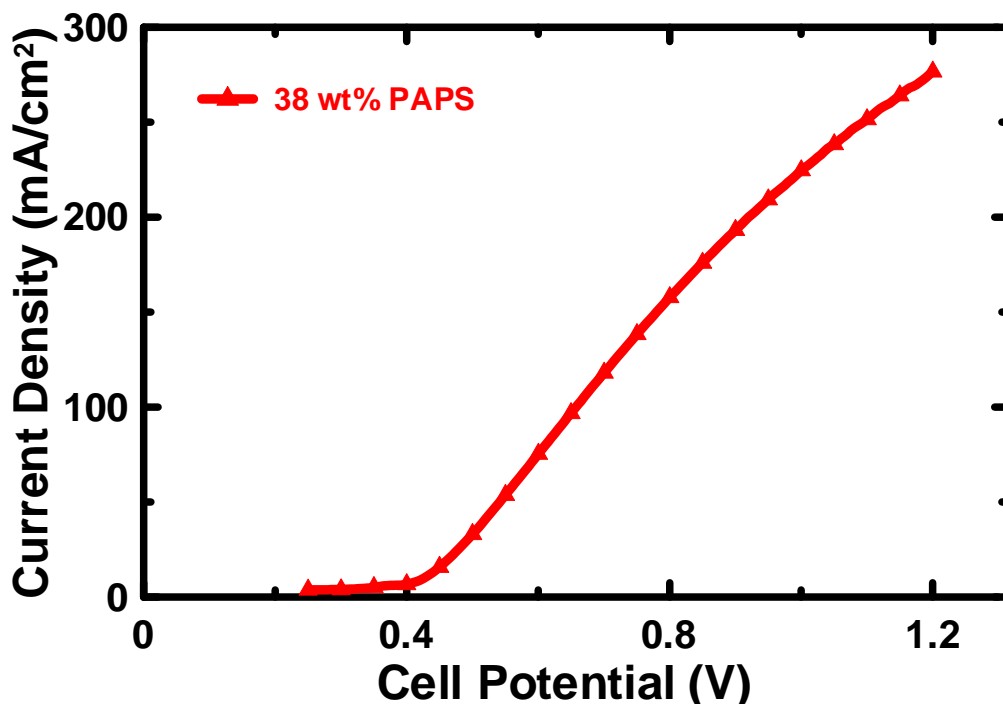


Figure 6: Fuel Cell polarization curve for the electrolysis of CuCl/HCl solution using a PAPS-based anode containing 38 wt% PAPS. Measurements were made at 25 °C with 0.2M CuCl in 2M HCl flowing at the anode, and pure water flowing at the cathode.

Conclusions

The morphology and electrochemical behaviour of PAPS-based CCEs have been evaluated. CV and EIS measurements provide clear evidence that 36 wt% PAPS gives the optimal combination of electrochemically active surface area, anionic and electronic conductivity. This is responsible for its high anodic performance in the CuCl/HCl electrolysis cell. Lower loadings of PAPS resulted in less porous electrode structures with lower electrochemically active surface areas. High PAPS loadings lead to catalyst layers with low carbon surface areas and high electronic resistance. Together, these results explain the origin of the variation of anodic performance in the electrochemical step of the Cu-Cl thermochemical cycle with PAPS loading within the CCE.

Acknowledgements

This work was supported by the Ontario Research Fund (ORF), Atomic Energy Canada Ltd. (AECL), the Natural Sciences and Engineering Research Council of Canada (NSERC) and UOIT. We also thank Dr. G. de Silveira (Canadian Centre for Electron Microscopy, McMaster University) for her assistance with measurements, and Lorne Stolberg (AECL) and Greg Naterer (UOIT) for useful discussions.

References

1. L. C. Brown, J. E. Funk, and S. K. Showalter. High efficiency generation of hydrogen fuels using nuclear power. **Report GA-A23451** (2000).
- Ref Type: Report
2. J. A. Staser, K. Norman, C. H. Fujimoto, M. A. Hickner, and J. W. Weidner, *J. Electrochem. Soc.*, **156**, B842 (2009).
3. J. A. Staser, M. B. Gorenssek, and J. W. Weidner, *J. Electrochem. Soc.*, **157**, B952 (2010).
4. M. Dokiya and Y. Kotera, *Int. J. Hydrogen Energy*, **1**, 117 (1976).
5. G. Naterer, S. Suppiah, M. Lewis, K. Gabriel, I. Dincer, M. A. Rosen, M. Fowler, G. Rizvi, E. B. Easton, B. M. Ikeda, M. H. Kaye, L. Lu, I. Pioro, P. Spekkens, P. Tremaine, J. Mostaghimi, J. Avsec, and J. Jiang, *Int. J. Hydrogen Energy*, **34**, 2901 (2009).
6. G. F. Naterer, S. Suppiah, L. Stolberg, M. Lewis, Z. Wang, V. Daggupati, K. Gabriel, I. Dincer, M. A. Rosen, P. Spekkens, S. N. Lvov, M. Fowler, P. Tremaine, J. Mostaghimi, E. B. Easton, L. Trevani, G. Rizvi, B. M. Ikeda, M. H. Kaye, L. Lu, I. Pioro, W. R. Smith, E. Secnik, J. Jiang, and J. Avsec, *Int. J. Hydrogen Energy*, **35**, 10905 (2010).
7. M. A. Lewis. R&D Status for the Cu-Cl Thermochemical Cycle. US Department of Energy FY2009 Progress Report. 392 (2004).
- Ref Type: Generic
8. L. Stolberg, H. Boniface, S. Suppiah, and S. York, in *Proceedings of the International Conference on Hydrogen Production*, Naterer, G. and Dincer, I., Editors, p167, Oshawa, ON, Canada (2009).
- File Location:** R:\references\PDF FILES\21000 CuCl\21016.pdf
9. L. Stolberg, H. A. Boniface, S. McMahon, S. Suppiah, and S. York, in *2008 4th International Topical Meeting on High Temperature Reactor Technology, HTR 2008*, Editors, p491, Washington, DC (2009).
- File Location:** R:\references\PDF FILES\21000 CuCl\21039.pdf
10. E. Passalacqua, F. Lufrano, G. Squadrito, A. Patti, and L. Giorgi, *Electrochim. Acta*, **46**, 799 (2001).
11. E. Antolini, *J. Appl. Electrochem.*, **34**, 563 (2004).
12. L. Trevani, J. Ehlerova, J. Sedlbauer, and P. R. Tremaine, *Int. J. Hydrogen Energy*, **35**, 4893 (2009).
13. M. TSIONSKY, G. GUN, V. Glezer, and O. LEV, *Anal. Chem.*, **66**, 1747 (1994).
14. J. I. Eastcott, K. M. Yarrow, A. W. Pedersen, and E. B. Easton, *J. Power Sources*, **197**, 102 (2012).
15. J. I. Eastcott, J. A. Powell, A. J. Vreugdenhil, and E. B. Easton, *ECS Transactions*, **41**, 853 (2011).
16. J. I. Eastcott and E. B. Easton, *Electrochim. Acta*, **54**, 3460 (2009).

17. L. Rabinovich and O. LEV, *Electroanalysis*, **13**, 265 (2001).
18. O. LEV, Z. Wu, S. Bharathi, V. Glezer, A. Modestov, J. Gun, L. Rabinovich, and S. Sampath, *Chem. Mater.*, **9**, 2354 (1997).
19. V. N. Balashov, R. S. Schatz, E. Chalkova, N. N. Akinfiev, M. V. Fedkin, and S. N. Lvov, *J. Electrochem. Soc.*, **158**, B266 (2011).
20. S. Ranganathan and E. B. Easton, *Int. J. Hydrogen Energy*, **35**, 4871 (2010).
21. S. Ranganathan and E. B. Easton, *Int. J. Hydrogen Energy*, **35**, 1001 (2010).
22. A. G. Pandolfo and A. F. Hollenkamp, *J. Power Sources*, **157**, 11 (2006).
23. X. M. Ren and P. G. Pickup, *Electrochim. Acta*, **46**, 4177 (2001).
24. G. C. Li and P. G. Pickup, *J. Electrochem. Soc.*, **150**, C745 (2003).
25. N. Y. Jia, R. B. Martin, Z. G. Qi, M. C. Lefebvre, and P. G. Pickup, *Electrochim. Acta*, **46**, 2863 (2001).
26. E. B. Easton and P. G. Pickup, *Electrochim. Acta*, **50**, 2469 (2005).

Very Low Impedance Battery Architecture for Electrified Vehicles

Thomas Kaun and Joel Sandahl

InvenTek Corporation,
320 Willow Street, New Lenox, IL 60451 USA

Rolled-Ribbon is design and manufacturing method for battery cells that incorporates features of very short path length to bring current flow as well as heat from the cell and battery. Disc-shaped cells can be stacked to form a dense and efficient battery architecture for electrified vehicles. Relative to competing architectures, Rolled-Ribbon combines the low-cost winding and dimensional stability of the cylindrical format with fully-tabbed, very short electrodes of a prismatic (that is replicated by winding). The very short electrode of the cells and the quasi-bipolar arrangement approximately lower cell structural impedance (ACIR) by 50% and DC-pulse impedance by 25% for Li-ion battery. As such, Rolled-Ribbon overcomes the power/energy tradeoffs faced by competing architectures. Specific energy is increased with larger cells and high power is maintained.

Rolled-RibbonTM Battery Technology

Broad adoption of EV (electric vehicles) is being held back by excessive cost of Li-ion batteries and excessive volume and weight to limit vehicle size and range. Adoption of Rolled-Ribbon battery architecture poses a cost-effective alternative to the cylindrical cell and “pouch/prismatic” battery with competitive advantages for safety, durability and sustainability. InvenTek’s proprietary (1) Rolled-Ribbon battery architecture promotes the volume efficiency and thermal management efficiency to operate safely at significantly (almost double) higher energy densities than state-of-art battery systems. Rolled-Ribbon (R-R) is particularly beneficial for the production of large-format cells (6-30 Ah capacity) for high power density. R-R battery packs with larger 30 Ah capacity cells display high energy density about double that of pouch/prismatic for EV.

The R-R cell technology (2) uses long, narrow electrodes with interwoven separator to fabricate large, disk-shaped cells. A typical cell might be 13mm in height by 125mm in diameter. The wound configuration is housed within a sealed, disc-shaped enclosure, where the entire faces of the housing, top and bottom cell terminals, make distributed pressure contact with the narrow electrode ribbons. The Rolled-Ribbon architecture eliminates the welded current collectors present in cylindrical and prismatic type cells, which increase cell resistance, robbing power from the cell and generating damaging heat. It enables efficient high power delivery. Further, the narrow electrodes are efficient in thermally conducting heat to the large diameter top and bottom housing covers, Figure 2. This results in uniform internal temperature distribution that can enable longer cell life in power applications, typical of hybrid and electric vehicles. An independent modeling of cell thermal properties at NREL (3) confirms that a disc-shaped, pancake cell affords the best heat dissipation to eliminate hotspots. The Rolled-Ribbon design is favored in a modeling trade-off study on electrical and thermal performance of various cylindrical cell designs. From FY 2008 DOE Progress Report Energy Storage Research and Development David Howell, January 2009, opposing terminal designs is favored over same-side terminal designs by promoting more uniform active material

usage. The R-R design replicates a very short ideal cell element in a roll-to-roll fabrication. Likewise, reducing electronic path length reduces heat generation, and increases power. As can be seen, electrical current and thermal heat travel the relatively short vertical distances across the narrow Rolled-Ribbon electrodes to the cell terminals. By contrast in the cylindrical format Figure 3, current collects along the length of the electrode. Without a ready path for internal heat dissipation, heat builds up at the core of the cylinder.

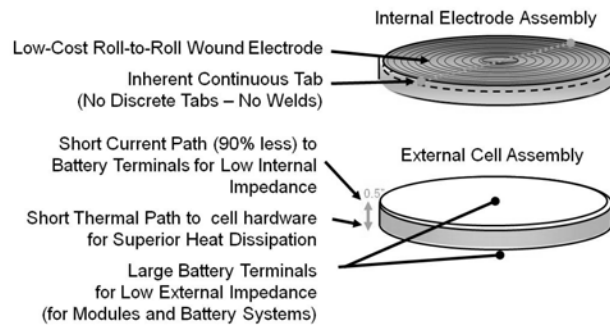


Figure 1, The disc-shaped Rolled-Ribbon cell consists of vertical oriented electrode in a peripherally-sealed housing that enables a stacked-cell battery

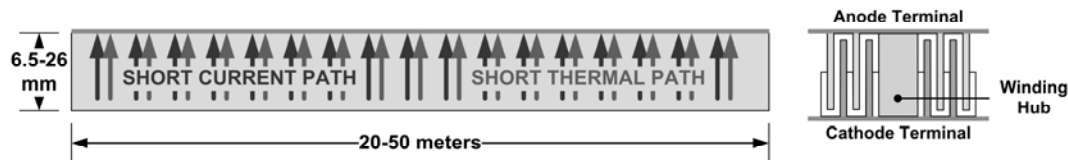


Figure 2, Rolled-Ribbon cell electrode structure brings current and heat effectively from the cell without causing hotspots

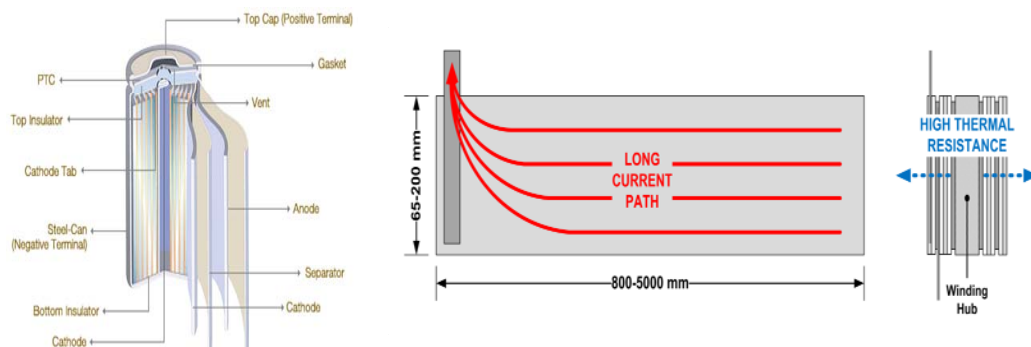


Figure 3, The cylindrical cell by design has a long current (and heat) path that concentrates at the tab to cause a “core” hotspot.

As in Fig. 4, InvenTek’s stacked-cell battery requires no added additional bulky terminals that in conventional cell/battery configurations introduce parasitic power loss from the battery, as well as the additional weight and volume of the terminals. Electrode in contact with the disc-shape R-R cell housing from a quasi-bipolar battery of individually-sealed cells. Flexibility of design is accomplished by varying cell diameter and cell width to package a range of power/energy objectives. These features of the Rolled-Ribbon™ battery lead to cost reductions at both the cell-level and battery level.

For large format batteries requiring 6 to 30Ah capacity, the Rolled-Ribbon™ cell provides 1-10 kW/kg depending on power pulse duration at specific energy exceeding 200 Wh/kg.



Figure 4, Rolled-Ribbon photos: open cell showing electrode ribbon edges, rigid-metal housed cell and stacked-cell battery

Lowered Cell Impedance

In scale-up, a 13 Ah R-R cell that addresses the PHEV (plug-in hybrid) application is twice the capacity of the HEV cell at 6.5Ah capacity. Rolled-Ribbon cell performance has scaled without compromise; cell impedance (DCIR from 10s pulses) of the doubled capacity PHEV cells is 50% of the HEV cells. AC impedance measurements, which measure a cell's impedance network, further verify the reduced impedance of the Rolled-Ribbon and that it has been cut in half for the doubled capacity cell. Reduced cell structural impedance (0.9 mohm, AC impedance) also translated to design efficiency, high utilization of capacity and 2.1 mohm impedance (DCIR).

The lower structural impedance of Rolled-Ribbon (R-R) cells has demonstrated power density increases of 50% or more in side-by-side tests, Figure 5. As a result of the short electrical path, the internal resistance of the cell dropped over 30% vs. a cylindrical test cell using the same chemistry and normalized cell capacity. Similar reduced impedance is measured for pouch cells. As in Figure 6, these cells have shown over 2000 cycles with stable cell impedance under abusive, high rate 10C charge/discharge conditions. This test serves as a verification of the stability of the non-welded electrode/current collector interface. Cells continue on life test with 6500-7000 C-rate cycles at 100% DOD. The magnitude increase in electrode contact to current collector (tabbing) relative to other designs eliminates hotspots. That is 40-50 meters of electrode ribbon edge contact to cell terminal per cell. At the battery level, cylindrical and prismatic cells require complex welded cell interconnect structures and materials. This added space and weight that reduces battery level energy density, adds cost and reduces battery performance. The payoff is that a compact stacked-cell battery facilitated by the R-R battery design, as shown in Figure 3 above, can reduce the space and weight for the total battery pack by up to 50% while improving battery performance.

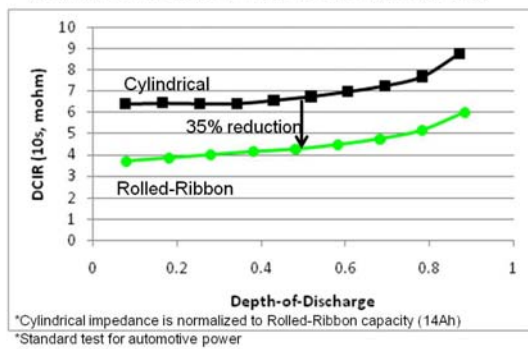


Figure 5, Normalized impedance (DCIR, 10-s pulse) vs. DOD at room temperature. Rolled-Ribbon reduces cell structural impedance.

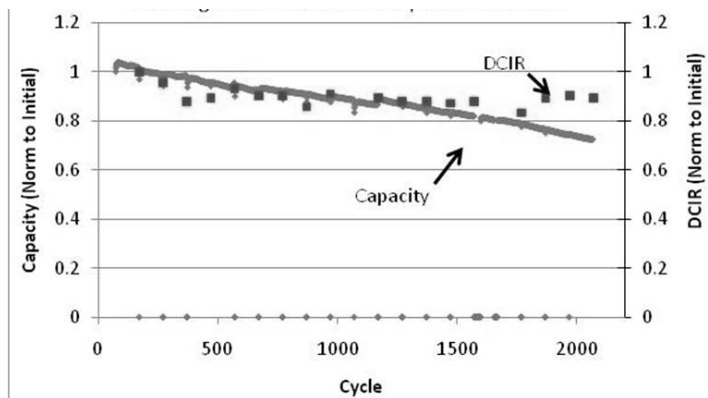


Figure 6, Cell impedance stability of Rolled-Ribbon cell cycled at 10-C rate charge and discharge (at 100% DOD)

Cell and Battery Improvements

Of interest to battery developers for electrified vehicles is the power performance of cells/batteries relative to their state of charge. Especially for the hybrid application (HEV), low impedance at each 10% of cell capacity relates to the batteries ability to accept regenerative braking energy and subsequently deliver it for vehicle acceleration. Figure 7 shows the comparatively low impedance (2.1 mΩ at 50% DOD) of a 13 Ah lithium iron phosphate cell. Cell impedance is determined with 10-sec pulses at every 10% of cell capacity. Here Rolled-Ribbon cell impedance (DCIR) relative to a pouch prismatic is 30% lower across the full capacity of the cell. Again, the structural impedance (ACIR) of the R-R cell is lower when using the same electrode as in the pouch prismatic. The lowered impedance and improved current distribution of R-R is further indicated by the full capacity discharge at high rates, Figure 8. Cell voltage/capacity at increasing C-rates (Peukert) is little changed. The reduced cell voltage is a consequence of the increased IR loss and negligible electrode polarization.

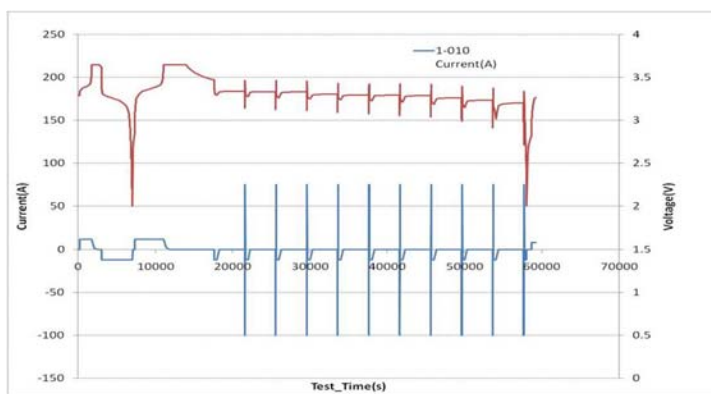


Figure 7, HPPC of Rolled-Ribbon PHEV Cell with 13 Ah capacity, $2.1 \text{ m}\Omega$ at 50% DOD for 100A 10s-pulse

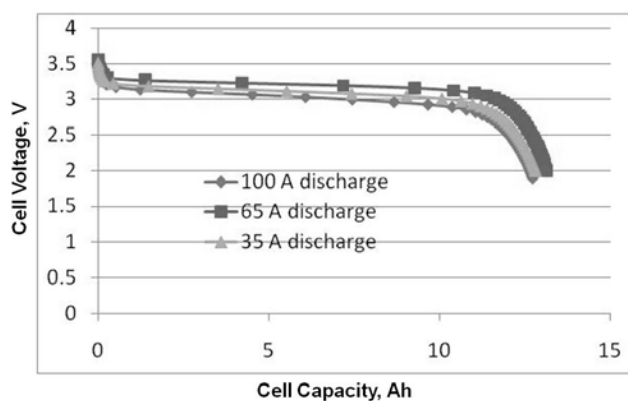


Figure 8, Stable Voltage/capacity of Rolled-Ribbon Cell, 13 Ah capacity, at constant current discharge rates up to 100A

Cell to cell contact via large disc faces transfers current in a quasi-bipolar configuration of individually-sealed cells. The stacked-cell battery can be assembled with less than 10% of additional weight and volume, Figure 4. Rolled-Ribbon cells are simply stacked on top of each other and in direct contact with each other. The large cell surface areas provide low impedance connectivity between the cells without bus bars and welded connections. Further, cell electrodes are in direct contact with cell surface areas, providing low thermal resistance for conducting heat to edges of the cells for battery system thermal management. The superior thermal performance of R-R cells reduces the space, weight and cost associated with battery thermal management, whereas a 100% of additional weight and volume is typically required to build a battery pack with “pouch” cells (also known as prismatic or polymer cells). That savings translates into lower cost, higher energy density Rolled-Ribbon battery with greater energy conversion efficiency. For example, a 50 volt battery pack (30Ah, 1.6 kWh) using C/LFP chemistry at 3.25 volts is 120 Wh/kg and over 200 Wh/liter with 2.5kW/kg. The thermal properties of a stacked-cell battery are seen in Figure 9. Temperature of cells in a Rolled-Ribbon battery (12 Cell Stack) vary less than 2°C during continuous 8C-Rate Discharge to 100% DOD. Each cell R-R dissipates heat independent of its position in the cell stack.

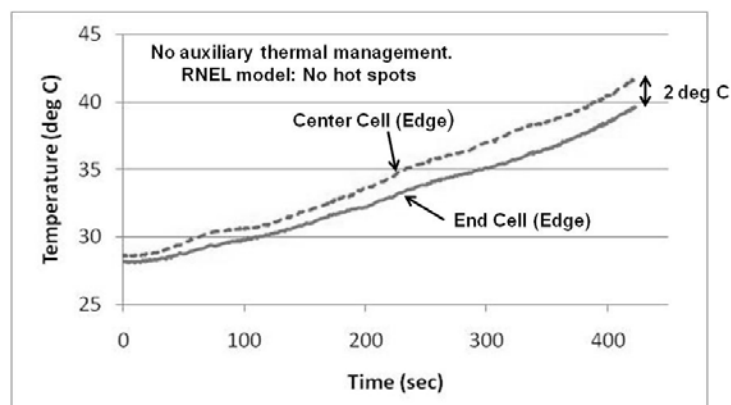


Figure 9, Temperature of Rolled-Ribbon cells in a stacked cell battery (12 Cell Stack) during continuous 8C-Rate Discharge to 100% DOD.

A prototype 220 volt Rolled-RibbonTM battery was installed in place of the NiMH battery of Toyota Prius to show viability of the Rolled-RibbonTM battery architecture for the HEV application. The 220 Volt Rolled-RibbonTM Li-ion battery consisted of five 12-cell modules that were interfaced with a battery management system from EnergyCS (Monrovia CA). Typical road tests with a shadowing car also recorded data from the stock Toyota Prius NiMH battery. The results for the battery performance for the two vehicles are plotted over the same scale of voltage/current to permit a quick visual assessment as in Fig. 10. The expectations of duplicate vehicle test profiles (road course) also seem to be fulfilled. That is, the timing and amplitude of the volt/current swings show great similarity for the two independent vehicles. By comparison, the battery voltage/current swings for the NiMH battery (standard Prius) are substantially larger than for the Rolled-RibbonTM Li-ion battery. Using the change in voltage over the change in current gives the relative battery internal resistances. The internal resistance of the Rolled-RibbonTM Li-ion battery is about 20% less than the stock NiMH battery. That is 20% less power loss and 20% less heat generated. Whereas temperature of the stock Prius battery rose by 10°C and was maintained by the cooling system, the replacement Rolled-Ribbon battery rose only 3°C without a cooling system.

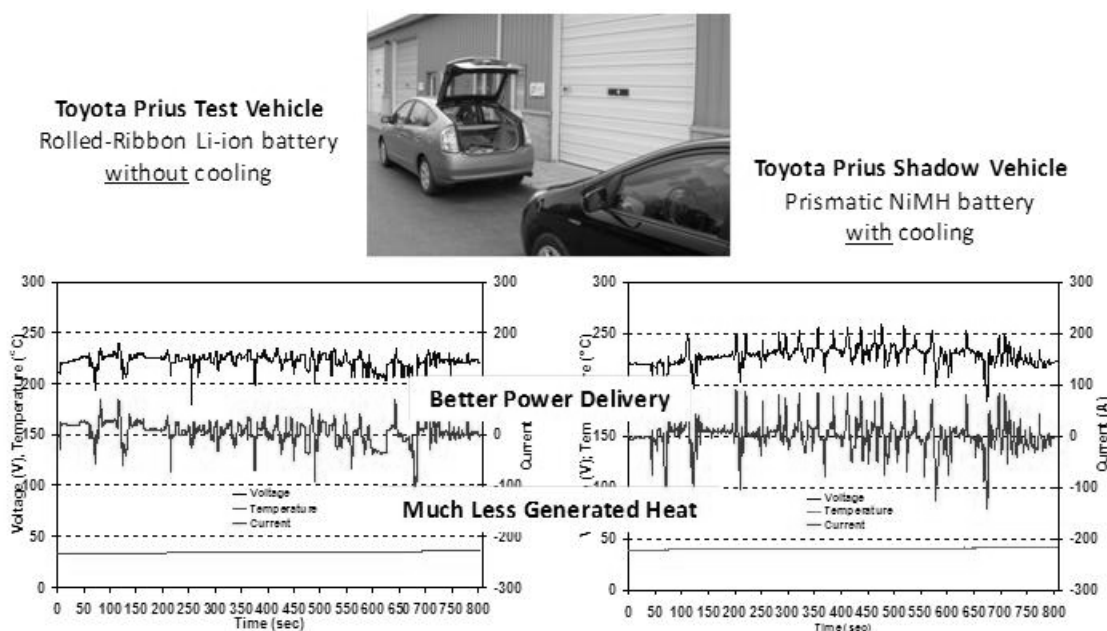


Figure 9, Road test results, voltage and current, of a 220Volt Rolled-Ribbon™ Li-ion battery (left) compared to Prius OEM NiMH battery (shadowing Prius, right) with repetitive acceleration and regen braking using EnergyCS data acquisition

Conclusion

InvenTek has conducted a series of validation tests of the Rolled-Ribbon™ cell format benchmarked against 18650-size cylindrical cell architecture and large pouch prismatic, with shared electrode sourcing. This evaluation has enabled InvenTek to perform a baseline quantification of its internal resistance improvement, and predict the potential cost reductions. Test results have confirmed a 25-35% reduction in internal resistance, as well as a lower cell temperature rise. Our testing also confirms modeling studies that R-R design eliminates hotspots. The Rolled-Ribbon™ cells were able to achieve C-rate full discharge as high as 20C, whereas the some cylindrical cells were unable to achieve a 30 sec pulse capability at 15C rate without excessive temperatures. For c/LFP chemistry, Rolled-Ribbon™ has demonstrated improved deep cycle life stability at greater than 5000 cycles with reduced performance/capacity loss. Also due to lower internal impedance and elimination of hotspots of cells, a R-R battery with stacked cells can be effectively thermal managed without core heating issues. InvenTek has built a 220V, 1.5kWh prototype Rolled-Ribbon™ battery pack and replaced the OEM NiMH pack in a Toyota Prius™. Field tests demonstrate the viability of the Rolled-Ribbon™ battery architecture for hybrid vehicles, without dependence on active thermal management. Compared to cylindrical and pouch cell formats, R-R cells in a stacked-cell battery provides almost doubled energy density along with superior thermal properties.

References

1. T.D. Kaun, US Patent 7,195,840, "Improved Cell Structure for Electrochemical Devices and Method of Making Same", issued March 27, 2007
2. T.D. Kaun, H. Joachin, J Starceвич, B. Kaun, and A. Rundle, "Prototype Rolled-Ribbon Li-ion Battery Testing", Proc. of the 43th Power Sources Symp. p453 (2008).
3. G-H. Kim, K. Smith, "Three-Dimensional Lithium-Ion Battery Model", 4th International Symposium on Large Lithium Lion Battery Technology and Application, Tampa, FL May12-14, 2008

Influence of Impurities in TiO₂ Coatings on Electrode Potential of Photocatalytic Anode Assembling to Marine Microbial Fuel Cell

S. Motoda^a, S. Uematsu^b and T. Shinohara^c

^a Faculty of Marine Engineering, Tokyo University of Marine Science and Technology
2-1-6, Etchujima, Koto-ku, Tokyo 135-8533 Japan

^b Structure Engineering Department, National Maritime Research Institute
6-38-1, Shinkawa, Mitaka, Tokyo 181-0004 Japan

^c Materials Reliability Unit, National Institute for Materials Science
1-2-1 Sengen, Tsukuba, Ibaraki 305-0047 Japan

The electrochemical measurement and surface morphology analysis of TiO₂ coatings were conducted to improve the performance of microbial fuel cell (MFC) in natural seawater. From the experimental results, the 95.2% TiO₂ purity electrode caused the noble shift of electrode potential which resulted from suppression of the photocatalytic effect. This phenomenon did not occur in 99.9% purity coatings, so the influence of impurities such as Si or Zr contained in the coatings was considered. Furthermore, the localized potential at the segregation of Si or Zr was higher than that of the rest, so the electrode potential of TiO₂ coated anode was considered to be affected by the localized corrosion which had occurred beneath the deteriorated TiO₂ coatings.

Introduction

It is well known that the TiO₂ as an n-type semiconductor exhibits the photocatalytic effect under the UV-ray irradiation. When a TiO₂ coated metal is irradiated by the UV light, excited electrons are transferred to the base metal and coating interface, resulting in the active shift of electrode potential. This photocatalytic phenomenon can be applied not only to the protection of corrosion(1), but also to the anodic electrode for a TiO₂ solar battery. On the other hand, ennoblement of potential of the stainless steel electrode by the formation of biofilm in sea water can lead to the development of a battery coupling with active anode. This type of bacterial battery has been referred to as the Microbial Fuel Cell (MFC)(2-9). We have investigated electrochemical characteristics of marine MFC composed of biofilm covered stainless steel cathode and TiO₂ coated stainless steel anode in natural seawater(10,11).

The present work attempted to investigate the influence of impurities into the TiO₂ coatings of anode on the electrochemical properties and to obtain the power density profile of marine MFC.

Experimental

TiO₂ coated Type 329J4L (UNS S32506) stainless steel (S.S.) disk (35mm in diameter, 3mm thickness) and A1050 (UNS A91050) Aluminum coupon (20mm ×

100mm, 2mm thickness) were used as a photocatalytic anode. TiO_2 coatings were accomplished by a plasma spraying onto a surface previously Al_2O_3 blasted. The TiO_2 powder was crushed and sieved to $-44+10\mu\text{m}$ in diameter from an original ore. The chemical composition of powder (wt.%) was as follows, Fe_2O_3 :0.7, ZrO_2 :0.6, SiO_2 :1.10, Al_2O_3 :0.40, P:0.01, S: 0.02, TiO_2 :95.2. For the comparison, a sintered TiO_2 powder which was purified to 99.9% was also used. The thickness of both coatings was 80~100 μm and the TiO_2 crystal structure was dominantly rutile. TiO_2 coated samples were immersed in 300mL artificial seawater and open circuit potential (OCP) was measured by a potentiostat (Syrinx,SDPS-501C) with a saturated calomel electrode (SCE) as reference. The schematic representation of experimental apparatus was shown in Figure 1. The TiO_2 coating was irradiated by the 150W Xenon lamp (Hamamatsu Photonics,L7810) in which a calibrated wave length was 250nm to 800nm. The quantity of light on the sample surface was 10.5mW/cm². The surface morphology and chemical analysis for the TiO_2 coatings were carried out by SEM/EDS.

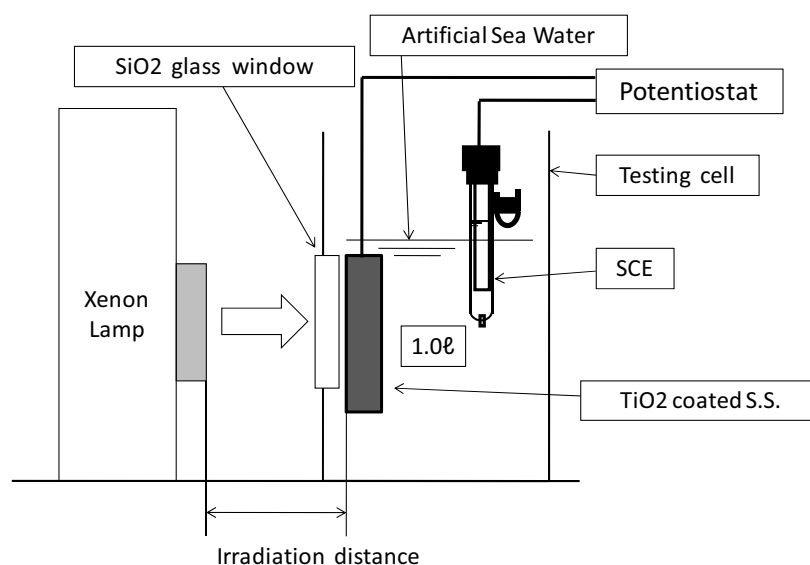


Figure 1. Schematic representation of experimental apparatus of Xe light irradiation and electrochemical cell.

Results and Discussion

Figure 2 show the time variations of electrode potential of TiO_2 coated Type 329J4L stainless steel and A1050 Aluminum immersed in the artificial seawater under the Xe light irradiation. For 99.9% purity TiO_2 sample, in Figure 2(a), potential before irradiation of $0.1V_{\text{SCE}}$ were shifted to $-0.5V_{\text{SCE}}$ in 10 min and stabilized by 120 min. However, for TiO_2 95.2% sample the potential shifted to $-0.33V_{\text{SCE}}$ but rebounded to noble direction at 20 min. The potential of 95.2% sample at 120 min was $-0.26V_{\text{SCE}}$ and was 0.24V higher than that of 99.9%. When former was assembled to the MFC as an anode it would be resulted in the decrease of power of cell. To confirm this deterioration of photocatalytic effect for 95.2% purity TiO_2 electrode the Aluminum base metal was used as shown in Figure 2(b).

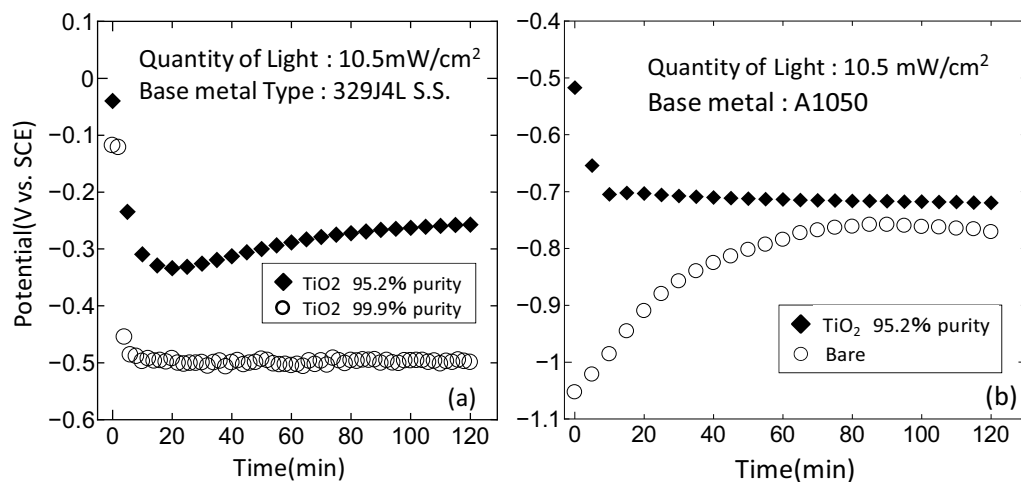


Figure 2. Time variations of electrode potential for TiO₂ coated samples on (a) Type 329J4L stainless steel and (b) A1050 Aluminum.

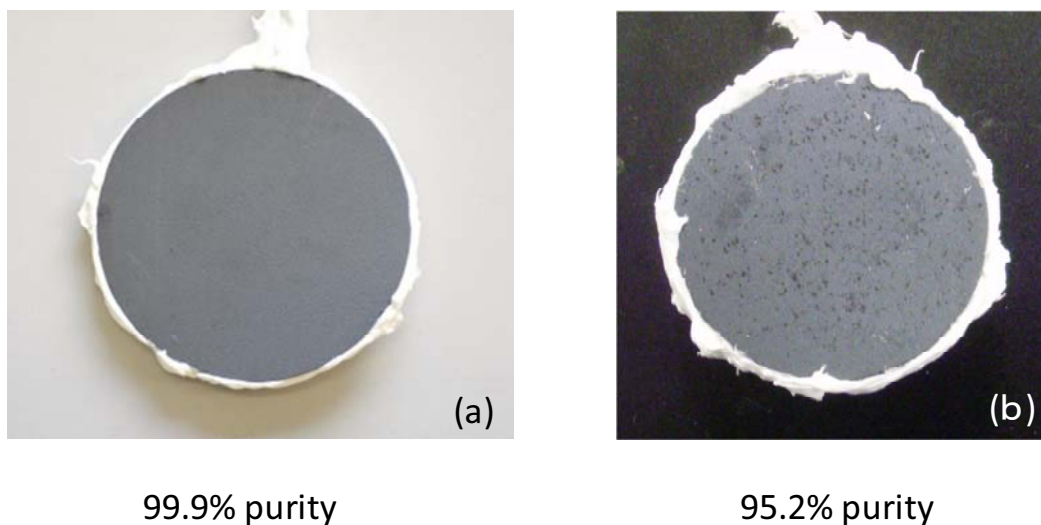


Figure 3. Appearance of Type 329J4L stainless steel base metals coated with (a) 95.2% and (b) 99.9% purity TiO₂ powder. On the surface of TiO₂ 95.2% sample, there appeared dark tarnishes under the Xenon light irradiation.

The potential of 95.2% purity TiO₂ sample coated on A1050 shifted to $-0.7V_{SCE}$ and stabilized by 120 min. However, as potential at 120 min was the almost same with that of bare A1050, so it was considered that the coatings of 95.2% purity TiO₂ showed insufficient photocatalytic effect on the both stainless steel and Aluminum base metals.

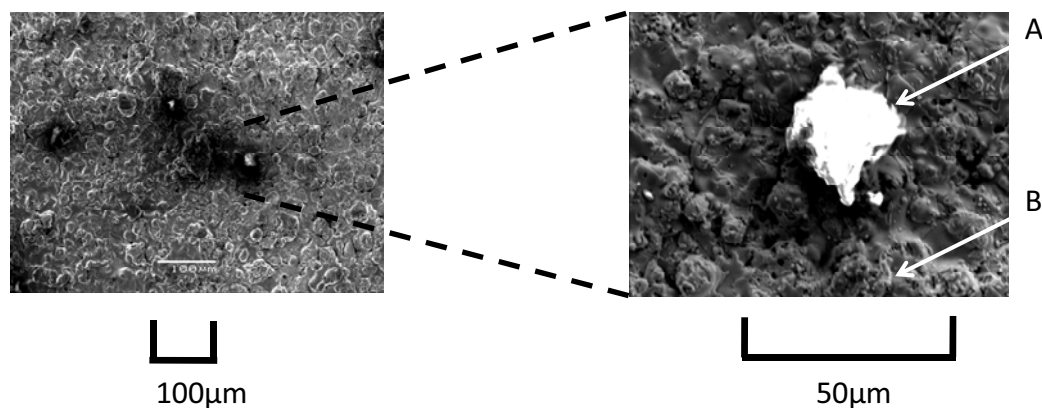


Figure 4. SEM image of tarnish on the TiO_2 95.2% coatings of Type 329J4L S.S. as shown in Figure 3(b) and its enlarged.

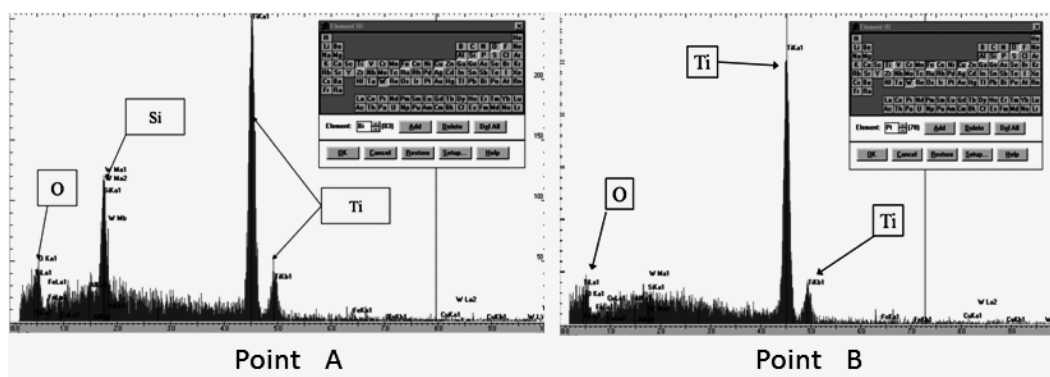


Figure 5. EDS patterns identified by the SEM observations at points “A” and “B” marked in Figure 4.

Only for the TiO_2 95.2% coated Type 329J4L samples, there appeared dark tarnishes (around 1mm in diameter) on the surface of coatings after Xe light irradiation as shown in Figure 3(b). At the center of the tarnish there identified a core around $30\mu\text{m}$ in diameter by the SEM observations as shown in Figure 4. Figure 5 show the results of EDS analysis where the core of marked “A” and its surroundings of marked “B” in Figure 4. From the analysis no impurities element detected at point “B”, instead Si was detected at point “A”. So the core of tarnish was estimated to be a segregation of SiO_2 which had been contained in the TiO_2 powder of coating material.

SEM / EDS analysis for the 95.2% purity TiO_2 coated sample on A1050 was conducted as shown in Figure 6 and Figure 7. The tarnish spot was also appeared in this sample, and Si was detected as shown in Figure 7(a). In other tarnished points, also Zr was detected (Figure 7(b)). Then the tarnish on the coatings of TiO_2 95.2% purity coatings for Type 329J4L and A1050 base metals appeared to be SiO_2 and ZrO_2 , both of them were considered to be the separately splashed materials on the coating surface during the plasma spray process, as contained with the impurities of TiO_2 powder material.

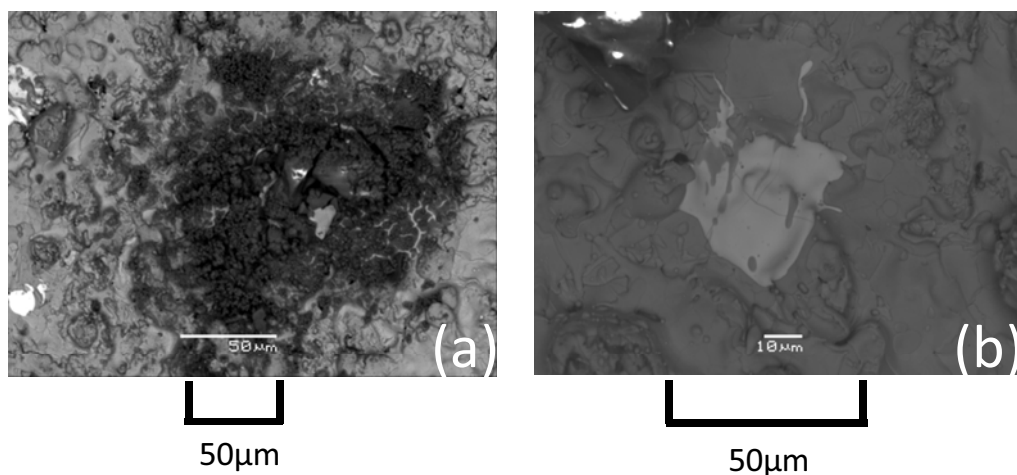


Figure 6. SEM images of tarnish after the irradiation of Xe light on the 95.2% purity TiO_2 sample coated on the A1050 substrate.

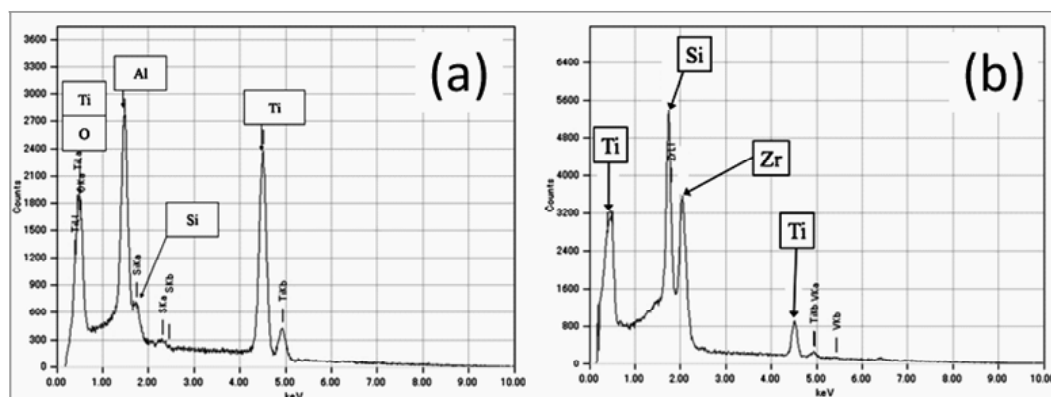


Figure 7. EDS patterns at the tarnishes identified by SEM observations those were shown in Figure 6(a) and (b).

Surface potential distribution by means of scanning vibrating micro-probe was shown in Figure 8 and 9. The localized potential at the tarnish was found to be 0.2V higher in maximum than that of surrounding of the tarnish. The critical potential of crevice corrosion for Type 316 S.S. substrate at 25°C in sea water is referred to as $-300\text{mV}_{\text{SCE}}$ (12). On the assumption that the critical potential for Type 329J4L S.S. is not so much different from that of Type 316 S.S., the potential of $-0.26\text{V}_{\text{SCE}}$ at 120min shown in Fig.2(a) is nobler than that of the critical potential. So the crevice corrosion followed by the restriction of photocatalytic reaction might have occurred beneath the tarnishes.

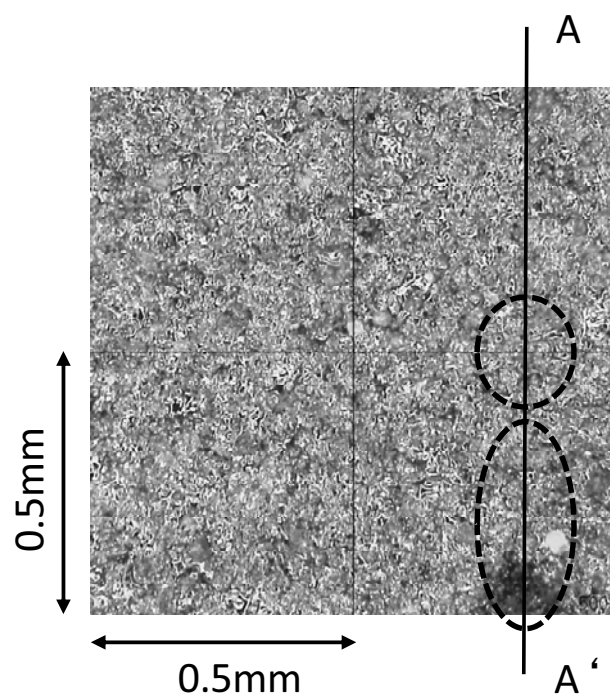


Figure 8. Appearance of 95.2% purity TiO_2 coated Type 329J4L under the Xe light irradiation. Circles indicate the tarnishes shown in Fig.3 (b), and the surface potential along the A-A' line was measured.

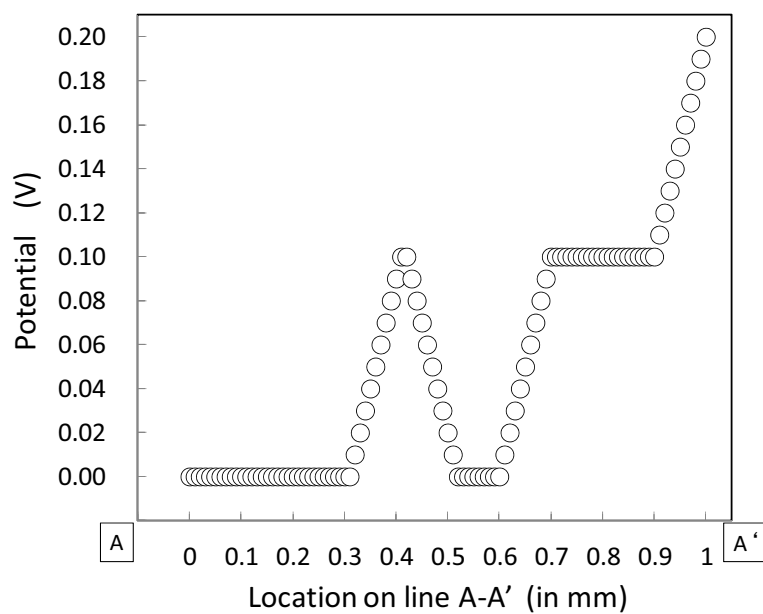


Figure 9. Localized surface potential distribution on the A-A' line of Fig.8.

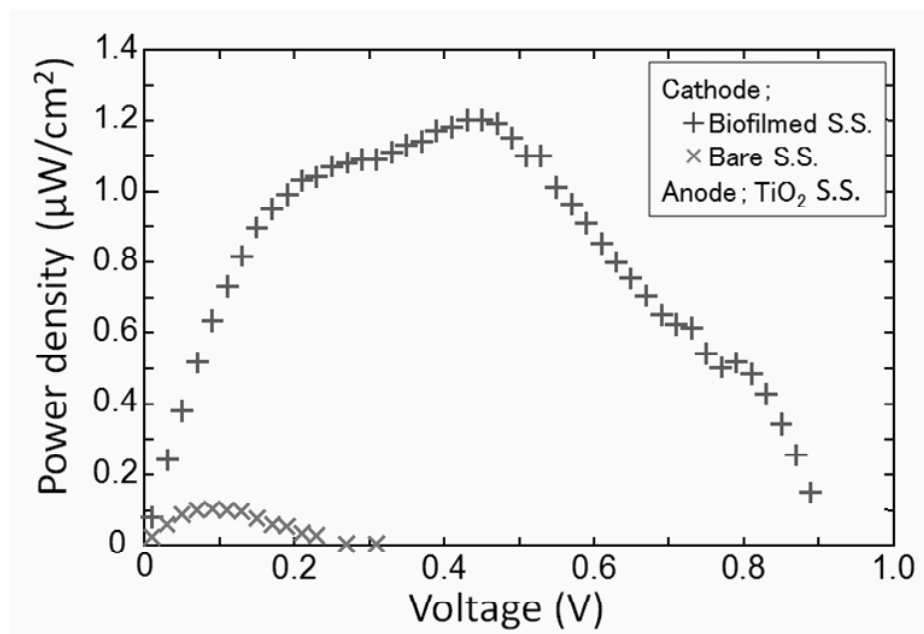


Figure 10. Power density profile of marine MFC composed of biofilm formed Type 316 S.S. cathode and 99.9% TiO_2 coated Type 329J4L S.S. anode under the irradiation of 10.5mW/cm^2 Xe light.

The power density profile of MFC composed of biofilm-covered Type 316 stainless steel cathode and TiO_2 coated Type 329J4L S.S. anodes was shown in Figure 10. The relation between cell voltage (V) and output current density (i) was measured by single sweep polarization, and electric power density was calculated. In the figure the peak power of $1.2\mu\text{W/cm}^2$ at 0.5V was obtained with biofilmed cathode couple, so the cell power should be resulted from action of microorganisms in sea water. On the other hand, the peak at 0.1V for without biofilmed cathode couple was estimated to be the oxygen reduction reaction on the TiO_2 anode. So, the MFC assembled TiO_2 99.9% purity anode was appeared to produce over $1\mu\text{W/cm}^2$ power density without any deterioration of TiO_2 coatings.

Conclusions

The present work investigated the effect of impurities into the TiO_2 coatings on the electrochemical characteristics. The deterioration of anode by the suppression of photocatalytic effect of coatings was considered to be the result from localized corrosion. Results obtained here are shown as follows;

1. The degradation of photocatalytic reaction observed in the 95.2% purity TiO_2 coatings did not appear in 99.9% purity coatings.
2. Assembling the anode coated in 99.9% purity TiO_2 to the MFC, over $1\mu\text{W/cm}^2$ power density was produced.

Acknowledgement

Part of this work was supported by a Grant-in-Aid for Scientific Research from the Japan Society for the Promotion of Science (No.18651043).

References

- 1.R.Fujisawa,T.Shinohara,and S.Tsujikawa:*Proceedings of 40th Japan Corrosion Conference*,p.37(1993)
- 2.L.M.Tender,C.E.Reimers,H.A.StecherIII,D.E.Homes,D.R.Bond,D.A.Lowy,K.Piobello S.J.Fertig and D.R.Lovley, *Nature Biotechnology*,**20**,815(2002).
- 3.C.E.Reimers,P.Girguis,H.A.StecherIII,L.M.Tender,N.Rycklynck and P.Whaling *Geobiology*, **4**, 123(2006) .
4. F.Mansfeld, *Electrochimica Acta* ,**52**, 7670 (2007) .
5. K.Scott and C. and Murano, *J. of Chem. Tech. and Biotech.*,**82** ,809(2007).
- 6.K.Scott,I.Cotlarciuc,I.Head,K.P.Katuri,D.Hall,J.B.Laleman,and D.Browing, *J. of Chem. Tech. and Biotech.*, **83**,1224(2008).
- 7.C.Dams,A.Mollica,D.Feron,R.Baaeguy,L.Etchevery,andA.Bergel, *Bioresource Tch.* **99**,8887(2008).
- 8.Z.Liu,H.LI,J.Liu,and Z.Su, *J. of Applied Microbiology*, **104**,1163(2008).
- 9.D.E.Holmes,J.S.Nicoll,D.R.Band,D.R.Lovely, *Applied and Environmental Microbiology*, **70**,60233(2004).
- 10.S.Motoda,M.J.Strom, and S.C.Dexter : *ECS transactions*,**16**,43,pp.155-162(2009).
11. S.Motoda,M.J.Strom, and S.C.Dexter :*ECS transactions*,**25**,35,pp.3-10(2010)
12. S.Tsujikawa,Y.Hisamatsu: *Corrosion Engineering of Japan*,**29**,37(1980)

Author Index

Abraham, K.	27	Lymberopoulos, N.	35
Asercion, J.	55		
		Maier, U.	43
Bocchetta, P.	79	Manabe, A.	1
Braustein, H. E.	9	Motoda, S.	129
Caillon-Caravanier, M.	65	Pal, U. B.	91
Claude-Montigny, B.	65	Powell, A. C.	91
Conciauro, F.	79		
Cubeta, U.	55	Rane-Fondacaro, M. V.	103
		Ranganathan, S.	111
Demeaux, J.	65		
Devarajan, T.	103	Sandahl, J.	121
Di Quarto, F.	79	Santamaria, M.	79
		Shinohara, T.	129
Easton, E.	111	Stuart, J.	55
Edge, P. S.	111		
		Uematsu, S.	129
Friedrich, K.	43		
		Wang, B.	55
Galiano, H.	65	Westner, C.	43
Guan, X.	91	Willich, C.	43
		Wu, H.	55
Haldar, P.	103		
Hashimoto, T.	1	Yazici, M.	35
Hatipoglu, M.	35		
Henke, M.	43	Zink, P. A.	91
Hettige, C.	55		
Higashiya, S.	103		
Kallo, J.	43		
Kashiwase, M.	1		
Kaun, T. D.	121		
Lau, J.	55		
Lemordant, D.	65		
Leucht, F.	43		
Licht, S.	55		